



Test Report No. 440873-01



**DEVELOPMENT OF A *MASH* TL-4 PORTABLE CONCRETE BARRIER
WITH LARGE SCUPPER**

Sponsored by the
Texas Department of Transportation (TxDOT)

TEXAS A&M TRANSPORTATION INSTITUTE PROVING GROUND

Roadside Safety & Physical Security
Texas A&M University System RELLIS Campus
Building 7091
1254 Avenue A
Bryan, TX 77807



1. Report No. FHWA/TX-23/0-7087-R1		2. Government Accession No.		3. Recipient's Catalog No.	
4. Title and Subtitle DEVELOPMENT OF A <i>MASH</i> TL-4 PORTABLE CONCRETE BARRIER WITH LARGE SCUPPER				5. Report Date Published: November 2024	
				6. Performing Organization Code	
7. Author(s) Roger P. Bligh, Chiara Silvestri-Dobrovolny, Blair A. Johnson, Michael E. Barrett, James Holyoke, Greg Hendrickson, Aniruddha Zalani, and William J. L. Schroeder				8. Performing Organization Report No. Report 0-7087-R1 Crash Report 440873-01	
9. Performing Organization Name and Address Texas A&M Transportation Institute The Texas A&M University System College Station, Texas 77843-3135				10. Work Unit No. (TRAIS)	
				11. Contract or Grant No. Project 0-7087	
12. Sponsoring Agency Name and Address Texas Department of Transportation Research and Technology Implementation Office 6230 E Stassney Lane Austin, Texas 78744				13. Type of Report and Period Covered Technical Report: August 2020–December 2022	
				14. Sponsoring Agency Code	
15. Supplementary Notes Project sponsored by the Texas Department of Transportation and the Federal Highway Administration. Project Title: Develop Standards for Temporary Concrete Median Barrier in Flood-Prone Areas URL: https://tti.tamu.edu/documents/0-7087-R1.pdf					
16. Abstract Portable concrete barriers are commonly used as temporary positive protection in work zone applications to shield motorists from hazards in the work zone and protect workers from errant vehicles. They are also used in permanent applications as a median barrier to mitigate serious cross-median crashes by preventing penetration of errant vehicles into oncoming traffic. When implemented in flood-prone areas, the solid nature of these portable concrete barriers can act as a dam to floodwaters, as seen in Texas during Hurricane Harvey. This damming effect can raise the height of floodwaters and increase the severity of flooding on highways and surrounding roads and in communities. Floodwaters can also push long lengths of free-standing portable concrete barriers across multiple lanes of a freeway, effectively closing the facility until the barrier can be disconnected and reinstalled or transported off site. In this study, a new portable concrete barrier with large openings (i.e., drainage scuppers) was developed to help mitigate the effects and consequences of severe flooding on a roadway and the adjacent community. Finite element simulations were used to evaluate design features, and laboratory testing was performed to evaluate the hydraulic efficiency of barrier designs in a variety of simulated flood conditions. A concrete single-slope profile median barrier with a large scupper was selected for crash testing in accordance with American Association of State Highway and Transportation Officials <i>Manual for Assessing Safety Hardware (MASH)</i> Test Level 4 (TL-4) impact conditions and evaluation criteria. The portable concrete barrier with large scuppers was determined to be <i>MASH</i> TL-4 compliant and is available for implementation in areas susceptible to flooding, with the goals of reducing flooding severity, decreasing risk to motorists, and reducing the level of flood damage to both highways and surrounding areas.					
17. Key Words Longitudinal Barrier, Portable Concrete Barrier, Single-Slope Concrete Barriers, <i>MASH</i> , Crash Test, Roadside Safety, Hydraulics, Hydraulic Testing, Drainage Scupper			18. Distribution Statement No restrictions. This document is available to the public through NTIS: National Technical Information Service Alexandria, Virginia 22312 http://www.ntis.gov		
19. Security Classif. (of this report) Unclassified		20. Security Classif. (of this page) Unclassified		21. No. of Pages 252	
				22. Price	

DEVELOPMENT OF A *MASH* TL-4 PORTABLE CONCRETE BARRIER WITH LARGE SCUPPER

by

Roger P. Bligh, Ph.D., P.E.
Senior Research Engineer
Texas A&M Transportation Institute

Chiara Silvestri-Dobrovolsky, Ph.D.
Former Research Scientist
Texas A&M Transportation Institute

Blair A. Johnson, Ph.D.
Assistant Professor
University of Texas at Austin

Michael E. Barrett, Ph.D., P.E.
Research Professor
University of Texas at Austin

James Holyoke
Graduate Research Assistant
University of Texas at Austin

Greg Hendrickson
Graduate Research Assistant
University of Texas at Austin

Aniruddha Zalani
Graduate Research Assistant
Texas A&M Transportation Institute

William J. L. Schroeder
Research Engineering Associate
Texas A&M Transportation Institute

Report 0-7087-R1
Project 0-7087

Project Title: Develop Standards for Temporary Concrete Median Barrier in Flood-Prone Areas

Sponsored by the
Texas Department of Transportation
and the
Federal Highway Administration

Published: November 2024

TEXAS A&M TRANSPORTATION INSTITUTE
College Station, Texas 77843-3135

DISCLAIMER


This research was sponsored by the Texas Department of Transportation (TxDOT) and the Federal Highway Administration (FHWA). The contents of this report reflect the views of the authors, who are responsible for the facts and the accuracy of the data presented herein. The contents do not necessarily reflect the official view or policies of FHWA or TxDOT. This report does not constitute a standard, specification, or regulation.

This report is not intended for construction, bidding, or permit purposes. The engineer (researcher) in charge of the project was Roger P. Bligh, P.E. # 78550.

TTI PROVING GROUND DISCLAIMER

The results of the crash testing reported herein apply only to the article tested.

REPORT AUTHORIZATION



Bill L. Griffith, Research Specialist
Deputy Quality Manager



William J. L. Schroeder, Research
Engineering Associate
Research, Evaluation, and Reporting



Matthew N. Robinson, Research
Specialist
Test Facility Manager & Technical
Manager



Roger P. Bligh, P.E., Senior Research
Scientist

ACKNOWLEDGMENTS

This project was sponsored by TxDOT and FHWA. The research team would like to thank Mr. Wade Odell, P.E., and Mr. Darrin Jensen (TxDOT project managers) along with the following Project Monitoring Committee members for their valuable assistance, input, and guidance on this project: Ken Mora, Rose Marie Klee, and Abderrahmane Maamar-Tayeb from the Design Division; Taya Retterer and John Riley from the Bridge Division; Adam Jack from the Beaumont District; and Prassana Chebbi from the Houston District. Portions of this research were conducted with computing resources provided by Texas A&M University High Performance Research Computing (<https://hprc.tamu.edu>).

TABLE OF CONTENTS

	Page
List of Figures	xii
List of Tables	xvii
Chapter 1. Introduction.....	1
Chapter 2. Literature Review	5
2.1. Floodway Encroachment	5
2.2. Energy in Open Channel Flow	5
2.2.1. Bernoulli's Equation	5
2.2.2. Weir Equation.....	7
2.3. Physical Model and Scaling	9
2.4. Charbeneau Model	10
2.4.1. Type 1 Flow	11
2.4.2. Type 2 Flow	11
2.4.3. Type 3 Flow	12
2.5. Experimental Methods for Charbeneau Model.....	13
2.6. Charbeneau Results	14
2.7. Streamlined Barrier Openings.....	15
2.7.1. Flow Separation	15
2.7.2. Drag Coefficients.....	16
2.8. Stability of Concrete Barrier	16
2.9. Buoyancy of Concrete Barrier	18
2.10. Conservation of Linear Momentum	19
2.11. Measurement of Hydrodynamic Forces	20
2.12. Impact Performance of Concrete Barrier Systems with Openings	21
2.13. Roadside Safety Pooled Fund Project 612831— <i>MASH</i> Evaluation of F-shape and Single-Slope Concrete Barriers with Drainage Scuppers.....	26
2.13.1. <i>MASH</i> Test 3-11 on Free-Standing F-shape Barrier with Drainage Scuppers.....	26
2.13.2. <i>MASH</i> Test 3-11 on Pinned F-shape Barrier with Drainage Scuppers...	27
2.13.3. <i>MASH</i> Test 4-12 on Embedded Single-Slope Barrier with Drainage Scuppers.....	27
2.14. TxDOT Project 0-6976—Development and <i>MASH</i> TL-4 Evaluation of TxDOT Large-Scupper Median Barrier for Flood-Prone Areas	28
2.15. Conclusions	29
Chapter 3. Design Options	31
3.1. Option A: 42-Inch-Tall Precast Single-Slope Concrete Median Barrier with One Scupper.....	31
3.2. Option B: 42-Inch-Tall Precast Single-Slope Concrete Median Barrier with Two Scuppers.....	31
3.3. Option C: 42-Inch-Tall Precast Single-Slope Concrete Median Barrier with Three Scuppers	34
3.4. Hydraulic Calculations for Proposed Designs	35
3.5. Conclusions	37

Chapter 4. Large-Scale Hydraulic Testing	39
4.1. Experimental Facility.....	39
4.1.1. Reservoir and Pipe Network	39
4.1.2. Test Channel.....	40
4.1.3. Return Channel.....	40
4.2. Barrier Construction	41
4.2.1. Support Base	41
4.2.2. Median Barrier Model.....	42
4.2.3. Setup in Channel.....	43
4.3. Instrumentation and Data Collection	43
4.3.1. Bubble Flow Meters	44
4.3.2. Upstream Water Depth	44
4.3.3. Discharge Weir.....	45
4.3.4. Point Gage and Flow Rate	46
4.3.5. Acoustic Doppler Velocimeter	47
4.3.6. Strain Gages	50
4.3.7. Data Acquisition System Configuration	51
4.3.8. Force Measurements	53
4.4. Hydraulic Testing Results and Analysis	53
4.4.1. Water Depth and Flow Rate	54
4.4.2. Rating Curve	55
4.4.3. Calibrated Model Curve for Model Median Barrier	56
4.4.4. Point Velocity	57
4.4.5. Hydrodynamic Force Calculations.....	63
4.4.6. Stability Calculations	63
4.4.7. Force on the Model Barrier	65
4.5. Summary and Conclusions	66
Chapter 5. Finite Element Simulation Analysis	69
5.1. Introduction	69
5.2. Single-Slope Barrier Models	70
5.3. Predictive Simulations of Single-Slope Barrier.....	71
5.3.1. Baseline Impact Simulations of <i>MASH</i> Tests on Single-Slope Barrier ...	71
5.3.2. Impact Simulations of Single-Slope Barrier with Scupper and J-J Hooks Connections	75
5.3.3. Conclusions for Impact Simulations of Single-Slope Barrier with Scupper and J-J Hooks Connections	83
5.3.4. Impact Simulations of Single-Slope Barrier with Scupper and X-bolt Connections	90
5.3.5. Conclusions for Impact Simulations of Single-Slope Barrier with Scupper and X-bolt Connections.....	97
5.4. Model Calibration	104
5.5. <i>MASH</i> Test 4-12 Predictive Simulation	105
Chapter 6. System Details	111
6.1. Test Article and Installation Details	111
6.2. Design Modifications during Tests	111
6.3. Material Specifications	116

Chapter 7. Test Requirements and Evaluation Criteria.....	117
7.1. Test Performed/Matrix	117
7.2. Evaluation Criteria.....	118
Chapter 8. Test Conditions.....	121
8.1. Test Facility.....	121
8.2. Vehicle Tow and Guidance System	121
8.3. Data Acquisition Systems	121
8.3.1. Vehicle Instrumentation and Data Processing	121
8.3.2. Anthropomorphic Dummy Instrumentation	122
8.3.3. Photographic Instrumentation Data Processing	123
Chapter 9. MASH Test 4-10 (Test 440873-01-1).....	125
9.1. Test Designation and Actual Impact Conditions	125
9.2. Weather Conditions	127
9.3. Test Vehicle	127
9.4. Test Description	129
9.5. Damage to Test Installation	129
9.6. Damage to Test Vehicle.....	131
9.7. Occupant Risk Factors.....	135
9.8. Test Summary.....	135
Chapter 10. MASH Test 4-11 (Test 440873-01-2).....	137
10.1. Test Designation and Actual Impact Conditions	137
10.2. Weather Conditions	139
10.3. Test Vehicle	139
10.4. Test Description	141
10.5. Damage to Test Installation	141
10.6. Damage to Test Vehicle.....	143
10.7. Occupant Risk Factors.....	146
10.8. Test Summary.....	147
Chapter 11. MASH Test 4-12 (Test 440873-01-3).....	149
11.1. Test Designation and Actual Impact Conditions	149
11.2. Weather Conditions	151
11.3. Test Vehicle	151
11.4. Test Description	153
11.5. Damage to Test Installation	153
11.6. Damage to Test Vehicle.....	155
11.7. Occupant Risk Factors.....	158
11.8. Test Summary.....	158
Chapter 12. Crash Test Summary and Conclusions	161
12.1. Assessment of Test Results	161
12.2. Conclusions	161
Chapter 13. Implementation	163
References	165
APPENDIX A. Details of Large-Scupper Portable Concrete Barrier	167
A.1. Details of Large-Scupper Portable Concrete Barrier for Tests 440873-01-1 and 440873-01-2.....	167
A.2. Details of Large-Scupper Portable Concrete Barriers for Test 440873-01-3....	177

APPENDIX B. Supporting Certification Documents	187
APPENDIX C. MASH Test 4-10 (Test 440873-01-1).....	199
C.1. Vehicle Properties and Information	199
C.2. Sequential Photographs.....	202
C.3. Vehicle Angular Displacements	205
C.4. Vehicle Accelerations.....	206
APPENDIX D. MASH Test 4-11 (Test 440873-01-2).....	209
D.1. Vehicle Properties and Information	209
D.2. Sequential Photographs.....	212
D.3. Vehicle Angular Displacements	215
D.4. Vehicle Accelerations.....	216
APPENDIX E. MASH Test 4-12 (Test 440873-01-3).....	219
E.1. Vehicle Properties and Information	219
E.2. Sequential Photographs.....	221
E.3. Vehicle Angular Displacements	224
E.4. Vehicle Accelerations.....	225
APPENDIX F. Value of Research.....	227
F.1. Introduction	227
F.2. Qualitative Benefit Areas	228
F.3. Economic Benefits	228
F.4. Computed Value of Research	229
F.5. Discussion	232
F.6. References	232

LIST OF FIGURES

	Page
Figure 1.1. Examples of Flooding Where Solid Concrete Median Barriers Were Installed (2, 3).	1
Figure 1.2. Examples of Flooding Where Portable Concrete Barrier Was Installed as Permanent Median Barrier (4, 5).	2
Figure 2.1. Specific Energy Curve (9).	6
Figure 2.2. Sharp-Crested Weir (11).	8
Figure 2.3. Three Flow Cases in Charbeneau Model (9).	10
Figure 2.4. Experimental Setup for Bridge Rail in Rectangular Channel (18).	13
Figure 2.5. Bridge Rail Rating Curves (9).	14
Figure 2.6. Bridge Rail Examples (9).	15
Figure 2.7. Free Body Diagram for Typical Median Barrier.	17
Figure 2.8. WSDOT Barrier Test 3-11 (22).	22
Figure 2.9. Revised WSDOT Barrier Test 3-11 (23).	22
Figure 2.10. Side-View Comparison of LaDOTD F-shape Barrier, TxDOT Wildlife Crossing Single-Slope Concrete Barrier (SSCB), and WSDOT Pin-and-Loop Barrier (24).	23
Figure 2.11. Opening in Concrete Barrier to Allow for Rubber Block Installation (25).	24
Figure 2.12. TxDOT SSCB (Wildlife Crossing) (24).	24
Figure 2.13. MassDOT F-shape PCB (26).	25
Figure 2.14. Concrete Crack after MASH Test 2-11 (26).	25
Figure 2.15. Concrete Crack after MASH Test 3-11 on MassDOT Retrofit PCB System (26).	26
Figure 2.16. Test Installation for Free-Standing F-shape Barrier with Drainage Scuppers (27).	27
Figure 2.17. Test Article for F-shape Barrier with Drainage Scuppers (27).	27
Figure 2.18. Test Article for Embedded Single-Slope Barrier (27).	28
Figure 2.19. TxDOT Large-Scupper Median Barrier Test Article for MASH TL-4 Testing (28).	28
Figure 3.1. Option A Preliminary Drawing.	32
Figure 3.2. Option B Preliminary Drawing.	33
Figure 3.3. Option C Preliminary Drawing.	34
Figure 4.1. Flume Layout (15).	39
Figure 4.2. Pump Outlets (15).	40
Figure 4.3. General Model Barrier (15).	41
Figure 4.4. Support Base Design and Installation (15).	42
Figure 4.5. SSCB Model Barrier Dimensions (not to scale).	43
Figure 4.6. Bubble Flow Meters and Solar Panel Housing Unit (15).	44
Figure 4.7. Upstream Water Depth Measurement Locations (15).	45
Figure 4.8. Discharge Weir and Orifice Gate (15).	46
Figure 4.9. Point Gage (15).	46
Figure 4.10. Nortek Vectrino (ADV) (31).	47

Figure 4.11. ADV Setup to Record Point Velocities Upstream of the Median Barrier....	48
Figure 4.12. ADV Setup in Scupper.	49
Figure 4.13. Strain Gage and Wiring on Barrier.	51
Figure 4.14. Strain Gage Setup after Environmental Coating.	51
Figure 4.15. cDAQ and NI 9237 Module Setup.	52
Figure 4.16. Screw Terminals.	52
Figure 4.17. Strain Gage Bonding Sites on Model Barrier (not to scale).	53
Figure 4.18. Rating Curve for SSCB Model Median Barrier.	56
Figure 4.19. Calibrated Model Curve for SSCB Model Median Barrier.	57
Figure 4.20. Mean Downstream (x) Velocity Profiles across Channel.	59
Figure 4.21. Mean Downstream (x) Velocity Profiles above Model Barrier Base.	61
Figure 4.22. Mean Downstream (x) Velocity Profiles inside Scupper Opening.	62
Figure 5.1. Bogie Model Positioned to Impact Center of Four-Segment Barrier Model.	70
Figure 5.2. Comparison of Bogie Vehicle Test (left) and Bogie Vehicle Impact Simulation (right).	71
Figure 5.3. Overhead Images of <i>MASH</i> Test 3-11 Simulation with Single-Slope Barrier.	72
Figure 5.4. End-View Images of <i>MASH</i> Test 3-11 with Single-Slope Barrier.	73
Figure 5.5. Overhead Images of <i>MASH</i> Test 3-10 Simulation with Single-Slope Barrier.	74
Figure 5.6. End-View Images of <i>MASH</i> Test 3-10 Simulation with Single-Slope Barrier.	75
Figure 5.7. Overhead Images of <i>MASH</i> Test 3-11 Simulation of Single-Slope Barrier with Scupper—Impact Location A.	77
Figure 5.8. End-View Images of <i>MASH</i> Test 3-11 Simulation of Single-Slope Barrier with Scupper—Impact Location A.	78
Figure 5.9. Overhead Images of <i>MASH</i> Test 3-11 Simulation of Single-Slope Barrier with Scupper—Impact Location B.	79
Figure 5.10. End-View Images of <i>MASH</i> Test 3-11 Simulation of Single-Slope Barrier with Scupper—Impact Location B.	80
Figure 5.11. Overhead Images of <i>MASH</i> Test 3-11 Simulation of Single-Slope Barrier with Scupper—Impact Location C.	81
Figure 5.12. End-View Images of <i>MASH</i> Test 3-11 Simulation of Single-Slope Barrier with Scupper—Impact Location C.	82
Figure 5.13. Overhead Images of <i>MASH</i> Test 3-10 Simulation of Single-Slope Barrier with Scupper—Impact Location A.	84
Figure 5.14. End-View Images of <i>MASH</i> Test 3-10 Simulation of Single-Slope Barrier with Scupper—Impact Location A.	85
Figure 5.15. Overhead Images of <i>MASH</i> Test 3-10 Simulation of Single-Slope Barrier with Scupper—Impact Location B.	86
Figure 5.16. End-View Images of <i>MASH</i> Test 3-10 Simulation of Single-Slope Barrier with Scupper—Impact Location B.	87
Figure 5.17. Overhead Images of <i>MASH</i> Test 3-10 Simulation of Single-Slope Barrier with Scupper—Impact Location C.	88

Figure 5.18. End-View Images of <i>MASH</i> Test 3-10 Simulation of Single-Slope Barrier with Scupper—Impact Location C.	89
Figure 5.19. Single-Slope PCB Model with X-bolt Connection.	90
Figure 5.20. Overhead Images of <i>MASH</i> Test 3-11 Simulation of Single-Slope Barrier with Scupper and X-bolt Connections—Impact Location A.	91
Figure 5.21. End-View Images of <i>MASH</i> Test 3-11 Simulation of Single-Slope Barrier with Scupper and X-bolt Connections—Impact Location A.	92
Figure 5.22. Overhead Images of <i>MASH</i> Test 3-11 Simulation of Single-Slope Barrier with Scupper and X-bolt Connections—Impact Location B.	93
Figure 5.23. End-View Images of <i>MASH</i> Test 3-11 Simulation of Single-Slope Barrier with Scupper and X-bolt Connections—Impact Location B.	94
Figure 5.24. Overhead Images of <i>MASH</i> Test 3-11 Simulation of Single-Slope Barrier with Scupper and X-bolt Connections—Impact Location C.	95
Figure 5.25. End-View Images of <i>MASH</i> Test 3-11 Simulation of Single-Slope Barrier with Scupper and X-bolt Connections—Impact Location C.	96
Figure 5.26. Overhead Images of <i>MASH</i> Test 3-10 Simulation of Single-Slope Barrier with Scupper and X-bolt Connections—Impact Location A.	98
Figure 5.27. End-View Images of <i>MASH</i> Test 3-10 Simulation of Single-Slope Barrier with Scupper and X-bolt Connections—Impact Location A.	99
Figure 5.28. Overhead Images of <i>MASH</i> Test 3-10 Simulation of Single-Slope Barrier with Scupper and X-bolt Connections—Impact Location B.	100
Figure 5.29. End-View Images of <i>MASH</i> Test 3-10 Simulation of Single-Slope Barrier with Scupper and X-bolt Connections—Impact Location B.	101
Figure 5.30. Overhead Images of <i>MASH</i> Test 3-10 Simulation of Single-Slope Barrier with Scupper and X-bolt Connections—Impact Location C.	102
Figure 5.31. End-View Images of <i>MASH</i> Test 3-10 Simulation of Single-Slope Barrier with Scupper and X-bolt Connections—Impact Location C.	103
Figure 5.32. Pre-impact Finite Element Model Setup for SUT.	106
Figure 5.33. Overhead Images of <i>MASH</i> Test 4-12 Simulation of Single-Slope Barrier with Scupper and X-bolt Connections.	107
Figure 5.34. End-View Images of <i>MASH</i> Test 4-12 Simulation of Single-Slope Barrier with Scupper and X-bolt Connections.	108
Figure 6.1. Details of Large-Scupper Portable Concrete Barrier.	112
Figure 6.2. Large-Scupper Portable Concrete Barrier prior to Testing.	113
Figure 6.3. Large-Scupper Portable Concrete Barrier at the Joint of Barriers 3 and 4 prior to Testing.	113
Figure 6.4. X-bolt Connection on the Large-Scupper Portable Concrete Barrier prior to Testing.	114
Figure 6.5. Close-Up of the End of the Scupper on the Large-Scupper Portable Concrete Barrier prior to Testing.	114
Figure 6.6. Upstream View of the Large-Scupper Portable Concrete Barrier prior to Testing.	115
Figure 6.7. Field Side of the Large-Scupper Portable Concrete Barrier prior to Testing.	115
Figure 7.1. Target CIP for <i>MASH</i> 4-10 and 4-11 Tests on Large-Scupper Portable Concrete Barrier.	117

Figure 7.2. Target CIP for <i>MASH</i> 4-12 Test on Large-Scupper Portable Concrete Barrier.	118
Figure 9.1. Large-Scupper Portable Concrete Barrier/Test Vehicle Geometrics for Test 440873-01-1.	126
Figure 9.2. Large-Scupper Portable Concrete Barrier/Test Vehicle Impact Location for Test 440873-01-1.	126
Figure 9.3. Impact Side of Test Vehicle before Test 440873-01-1.	127
Figure 9.4. Opposite Impact Side of Test Vehicle before Test 440873-01-1.	128
Figure 9.5. Large-Scupper Portable Concrete Barrier after Test at Impact Location for Test 440873-01-1.	130
Figure 9.6. Large-Scupper Portable Concrete Barrier after Test at the Joint between Segments 3 and 4 for Test 440873-01-1.	131
Figure 9.7. Impact Side of Test Vehicle after Test 440873-01-1.	131
Figure 9.8. Rear Impact Side of Test Vehicle after Test 440873-01-1.	132
Figure 9.9. Overall Interior of Test Vehicle after Test 440873-01-1.	132
Figure 9.10. Interior of Test Vehicle on Impact Side after Test 440873-01-1.	133
Figure 9.11. Summary of Results for <i>MASH</i> Test 4-10 on Large-Scupper Portable Concrete Barrier.	136
Figure 10.1. Large-Scupper Portable Concrete Barrier/Test Vehicle Geometrics for Test 440873-01-2.	138
Figure 10.2. Large-Scupper Portable Concrete Barrier/Test Vehicle Impact Location for Test 440873-01-2.	138
Figure 10.3. Impact Side of Test Vehicle before Test 440873-01-2.	139
Figure 10.4. Opposite Impact Side of Test Vehicle before Test 440873-01-2.	140
Figure 10.5. Large-Scupper Portable Concrete Barrier after Test at Impact Location for Test 440873-01-2.	142
Figure 10.6. Large-Scupper Portable Concrete Barrier at the Joint of Barriers 3 and 4 after Test 440873-01-2.	143
Figure 10.7. Impact Side of Test Vehicle after Test 440873-01-2.	143
Figure 10.8. Rear Impact Side of Test Vehicle after Test 440873-01-2.	144
Figure 10.9. Overall Interior of Test Vehicle after Test 440873-01-2.	144
Figure 10.10. Interior of Test Vehicle on Impact Side after Test 440873-01-2.	145
Figure 10.11. Summary of Results for <i>MASH</i> Test 4-11 on Large-Scupper Portable Concrete Barrier.	148
Figure 11.1. Large-Scupper Portable Concrete Barrier/Test Vehicle Geometrics for Test 440873-01-3.	150
Figure 11.2. Large-Scupper Portable Concrete Barrier/Test Vehicle Impact Location for Test 440873-01-3.	150
Figure 11.3. Impact Side of Test Vehicle before Test 440873-01-3.	151
Figure 11.4. Opposite Impact Side of Test Vehicle before Test 440873-01-3.	152
Figure 11.5. Large-Scupper Portable Concrete Barrier at Impact Location after Test 440873-01-3.	154
Figure 11.6. Large-Scupper Portable Concrete Barrier at the Field Side after Test 440873-01-3.	155
Figure 11.7. Impact Side of Test Vehicle after Test 440873-01-3.	155
Figure 11.8. Rear Impact Side of Test Vehicle after Test 440873-01-3.	156

Figure 11.9. Overall Interior of Test Vehicle after Test 440873-01-3.....	156
Figure 11.10. Interior of Test Vehicle on Impact Side after Test 440873-01-3.	157
Figure 11.11. Summary of Results for <i>MASH</i> Test 4-12 on Large-Scupper Portable Concrete Barrier.....	159
Figure C.1. Vehicle Properties for Test 440873-01-1.	199
Figure C.2. Exterior Crush Measurements for Test 440873-01-1.....	200
Figure C.3. Occupant Compartment Measurements for Test 440873-01-1.....	201
Figure C.4. Sequential Photographs for Test 440873-01-1 (Overhead Views).	202
Figure C.5. Sequential Photographs for Test 440873-01-1 (Frontal Views).	203
Figure C.6. Sequential Photographs for Test 440873-01-1 (Rear Views).	204
Figure C.7. Vehicle Angular Displacements for Test 440873-01-1.....	205
Figure C.8. Vehicle Longitudinal Accelerometer Trace for Test 440873-01-1 (Accelerometer Located at Center of Gravity).....	206
Figure C.9. Vehicle Lateral Accelerometer Trace for Test 440873-01-1 (Accelerometer Located at Center of Gravity).....	206
Figure C.10. Vehicle Vertical Accelerometer Trace for Test 440873-01-1 (Accelerometer Located at Center of Gravity).....	207
Figure D.1. Vehicle Properties for Test 440873-01-2.	209
Figure D.2. Exterior Crush Measurements for Test 440873-01-2.....	210
Figure D.3. Occupant Compartment Measurements for Test 440873-01-2.....	211
Figure D.4. Sequential Photographs for Test 440873-01-2 (Overhead Views).	212
Figure D.5. Sequential Photographs for Test 440873-01-2 (Frontal Views).	213
Figure D.6. Sequential Photographs for Test 440873-01-2 (Rear Views).	214
Figure D.7. Vehicle Angular Displacements for Test 440873-01-2.....	215
Figure D.8. Vehicle Longitudinal Accelerometer Trace for Test 440873-01-2 (Accelerometer Located at Center of Gravity).....	216
Figure D.9. Vehicle Lateral Accelerometer Trace for Test 440873-01-2 (Accelerometer Located at Center of Gravity).....	216
Figure D.10. Vehicle Vertical Accelerometer Trace for Test 440873-01-2 (Accelerometer Located at Center of Gravity).....	217
Figure E.1. Vehicle Properties for Test 440873-01-3.	219
Figure E.2. Sequential Photographs for Test 440873-01-3 (Overhead Views).....	221
Figure E.3. Sequential Photographs for Test 440873-01-3 (Frontal Views).	222
Figure E.4. Sequential Photographs for Test 440873-01-3 (Rear Views).....	223
Figure E.5. Vehicle Angular Displacements for Test 440873-01-3.....	224
Figure E.6. Vehicle Longitudinal Accelerometer Trace for Test 440873-01-3 (Accelerometer Located at Center of Gravity).....	225
Figure E.7. Vehicle Lateral Accelerometer Trace for Test 440873-01-3 (Accelerometer Located at Center of Gravity).....	225
Figure E.8. Vehicle Vertical Accelerometer Trace for Test 440873-01-3 (Accelerometer Located at Center of Gravity).....	226

LIST OF TABLES

	Page
Table 2.1. Summary of Evaluated Concrete Barriers with Drainage Scuppers.	30
Table 3.1. Option A Perceived Advantages and Disadvantages.	32
Table 3.2. Option B Perceived Advantages and Disadvantages.	33
Table 3.3. Option C Perceived Advantages and Disadvantages.	35
Table 3.4. Comparison of Some Characteristics of Proposal Design Concepts.	35
Table 3.5. Volume of Proposed Barrier Designs, Theoretical Barrier Weights, and Buoyant Forces.	36
Table 3.6. Calculations to Determine Factors of Safety against Sliding and Overturning.	37
Table 4.1. ADV Measurement Locations.	50
Table 4.2. Hydraulic Efficiency Data.	55
Table 4.3. Theoretical Force on the Model Barrier Due to Upstream Flow.	63
Table 4.4. Moments and Forces on the Model Barrier.	64
Table 4.5. Force at Different Locations on the Barrier.	66
Table 5.1. Occupant Risk Values for Pickup Truck Impacting Single-Slope Barrier.	73
Table 5.2. Occupant Risk Values for Passenger Car Impacting Single-Slope Barrier.	75
Table 5.3. Occupant Risk Values for Pickup Truck Impacting Single-Slope Barrier with Scupper—Impact Location A.	78
Table 5.4. Occupant Risk Values for Pickup Truck Impacting Single-Slope Barrier with Scupper—Impact Location B.	80
Table 5.5. Occupant Risk Values for Pickup Truck Impacting Single-Slope Barrier with Scupper—Impact Location C.	82
Table 5.6. Occupant Risk Values for Passenger Car Impacting Single-Slope Barrier with Scupper—Impact Location A.	85
Table 5.7. Occupant Risk Values for Passenger Car Impacting Single-Slope Barrier with Scupper—Impact Location B.	87
Table 5.8. Occupant Risk Values for Passenger Car Impacting Single-Slope Barrier with Scupper—Impact Location C.	89
Table 5.9. Occupant Risk Values for Pickup Truck Impacting Single-Slope Barrier with Scupper and X-bolt Connections—Impact Location A.	93
Table 5.10. Occupant Risk Values for Pickup Truck Impacting Single-Slope Barrier with Scupper and X-bolt Connections—Impact Location B.	95
Table 5.11. Occupant Risk Values for Pickup Truck Impacting Single-Slope Barrier with Scupper and X-bolt Connections—Impact Location C.	97
Table 5.12. Occupant Risk Values for Passenger Car Impacting Single-Slope Barrier with Scupper and X-bolt Connections—Impact Location A.	99
Table 5.13. Occupant Risk Values for Passenger Car Impacting Single-Slope Barrier with Scupper and X-bolt Connections—Impact Location B.	102
Table 5.14. Occupant Risk Values for Passenger Car Impacting Single-Slope Barrier with Scupper and X-bolt Connections—Impact Location C.	103
Table 5.15. Lateral Deflection for Predictive Simulations and Crash Tests.	104

Table 5.16. Friction Coefficient Values for the Calibrated Simulation.....	104
Table 5.17. Lateral Deflection for Crash Test and Calibrated Simulation.	104
Table 5.18. Occupant Risk Factors for Single-Slope Barrier with Passenger Car.	105
Table 5.19. Occupant Risk Factors for Single-Slope Barrier with Pickup Truck.	105
Table 5.20. Occupant Risk Values.	109
Table 6.1. Concrete Strength.	116
Table 7.1. Test Conditions and Evaluation Criteria Specified for <i>MASH</i> TL-4 Longitudinal Barriers.	117
Table 7.2. Evaluation Criteria Required for <i>MASH</i> Testing.	118
Table 9.1. Impact Conditions for <i>MASH</i> Test 4-10 (440873-01-1).	125
Table 9.2. Exit Parameters for <i>MASH</i> Test 4-10 (440873-01-1).....	125
Table 9.3. Weather Conditions for Test 440873-01-1.....	127
Table 9.4. Vehicle Measurements for Test 440873-01-1.....	128
Table 9.5. Events during Test 440873-01-1.	129
Table 9.6. Movement of the Large-Scupper Portable Concrete Barrier at the Joints for Test 440873-01-1.	129
Table 9.7. Damage to Large-Scupper Portable Concrete Barrier for Test 440873-01-1.....	130
Table 9.8. Occupant Compartment Deformation for Test 440873-01-1.....	133
Table 9.9. Exterior Vehicle Damage for Test 440873-01-1.	134
Table 9.10. Occupant Risk Factors for Test 440873-01-1.....	135
Table 10.1. Impact Conditions for <i>MASH</i> Test 4-11 (440873-01-2).	137
Table 10.2. Exit Parameters for <i>MASH</i> Test 4-11 (440873-01-2).....	137
Table 10.3. Weather Conditions for Test 440873-01-2.....	139
Table 10.4. Vehicle Measurements for Test 440873-01-2.....	140
Table 10.5. Events during Test 440873-01-2.	141
Table 10.6. Movement of the Large-Scupper Portable Concrete Barrier at the Joints for Test 440873-01-2.	141
Table 10.7. Deflection of the Large-Scupper Portable Concrete Barrier for Test 440873-01-2.....	142
Table 10.8. Occupant Compartment Deformation for Test 440873-01-2.....	145
Table 10.9. Exterior Vehicle Damage for Test 440873-01-2.	146
Table 10.10. Occupant Risk Factors for Test 440873-01-2.....	146
Table 11.1. Impact Conditions for <i>MASH</i> Test 4-12 (440873-01-3).	149
Table 11.2. Exit Parameters for <i>MASH</i> Test 4-12 (440873-01-3).....	149
Table 11.3. Weather Conditions for Test 440873-01-3.....	151
Table 11.4. Vehicle Measurements for Test 440873-01-3.....	152
Table 11.5. Events during Test 440873-01-3.	153
Table 11.6. Movement of the Large-Scupper Portable Concrete Barrier at the Joints for Test 440873-01-3.	153
Table 11.7. Deflection and Working Width of the Large-Scupper Portable Concrete Barrier for Test 440873-01-3.....	154
Table 11.8. Occupant Compartment Deformation for Test 440873-01-3.....	157
Table 11.9. Exterior Vehicle Damage for Test 440873-01-3.	157
Table 11.10. Occupant Risk Factors for Test 440873-01-3.....	158

Table 12.1. Assessment Summary for <i>MASH</i> TL-4 Tests on Large-Scupper Portable Concrete Barrier.....	161
Table F.1. Selected Benefit Areas for Project 0-7087.	227

SI* (MODERN METRIC) CONVERSION FACTORS				
APPROXIMATE CONVERSIONS TO SI UNITS				
Symbol	When You Know	Multiply By	To Find	Symbol
LENGTH				
in	inches	25.4	millimeters	mm
ft	feet	0.305	meters	m
yd	yards	0.914	meters	m
mi	miles	1.61	kilometers	km
AREA				
in ²	square inches	645.2	square millimeters	mm ²
ft ²	square feet	0.093	square meters	m ²
yd ²	square yards	0.836	square meters	m ²
ac	acres	0.405	hectares	ha
mi ²	square miles	2.59	square kilometers	km ²
VOLUME				
fl oz	fluid ounces	29.57	milliliters	mL
gal	gallons	3.785	liters	L
ft ³	cubic feet	0.028	cubic meters	m ³
yd ³	cubic yards	0.765	cubic meters	m ³
NOTE: volumes greater than 1000L shall be shown in m ³				
MASS				
oz	ounces	28.35	grams	g
lb	pounds	0.454	kilograms	kg
T	short tons (2000 lb)	0.907	megagrams (or metric ton")	Mg (or "t")
TEMPERATURE (exact degrees)				
°F	Fahrenheit	5(F-32)/9 or (F-32)/1.8	Celsius	°C
FORCE and PRESSURE or STRESS				
lbf	poundforce	4.45	newtons	N
lbf/in ²	poundforce per square inch	6.89	kilopascals	kPa
APPROXIMATE CONVERSIONS FROM SI UNITS				
Symbol	When You Know	Multiply By	To Find	Symbol
LENGTH				
mm	millimeters	0.039	inches	in
m	meters	3.28	feet	ft
m	meters	1.09	yards	yd
km	kilometers	0.621	miles	mi
AREA				
mm ²	square millimeters	0.0016	square inches	in ²
m ²	square meters	10.764	square feet	ft ²
m ²	square meters	1.195	square yards	yd ²
ha	hectares	2.47	acres	ac
km ²	Square kilometers	0.386	square miles	mi ²
VOLUME				
mL	milliliters	0.034	fluid ounces	oz
L	liters	0.264	gallons	gal
m ³	cubic meters	35.314	cubic feet	ft ³
m ³	cubic meters	1.307	cubic yards	yd ³
MASS				
g	grams	0.035	ounces	oz
kg	kilograms	2.202	pounds	lb
Mg (or "t")	megagrams (or "metric ton")	1.103	short tons (2000lb)	T
TEMPERATURE (exact degrees)				
°C	Celsius	1.8C+32	Fahrenheit	°F
FORCE and PRESSURE or STRESS				
N	newtons	0.225	poundforce	lbf
kPa	kilopascals	0.145	poundforce per square inch	lb/in ²

*SI is the symbol for the International System of Units

Chapter 1. INTRODUCTION

Concrete median barriers are used to prevent serious cross-median crashes by preventing penetration of passenger vehicles and trucks into oncoming traffic. Concrete median barriers are used on highways with high speeds and high traffic volume to provide positive containment of vehicles in a manner that requires limited maintenance and repair (1). Any required barrier maintenance or repair increases risk to maintenance personnel and can result in significant congestion if a lane closure is required.

During Hurricane Harvey, it was observed that solid concrete median barriers can act as a dam for floodwaters. This situation raises the height of floodwaters and increases the severity of flooding on both the highway and the surrounding roads and in the community. This rise in floodwaters increases the risk to both motorists and others in the area and can also increase the level of flood damage to the road network and any nearby structures. Numerous highways in the Houston and Beaumont areas were severely affected by the damming of water caused by solid concrete median barriers, including Interstate Highway (IH) 10 and United States Highway (US) 59 in Houston and US 96 in Beaumont. In the Beaumont area, explosives were used to remove several sections of median barrier to help mitigate the increased flooding being caused by the solid concrete barrier.

A severe storm in Louisiana along IH 12 resulted in a similar scenario to the one experienced in Texas. A 19-mi length of solid concrete median barrier that was constructed to divide the eastbound and westbound lanes of IH 12 to prevent head-on crashes on the heavily traveled highway acted as a dam, causing greater flood damage to areas north of the highway. Figure 1.1 illustrates examples of flooding where solid concrete median barriers were implemented.



a. Beaumont, Texas



b. Louisiana

Figure 1.1. Examples of Flooding Where Solid Concrete Median Barriers Were Installed (2, 3).

In the Houston area, large sections of solid portable concrete barriers (PCBs) used as permanent median applications were displaced across the highway or broken by the floodwaters. These situations required significant repair before the highways

could be reopened and a level of safety restored for motorists. Figure 1.2 illustrates examples of flooding where PCBs were installed as permanent median barriers.



a. Portable concrete median barrier in Humble, Texas.



b. Barrier on US 59

Figure 1.2. Examples of Flooding Where Portable Concrete Barrier Was Installed as Permanent Median Barrier (4, 5).

Because median barriers are an important safety feature that provide an increased level of safety for motorists, concrete median barriers cannot be removed. Consequently, a need exists for crashworthy median barriers designed to accommodate the passage of floodwater during severe weather events. When implemented in flood-prone areas, such barriers would reduce the severity of flooding, decrease risk to motorists and others in the area, and reduce the level of damage to the highway and surrounding area.

Under Texas Department of Transportation (TxDOT) Project 0-6976, a hydraulically efficient, cast-in-place, concrete median barrier was developed for use in flood-prone areas. The 42-inch-tall single-slope concrete barrier incorporated 13-inch-high × 18-ft-long scuppers spaced on 30-ft intervals. The median barrier was successfully tested to American Association of State Highway and Transportation Officials (AASHTO) *Manual for Assessing Safety Hardware (MASH)* Test Level 4 (TL-4) impact conditions and evaluation criteria. It has since been incorporated into TxDOT

standards SSCHEB-21 and SSCHEB2-21 and implemented along IH 10 and other locations.

Under this project, a PCB with large scuppers was developed and evaluated through engineering analyses, computer simulations, hydraulic large-scale testing, and full-scale vehicular crash testing following *MASH* TL-4 criteria. Details of this research are described in subsequent chapters of this report.

Chapter 2. LITERATURE REVIEW

A literature search was performed to identify relevant research studies that addressed the following areas:

- Cross-highway water flow requirements during severe weather events required to prevent a significant rise in floodwater by a highway barrier, including concrete bridge barriers.
- Concrete barrier systems designed to permit passage of water, including concrete bridge barriers.
- Testing and impact performance of barriers with openings or drainage scuppers.

2.1. FLOODWAY ENCROACHMENT

The Federal Highway Administration (FHWA) defines an encroachment as an action or development within the limits of a base floodplain that could impede flood flows (6). According to the TxDOT *Hydraulic Design Manual* (7), any project in which FHWA participates that involves an encroachment on the 1 percent (100-year event) annual exceedance probability floodplain must comply with FHWA Policy 23 CFR 650, Subpart A for the location and design of the project. Additionally, this policy specifies a “regulatory floodway” as a floodplain area that is reserved in an open manner by federal, state, or local requirements. Therefore, a regulatory floodway is not confined or obstructed either horizontally or vertically to provide for the discharge of the base flood so that the cumulative increase in water surface elevation is no more than a designated amount. The Federal Emergency Management Agency (FEMA) establishes this amount as 1 ft (6). If an encroachment results in the increase of the water surface elevation by more than 1 ft, the FEMA floodplain map must then be redrawn.

2.2. ENERGY IN OPEN CHANNEL FLOW

2.2.1. Bernoulli’s Equation

In an open channel, the energy head at two locations can be described by the general energy equation (8). In this form of the energy equation, the unit weight of the fluid is used to normalize the terms. Therefore, the terms shown in Equation 2.1 all have dimensions of length, and each term represents the energy head due to a different force. This form of the energy equation is known as Bernoulli’s equation neglecting head losses, and it accounts for nonuniform flow distribution (α_1, α_2) and energy lost from friction (h_L). The z term represents the depth relative to a datum, while h is the total fluid depth, and v is the velocity at a specific location. Finally, g represents the gravitational constant.

$$z_1 + h_1 + \alpha_1 \left(\frac{v_1^2}{2g} \right) = h_L + z_2 + h_2 + \alpha_2 \left(\frac{v_2^2}{2g} \right) \quad (2.1)$$

Charbeneau et al. (9) presented Equation 2.1 using several simplifications that are shown below. The first simplification relies on the assumption that a small channel

slope results in approximately equal z values, and therefore the z terms cancel out one another. The second simplification is one of steady-state scenarios. Assuming the velocity is constant, α_1 and α_2 are both equal to 1 and can be omitted from the equation. The third simplification assumes that friction losses are negligible. In this case, the specific energy can be expressed as Equation 2.2, where A represents the cross-sectional area of the flow and Q is the volumetric flow rate. By applying these three assumptions, the specific energy in a channel can be defined as the energy per unit weight of water at any segment of a channel measured with respect to the channel bottom (8).

$$E = h + \frac{v^2}{2g} = h + Q^2/2gA^2 \quad (2.2)$$

The unit flow rate, q , may be defined as the volumetric flow rate per unit width of the channel, b , if the channel is rectangular.

$$q = \frac{Q}{b} = \frac{vA}{b} = \frac{vbh}{b} = vh \quad (2.3)$$

Equations 2.2 and 2.3 use the flow rate equation, $Q = vA$. Equation 2.2 can be simplified by separating the area into height and width components, which yields the unit flow rate in terms of the fluid velocity and height. Rearranging the equation results in Equation 2.4:

$$E = h + q^2/2gh^2 \quad (2.4)$$

While this equation has three roots, one of them is negative and has no value. The other two roots, on the other hand, exist at every point greater than the value at the critical point. Figure 2.1 shows how water depth and specific energy are related, and the horizontal peak represents the critical value.

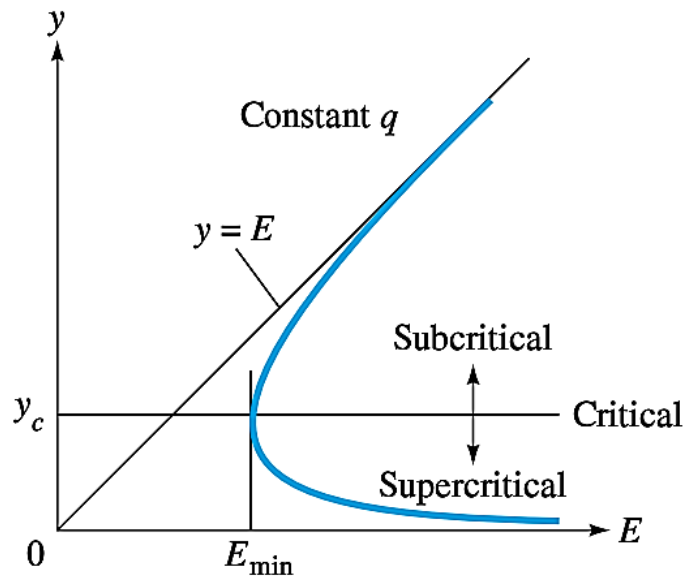


Figure 2.1. Specific Energy Curve (9).

The diagonal line shown in Figure 2.1 is an $E = h$ line, and it represents the potential energy if a fluid is completely static. To keep the notation constant throughout, y in Figure 2.1 is referred to as the water depth, h . This line's abscissa is the water depth, and the difference between this value and the curve's abscissa is the kinetic energy. Therefore, the addition of these two values results in the total specific energy. The critical depth can then be found by taking the derivative of Equation 2.4 with respect to h , where $dE/dh = 0$.

$$h_{critical} = \left(\frac{q^2}{g}\right)^{1/3} \quad (2.5)$$

The minimum specific energy, or critical energy, can also be found by setting the derivative of Equation 2.4 equal to 0. Any flow at a water depth above this point is known as a subcritical flow, and water depths below this critical point are referred to as supercritical flows. Subcritical flows tend to have a lower velocity, while supercritical flows have a larger velocity.

Equation 2.5 can be directly applied to a highway median barrier in the sense that it yields the water depth that causes a critical flow state at a location. Bin-Shafique et al. (10) showed that the energy equation, if rewritten, can describe the critical depth as a function of the upstream water depth if the critical depth occurs farther upstream. Equation 2.6 describes this arrangement, and the subscript u denotes the upstream location, while c represents the critical location.

$$h_c + \frac{\alpha_c v_c^2}{2g} = h_u + \frac{\alpha_u v_u^2}{2g} + h_L \quad (2.6)$$

Equation 2.6 can be further simplified by assuming a subcritical state in the upstream flow that is due to the median barrier obstruction. Figure 2.1 illustrates that the assumption of a subcritical upstream flow will yield a negligible kinetic energy in comparison to the potential energy at that point ($\frac{v_u^2}{2g} \ll h_u$). Furthermore, if Equation 2.3 is inserted and uniform flow and negligible frictional losses are assumed, the specific energy becomes:

$$h_c + \frac{q^2}{2gh_c^2} = h_u \quad (2.7)$$

The unit flow rate can be found using Equation 2.5 rearranged as $q^2 = gh_c^3$. This can be inserted into Equation 2.7 to then solve for h_c .

$$h_c = 2/3 h_u \quad (2.8)$$

In Equation 2.8, the critical depth is a function of the upstream depth, and because the critical depth is not a measurable quantity, the equation is an estimate that can be used in mathematical models.

2.2.2. Weir Equation

A weir is a device or overflow structure that is placed perpendicular to a flow to regulate that flow. As the flow contacts the weir, the water level rises until it reaches a critical point and flows over the crest of the weir (11). A sharp-crested weir has a sharp

edge at the top that allows the nappe to separate from the weir and flow according to projectile motion (8). Figure 2.2 shows a sharp-crested weir, where P_w is the weir height and H is the head above the weir crest.

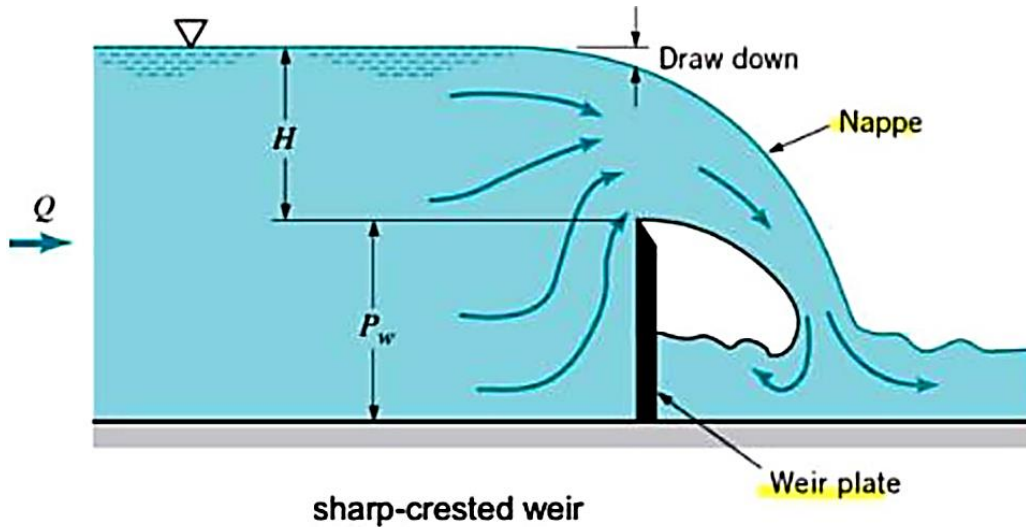


Figure 2.2. Sharp-Crested Weir (11).

The experiments conducted in this research used a sharp-crested weir to measure the average flow rate through a rectangular channel. For a sharp-crested weir in a rectangular channel, the following equation is used, where Q is the average channel volumetric flow rate, C_d is the weir discharge coefficient, B is the channel width, and H is the head above the weir crest.

$$Q = 2/3 C_d \sqrt{2g} B H^{3/2} \quad (2.9)$$

C_d accounts for the non-parallel streamlines shown in Figure 2.2 that are induced by the drawdown effect and crest contractions. Mays (11) showed that this constant is approximately 0.62. A nappe is created on the downstream side when the crest contraction forces the streamline immediately upstream to flow over the weir crest (12). Equation 2.9 assumes that the nappe is fully aerated and that both the upper and lower nappe surfaces are subject to atmospheric pressure. If the aeration is incomplete, the pressure beneath the nappe is reduced and can lead to three consequences that introduce uncertainty into the flow measurements: (a) the shape of the nappe will change; (b) an increase in discharge can result in a pulsating nappe; and (c) unstable performance of the weir model can occur (8).

Equation 2.9 can simplify the experimental flow rate measurement because only a single water depth measurement is required to quantify volumetric discharge. This measurement is best taken at a location where the flow is approximately even and drawdown effects are negligible. In practical applications, this location is typically five times the depth of the drawdown away from the weir.

2.3. PHYSICAL MODEL AND SCALING

Physical models are an effective method of examining large-scale flow conditions and phenomena in a controlled laboratory setting. To relate lab-scale results to field data, hydraulic similitude must be maintained between the physical model and the prototype. This similitude can be maintained using dimensional analysis to hold specific dimensionless parameters constant between the model and the prototype. One of the most important dimensionless parameters in open channel flow is the Froude number (13).

$$F_r = v/\sqrt{gL} \quad (2.10)$$

where F_r is the Froude number, v is the velocity, and L is a characteristic length (e.g., water depth).

The Froude number is the ratio between inertial forces to gravitational forces, and it is used when large-scale phenomena control the fluid behavior (inertial forces are more important than viscous forces). $F_{rm} = F_{rp}$ must always remain valid for the Froude number to be used in modeling relationships. In this equation and for the rest of this section, m represents model parameters, while p represents prototype parameters. In addition to hydraulic similitude, kinematic and geometric similitude must also be maintained by velocity and length ratios (13). The length ratio is shown in Equation 2.11.

$$L_r = L_m/L_p \quad (2.11)$$

If this ratio remains true for all length dimensions, geometric similarity is maintained. If kinematic similarity is maintained, then a velocity ratio can also be developed.

$$V_r = v_m/v_p \quad (2.12)$$

Because the model and prototype Froude numbers are held equal during Froude number modeling, the following relationship can be established:

$$\frac{v_m}{\sqrt{gL_m}} = \frac{v_p}{\sqrt{gL_p}} \quad (2.13)$$

Equation 2.13 can then be rearranged, and plugging in the ratios defined in Equations 2.11 and 2.12 results in the following:

$$V_r = \sqrt{L_r} \quad (2.14)$$

If the volumetric flow rate is defined as $Q = vA$, Equation 2.14 can be rearranged as:

$$Q = V_r L_r^2 \quad (2.15)$$

This ratio can further be simplified by inserting the ratio established in Equation 2.14.

$$Q_r = L_r^{5/2} \quad (2.16)$$

By utilizing this process of Froude number modeling, the proper relationship between model and prototype can be found. The volumetric flow rate ratio can be determined from the ratio of the median barrier dimensions to the model barrier dimensions. The Froude number can also be utilized to determine the location at which the critical depth occurs. At $F_r = 1$, the flow passes through the critical point, and supercritical flow occurs when $F_r > 1$, while subcritical flow occurs when $F_r < 1$.

2.4. CHARBENEAU MODEL

The hydraulic performance of various bridge rail and median barriers was studied by Charbeneau et al. (9) to determine how different rails impact surrounding floodplains during storms. The primary result of this research was a three-parameter model that predicts the free-flow rail rating curve. With the energy equations discussed previously, the model can be used to estimate flow through bridge rails given an upstream water depth. The model is an extension of a previous two-parameter model developed by Charbeneau et al. (14). The model developed rating curves to define the hydraulic performance in an inlet-controlled highway culvert. Charbeneau et al. (9) added a third parameter to this model to define all possible flow scenarios through a bridge rail, as shown in Figure 2.3.

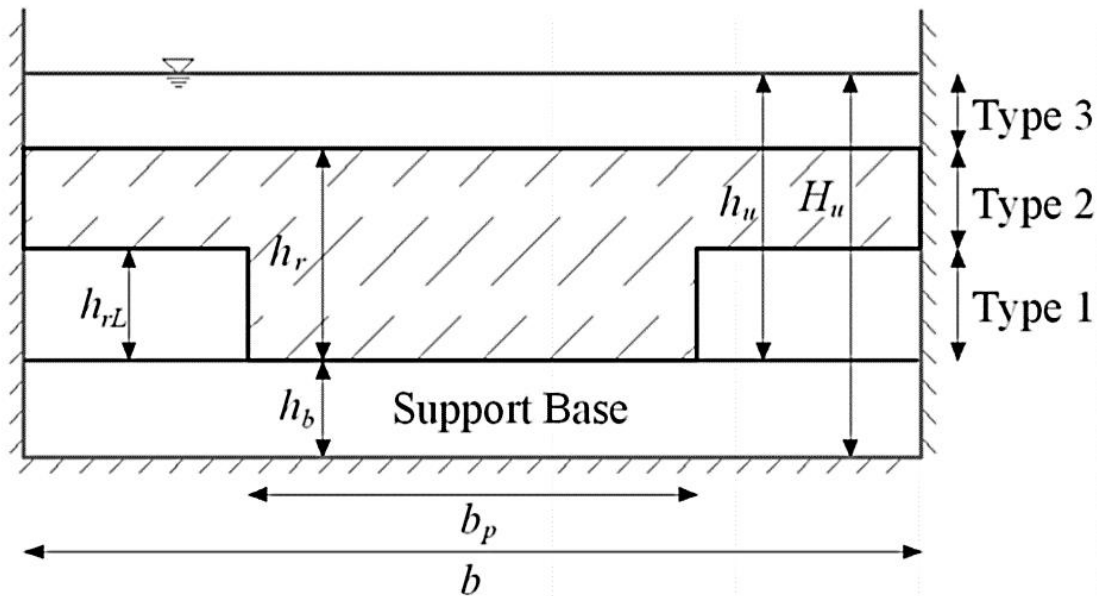


Figure 2.3. Three Flow Cases in Charbeneau Model (9).

Three different flow types, defined as Type 1, 2, and 3, were previously studied (9). Type 1 flow occurs when the water depth at the rail is less than the height of the bridge rail opening ($h_u < h_{rL}$). This is an unsubmerged flow condition that can be described by $Q = vA$. Type 2 flow is a submerged condition where the water depth at the rail is greater than the height of the opening but less than the total rail height ($h_{rL} < h_u < h_r$). This condition is governed by the orifice flow equations. Type 3 flow is a fully

submerged condition in which the water depth at the rail is greater than the total rail height.

2.4.1. Type 1 Flow

The model assumes that the critical depth occurs at the obstruction due to choking from the rail for unsubmerged flow through the bridge rail opening (15). Therefore, the base of the rail is selected as the model datum to separate the rail hydraulics from the bridge hydraulics. By choosing this datum, the bridge height (H_u) can be omitted from the model, which leaves only the bridge rail height necessary to compute the specific energy. The flow in this case is then governed by the volumetric flow rate equation, and the area and velocity can be expanded to include the bridge rail parameters.

$$Q = Av_c = C_b(b - b_p)h_c\sqrt{gh_c} \quad (2.17)$$

If an equivalent Froude number as described in Equation 2.10 is assumed, the critical velocity (v_c) can be set equal to $\sqrt{gh_c}$, as shown in Equation 2.17 (16). In critical flow through a rectangular opening, the upstream specific energy, E_u , is approximately equal to $h_c = 2/3E_c$, where E_c is the critical energy (13). The width of the bridge rail opening is $b - b_p$, which is the difference between the total rail width in the section and the rail support. The energy losses between the upstream flow and the rail are represented by the coefficient C_b (14). To apply this factor, the model creates a new effective width of the bridge rail opening that is reduced from the physical width.

$$\frac{Q}{A_r\sqrt{gh_r}} = C_b F_0 \left(\frac{h_r}{h_{rL}}\right) \left(\frac{2E_u}{3h_r}\right)^{1.5} \quad (2.18)$$

Equation 2.18 is the result of rearranging Equation 2.17 to solve for the dimensionless flow rate, $\frac{Q}{A_r\sqrt{gh_r}}$, and substituting the critical depth. F_0 is the fractional open space in the bridge rail, while A_r is the total rail area. The fractional open space represents the ratio of the rail opening area to the total rail area, A_o/A_r . This ratio can be further expanded to include the model parameters, as shown in Equation 2.19.

$$F_0 = \frac{A_o}{A_r} = \frac{(b - b_p)h_{rL}}{bh_r} \quad (2.19)$$

2.4.2. Type 2 Flow

Because the water depth for Type 2 flow is greater than the opening height but less than the total rail height, it can be modeled as flow through an orifice or sluice gate, as shown in Equation 2.20 (14).

$$E_u \approx h_m + \frac{v_m^2}{2g} = C_c h_{rL} + \frac{v_m^2}{2g} \quad (2.20)$$

In Equation 2.20, h_m is the water depth at the point where the stream diameter is minimized, and v_m is the velocity at the model rail. As shown, the depth is equal to $C_c h_{rL}$, where C_c is the vertical contraction coefficient; this term creates a new effective height

for the opening. C_c represents energy losses between the upstream flow and the rail (14).

$$\frac{Q}{A_r \sqrt{g h_r}} = C_b C_c F_0 \sqrt{2 \left(\frac{E_u}{h_r} - \frac{C_c h_{rL}}{h_r} \right)} \quad (2.21)$$

Equation 2.21 is obtained by substituting the continuity equation into Equation 2.20 and solving for the dimensionless flow rate, $\frac{Q}{A_r \sqrt{g h_r}}$. It is necessary to determine a threshold between Type 1 and Type 2 flow. This can be obtained by setting Equations 2.5 and 2.7 equal to one another and solving for E_u . The result is a cubic function, although one of the roots is negative and therefore has no purpose in the model. The other two roots, however, are accounted for in the double root $3/2$. The specific energy can then be found at this point using Equation 2.22, in which the specific energy is normalized by the rail height. The transition between the two flow types is smooth because both the rating curve and its slope are continuous.

$$E_u / h_r = 3/2 C_c h_{rL} / h_r \quad (2.22)$$

2.4.3. Type 3 Flow

For Type 3 flow, the water depth of the flow is greater than the total rail height, and the water flows not only through the fully submerged rail but also over the top of the rail. This flow is best modeled as a combination of orifice and weir flows. Based on the ratio of the difference between the upstream specific energy of the rail height to the thickness of the rail, flow over the rail can be modeled as flow over a broad-crested weir (16). In Equation 2.23, C_d is the weir discharge coefficient, and it differentiates the values calculated from different weir types. It is larger for a short-crested weir than for a broad-crested weir (17).

$$Q = \frac{2C_d}{3} b \sqrt{\frac{2g}{3}} (E_u - h_r)^{1.5} \quad (2.23)$$

To find the Type 3 rating curve, Equation 2.23 can be rearranged to solve for the dimensionless flow rate and added to the Type 2 rating curve, Equation 2.21. This results in Equation 2.24:

$$\frac{Q}{A_r \sqrt{g h_r}} = C_b C_c F_0 \sqrt{2 \left(\frac{E_u}{h_r} - \frac{C_c h_{rL}}{h_r} \right)} + C_d \left(\frac{2}{3} \right)^{1.5} \left(\frac{E_u}{h_r} - 1 \right)^{1.5} \quad (2.24)$$

The transition point between Type 2 and Type 3 flow occurs when the upstream specific energy is greater than the height of the rail, as shown in Equation 2.25.

$$\frac{E_u}{h_r} \geq 1 \quad (2.25)$$

Based on the above discussion, the free-flow rating curve for a bridge rail can be determined based on the three flow types defined in Equations 2.18, 2.21, and 2.24, and their transition points are defined by Equations 2.22 and 2.25.

2.5. EXPERIMENTAL METHODS FOR CHARBENEAU MODEL

To use the Charbeneau model, the parameters must be experimentally obtained (18). Experimental testing was conducted for nine bridge rails in a zero-slope rectangular channel with a width of 150 cm (5 ft), shown in Figure 2.4. The nine bridge rails that were tested were the single-slope traffic rail (SSTR), T221, T501, T411, T203, T101, T101D, weir rail, and Wyoming rail. In these experiments, upstream and downstream water depths were collected using pitot tubes connected to an inclined manometer board, and the model rails were scaled to half the size of standard TxDOT dimensions. The rails were constructed with wood; however, the T101 and Wyoming rails were constructed using metal. All wooden surfaces were coated with waterproof primer to mitigate swelling and maintain the structural integrity of the wood. The bases of all the rails were anchored to the channel to ensure hydraulic stability.



Figure 2.4. Experimental Setup for Bridge Rail in Rectangular Channel (18).

To ensure accurate flow characteristics, the flow rate was held constant and allowed to reach a steady state in the channel before measurements were recorded. Once a steady state was achieved, the upstream water depth and flow rate were measured. If the flow rate was changed at any point, the flow was again allowed to reach a steady state before measurements were recorded. To carry out submergence testing, a tailwater gate was used to vary the downstream depth by means of a hydraulic jump while the flow rate was still held constant. Each time the tailwater gate was adjusted, the upstream and downstream water depths were measured again.

C_b , C_c , and C_d are the three unknown parameter values in the models discussed above, and they are used in the model equations that can be compared to experimental data in nondimensional form. Using Equation 2.26, the standard error (S.E.) between the experimental data and the model results can be minimized to determine appropriate parameters for the model. S.E. is the standard error for N observed data points, and d corresponds to the measured data for the dimensionless flow rate, while m represents the model results. To minimize the standard error, the model parameter values are changed so that the model results closely match the observed data:

$$S.E. = \sqrt{\frac{1}{N} \sum_{i=1}^N \left[\left(\frac{E_u}{h_r} \right)_d - \left(\frac{E_u}{h_r} \right)_m \right]^2} \quad (2.26)$$

2.6. CHARBENEAU RESULTS

Charbeneau (9) plotted the dimensionless upstream specific energy $\left(\frac{E_u}{h_r} \right)$ as a function of the dimensionless flow rate $\left(\frac{Q}{A_r \sqrt{gh_r}} \right)$ to determine the free-flow rating curve for each of the nine tested bridge rails, as shown in Figure 2.5. The Wyoming rail and T101 were the most hydraulically efficient rails (i.e., least impact on upstream water depth), and the Wyoming rail performed best at higher flow rates. The T411 and T203 rails were the next most hydraulically efficient rails, and the five other rail types performed significantly less efficiently.

The primary determining factor of hydraulic efficiency is the fractional open space, which can be observed by simply comparing the data in Figure 2.5 with the bridge rails seen in Figure 2.6. The five rails not shown in the figure are all mostly solid with minimal open space, hence their lower hydraulic efficiency. Also, while the open spaces between rails T203 and T411 are similar, the lower location and greater width of the opening can improve the hydraulic efficiency, especially at lower flow rates.

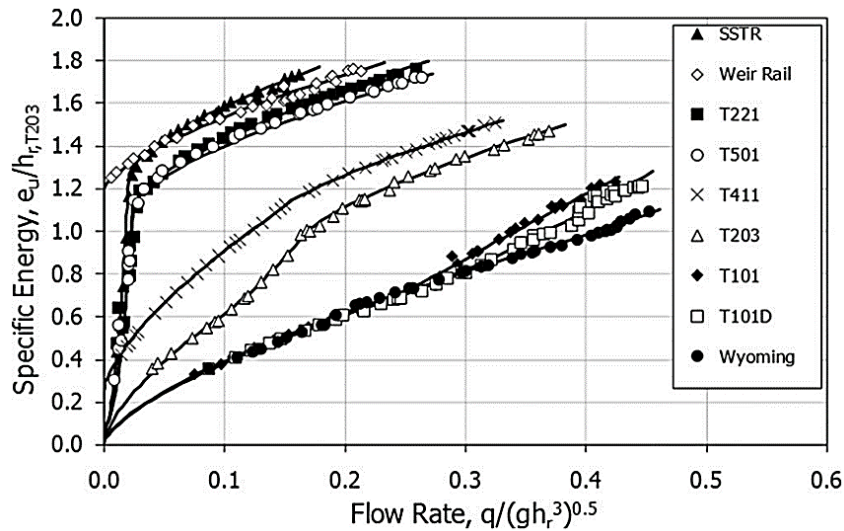


Figure 2.5. Bridge Rail Rating Curves (9).



a. T101



b. Wyoming rail



c. T203



d. T411

Figure 2.6. Bridge Rail Examples (9).

2.7. STREAMLINED BARRIER OPENINGS

2.7.1. Flow Separation

In a viscous fluid, the no-slip condition explains the phenomena that the velocity at the surface of a solid boundary is zero, while the free-stream velocity away from the interface is non-zero. Between these two flow conditions is the boundary layer, an area where the velocity increases from zero to the free-stream velocity. Flow around obstructions can at times result in flow separation, which occurs when the separation of a fluid from the boundary layer is followed by subsequent recirculatory flows commonly referred to as turbulent eddies (12). This separation can alter the effective flow area through an orifice. Flow separation is typically a function of the obstruction shape, roughness, and the Reynolds number, shown in Equation 2.27.

$$Re = \frac{VD}{\nu} = \frac{VR_h}{\nu} \quad (2.27)$$

where V is the fluid velocity, D is the diameter or width of the barrier opening, ν is the kinematic viscosity, and R_h is the hydraulic radius of the channel.

The Reynolds number is a useful parameter since values less than 500 indicate laminar flow, while values greater than 750 indicate turbulent flow. However, in terms of flow separation, the effects are negligible when $Re < 50$, and the effects increase from 50 as Re increases.

2.7.2. Drag Coefficients

The drag coefficient is another parameter that is affected by orifice geometry. For example, streamlining a square corner can greatly reduce the drag coefficient for flow through an orifice, which in turn reduces the wear along the barrier opening. Akiba et al. (19) studied how orifice shapes can alter the overall drag coefficient. It was reported that curvature and the drag coefficient are inversely related; as the orifice edge curvature of the corners increases, the drag coefficient decreases. However, since the number of storm events that lead to flow through barrier openings is limited, drag was assumed to have a negligible effect on the lifespan of the barrier.

2.8. STABILITY OF CONCRETE BARRIER

During flood events, concrete barriers most often fail by overturning or sliding (20). Bin-Shafique et al. (10) further detailed the process used to study the forces responsible for these two failure modes. The factor of safety (FS) against overturning about a point C shown in Figure 2.7 is expressed as shown in Equation 2.28. This equation matches the equation used by Hibbeler (21).

$$FS_{\text{overturning}} = \frac{\sum M_R}{\sum M_0} \quad (2.28)$$

where,

$\sum M_0$ = Sum of the moments of forces overturning about point C.

$\sum M_R$ = Sum of the moments of forces resisting overturning.

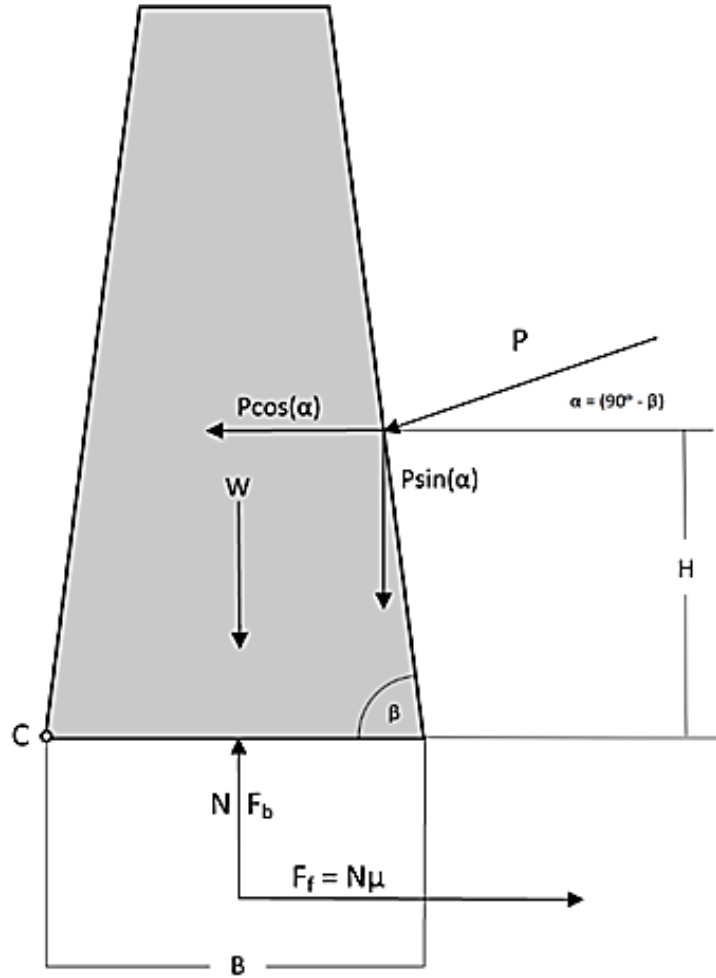


Figure 2.7. Free Body Diagram for Typical Median Barrier.

Equation 2.29 can then be formed by summing the resistive moments of point C:

$$\sum M_R = W * \frac{B}{2} + [P \sin(\alpha)] * [B - H \cot(\beta)] \quad (2.29)$$

where W is the weight of the barrier, B is the width of the barrier at the base, P is the hydrostatic and/or hydrodynamic force on the barrier, and H is the height of the resultant force.

Summing the overturning moments yields Equation 2.30:

$$\sum M_0 = P \cos(\alpha) * H + F_b * \frac{B}{2} \quad (2.30)$$

where F_b is the buoyant force acting upward on the barrier from the displacement fluid. F_b is defined as the weight of the volume of fluid displaced by a submerged object:

$$F_b = \gamma V_b \quad (2.31)$$

where γ is the specific weight of water and V_b is the volume of displaced fluid.

The factor of safety against sliding is expressed in Equation 2.32:

$$FS_{sliding} = \frac{\sum F_R}{\sum F_d} \quad (2.32)$$

where,

$\sum F_R$ = Sum of horizontal resisting forces.

$\sum F_d$ = Sum of horizontal driving forces.

As seen in Figure 2.7, the only horizontal resistive force is due to friction. Therefore, the resistive force can be defined as the normal forces multiplied by the coefficient of static friction (μ):

$$\sum F_R = N\mu = \mu[W + P\sin(\alpha)] \quad (2.33)$$

Similarly, the horizontal drive force is defined as:

$$\sum F_d = P\cos(\alpha) \quad (2.34)$$

While a permanent concrete median barrier is quite resilient to sliding and overturning, portable concrete median barriers are much more susceptible to mobilization. Bin-Shafique et al. (10) studied the effects of friction and buoyancy on the stability of portable concrete traffic barriers. For a variety of upstream and downstream water depths, including fully submerged flow conditions, the buoyant force acting on the median barrier varied from 45 percent to 48 percent of the opposing gravitational force. The coefficient of friction was highly dependent on the roadway surface type, along with the presence of sand or silt particles underneath the barrier.

2.9. BUOYANCY OF CONCRETE BARRIER

Although permanent concrete median barriers are normally affixed to the road, portable concrete traffic barriers are not, and they are therefore susceptible to the buoyant forces mentioned in the previous section. Depending on the magnitude of the flow through the portable concrete traffic barriers, these barriers can at times be swept away from their position if the force of the flow is great enough. To better understand this process, it is useful to rewrite the equation for the buoyant force given in Equation 2.31 as shown in Equation 2.35:

$$F_b = \rho g A (h_{bottom} - h_{top}) \quad (2.35)$$

where ρ is the density of the fluid, g is the gravitational acceleration, A is the area of the object, and $(h_{bottom} - h_{top})$ is the height of the object.

The area of the object will be dependent on both the object and the type of flow through the barrier. The size of the barrier opening will affect the area of the barrier and in turn the buoyant force acting on the barrier based on the volume of water being displaced. Additionally, the location of the opening in conjunction with the type of flow will affect the buoyant force. For Types 2 and 3 flow in which the barrier opening is fully submerged, only the size of the opening will alter the buoyant force. However, for Type 1 flow, the location of the opening and flow depth can determine how much flow runs through the opening and therefore the magnitude of the buoyant force acting on the barrier.

To determine if the barrier has enough upward buoyant force to either slide or overturn given a specific flow condition, it is useful to again to rewrite the buoyancy equation, as shown in Equation 2.36:

$$F_b = \rho g V \quad (2.36)$$

where ρ is the density of the fluid, g is the gravitational acceleration, and V is the volume of the fluid that is displaced by the object.

Using a simple mass balance, as in Equation 2.37, it can be shown that the buoyant force can be equated to the weight of the fluid displaced:

$$F_b = m_f g = W_f \quad (2.37)$$

$$m_f = \rho V_f \quad (2.38)$$

where m_f is the mass of the fluid displaced and V_f is the volume of the fluid displaced.

Therefore, it can be shown that if the weight of the fluid displaced is greater than the weight of the barrier, the barrier can become buoyant and move away from its proper location.

2.10. CONSERVATION OF LINEAR MOMENTUM

In studying the dynamics of solid bodies, conservation laws can be derived by considering an easily identified system. However, in the study of fluid flows, it is difficult to follow a system, and it is therefore more useful to study a region of interest, or control volume, as parcels of matter pass through it. The Reynolds Transport Theorem defines a control volume as a fixed region in space that is surrounded by a control surface, which is the boundary of the control volume. If the Reynolds Transport Theorem is applied to the conservation of linear momentum, Newton's second law of motion can be defined such that the time rate of change of momentum is equal to the time rate of change of momentum inside the control volume plus the sum of the forces acting on the control volume (22), as shown in 2.39:

$$\frac{d(\dot{m} * v)}{dt} = \frac{d}{dt} \int_{CV} (\dot{m} * v * \rho) dV + \sum_{CS} (\dot{m} * v * \rho * (v * A)) \quad (2.39)$$

where \dot{m} is the time rate of change of mass, v is the fluid velocity, ρ is the fluid density, V is the volume of the control volume, A is the area, CV is the control volume, and CS is the control surface.

If the flow is assumed to be at a steady state, or not changing through time, this equation can be rewritten as Equation 2.40:

$$\sum F = (\dot{m} * v)_{out} - (\dot{m} * v)_{in} = (\rho * A * v^2)_{out} - (\rho * A * v^2)_{in} \quad (2.40)$$

where $\sum F$ is the sum of forces acting on the control volume, \dot{m} is the time rate of change of mass, v is the fluid velocity, ρ is the fluid density, and A is the area.

To apply this equation to a model median barrier, a control volume can be theoretically drawn where the upstream control surface is an arbitrary location in the channel upstream of the barrier. The downstream control surface can be drawn as the outlet of the scupper opening. Using this control volume and knowing the area of the

channel and scupper opening leaves the incoming and outgoing velocities as the only unknowns. If using a known volumetric flow rate and the area of the channel and scupper, however, the incoming and outgoing velocities can be calculated. Equation 2.40 can then be solved to calculate the theoretical force acting on the model median barrier due to the momentum flux of the flow.

2.11. MEASUREMENT OF HYDRODYNAMIC FORCES

While hydrodynamic forces can be theoretically calculated using the concept of the conservation of linear momentum, it is easiest to measure forces in an experimental setting using sensors that can be bonded to specific locations on the barrier. Sensors, such as strain gages, force sensors, or pressure transducers, can be applied to the barrier to collect point measurements. Measurements of strain, force, and pressure are obtainable, and these measurements can be compared to one another based on the properties of the object and the area of the measurement location (21).

Strain is a unitless measurement (units technically length/length) that describes the relative deformation of an object when subjected to a force. This deformation occurs as a material is either stretched or compressed due to an applied force. Strain can be divided into normal and shear strain, where a normal strain is caused by forces perpendicular to a plane, and a shear strain is caused by forces parallel to the plane (21). In the case of this application, normal strain is the measurement of interest as the flow of the water makes contact with the barrier in a direction perpendicular to the barrier face.

Stress and pressure are both defined as forces per unit area that arise due to an externally applied force (21). When collecting strain measurements, the subsequent stress measurement can be determined using the relationship shown in 2.41:

$$\sigma = E * \epsilon \quad (2.41)$$

where ϵ is the unitless measurement of strain, E is the Young's modulus of elasticity, and σ is stress, or force per area.

The Young's modulus of elasticity is a property of the material that details how easily a material can deform, and it is a ratio of stress to strain. Since strain is a unitless measurement, it carries the same units as stress, force per unit area. By knowing the Young's modulus of elasticity, the conversion from strain to stress can be made (21). By multiplying the stress by the area of the measurement, stress can be converted to a force applied at that measurement location. With this method of conversion, strain gages can be used to record force measurements at specific locations on an object. The strain gage is typically installed and connected to a data acquisition system to record the measurements of strain. Then, using postprocessing techniques, the strain is converted to a measurement of force for the corresponding locations over a testing period.

2.12. IMPACT PERFORMANCE OF CONCRETE BARRIER SYSTEMS WITH OPENINGS

In 2010, Williams et al. (23) completed a research study that evaluated the Washington State Department of Transportation (WSDOT) pin-and-loop concrete barrier with drainage slots per *MASH* Test 3-11. The barrier had a height of 34 inches and consisted of 12-ft 6-inch-long segments. The barrier had a single-slope profile with a 21-inch base width and an 8-inch top width. A rectangular drainage scupper opening was incorporated at the center of each barrier segment. This opening had a height of 9 inches and a length of 28 inches. The barrier segments were connected to each other using pin-and-loop connections consisting of $\frac{3}{4}$ -inch A36 steel loops and 1-inch-diameter AISI 4142 pins. A finite element model (FEM) analysis revealed a maximum lateral barrier deflection of 53 inches and displayed noticeable deformation of the pin-and-loop connection as well. Additional FEM analysis showed no risk of wheel snagging against the drainage scupper.

A 2004 Dodge RAM 1500 quad-cab truck impacted the barrier at a speed of 60.2 mi/h and an angle of 26.2 degrees at the critical point of impact—4.3 ft upstream of a segment joint. The vehicle was contained and redirected but rolled onto its side after exiting from the barrier. Although the barrier did not satisfy *MASH* testing evaluation criteria, the researchers observed that the “drainage slots and scupper opening did not appear in any way to adversely affect the crash performance of the barrier system” (23). Figure 2.8 provides photos from this test (23).

In 2011, a variation of the Washington pin-and-loop barrier was retested (24). In this second crash test, the 1-inch-diameter AISI 4142 pins were replaced with 1¼-inch-diameter F1554-grade 105 steel rods. The vehicle appeared to perform better than in the previous test; however, the vehicle still overturned after exiting the barrier, and the barrier did not meet *MASH* Test Level 3 (TL-3) requirements. Figure 2.8 and Figure 2.9 show photos of the 2011 test (24).

In 2010, an evaluation was performed on the Louisiana Department of Transportation and Development (LaDOTD) F-shape concrete barrier, which was designed with drainage slots to accommodate drainage through the bridge rail into scuppers or off the sides of the bridge (25). The purpose of this evaluation was to investigate and compare the LaDOTD barrier strength to other existing barriers with similar openings. The barrier was 32 inches high and had a base width of 13.25 inches. The openings for the LaDOTD F-shape barrier were 6 inches high and 24 inches long. The potential for vehicle snagging during interaction with the openings was determined to be low. Compared to TxDOT's wildlife crossing barrier and the Washington pin-and-loop barrier, the openings of the LaDOTD barrier had a lower height (see Figure 2.10). The LaDOTD F-shape barrier with drainage slots was considered acceptable per National Cooperative Highway Research Program (NCHRP) Report 350 TL-4 standards.



a. Test article before impact



b. Test article after impact

Figure 2.8. WSDOT Barrier Test 3-11 (23).



a. Test article before impact



b. Test article after impact

Figure 2.9. Revised WSDOT Barrier Test 3-11 (24).

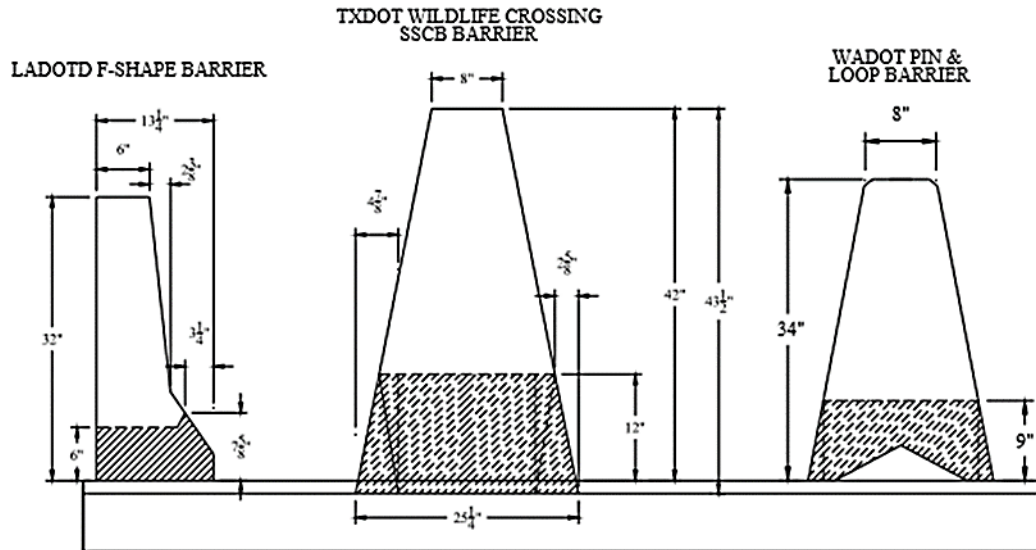


Figure 2.10. Side-View Comparison of LaDOTD F-shape Barrier, TxDOT Wildlife Crossing Single-Slope Concrete Barrier (SSCB), and WSDOT Pin-and-Loop Barrier (25).

Under a TxDOT-sponsored project, Texas A&M Transportation Institute (TTI) researchers evaluated a new median barrier that was developed (26). The barrier was analyzed using computer simulation and full-scale crash testing. The final design included anchoring a 42-inch-tall SSCB with a set of rubber anchor blocks bolted to the ground. Typically, rigid SSCBs are anchored with steel anchorage rebar connecting the barrier to the concrete pavement. This anchorage results in the barrier behaving rigidly, with no significant deflection. The new design with rubber blocks was intended to allow some barrier movement to reduce occupant severity while retaining the low-maintenance characteristic of a concrete barrier. Figure 2.11 shows an opening in the barrier with the installed rubber block. Although these openings were not introduced for drainage purposes, they have similar effects in terms of creating stress concentrations and affecting barrier capacity. When the system was tested following *MASH* Test 3-11 conditions with the 2270P pickup truck, large cracks originated from the corners of these openings. This information was used under the current project in terms of methods and areas of reinforcement.



Figure 2.11. Opening in Concrete Barrier to Allow for Rubber Block Installation (26).

While the subject of the research was the use of openings to enhance flow of water during heavy rains and flooding, barrier openings may also provide another safety benefit. Vehicular impacts with animals are becoming more common today as development further encroaches into wildlife habitats. When animals enter the roadway, they can become trapped by a concrete median barrier. As vehicles approach, they will often try to return to the roadside, and a crash can result due to the vehicle striking the animal or making an evasive maneuver to avoid striking the animal. If animals have a means of egress through the barrier, it might hasten their crossing and mitigate the likelihood of a crash occurring. The TxDOT wildlife crossing barrier was designed with this specific intent (25).

The TxDOT wildlife crossing barrier is 42 inches in height and has openings for wildlife access through the barrier (see Figure 2.12). A 30-ft length of barrier contains two openings that are 12 inches high and 5 ft long. Based on a review of the geometric features of this barrier, it was determined that the TxDOT wildlife crossing barrier was crashworthy with respect to NCHRP Report 350 TL-3 criteria.



Figure 2.12. TxDOT SSCB (Wildlife Crossing) (25).

As previously noted, one of the concerns pertaining to concrete barriers with openings or drainage scuppers is that they can become a location for high stress

concentration during an impact event. The Massachusetts Department of Transportation (MassDOT) Highway Division tested its 32-inch-tall, precast F-shape PCB system, shown in Figure 2.13, to determine if it was *MASH* compliant (27). The 10-ft-long barrier segments were precast with a single drainage relief/forklift slot in the center of the barrier that was 3 ft 4 inches long \times 3 inches high. The barrier was crash tested and performed acceptably for *MASH* TL-2 impact conditions. However, it was noted that the impact segment was cracked completely through the cross section near the center of the segment after *MASH* Test 2-11 (see Figure 2.14) (27).



Figure 2.13. MassDOT F-shape PCB (27).



Figure 2.14. Concrete Crack after *MASH* Test 2-11 (27).

This barrier was then retrofitted and tested in accordance with *MASH* TL-3 impact conditions (27). A 9-ft-long, 6-inch \times 4-inch \times $\frac{1}{2}$ -inch steel angle was secured to the back (field) side of each barrier segment with six screw anchors to increase barrier capacity. The retrofit MassDOT PCB performed acceptably for *MASH* TL-3 impact conditions. A significant fracture near the center of the impact segment (see Figure 2.15) confirmed the need for the additional capacity provided by the steel angle (27).



Figure 2.15. Concrete Crack after *MASH* Test 3-11 on MassDOT Retrofit PCB System (27).

2.13. ROADSIDE SAFETY POOLED FUND PROJECT 612831—*MASH* EVALUATION OF F-SHAPE AND SINGLE-SLOPE CONCRETE BARRIERS WITH DRAINAGE SCUPPERS

TTI researchers performed a research project funded by the Roadside Safety Pooled Fund group to evaluate the impact performance of free-standing and anchored configurations of an F-shape PCB in accordance with *MASH* TL-3 criteria and an embedded single-slope PCB following *MASH* TL-4 criteria (28). The critical tests were performed on each barrier configuration, and an engineering justification was provided for the noncritical tests based on previous testing of other barrier systems.

2.13.1. *MASH* Test 3-11 on Free-Standing F-shape Barrier with Drainage Scuppers

The F-shape barrier segments were 32 inches tall, incorporated two 6-inch-tall drainage scuppers, and were attached to each other using pin-and-loop connections. This system was evaluated by performing *MASH* Test 3-11. Figure 2.16 shows the free-standing F-shape barrier test installation before and after *MASH* Test 3-11. The free-standing F-shape barrier with drainage scuppers passed the performance criteria for *MASH* Test 3-11 for longitudinal barriers.



a. Before crash test



b. After crash test

Figure 2.16. Test Installation for Free-Standing F-shape Barrier with Drainage Scuppers (28).

2.13.2. *MASH* Test 3-11 on Pinned F-shape Barrier with Drainage Scuppers

The same 32-inch-tall F-shape barrier with drainage scuppers and pin-and-loop connections was anchored to a 4-inch-thick layer of asphalt pavement using three anchoring pins per segment. Figure 2.17 depicts the F-shape barrier test article before and after *MASH* Test 3-11. The F-shape barrier with drainage scuppers, pinned on 4 inches of asphalt, passed the performance criteria for *MASH* Test 3-11 for longitudinal barriers (28).



a. Before crash test



b. After crash test

Figure 2.17. Test Article for F-shape Barrier with Drainage Scuppers (28).

2.13.3. *MASH* Test 4-12 on Embedded Single-Slope Barrier with Drainage Scuppers

A 42-inch-tall single-slope concrete barrier system with grouted rebar-grid connections and drainage scuppers was embedded 4 inches in asphalt for an above-grade measurement of 38 inches (28). Each precast barrier segment had three 10-inch-tall drainage scuppers at the bottom, which provided 6-inch openings above grade after the segments were embedded in asphalt. This system was evaluated by performing *MASH* Test 4-12. Figure 2.18 depicts the single-slope barrier test installation before and

after *MASH* Test 4-12. The embedded single-slope barrier with drainage scuppers passed the performance criteria for *MASH* Test 4-12 for longitudinal barriers (28).



a. Before crash test



b. After crash test

Figure 2.18. Test Article for Embedded Single-Slope Barrier (28).

2.14. TXDOT PROJECT 0-6976—DEVELOPMENT AND *MASH* TL-4 EVALUATION OF TXDOT LARGE-SCUPPER MEDIAN BARRIER FOR FLOOD-PRONE AREAS

Under TxDOT Project 0-6976, TTI researchers developed a new hydraulically efficient cast-in-place concrete median barrier for use in flood-prone areas (29). The researchers designed and evaluated the *MASH* TL-4 compliant concrete median barrier through engineering analyses, computer simulation, hydraulic large-scale testing, and full-scale vehicular crash testing.

The hydraulically efficient barrier (HEB) has a single-slope profile, an overall height of 42 inches above grade, a bottom width of 24 inches, and a top width of 8 inches. The HEB incorporates a 13-inch-high, 18-ft-long scupper on 30-ft centers. A photo of the HEB test installation is shown in Figure 2.19 (29).



Figure 2.19. TxDOT Large-Scupper Median Barrier Test Article for *MASH* TL-4 Testing (29).

The full *MASH* TL-4 matrix was successfully performed on the HEB. The full-scale crash tests included *MASH* test designations 4-10 (small passenger car), 4-11 (pickup truck), and 4-12 (single-unit truck). The HEB is detailed in TxDOT standards SSCHEB-21 and SSCHEB2-21 and has been implemented along IH 10 and other highways in Texas.

2.15. CONCLUSIONS

Some observations from the literature are reported below. The hydraulics portion of the literature review revealed the following:

- Hydraulic efficiency is primarily affected by the dimensions of the fractional open space.
- As the barrier opening width increases and the opening gets closer to the road surface, the hydraulic efficiency increases.
- The model presented in Charbeneau et al. (9) can accurately predict flow characteristics by using experimentally determined parameters. By adjusting the fractional open space parameter, different flow obstructions in barrier openings can be modeled.
- The drag coefficient and flow separation can be reduced by streamlining barrier openings; however, due to the frequency of heavy storm events, this reduction is expected to have a minimal impact on conveyance capacity and barrier lifespan.
- Portable concrete traffic barriers can become buoyant objects during flood events depending on the volume of water being displaced compared to the volume of the barrier. Both the location and size of the scupper can affect the buoyancy properties of the barrier depending on the type of flow under consideration.

The barrier design and crash testing portion of the literature review revealed the following information:

- Very limited research and testing have been performed to investigate the structural adequacy and crashworthiness of concrete barriers with large openings.
- A significant development for possible flood mitigation is the hydraulically efficient, cast-in-place, concrete median barrier developed under TxDOT Project 0-6976, which satisfied *MASH* TL-4 criteria. Although the project focused on developing a rigid concrete barrier with a large scupper, the geometric and structural design of the barrier may have applications to portable concrete barriers with large scuppers.
- Most existing portable concrete barriers are designed with relatively small scuppers (e.g., 3 inches tall × 36 inches long), which provides limited cross-drainage capacity.
- The structural capacity of a barrier with large scuppers needs to be carefully evaluated because openings in the barriers have been shown to become areas of high stress concentration.
- The opening size and treatment should be designed to limit vehicle snagging potential that can lead to high occupant risk and vehicle instability.

Table 2.1 summarizes the tested concrete barrier systems with various drainage scuppers that were reviewed.

Table 2.1. Summary of Evaluated Concrete Barriers with Drainage Scuppers.

Project No.	Type of Barrier	Scupper Height (inch)	Scupper Width (inch)	No. and Location of Scuppers	Test Designation	Results
405160-30-1 (23)	Free-Standing Single-Slope	9	28	One scupper at center of barrier segment	MASH Test 3-11	Fail
405160-18-1 (24)	Free-Standing Single-Slope	9	28	One scupper at center of barrier segment	MASH Test 3-11	Fail
612831-01 (28)	Pinned F-shape	6	28	Two scuppers at equal spacing	MASH Test 3-11	Pass
612831-01 (28)	Free-Standing F-shape	6	28	Two scuppers at equal spacing	MASH Test 3-11	Pass
612831-01 (28)	Embedded Single-Slope	10	18	Three scuppers at equal spacing	MASH Test 4-12	Pass
0-6976 (29)	Rigid Single-Slope	13	216	One scupper at center of barrier segment	MASH TL-4	Pass

Chapter 3. DESIGN OPTIONS

The TxDOT project panel identified specific design preferences and requirements for the hydraulically efficient portable concrete median barrier system with large scuppers. TxDOT standards for portable concrete median barriers include a 32-inch-tall F-shape barrier (CSB[1]-10) and a 42-inch-tall single-slope barrier (SSCB[2]-10). The project panel opted for the 42-inch SSCB with 30-ft-long segments based on its increasing frequency of use and potential for accommodating larger scupper openings.

TxDOT standards include options for three different connection types for single-slope portable concrete barriers: Type X (X-bolt), Type Q (quick-bolt), and Type R (J-J Hooks®). The project panel preferred that both the J-J Hooks and a modified X-bolt connection be investigated. The project panel also stipulated that the barrier design must comply with *MASH* TL-3 criteria.

Based on the information gleaned from the literature review and experience of the research team with the design and testing of PCB systems, three design options for a hydraulically efficient PCB with large scuppers were developed. The options differed in terms of the number and size of scuppers in a 30-ft barrier segment. A description of each barrier design concept is provided in this chapter, along with a preliminary drawing and perceived advantages and disadvantages.

3.1. OPTION A: 42-INCH-TALL PRECAST SINGLE-SLOPE CONCRETE MEDIAN BARRIER WITH ONE SCUPPER

Figure 3.1 shows the 42-inch-tall precast single-slope (SS) median barrier with one large scupper. The base of the barrier segment was 24 inches wide, and the barrier was 8 inches wide at the top. The proposed opening was 13 inches tall and 18 ft long. The ends of the opening would be sloped laterally to limit risk of vehicle snagging during an impact. The flare rate for this transition slope to the full single-slope profile was conceptually 1:9.2 (6.2 degrees). It was recognized that results from large-scale hydraulic testing, finite element computer simulations, and engineering analyses might dictate changes to these dimensions. Table 3.1 lists the advantages and disadvantages of Option A.

3.2. OPTION B: 42-INCH-TALL PRECAST SINGLE-SLOPE CONCRETE MEDIAN BARRIER WITH TWO SCUPPERS

Figure 3.2 depicts Option B, which incorporated two scuppers that were conceptually each 12 inches tall and 6 ft long. The determination of appropriate opening size (height and length) would be dictated by large-scale hydraulic testing, finite element computer simulations, and engineering analyses. The transition slope to the full single-slope profile was 1:6.75 (8.4 degrees). This angle was influenced by the available transition length while trying to maximize the length of the openings. Table 3.2 lists the advantages and disadvantages of Option B.

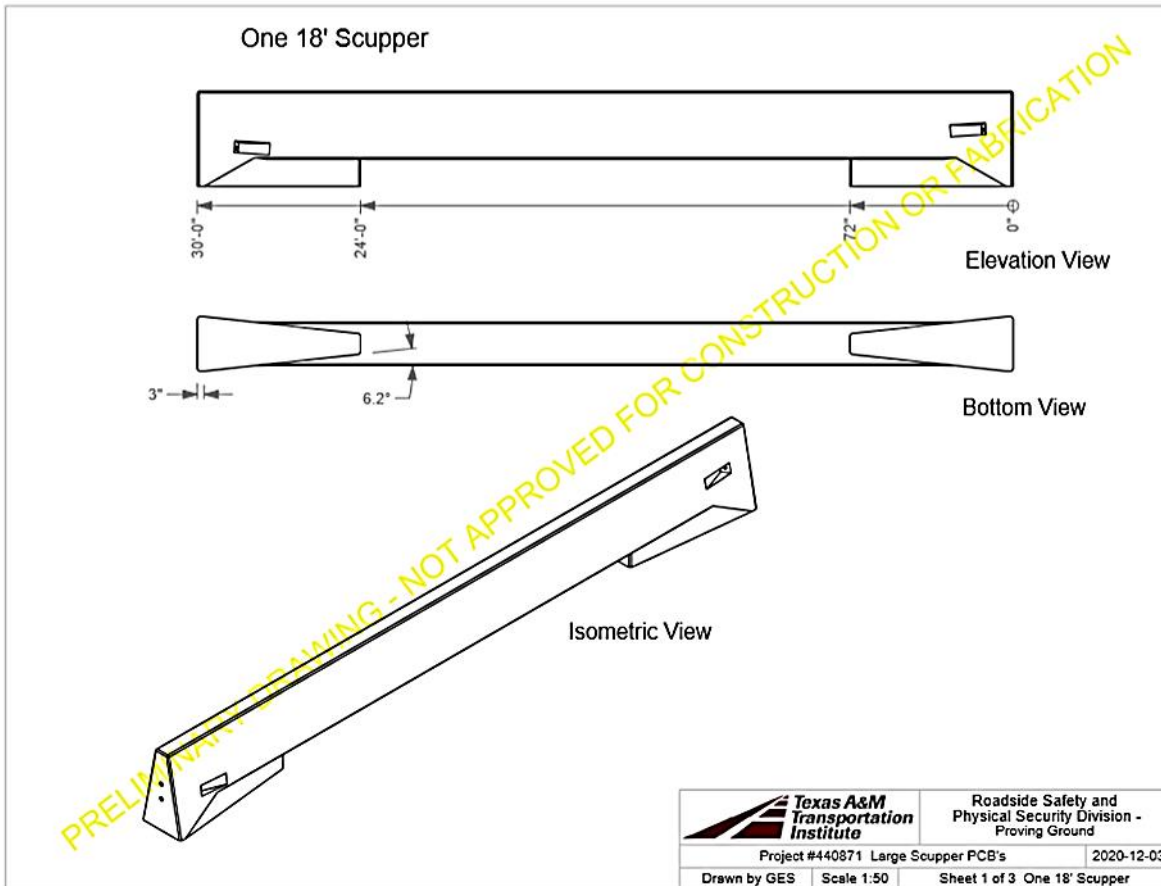


Figure 3.1. Option A Preliminary Drawing.

Table 3.1. Option A Perceived Advantages and Disadvantages.

Advantages	Disadvantages
Post sections flared laterally at shallowest rate may reduce vehicle snagging during an impact	Long span may require additional reinforcement from a structural capacity perspective
Largest opening allows the most water to flow through	Longest length of slope transition to opening may increase chance of contact and possible spalling and other damage during impact
Single span may allow for simplest reinforcement layout	Most complex to precast because of required flow length for concrete beam associated with opening when precasting segment upside down in mold

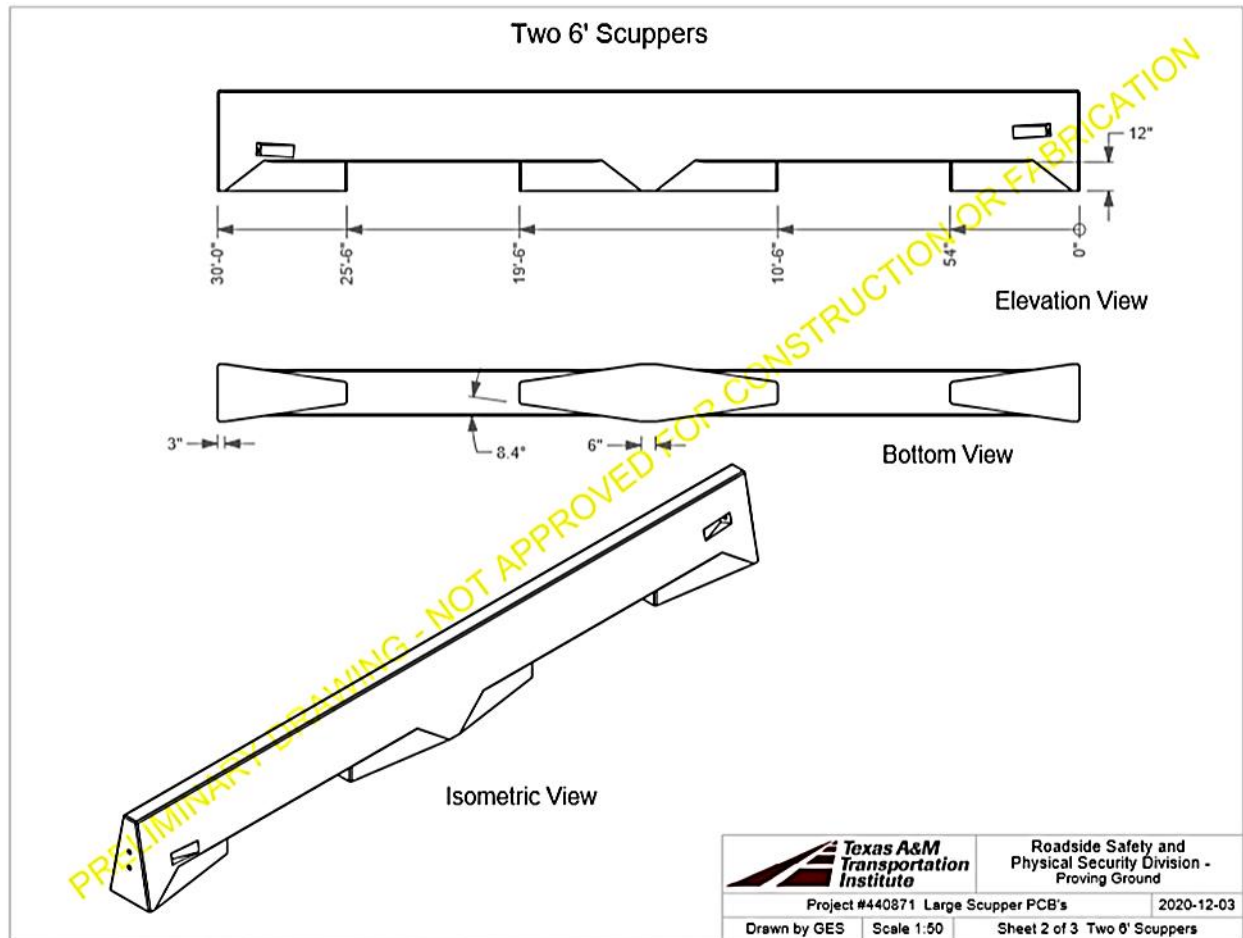


Figure 3.2. Option B Preliminary Drawing.

Table 3.2. Option B Perceived Advantages and Disadvantages.

Advantages	Disadvantages
Shorter beam spans associated with openings may reduce amount of required reinforcement from a structural capacity perspective	Steeper slope transition rate may increase vehicle snagging severity if contact does occur during an impact
Shorter length of slope transition to opening may decrease chance of contact and possible spalling and other damage during impact	Smaller openings allow less water to flow through compared to Option A
Shorter beams above openings reduce flow length for concrete when precasting segment upside down in mold	Additional “post” created by two scuppers may complicate reinforcement layout

3.3. OPTION C: 42-INCH-TALL PRECAST SINGLE-SLOPE CONCRETE MEDIAN BARRIER WITH THREE SCUPPERS

Figure 3.3 depicts Option C, which incorporated three identical scuppers that were conceptually 10 inches tall and 5 ft long. The determination of appropriate opening size (height and length) would be dictated by large-scale hydraulic testing, finite element computer simulations, and engineering analyses. The transition slope to the full single-slope profile was 1:3.6 (15.5 degrees). This angle was influenced by the available transition length while trying to maximize the length of the openings. Table 3.3 lists the advantages and disadvantages of Option C.

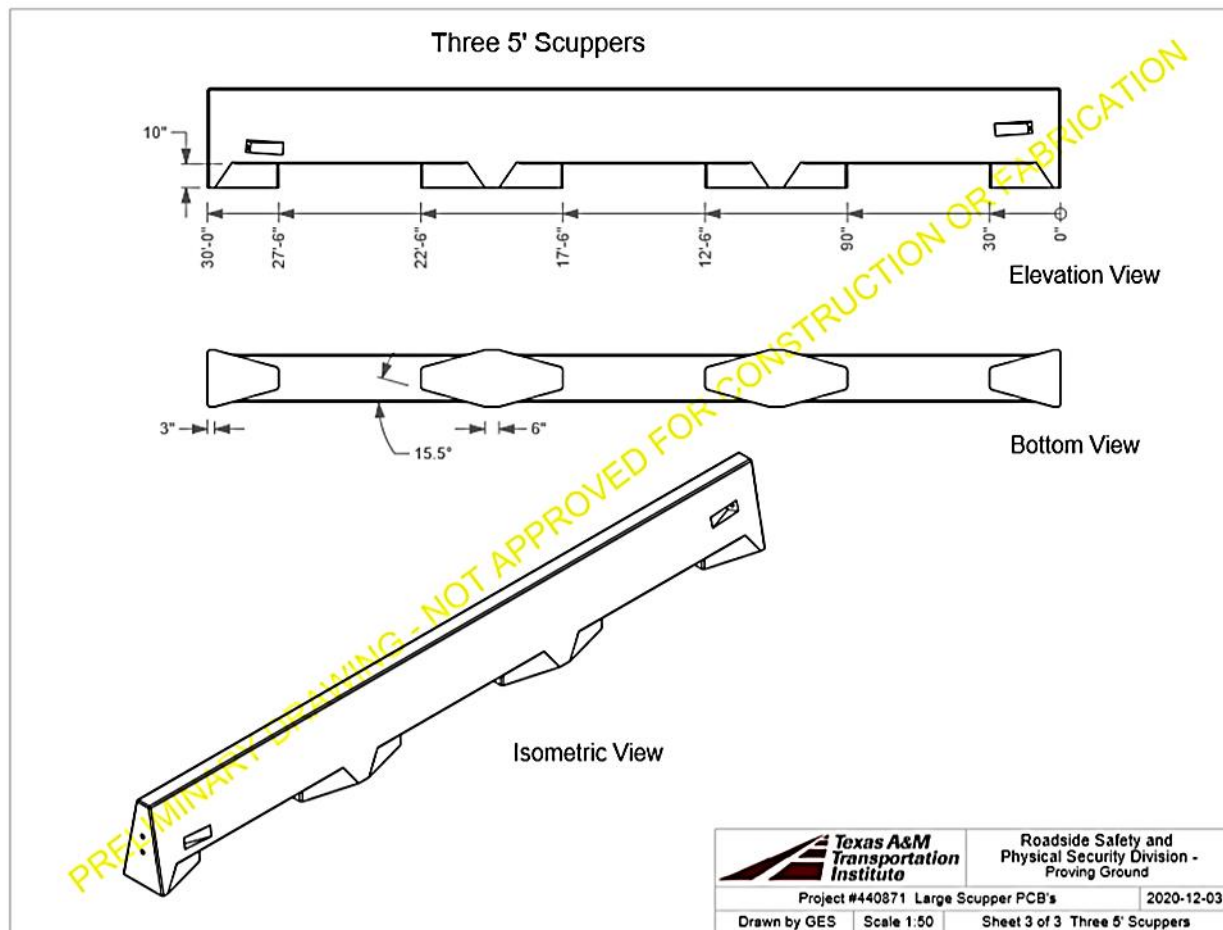


Figure 3.3. Option C Preliminary Drawing.

Table 3.3. Option C Perceived Advantages and Disadvantages.

Advantages	Disadvantages
Shortest span may further reduce amount of required reinforcement from a structural capacity perspective	Steepest slope transition rate may increase vehicle snagging severity if contact does occur during an impact
Shortest length of slope transition to opening may further reduce chance of vehicle contact and possible spalling and other damage during impact	Smaller openings allow less water to flow through
Simplest to precast because of shortest required flow length for concrete beam sections when precasting upside down in mold	Several “post” sections introduced by multiple scuppers may complicate reinforcement layout

3.4. HYDRAULIC CALCULATIONS FOR PROPOSED DESIGNS

The volume of fluid that can be displaced by the barrier is related to the size of the barrier openings. It is only necessary to consider the size and shape of the openings in conjunction with the type of flow present. The location of the openings within the segment will not impact the volume calculation. All barrier design options were 30 ft long and 42 inches tall, and all had a bottom width of 24 inches and a top width of 8 inches. Using these dimensions, the original single-slope barrier had a volume of 140 ft³ without accounting for any scupper volume. The volume of the openings could be simply calculated. Table 3.4 provides the percentage of mass removed from the original single-slope barrier due to the introduction of the proposed scuppers within each design option. The percentage of the original contact area with ground was also calculated for each design option.

Table 3.4. Comparison of Some Characteristics of Proposal Design Concepts.

Design Concept	Missing Mass (%)	Provided Contact Area with Ground (%)
Option A	25	27
Option B	15.5	40
Option C	16.5	32.5

Table 3.5 shows the adjusted volume of the proposed barrier options accounting for the scuppers. The weight of each barrier segment option was also calculated, assuming the unit weight of concrete was 150 lb/ft³. If the unit weight of water was 62.4 lb/ft³, and its displaced volume was equal to the volume of the barrier, the buoyant force could also be calculated for Type 3 flow in which the barrier was fully submerged, as shown in Table 3.5. Furthermore, the buoyant force could be calculated at any depth by altering the flow depth, which would in turn change the volume being displaced.

Using the free body diagram in Figure 2.7, the sum of the forces acting downward on the barrier could be calculated and compared to the upward acting buoyant force on the barrier.

Table 3.5. Volume of Proposed Barrier Designs, Theoretical Barrier Weights, and Buoyant Forces.

Design Concepts	Number of Scuppers	Original Barrier Volume (ft ³)	Missing Volume (%)	Adjusted Barrier Volume (accounting for scuppers) (ft ³)	Barrier Weight (lb)	Buoyant Force (lb)
Option A	1	140	25	105	15,750	6559.1
Option B	2	140	15.5	118.3	17,745	7390.0
Option C	3	140	16.5	116.9	17,535	7302.5

Once the weight of the barrier was calculated, it was also possible to determine the resistive and overturning moments, along with the horizontal resisting and driving forces, which allowed for the calculation of the factors of safety against overturning and sliding. To do so, it was first necessary to determine P, the hydrodynamic or hydrostatic force on the barrier. The hydrodynamic force on the barrier could be theoretically calculated using Equations 2.39 and 2.40.

At this stage in the project, since no flow data had been collected for these new barrier design options, it was necessary to make some simplifying assumptions. For ease of calculation, only the hydrostatic pressure acting on the barrier was calculated for Type 3 flow. This resulted in a force of 3279.6 lb, and the resultant force height was 1.167 ft above the base of the barrier. Based on the geometry of the barrier designs, $\alpha = 10.78$ degrees, and $\beta = 79.22$ degrees. The coefficient of static friction in Equation 2.33 is assumed to be the coefficient between concrete and asphalt, which was taken as 0.55. The sum of the moments of forces overturning about point C, the sum of the moments of forces resisting overturning about point C, the sum of horizontal resisting forces, and the sum of horizontal driving forces could then be found using Equations 2.29, 2.30, 2.33, and 2.34. Subsequently, the factors of safety against sliding and overturning could be calculated using Equations 2.28 and 2.32.

The results of this analysis are shown in Table 3.6. While the factors of safety appear to be acceptable, hydrodynamic forces were not theoretically calculated, and if they are included, it is reasonable to assume that the factors of safety would decrease significantly and could be less than 1. As the factors of safety are reduced, it becomes increasingly probable that the barriers will either slide or overturn under Type 3 flow, and possibly under Type 2 conditions depending on the flow depth.

Table 3.6. Calculations to Determine Factors of Safety against Sliding and Overturning.

Design Concepts	Number of Scuppers	$\sum M_R$ (ft·lb)	$\sum M_0$ (ft·lb)	$FS_{overturning}$	$\sum F_R$ (lb)	$\sum F_d$ (lb)	$FS_{sliding}$
Option A	1	16,840	10,317	1.63	8999.9	3221.7	2.79
Option B	2	18,835	11,148	1.69	10,097	3221.7	3.13
Option C	3	18,625	11,061	1.68	9981.6	3221.7	3.10

3.5. CONCLUSIONS

Design options for a hydraulically efficient portable concrete barrier were developed. The designs considered impact performance and the action of hydraulic hydrodynamic forces. After consideration of this information, the TxDOT project panel selected Option A for further development and evaluation through large-scale hydraulic testing and finite element impact simulations. This option included one large opening in the 30-ft segment of the 42-inch-tall single-slope concrete median barrier. The following chapters describe the analysis, testing, and evaluation of this design concept.

Chapter 4. LARGE-SCALE HYDRAULIC TESTING

Large-scale hydraulic testing was performed to determine the hydraulic efficiency of a median barrier with a scupper. By using a properly scaled model median barrier in an experimental channel, a variety of pertinent measurements can be gathered to explain the most effective methods for studying portable median barriers. In turn, further work can be conducted to determine important hydraulic parameters that should be considered when implementing portable median barrier designs throughout the roadways of Texas. The model barrier was designed and installed in a concrete channel for hydraulic testing at the Center for Water and the Environment on the J.J. Pickle Research Campus, University of Texas at Austin.

4.1. EXPERIMENTAL FACILITY

Hydraulic testing was carried out in an outdoor concrete flume, which was fed from an on-site reservoir by means of an integrated pipe system, meaning water could be continuously recirculated without delay for the duration of the testing. Figure 4.1 depicts an overhead layout of the flume.

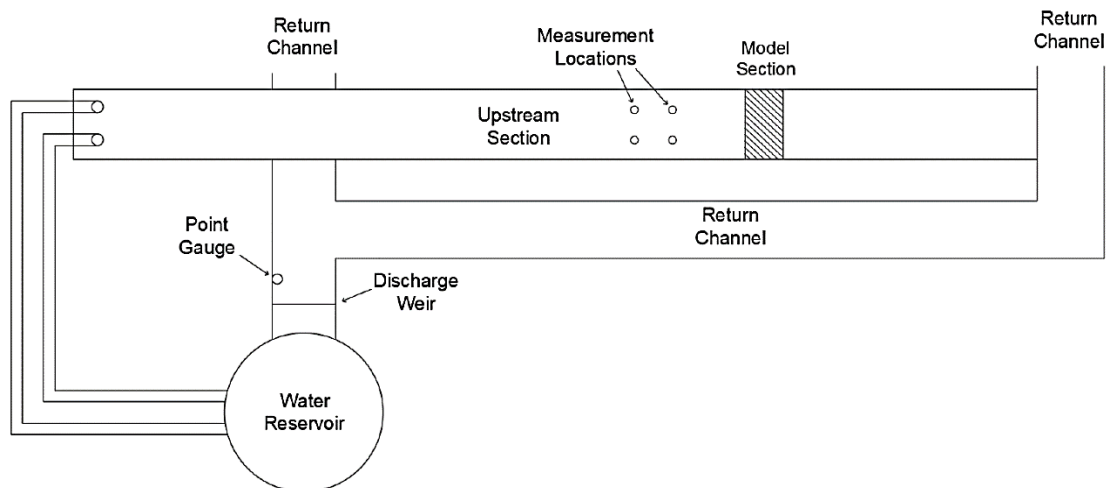


Figure 4.1. Flume Layout (15).

4.1.1. Reservoir and Pipe Network

The reservoir held approximately half a million gallons of water, and two pumps, each controlled by a valve, were used to transfer water through the pipe network to the outdoor flume. By adjusting the valves, the pump flow rate into the channel was controlled. Furthermore, this recirculation allowed for the system to reach a steady state with a constant flow rate, which was significant for the testing to be done properly.

4.1.2. Test Channel

The outdoor channel was a rectangular concrete flume that was 5 ft wide, 2 ft 8 inches high, and approximately 125 ft long. The channel bed slope in both the spanwise and lengthwise directions was approximately 0 degrees, and the walls were all at approximately 90-degree angles with the channel bed. The water entered the flume through two pipe outlets at the head of the channel, as shown in Figure 4.2, and it flowed through the entire length of the channel before spilling into the return channel.

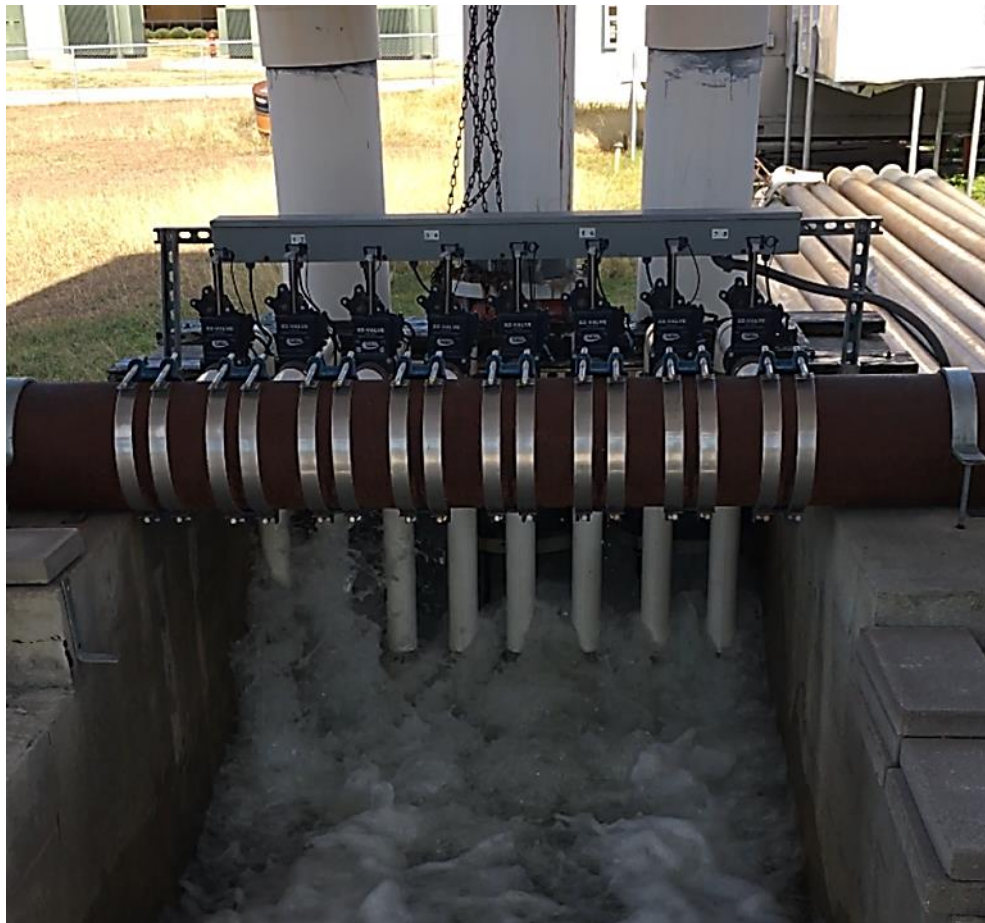


Figure 4.2. Pump Outlets (15).

4.1.3. Return Channel

The flow continued through the return channel until it reached the discharge weir, which acted as a dam to build up water upstream in the channel. Eventually, the water flowed over the crest of the weir and continued through the remainder of the channel into the reservoir. Shortly upstream of the weir, a point gage was used to measure the head above the weir crest, which was used to determine the steady-state flow rate.

4.2. BARRIER CONSTRUCTION

The median barrier used in the hydraulic testing was an SSCB model barrier designed at TTI. The vertical dimensions of the barrier were scaled down to a 2:1 ratio to allow the barrier to fit best in the channel while still maintaining space for flow over the barrier crest. The horizontal dimensions were set to a 6:1 ratio from the prototype to model. The scupper length and height were appropriately scaled to these dimensions as well to ensure the fractional opening was maintained from prototype to model. The model barrier was constructed entirely of wood, and it was anchored to a support base in the channel to ensure structural integrity and stability against hydrodynamic forces generated by the upstream flow. All edges of the model were sealed with silicone caulk to ensure that water only flowed through the scupper or over the crest of the barrier, and not through any cracks or open spaces on the barrier. In addition, all exposed faces of the barrier were coated with multiple layers of waterproof paint to prevent any infiltration and wood swelling. A sketch of the front view of the model barrier is shown in Figure 4.3.

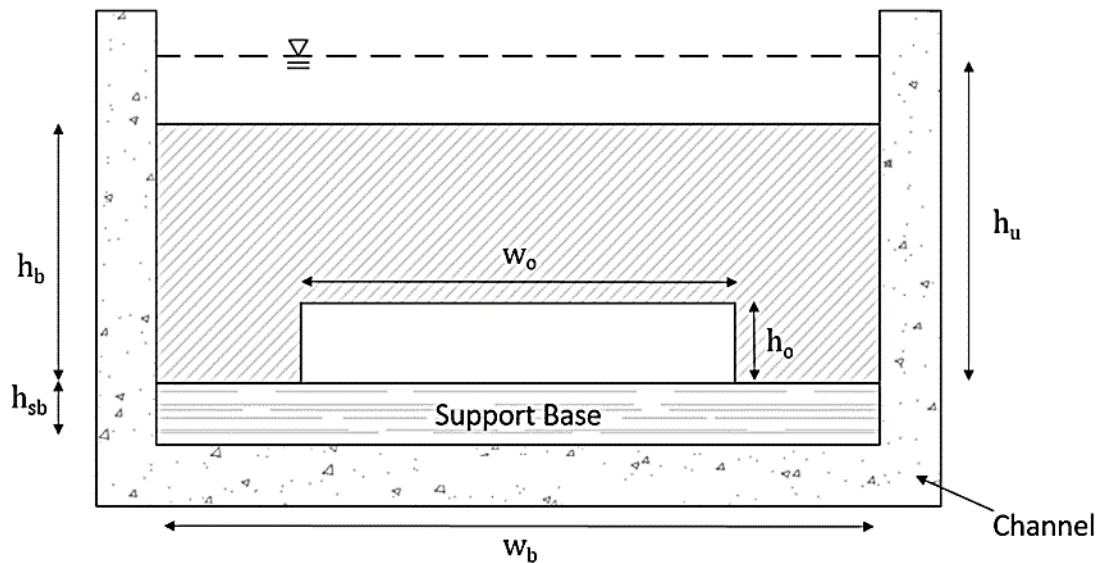


Figure 4.3. General Model Barrier (15).

4.2.1. Support Base

The support base was previously used for hydraulic testing on median barriers (15), and since it was still intact, it was resealed and waterproofed for use. The purpose of the base was to anchor the median barrier in place while allowing for its removal at the end of testing. The dimensions of the base were 57 inches \times 36 inches \times 4.25 inches. Wood planks were installed on both sides of the base to fill the 5-ft-wide channel when in place while allowing the water to drain completely from the channel when removed. The frame of the base was built using two 3.5-inch \times 3.5-inch wood planks on top of and underneath 0.75-inch plywood sections. The base was fastened to the channel with concrete bolts approximately 90 ft downstream of the pumps. Eight

removable machine screws were used to secure the barrier to the support base, with four screws in each plank. The front, back, and center sections of the support base were filled with concrete blocks to provide added weight. Figure 4.4 shows the support base design and the physical base without the top section of plywood.



Figure 4.4. Support Base Design and Installation (15).

4.2.2. Median Barrier Model

The dimensions of the SSCB model barrier are shown in Figure 4.5. The barrier was 59 inches long and 21 inches tall, and it was 12 inches wide at the base. It then sloped to a width of 4.75 inches at its crest. The scupper was 3 ft wide and 6 inches tall, and the barrier sat in the middle of the support base. The barrier supports at the barrier edge were 1 ft wide and tapered to a width of 4.6 inches at the scupper edge. To ensure the structural integrity of the barrier, 1.5-inch-wide internal supports were placed 20 inches from the barrier edges, and these further reinforced the plywood sheet faces of the barrier. In addition, the barrier was anchored to a 1-inch-thick sheet of plywood that was the base of the barrier. This barrier base fit in place in the support base, with eight screws being drilled through this plywood and into the support base. While the purpose of this study was to investigate portable median barriers, the model barrier was anchored to the base to prevent damage to the barrier and channel in the event of overturning or sliding, with predictions of barrier failure determined from analysis of data collected via barrier instrumentation and flow parameters.

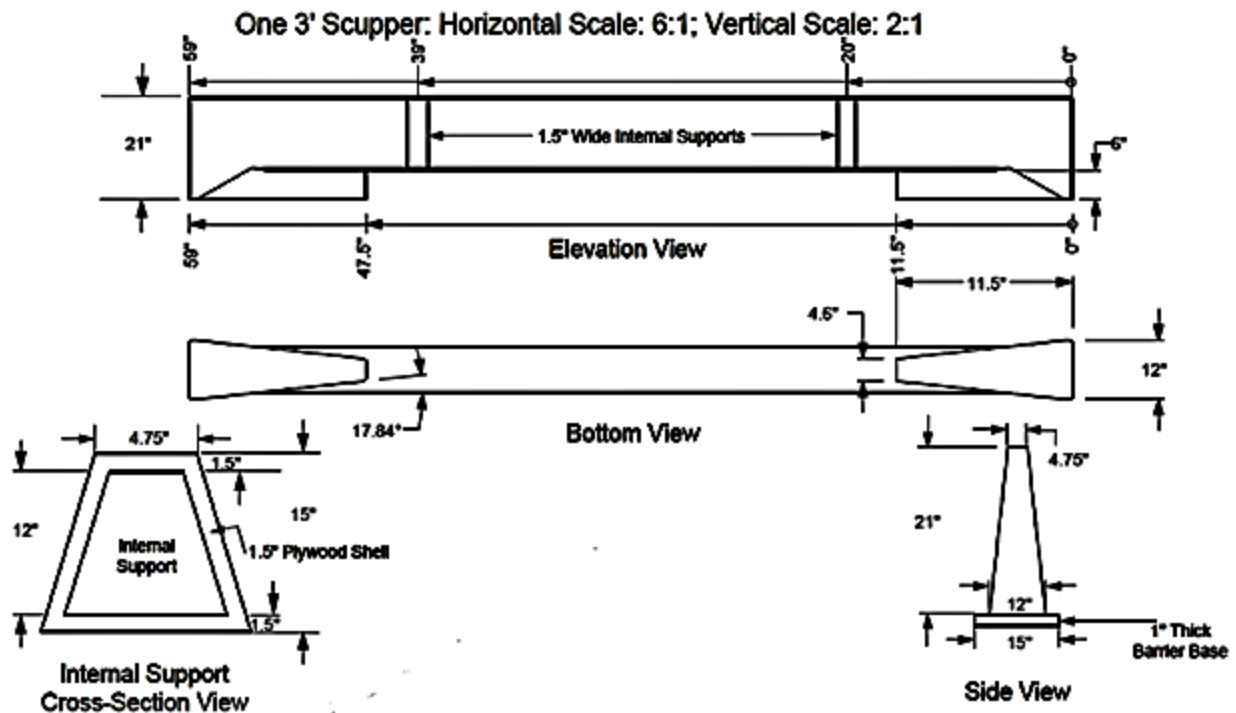


Figure 4.5. SSCB Model Barrier Dimensions (not to scale).

4.2.3. Setup in Channel

Once the barrier was anchored to the support base, the edges between the channel bed and upstream and downstream support base faces were resealed with silicone caulk. The median barrier was constructed 1 inch short of the 5-ft width of the channel to allow for ease of installation. To increase the frictional support of the barrier-channel interface, five wood shims were wedged between the barrier and the channel on each side. The excess shim pieces were then trimmed using a hand saw. To complete the installation, all edges of the barrier were sealed with silicone caulk to prevent any flow around the sides of the barrier. Since the prototype portable barriers would have gaps between adjacent barriers, this method ensured a conservative approach to the barrier design.

4.3. INSTRUMENTATION AND DATA COLLECTION

Three main topics of interest were evaluated in this study. The first was building a rating curve for the model barrier. The variables needed to build this curve were flow rate and upstream water depth. The flow rate was determined by measuring the water depth above the discharge weir and using the weir equation that was introduced in the literature review. Then, the upstream water depth was found using ISCO 4230 bubble flow meters connected to the channel via vinyl tubing attached to the channel bed.

The second topic was the measurement of point velocities both upstream and inside the scupper of the barrier. These velocities were recorded using acoustic Doppler velocimeters (ADV; Nortek Vectrinos) mounted to platforms above the channel.

Third was the measurement of force using sensors placed on the upstream face of the barrier. The use of the sensors allowed the hydrodynamic force at various locations on the barrier to be recorded, and the measurements could then be used to determine how much force was acting on the barrier. Details on instrumentation and data acquisition are provided next.

4.3.1. Bubble Flow Meters

The flow meters were housed in a 12V solar-powered housing unit that provided a constant power source and protected the instruments from the outdoor environment. The solar panel was attached to the top of the housing unit and was connected to a marine battery inside that powered all four of the bubble flow meters. The flow meters recorded the water depth by measuring the pressure required to send a small air bubble through the length of the $\frac{1}{8}$ -inch I.D. vinyl tubing. The required pressure was equal to the water at the depth of the tube outlet, and water depth, h_u , was calculated from the measured pressure, P , water density, ρ_w , and gravitational constant, g :

$$h_u = \frac{P}{\rho_w g} \quad (4-1)$$

Each flow meter was set to measure at a frequency of 1 Hz, while the reporting frequency was 0.2 Hz. Under these settings, the flow meters reported the mean value from five measurements every 5 seconds. The tubes were fed through the housing unit and into the channel. They ran down the channel walls and across the channel bed, perpendicular to the direction of the flow, which therefore negated interference from the fluid velocity at the tube outlet. Silicone caulk was applied to the tubing to keep it completely attached to the channel bed. Figure 4.6 shows the flow meters and housing unit.



Figure 4.6. Bubble Flow Meters and Solar Panel Housing Unit (15).

4.3.2. Upstream Water Depth

Four upstream water depth measurements were recorded 18 ft and 26 ft upstream of the barrier face. For each flow rate, three recordings were taken at all

locations to account for any small waves in the surface flow or discrepancies in instrument measurements. A mean was then taken from these 12 recordings to produce an upstream water depth value for the specified flow rate. Figure 4.7 shows the measurement locations relative to the model barrier.

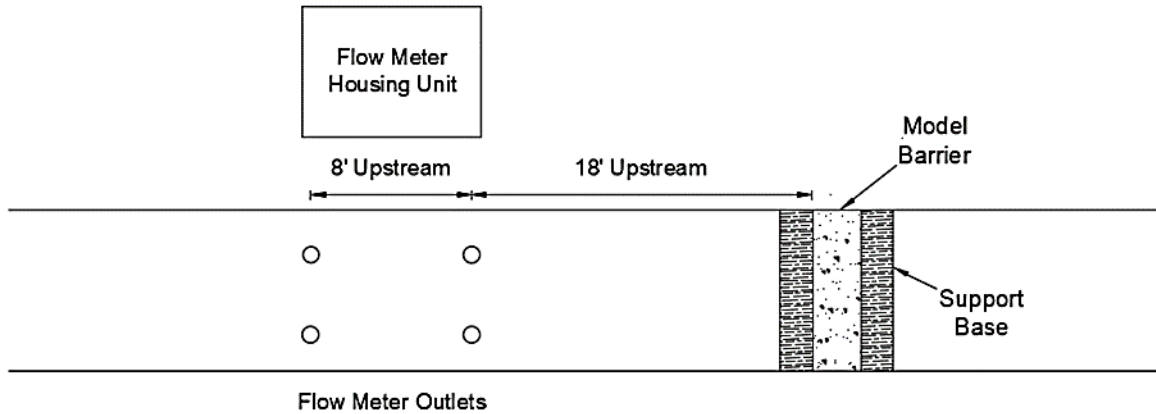


Figure 4.7. Upstream Water Depth Measurement Locations (15).

4.3.3. Discharge Weir

The discharge weir was a rectangular, sharp-crested weir located approximately 30 ft upstream from the entrance to the reservoir in the return channel. The weir was a 5-ft by 2-ft metal plate sealed with silicone caulk on all sides to prevent any leakage. The weir was treated as a rectangle, even though there was a small vertical slope that spanned across the weir crest. However, the effect of this slope on the flow rate measurements was considered negligible. A 1-ft-tall by 8-inch-wide rectangular orifice was located at the center of the base of the weir. During testing, a hinged gate was closed over the orifice and all openings were again sealed with silicone caulk. A chain was used to pull the orifice gate open to allow the channel to drain at the conclusion of testing. The weir and gate are shown in Figure 4.8. Additionally, the chain served the secondary purpose of providing a small amount of turbulence because of its flow obstruction in the nappe. This introduced aeration to the nappe, which assisted in steadying the upstream flow and allowed 4-2 for sharp-crested weir flow to remain valid. The discharge coefficient, C_d , for this weir was found to be 0.618 from past experiments (30).

$$Q = C_d * \frac{2}{3} * \sqrt{2g} * B * H^{\frac{3}{2}} \quad (4-2)$$



Figure 4.8. Discharge Weir and Orifice Gate (15).

4.3.4. Point Gage and Flow Rate

A point gage was located 16 ft upstream of the discharge weir, and it measured the water depth in the return channel to one thousandth of a foot. At this location, it was assumed that there were no negligible drawdown effects from the weir; however, there were slight variations in the water depth at any given moment due to turbulent effects from a 90-degree bend in the channel 27 ft upstream. To suppress these small waves, the point gage resided in a 2-inch-diameter plastic stilling well. This setup is shown in Figure 4.9. The datum was set at the weir crest so that the water depth over the weir could be measured. To measure this datum, the return channel was filled completely with water, at which point the pumps were shut off and water was allowed to drain to the weir height. Due to the small slope of the weir, the datum was set at the center of the weir span. The measurement process was repeated multiple times to increase accuracy, and the gage reading for the weir crest was determined to be 0.958 ft.



Figure 4.9. Point Gage (15).

4.3.5. Acoustic Doppler Velocimeter

To collect point velocity data, a Nortek Vectrino ADV was installed to collect measurements at several locations, including upstream of the model barrier and inside the scupper opening (see Figure 4.10). It was attached to a 2-inch x 4-inch wood plank fastened to a platform that spanned the width of the channel. This allowed both the height above the channel bed and the lateral position of the ADV within the channel to be precisely controlled. The ADV was attached to a power source and a laptop with the Vectrino software and “plus” firmware by using a RS232-USB converter so that data could be simultaneously collected, recorded, and stored. The software allowed the sampling frequency, the velocity range, and a number of other data collection parameters to be controlled. The data from the ADV were then exported in a .dat file and loaded into a MATLAB script developed in-house that performed the necessary data filtering and analysis.

The ADV captured data in a sampling volume located 5 cm below the probe (31). The plus firmware allowed for a sampling rate of 1–200 Hz, and 200 Hz was chosen as the sampling rate for all data collection. To provide optimal data quality, the nominal velocity range was changed depending on the location of the ADV in the channel. Near the barrier base and inside the scupper opening, the nominal velocity range was 2.50 m/s. Near the channel wall, the nominal velocity range was 1.00 m/s. All other locations were sampled at a nominal velocity range of 4.00 m/s. These ranges ensured the highest possible correlation between data points and signal-to-noise ratio. Two ADVs were employed throughout testing. The ADV upstream of the barrier consisted of a waterproof electronics housing unit connected to a metal rod that had the metal probe on its other end. On the other hand, the ADV that was placed inside the scupper used a cord to attach the housing unit to the probe. This allowed the scupper ADV to be easily positioned without interfering with flow through the scupper. The ADV had an accuracy of ± 1 percent of the measured value. This instrument worked via scattering of acoustic waves on seeding matter suspended in the water; because the water in this channel was stored in an outdoor reservoir, the natural seeding from organic matter was enough to ensure sufficient data quality.



Figure 4.10. Nortek Vectrino (ADV) (31).

The ADV was used to measure point velocities in the x (downstream or u), y (cross-stream or v), and z (vertical or w) directions in the channel, although the downstream direction was of utmost importance in quantifying how quickly the water approached the barrier. By collecting flow velocities at different lateral positions and depths through the channel, velocity profiles could be created to explain how water moved through the channel and, in particular, through the scupper opening. Figure 4.11 shows the ADV mounted above the channel to record upstream point velocities, and Figure 4.12 shows the ADV mounted inside the scupper opening.



Figure 4.11. ADV Setup to Record Point Velocities Upstream of the Median Barrier.



Figure 4.12. ADV Setup in Scupper.

In prior experiments (15, 18), only the volumetric discharge and bulk water depths were measured and used for understanding conveyance of water through the barriers. The ADV provided an advantage in that it could identify regions of fast-moving waters potentially capable of destabilizing the median barrier or contributing to failure. Two types of velocity profiles were created from the measurements: one spanning the width of the channel and one spanning the vertical depth of the flow above the model base. ADV measurements were made at nine lateral positions that spanned the width of the channel, and several measurements were made in the lateral center of the channel at varying vertical positions above the model base, depending on the flow depth upstream of the barrier.

The measurements spanning the width of the channel were all taken 3 inches above the barrier base, which was half of the height of the scupper opening. This was done to ensure that the difference between velocity near the channel walls and in front of the scupper was noticeable. Each measurement period lasted 2 minutes. The data signals were filtered in MATLAB to reduce contamination from instrument noise or instantaneously low seeding; then the remaining were temporally averaged. The average measurement at each location was then plotted to create profiles at varying flow rates. All of these measurements were recorded 5 cm or 10 cm upstream of the barrier, and they allowed for the construction of upstream velocity profiles of flow moving downstream (x) toward and/or through the barrier. In addition, measurements were taken inside the scupper opening at lateral increments of 4 inches to observe how the flow velocity evolved through the scupper. Measurements inside the scupper were made at the upstream opening of the scupper, as well as halfway through the thickness

of the scupper. Measurement locations are shown in Table 4.1, and further details of the profiles are discussed in Section 4.4.

Table 4.1. ADV Measurement Locations.

Lateral Span across the Channel (inch)	Vertical Depth above Model Base (inch)	Lateral Span inside the Scupper (inch)
6	½	4
12	1	8
18	2	12
24	3	16
30	4	20
36	5	24
42	6	28
48	8	32
54	10	N/A
N/A	12	N/A

4.3.6. Strain Gages

To quantify the forces that the upstream flow imposed on the barrier, strain gages were placed on the barrier at a number of locations. A strain gage is a sensor that produces an electrical resistance that varies with changes in strain. The resultant resistance measurement is correlated to a strain based on the properties of the strain gage and the material to which it is applied. Once the measurement is converted to a strain, it can then be converted into a stress, and in turn a measurement of force.

Linear gages (Micro Measurements, CEA-06-250UWA-350 MMF4039229) were used to measure the strain at several locations on the barrier face, held in place using M-Bond AE10. To properly configure the strain gages with the data acquisition system, and to increase the measurement accuracy, an external resistor was soldered to the strain gage, along with the lead wires to create a half-bridge circuit, as shown in Figure 4.13. Teflon tape was then placed over the strain gages and open wires for insulation, and M-Coat W1 microcrystalline wax was layered over the bonding site. M-Coat JA, a polysulfide liquid polymer compound, was then pasted on top for waterproofing. Figure 4.14 shows the strain gages installed on the barrier after they had been waterproofed.

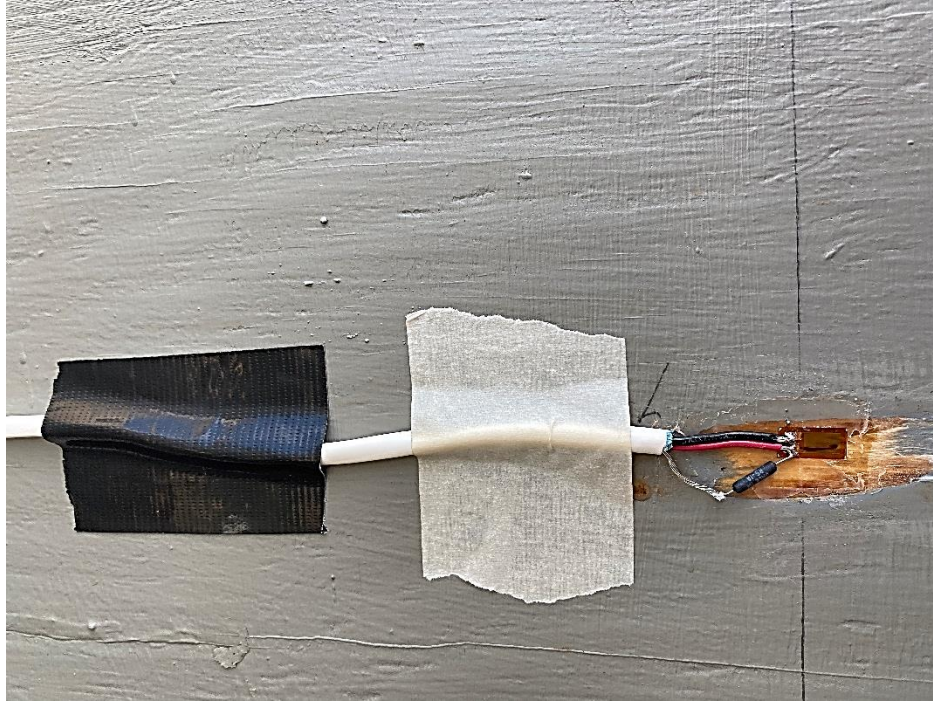


Figure 4.13. Strain Gage and Wiring on Barrier.



Figure 4.14. Strain Gage Setup after Environmental Coating.

4.3.7. Data Acquisition System Configuration

To record and store force measurements, the strain gages were configured with a data acquisition system. The data acquisition system was an NI cDAQ-9174 chassis capable of holding up to four modules. The modules that connected to the cDAQ were

NI 9237 4-channel bridge modules. These modules could each record data from up to four sensors at once, and to do so, the modules were connected to NI 9949 RJ-50 screw terminal adaptors. To connect the strain gages, the three wires soldered to the strain gages were connected to these screw terminal adaptors in the proper terminal configuration. Figure 4.15 and Figure 4.16 show the cDAQ and NI 9237 module setup and the NI 9949 screw terminals, respectively.

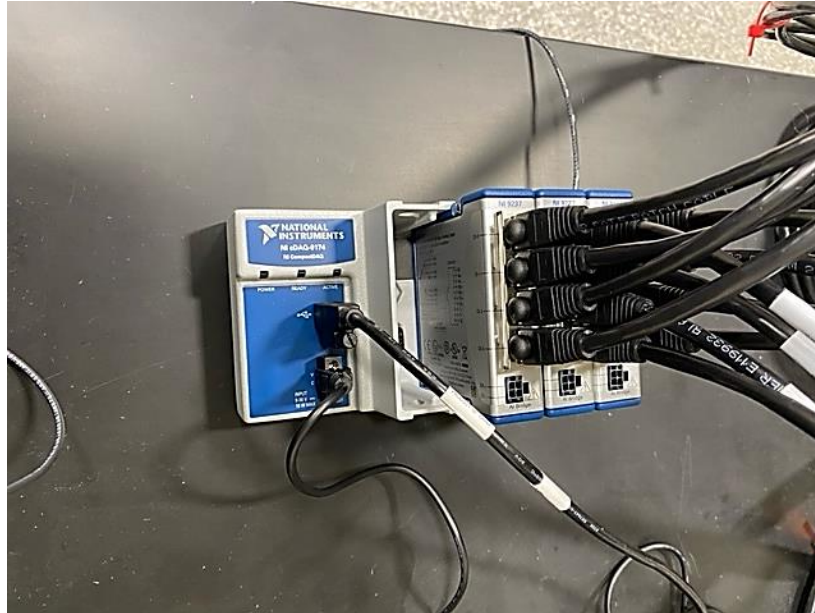


Figure 4.15. cDAQ and NI 9237 Module Setup.



Figure 4.16. Screw Terminals.

A LabVIEW program was designed to collect and store strain measurements for postprocessing. The measurements were recorded for 3 minutes at a sampling rate of 1000 Hz. The measurements were plotted in real time in LabVIEW. The data were

imported to a MATLAB algorithm where the strain measurements were converted to force measurements, and the average force measurement was recorded.

4.3.8. Force Measurements

To gather the necessary force measurements, 10 strain gages were applied at varying locations on the barrier, as shown in Figure 4.17. Since the barrier was designed to be symmetric, the majority of strain gages were located on the left upstream face of the barrier. However, a few gages were placed on the right side to allow more space to run the wiring from the strain gages on the barrier to the data acquisition system. The sensors were applied in locations such that the measurements could be compared between locations to determine if more force was placed on the barrier in and around the scupper opening. As shown in Figure 4.17, a number of gages were placed along the scupper edges at varying lateral locations and heights above the base of the barrier. In addition, a number of gages were placed away from the scupper where less-intense flow would occur.

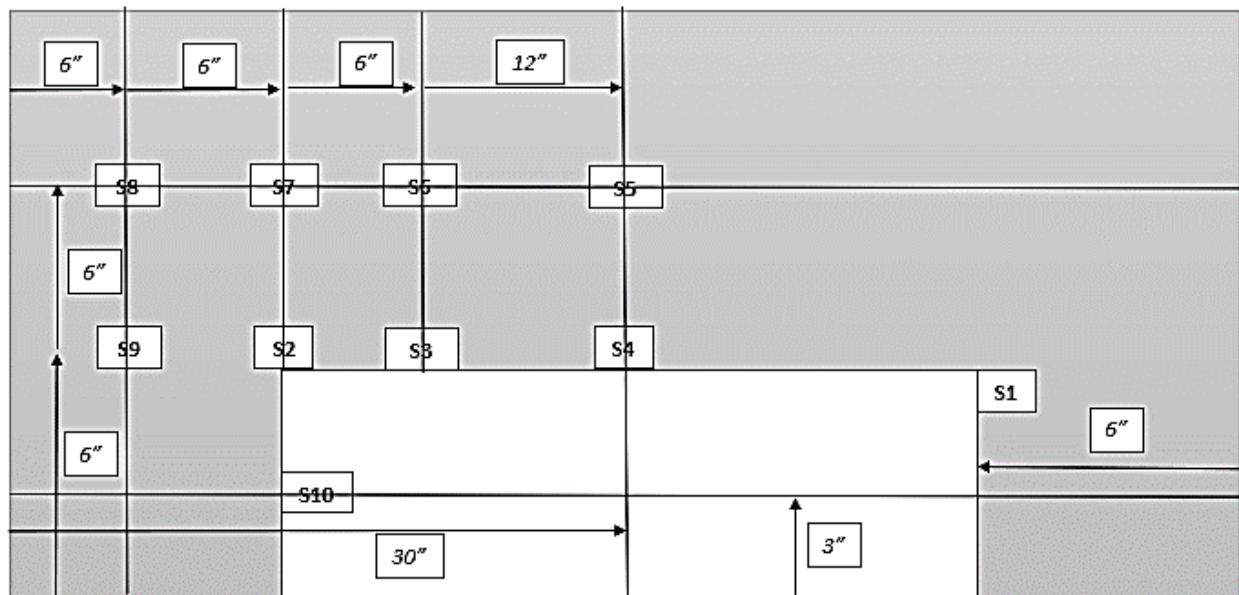


Figure 4.17. Strain Gage Bonding Sites on Model Barrier (not to scale).

4.4. HYDRAULIC TESTING RESULTS AND ANALYSIS

This section discusses the hydraulic testing results and analysis. Data collected using the bubble flow meters, point gage, and discharge weir were compiled into a rating curve for the SSCB model barrier. Velocity profiles obtained from the ADV are detailed below. Theoretical calculations for different forces acting on the barrier are then presented. Finally, the use of strain gages to measure the force imposed on varying locations of the barrier due to water flowing into the barrier face and through the scupper opening is discussed. The force measurements could be compared based on their location on the barrier and the flow rate at which the measurements were obtained.

4.4.1. Water Depth and Flow Rate

Hydraulic efficiency was measured using the bubble flow meters, point gage, and discharge weir. Data were collected for eight different flow rates, and the resultant data are shown in Table 4.2. The upstream water depth, H_{avg} , was recorded using the bubble flow meters, and three different upstream water depths were collected for each of the four flow meters. This yielded 12 measurements that were averaged to calculate the value shown in Table 4.2; the standard deviation of these measurements is reported as $stdv_H$. Additionally, three point gage height readings were recorded, from which the flow rate in the channel was calculated. The flow rates for the three measurements were then averaged, as were the point gage heights (H_{gage}), and are shown in Table 4.2 as Q_{avg} ; the standard deviation of these measurements is shown as $stdv_Q$. For each test, the pump was opened at increasing intervals of $\frac{1}{8}$ of the total pump capacity until the valve was completely open, yielding eight tests.

Partway through the project duration, much of the outdoor experimental setup underwent renovation, including the pump and pipes connecting it to the reservoir. Once the renovations were complete, the same eight tests were repeated to both gather more measurements and gather measurements with the pump running more efficiently. The tests carried out after the renovations are marked in Table 4.2 and subsequent text references with an asterisk. Because the pump ran more efficiently in these tests, the upstream water depth and flow rate were greater compared to corresponding tests carried out prior to the renovations. The ratio of upstream water depth to total barrier height is shown as H_{avg}/H_{bar} . Since the height of the scupper opening was 6 inches, the first two tests were considered Type 1 flow, while all other tests were considered Type 2 flow; Type 3 flow, where water flows over the crest of the barrier, was not achieved in any of these tests. The transition from Type 1 to Type 2 flow yielded a substantial increase in upstream water depth, gage height, and flow rate.

Table 4.2. Hydraulic Efficiency Data.

Test Number	H_avg (ft)	Q_avg (cfs)	Pump (% open)	H_gage (ft)	stdv_H (ft)	stdv_Q (cfs)	H_avg /H_bar (%)
1	0.303	0.539	12.5	0.102	0.001	0.036	16.9
2	0.432	1.855	25.0	0.233	0.010	0.002	24.1
3	0.635	3.665	37.5	0.366	0.005	0.001	35.4
4	1.048	6.033	50.0	0.511	0.002	0.002	58.5
5	1.229	6.841	62.5	0.555	0.005	0.005	68.6
6	1.305	7.133	75.0	0.571	0.003	0.002	72.8
7	1.354	7.277	87.5	0.579	0.003	0.001	75.6
8	1.376	7.334	100.0	0.582	0.003	0.003	76.8
9*	0.243	0.716	0.125	0.123	0.005	0.016	13.9
10*	0.475	2.133	0.250	0.255	0.004	0.005	27.1
11*	0.726	4.130	0.375	0.397	0.004	0.004	41.5
12*	1.254	6.749	0.500	0.550	0.003	0.004	71.7
13*	1.500	7.454	0.625	0.588	0.008	0.001	85.7
14*	1.573	7.850	0.750	0.609	0.006	0.006	89.9
15*	1.598	8.031	0.875	0.618	0.004	0.005	91.3
16*	1.625	8.155	1.000	0.624	0.003	0.003	92.9

* Test carried out after the pump renovations.

4.4.2. Rating Curve

A rating curve was constructed for the SSCB model barrier, as shown in Figure 4.18, by plotting the upstream water depth versus the downstream flow rate for the 16 different tests carried out. Each point in the figure represents a different test, with the flow rate presented along the abscissa and the upstream water depth presented along the ordinate. Similar to what was discussed above, there was a noticeable increase in flow rate as the flow transitioned from Type 1 flow, where the upstream water depth was less than the scupper height, to Type 2 flow, where the upstream water depth was greater than the scupper height. In addition, there was a significant increase in flow rate once the upstream water depth became substantially higher than the scupper height. However, once the upstream water depth was sufficiently higher than the scupper height, the measurements for flow rate and upstream water depth did not increase significantly between tests.

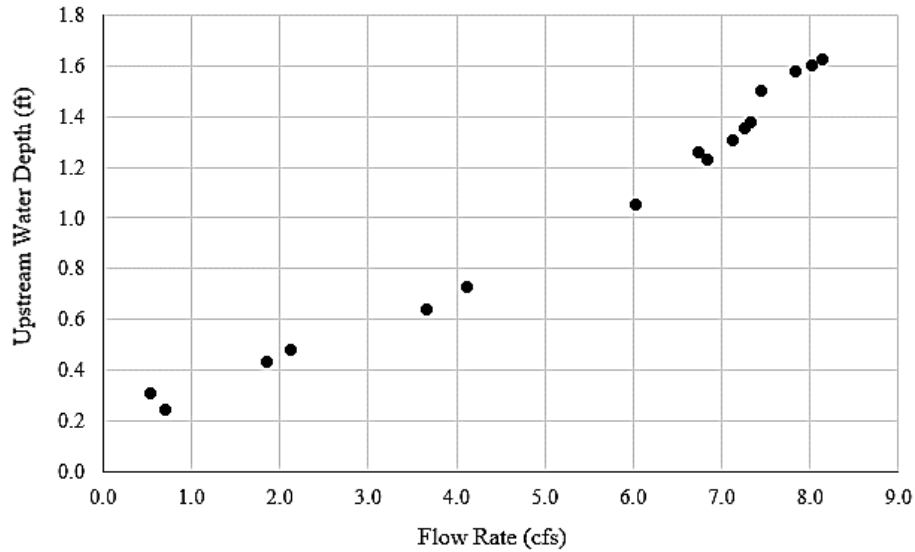


Figure 4.18. Rating Curve for SSCB Model Median Barrier.

4.4.3. Calibrated Model Curve for Model Median Barrier

In addition to creating a rating curve using the raw data for the SSCB model barrier, a nondimensional rating curve was also created for the model barrier, as shown in Figure 4.19. To do so, the dimensionless specific energy versus the dimensionless flow rate was plotted, and each data point in the figure represents a different test that was carried out on the model barrier. In addition, the solid line represents a curve that was fit to the data using a three-parameter model developed in past research (9). By nondimensionalizing the data, rating curves for barriers of different geometries could be compared. Microsoft Excel Solver was used to fit the three coefficients to the model. The parameters for this model barrier were as follows: $C_b = 0.728$, $C_c = 0.732$, and $C_d = 0.789$; the standard error was determined to be 0.001.

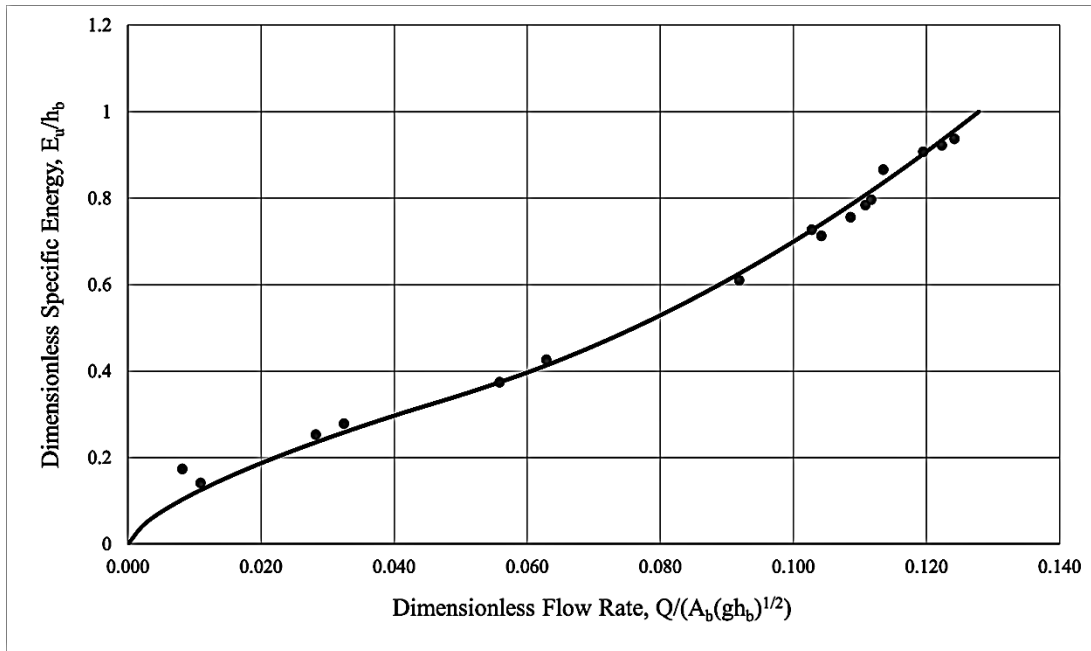


Figure 4.19. Calibrated Model Curve for SSCB Model Median Barrier.

4.4.4. Point Velocity

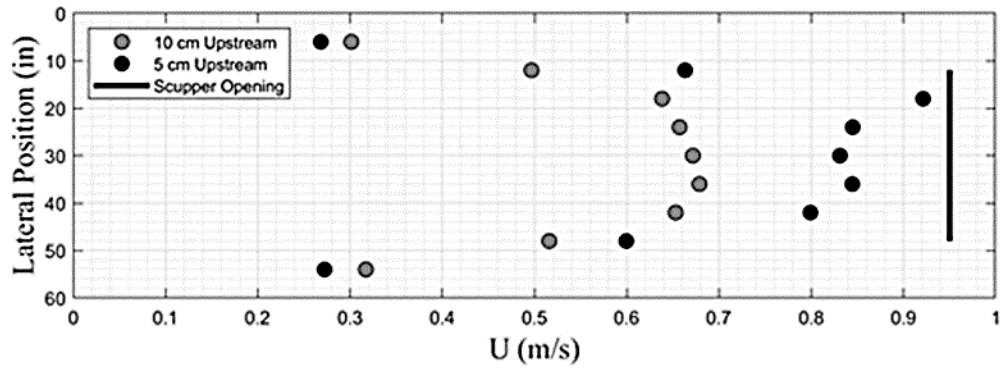
By utilizing the ADV data, velocity profiles were created that spanned the width of the channel and the depth of the channel above the barrier base. Measurements upstream of the barrier were recorded at either 10 cm (~4 inches) or 5 cm (~2 inches) upstream of the barrier face to measure the flow just before it reached the model median barrier. Measurements inside the scupper were recorded at the upstream entrance of the scupper, as well as halfway through the width of the scupper. The point velocity data were recorded during Test Numbers 6, 8, and 16* with the pump at $\frac{6}{8}$ (75 percent open), $\frac{8}{8}$ (100 percent open), and $\frac{8}{8}^*$ (100 percent open) capacity, respectively. Recall that Tests 6 and 8 were performed before repairs were performed and were thus at a lower efficiency than Test 1. Data were gathered during these tests to ensure that the velocities represented flow conditions during significant flooding events. Tests 8 and 16 were both carried out while the valve was completely open; however, data for Test 16 were collected after the pump system was renovated (as denoted by the asterisk). This was done to ensure profiles were created for the greatest flooding scenario. Based on the flow rates in Table 4.2, Test 16 had the highest flow rate. Plotting the temporally averaged value of each velocity at its measurement location in the channel resulted in a profile that depicted velocity as a function of position.

Lateral profiles were composed of nine measurements taken across the lateral span of the channel. All measurements were recorded 3 inches above the model barrier base. Measurements began 6 inches away from one channel wall and ended 6 inches away from the other channel wall. For vertical profiles, measurements began $\frac{1}{2}$ inch above the barrier base centered laterally in the channel, and they were recorded at 1-inch increments from 1 inch above the barrier base to 6 inches above the base, or the top of the scupper opening. Measurements were then recorded at 2-inch increments

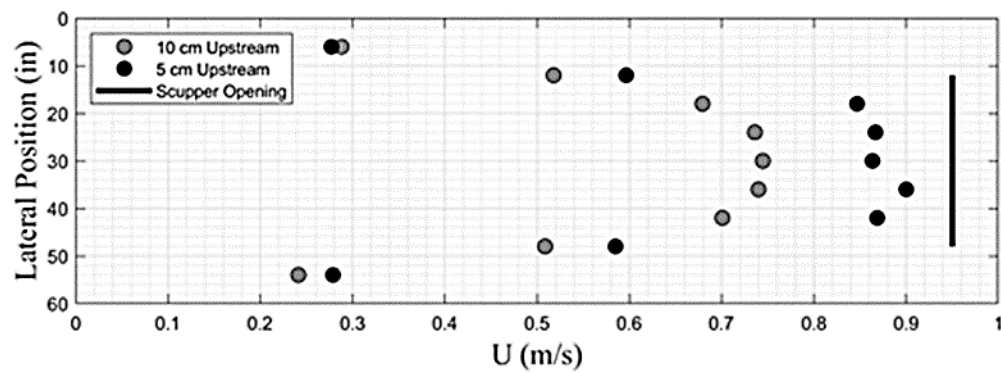
above the scupper opening to the surface of the upstream flow. Recording these measurements at nonuniform increments allowed for a more detailed profile to be created in front of the scupper opening. Measurements inside the scupper were recorded at eight locations across the width of the scupper. Since the scupper opening was 3 ft (or 36 inches) wide, measurements were recorded at 4-inch increments both at the front of the scupper opening and midway through the opening.

The mean velocity profiles for flow at different lateral positions in the channel upstream of the barrier are shown in Figure 4.20, and the width of the scupper opening is indicated in the figure for reference. Profiles are shown at 10 and 5 cm upstream of the barrier for Tests 6, 8, and 16. The maximum velocities were recorded near the center of the channel in front of the scupper opening, and the velocity decreased as the flow got closer to the channel walls and farther from the scupper opening. This was due in part to the boundary layer that existed near the channel walls as well as to the fact that much of the flow farther from the center of the channel was not able to move through the scupper opening and was instead blocked by the barrier face. Therefore, flow on the edges of the channel decelerated as it approached the barrier, while flow in the center of the channel accelerated as it was forced into the scupper opening. Because the flow velocity was highest in front of the scupper, it was likely that the maximum forces on the barrier would also be found in and around the scupper opening. Furthermore, the profiles showed a small, but noticeable, increase in velocities in front of the scupper opening between Tests 6 and 8. This finding makes sense given that the pump was operating at a higher flow rate. In addition, there was a large increase in the point velocities 5 cm upstream of the barrier face compared to point velocities 10 cm upstream of the barrier. In Test 6, the maximum velocity 10 cm upstream of the barrier was approximately 0.65–0.70 m/s, while it was about 0.85 m/s 5 cm upstream of the barrier. In Test 8, the maximum velocity 10 cm upstream of the barrier was approximately 0.70–0.75 m/s, while it was 0.85–0.90 m/s 5 cm upstream of the barrier. During Test 16, the maximum velocity 10 cm upstream of the barrier was approximately 0.75–0.80 m/s, and it was approximately 0.90 m/s 5 cm upstream of the barrier. This finding suggests that while the velocity increased as the volumetric flow rate increased, the velocity also increased as flow continued to approach the upstream face of the barrier, and it would likely continue to increase as water moved through the scupper opening.

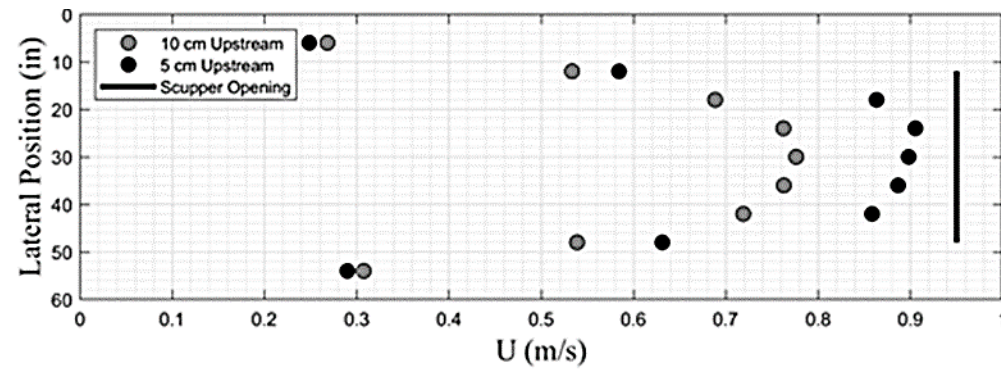
By using the volumetric flow rates for Tests 6, 8, and 16 that are shown in Table 4.2, it was possible to calculate the theoretical average flow velocity through the scupper. Using the scupper dimensions of 3.0 ft × 0.5 ft and flow rates of 7.133 cfs, 7.334 cfs, and 8.155 cfs, the average flow velocity through the scupper for Tests 6, 8, and 16 were calculated as 4.76 ft/s, 4.89 ft/s, and 5.44 ft/s, or 1.45 m/s, 1.49 m/s, and 1.66 m/s, respectively. This is a substantial increase from point velocities shown in Figure 4.20, implying the velocity will continue to increase as flow is forced from the large channel area into the smaller scupper opening. Furthermore, this finding also indicates that flow becomes substantially faster downstream of a barrier after being forced through a scupper. This increase in velocity through the scupper compared to point velocities immediately upstream of the barrier also indicates that measurements must be made on the upstream face of the barrier to determine the true hydrodynamic forces acting on or near the scupper edge.



a. Velocity profile test 6



b. Velocity profile test 8

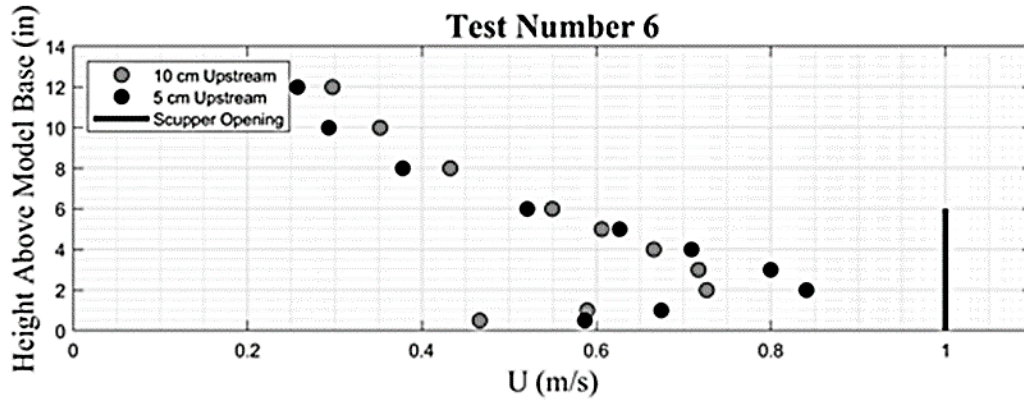


c. Velocity profile test 16

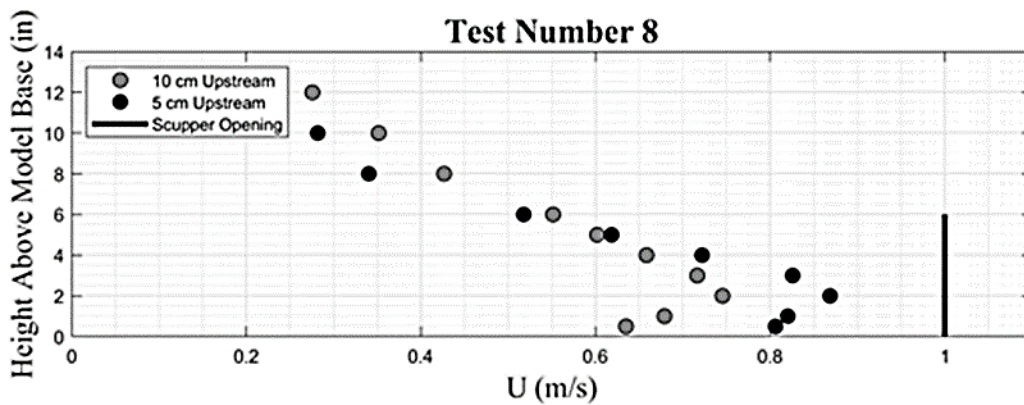
Figure 4.20. Mean Downstream (x) Velocity Profiles across Channel.

Figure 4.21 shows the mean downstream velocity profiles above the model barrier base for Tests 6, 8, and 16 at 10 cm and 5 cm upstream of the barrier. The location of the scupper opening is included for reference in the figure. Similar to the lateral profiles, the velocity was greatest in front of the scupper opening, although it decreased near the bottom of the channel due to the existence of the boundary layer along the model support base. The velocity also decreased above the height of the scupper opening as water decelerated upon approaching the upstream face of the barrier. In Test 6, the maximum velocity 10 cm upstream of the barrier was approximately 0.70–0.75 m/s, while it was about 0.85 m/s 5 cm upstream of the barrier. In Test 8, the maximum velocity 10 cm upstream of the barrier was approximately 0.75 m/s, while it was 0.85–0.90 m/s 5 cm upstream of the barrier. In Test 16, the maximum velocity 10 cm upstream of the barrier was approximately 0.75–0.80 m/s, and it was approximately 0.95 m/s 5 cm upstream of the barrier. These findings are similar to the maximum velocities for corresponding lateral profiles shown in Figure 4.20, further implying that velocity increases as flow continues to approach a barrier.

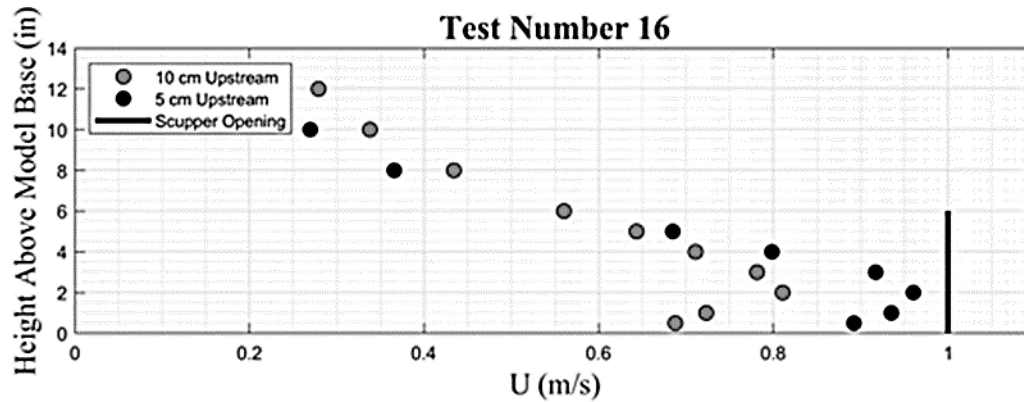
Figure 4.22 shows the mean downstream velocity profiles for flow through the scupper opening, and the width of the scupper opening is included for reference. Profiles were created for Tests 6, 8, and 16 at the upstream entrance to the scupper and midway through the scupper opening. Compared to the profiles shown in Figure 4.20 and Figure 4.21, the velocity was significantly greater inside the scupper opening than upstream of the barrier. This finding confirms that velocity does increase as flow is forced from the large channel area into the smaller scupper area. At the entrance of the scupper, the average velocity was approximately 1.25 m/s for both Test 6 and Test 8 and approximately 1.50 m/s for Test 16; midway through the scupper, the average velocity was approximately 1.90 m/s for Tests 6, 8, and 16. These magnitudes are similar to the theoretically calculated average velocities of 1.45 m/s, 1.49 m/s, and 1.66 m/s for Tests 6, 8, and 16, respectively, and if the velocities at the front and middle of the scupper for each test are averaged, they are very similar to the theoretical velocities.



a. Velocity profile test 6

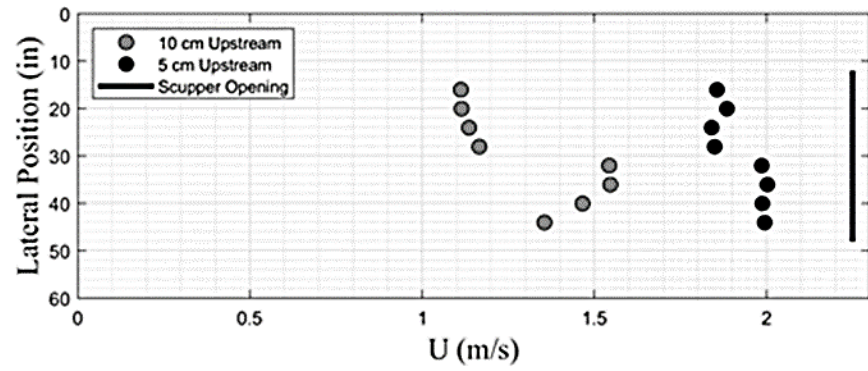


b. Velocity profile test 8

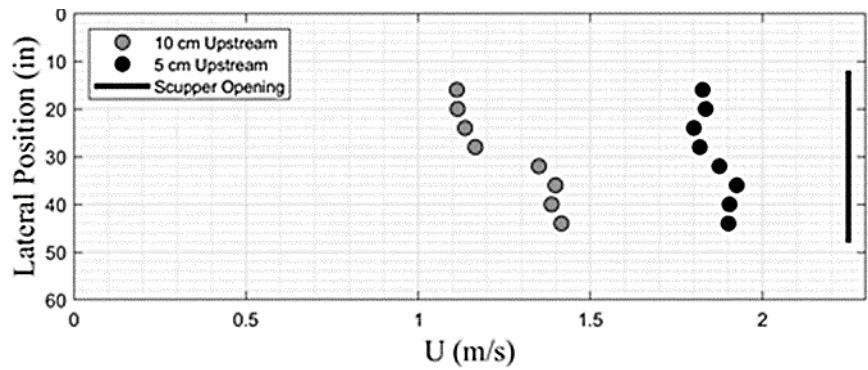


c. Velocity profile test 16

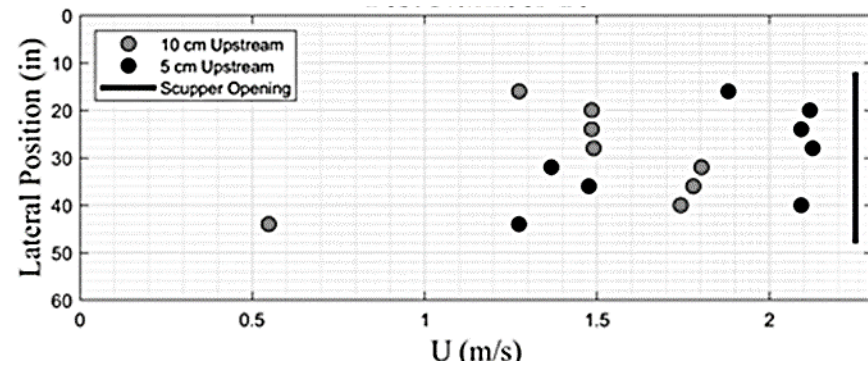
Figure 4.21. Mean Downstream (x) Velocity Profiles above Model Barrier Base.



a. Velocity profile test 6



b. Velocity profile test 8



c. Velocity profile test 16

Figure 4.22. Mean Downstream (x) Velocity Profiles inside Scupper Opening.

4.4.5. Hydrodynamic Force Calculations

Theoretical calculations of the hydrodynamic force acting on the barrier during different tests can be done by applying conservation of linear momentum to the Reynolds Transport Theorem. By taking the upstream flow area as one control surface and the area of the scupper as a second control surface, the flow rates in Table 4.2 were converted to velocities. These velocities and control surface areas were used to calculate the hydrodynamic force due to the momentum flux by solving Equation 2.40. The resulting hydrodynamic forces for all 16 tests are shown in Table 4.3, along with the scupper and upstream areas and velocities for reference. In addition, the theoretical hydrostatic forces on the barrier were calculated and are shown. The hydrodynamic force was significantly larger than the hydrostatic force in all tests except Tests 1, 2, 9, and 10; these tests had the lowest flow rates tested. Therefore, as the upstream water depth and flow rate increase, so does the hydrodynamic force on the barrier, which poses possible risk to the stability of a barrier.

Table 4.3. Theoretical Force on the Model Barrier Due to Upstream Flow.

Test Number	A _{scupper} (ft ²)	A _{upstream} (ft ²)	V _{scupper} (ft/s)	V _{upstream} (ft/s)	P _{dynamic} (lb)	P _{static} (lb)
1	1.5	1.52	0.36	0.36	0.13	28.7
2	1.5	2.16	1.24	0.86	43.7	58.1
3	1.5	3.17	2.44	1.15	295	126
4	1.5	5.24	4.02	1.15	1081	346
5	1.5	6.14	4.56	1.11	1472	471
6	1.5	6.52	4.76	1.09	1631	531
7	1.5	6.77	4.85	1.08	1716	572
8	1.5	6.88	4.89	1.07	1750	591
9*	1.5	1.22	0.48	0.59	5.01	18.4
10*	1.5	2.38	1.42	0.90	69.8	70.4
11*	1.5	3.63	2.75	1.14	417	165
12*	1.5	6.27	4.50	1.08	1442	491
13*	1.5	7.50	4.97	0.99	1850	702
14*	1.5	7.87	5.23	1.00	2076	772
15*	1.5	7.99	5.35	1.01	2180	797
16*	1.5	8.13	5.44	1.00	2257	824

* Test carried out after the pump renovations.

4.4.6. Stability Calculations

Using the hydrodynamic forces in Table 4.3 and the equations detailed in Chapter 2, researchers performed theoretical stability calculations for all 16 tests. These calculations yielded the buoyant force, F_b , along with the factor of safety against overturning, FS_o , and the factor of safety against sliding, FS_s ; the results are shown in Table 4.4. In addition, although the model barrier was made of plywood and bolted to

the concrete channel, the calculations treated the barrier as though it were made entirely of concrete to reflect the composition of the prototype barrier. The theoretical weight of the concrete model barrier was calculated as 685.5 lb, which is far smaller than the calculated hydrodynamic forces acting on the barrier at larger flow rates. Furthermore, the results in Table 4.4 indicate that the barrier will potentially overturn and/or slide in most cases where Type 2 flow occurs. This is especially true for tests in which the upstream water depth is near to the height of the barrier, as reflected by the extremely small factors of safety for these cases. Comparing these results to the data in Table 4.2 and Table 4.3 makes it clear that the barrier is susceptible to sliding and overturning when the upstream water depth is greater than half of the barrier height; when this occurs, the hydrodynamic force on the barrier is greater than the weight of the barrier. However, the barrier is not expected to become buoyant under any of the conditions that were tested since the buoyant force is never greater than the weight of the barrier. These are extremely conservative estimates that treat the barrier as a standalone structure in rushing (i.e., not quiescent) floodwaters. In reality, there are barrier-to-barrier connections providing support at various locations along the sides of the barrier. As long as these connections are able to resist the hydrodynamic forces, the barriers can remain stable in extreme flooding scenarios.

Table 4.4. Moments and Forces on the Model Barrier.

Test Number	M_R (lb-ft)	M_O (lb-ft)	FS_O	F_R (lb)	F_d (lb)	FS_s	F_b (lb)
1	343	24.7	13.9	377.05	0.12	3020	49.5
2	355	41.1	8.64	385.10	41.1	9.36	70.4
3	418	111	3.78	431.58	278	1.55	104
4	563	441	1.28	576.95	1020	0.57	171
5	609	668	0.91	649.34	1390	0.47	200
6	622	774	0.80	678.60	1540	0.44	213
7	626	839	0.75	694.31	1620	0.43	221
8	627	868	0.72	700.74	1650	0.43	224
9*	344	20.2	17.1	377.95	4.72	80.1	39.6
10*	362	49.1	7.37	389.93	65.7	5.93	77.4
11*	445	154	2.88	454.07	392	1.16	118
12*	599	670	0.89	643.76	1360	0.47	204
13*	614	993	0.62	719.18	1740	0.41	245
14*	628	1153	0.54	760.91	1950	0.39	256
15*	636	1224	0.52	780.29	2050	0.38	261
16*	638	1284	0.50	794.44	2130	0.37	265

* Test carried out after the pump renovations.

In order to determine whether failure of the barrier-to-barrier connections can be anticipated due to hydrostatic or hydrodynamic forces, the forces imposed on the full-scale barrier geometry can be estimated. Considering the worst-case scenario in which water rises to the top of the barrier, the hydrostatic force due to water on the barrier was

calculated to be nearly 9500 lb, which is significantly lower than the 67.5 kip shear strength of the barrier connections. While the hydrodynamic force of the prototype barrier cannot be readily estimated without full-scale instrumentation, the worst-case measured F_d value (2130 lb) can be scaled up from the hydraulic tests presented above. Given the ratio of hydrostatic forces between the prototype and laboratory barrier (430 lb), researchers approximated the total driving force on the prototype barrier to be 47,000 lb, still below the shear strength for the connections. The combined forces were estimated to stay below 57,000 lb. While this is not significantly lower than the shear strength of the connections, note that this is the worst-case scenario in which the water level reaches the top of the barrier, a likely scenario only in extreme events. Thus, while there is the possibility of sliding and overturning for significant water depth, researchers estimated that the entire barrier system, when properly connected, should remain stable for mild to moderate flooding conditions.

4.4.7. Force on the Model Barrier

The data recorded using the strain gages were utilized to determine point force measurements acting on different locations on the upstream face of the barrier during hydraulic testing. Ten strain gages were installed on the barrier, although four of them were damaged early on during testing, likely due to water damage, and their measurements are therefore not shown in Table 4.5. Additionally, strain gage 10 was damaged later in testing, so only the reliable measurements are included. The missing measurements for strain gages 5 and 8 occurred when the upstream water depth was less than the height of the gage locations, and therefore no hydrodynamic force acted on that location on the barrier during the test. The locations of the strain gages are shown in Figure 4.17, and the force measurements are shown in Table 4.5. Measurements were recorded during Tests 11–16, and Type 2 flow was present in all of the scenarios. Type 1 flow was not of interest because the lower flow rates and upstream water depths did not pose a threat to the stability of the barrier.

Based on the force measurements, it appears that more force was applied to the barrier face's center as opposed to locations closer to the channel walls. In addition, the force acting on the barrier was actually greater when the measurement was taken farther from the scupper opening. This finding is likely due to the fact that around the scupper entrance, flow was being forced downward into the scupper in addition to downstream. The flow here was moving both downstream and vertically downward, so the force was not acting perpendicular to the barrier face but instead at an angle, thus reducing its magnitude. Farther away from the scupper entrance, the flow was moving only downstream and perpendicular to the barrier face. Strain gage 10 was installed inside the post of the scupper, and it was subject to the smallest force magnitude. The small measurements occurred because the barrier face inside the post was parallel to the flow direction, not perpendicular. The flow therefore moved by the measurement location instead of directly into it. Furthermore, because the upstream flow was choked into the scupper, the flow was essentially forced past this inside post instead of toward it.

Large force magnitudes, however, likely did occur on the upstream face of the post as upstream flow was both moving downstream and being choked toward it. This large force and corresponding probability of water intrusion is likely why this gage failed. The failure could be further due to the drag force that was imposed on this location. Since the posts of the scupper were not rounded edges and the gage was installed at the upstream edge, a greater drag force should occur here than on any other location on the barrier. Finally, although the force measurements generally increased as the flow rate increased, the increase in magnitude was relatively small, which corresponded to the relatively small increases in flow rate and upstream water depth for these tests. Similar results can be seen in the theoretical calculation of the theoretical hydrodynamic forces acting on the barrier.

Table 4.5. Force at Different Locations on the Barrier.

Test Number	11	12	13	14	15	16
SG2 (lb)	20.31	27.94	34.61	35.91	36.73	31.59
SG3 (lb)	34.55	34.57	34.88	34.91	21.03	23.92
SG4 (lb)	42.77	38.83	37.56	40.78	30.34	30.72
SG5 (lb)	N/A	N/A	54.41	59.02	61.00	58.87
SG8 (lb)	N/A	N/A	35.74	44.27	45.98	45.44
SG10 (lb)	2.633	16.158	18.80	20.42	N/A	N/A

4.5. SUMMARY AND CONCLUSIONS

For the hydraulic testing, a SSCB model median barrier was constructed and assessed to determine its hydraulic performance. The barrier was fastened to a base, which was then attached to a support base bolted to the channel bed to ensure that the model barrier remained stable and intact for the duration of the testing. Bubble flow meters were placed upstream of the barrier to record upstream water depth, while a point gage and a discharge weir were placed at the downstream end of the return channel to determine the volumetric flow rate in the channel. Sixteen tests were performed on the model barrier, and the tests used a pump operating at increasing increments of $\frac{1}{8}$ open until the pump valve was completely open. By plotting the upstream water depth versus the volumetric flow rate, a rating curve was generated for the barrier to explain its hydraulic efficiency. Additionally, for pump capacities of $\frac{1}{8}$ and $\frac{3}{8}$ open, an ADV was placed 5 cm and 10 cm upstream of the barrier at varying lateral and vertical locations to collect point velocities in the downstream, x, direction as the flow approached the barrier. From these tests, velocity profiles were created that spanned the lateral distance across the channel, as well as the vertical distance from the base of the barrier to the upstream water surface. In addition, point velocities were also collected inside the scupper, both at the entrance to the scupper and midway through the scupper's length. Finally, strain gages were used to record strain and in turn the force that was acting on the barrier at various locations at different flow rates. Using the rating curve, point velocities, and force measurements, various hydraulic parameters of the barrier could be better explained in hopes of creating an optimized

scupper design to allow the greatest hydraulic efficiency while still maintaining the structural integrity of the barrier. The main conclusions of the preliminary testing of the hydraulic instrumentation are detailed below:

- There is a significant increase in both upstream water depth and flow rate when the flow transitions from Type 1 to Type 2 flow. Although Type 3 flow was not achieved in this testing, it is expected that the upstream water depth and flow rate would again significantly increase between the transition from Type 2 to Type 3 flow.
- The maximum downstream velocities 5 cm and 10 cm upstream of the barrier are found in front of the scupper opening in both the lateral and vertical directions. This finding suggests that the scupper allows water to accelerate upon approaching the barrier because flow can pass through the scupper opening, while the barrier face slows the velocity since water cannot continue to flow downstream.
- If the dimensions or location of the scupper are altered, the velocity profiles likely will also be altered to show maximum point velocities upstream of the new scupper design.
- The velocity through the scupper is much larger than the flow velocity just upstream of the barrier, indicating that the flow velocity is significantly increased when the flow is forced through the scupper opening. Additionally, the flow velocity continues to increase as it moves farther through the scupper, implying the velocity downstream of the barrier will be greater than the velocity upstream.
- The theoretical hydrodynamic force on the barrier is significantly larger than the corresponding hydrostatic force on the barrier. Therefore, it is important to measure hydrodynamic force when studying the hydraulic efficiency of a median barrier and accordingly design the barrier-to-barrier connections to withstand mobility during significant flooding.
- The barrier is susceptible to sliding and overturning when the upstream water depth is greater than half of the barrier height. Under these conditions, the hydrodynamic force on the barrier is also greater than the weight of the barrier.
- Point force measurements are greatest near the center of the barrier face, although the forces are actually larger away from the scupper entrance. This occurs because around the scupper entrance, flow is moving both downstream and vertically downward, not just downstream. Increases in point force magnitude are fairly small and correspond to fairly small increases in upstream water depth, flow rate, and theoretical hydrodynamic forces.

Chapter 5. FINITE ELEMENT SIMULATION ANALYSIS

5.1. INTRODUCTION

As noted previously, the design option that was selected for further analysis was the 42-inch-tall single-slope portable concrete barrier with a single large scupper. Both J-J Hooks segment connections and X-bolt segment connections were considered in the analysis. Finite element analyses were performed to evaluate the crash behavior of the proposed design options in a predictive manner following *MASH* TL-3 impact conditions. The *MASH* TL-3 matrix for longitudinal barriers includes Test 3-10 with a 2420-lb passenger car (denoted 1100C) and Test 3-11 with a 5000-lb pickup truck (denoted 2270P). In both tests, the vehicle impacts the barrier at a nominal speed of 62.2 mi/h and a nominal angle of 25 degrees.

Finite element models of the single-slope barrier along with segment connection details were developed in LS-DYNA (32). The behavior of the J-J Hooks barrier segment connections was calibrated against component testing conducted under TxDOT Project 0-7059 (33). These dynamic component tests were conducted using a surrogate (bogie) vehicle. The lateral displacement of the barrier system as well as the general behavior of the impacted barriers during the impact were considered the basis of validation.

The finite element impact simulations were then performed on the model of the single-slope portable concrete barrier with single large scupper using available *MASH* vehicle models. A 5000-lb, four-door RAM pickup truck model represented the *MASH* 2270P vehicle, and a 2425-lb Toyota Yaris passenger car represented the *MASH* 1100C vehicle. These models were developed by researchers at George Mason University under sponsorship of FHWA (34) and have been modified by TTI researchers to improve robustness and fidelity for different applications over the course of various simulation projects.

Angular velocities and linear accelerations were extracted from the simulations and further processed through the Test Risk Assessment Program (TRAP) software. TRAP analysis provided vehicle angular displacements (pitch, roll, and yaw angles) and occupant risk metrics (occupant impact velocity [OIV] and ridedown acceleration [RA]) for both the RAM pickup truck and Yaris passenger car impacts. The results were compared against the corresponding limits prescribed in *MASH*.

After successful *MASH* TL-3 performance was demonstrated through crash testing, the scope was changed to include *MASH* TL-4 evaluation. The finite element barrier model was further calibrated against the *MASH* TL-3 crash test results, and a predictive simulation following *MASH* Test 4-12 impact conditions was performed. This test involves a 22,000-lb single-unit truck impacting the barrier at a nominal speed of 56 mi/h and a nominal angle of 15 degrees.

5.2. SINGLE-SLOPE BARRIER MODELS

Finite element models were developed for the single-slope barrier using the geometric details provided in TxDOT standard drawings. The 30-ft-long symmetric single-slope barrier segments were 42 inches tall, had a top width of 8 inches, and had a bottom width of 24 inches. The concrete barrier segments were modeled using solid elements and material 159_CSCM, which is a continuous surface cap model. The reinforcement was explicitly modeled using beam elements and material model 024_Piecewise_Linear_Plasticity. The segment connection details consisted of curvilinear J-J Hooks steel connection plates, as well as steel angle plates and additional rebar components. The J-J Hooks and angle plates were modeled using shell elements and constrained within the solid concrete barrier using the Constrained_Lagrange_In_Solid coupling method.

The threaded rods in the X-bolt connection were modeled with elastic-plastic material representation. The reinforcement cage inside the concrete barrier segments consisted of longitudinal bars and vertical stirrups that were constrained within the concrete barrier model for both connection options.

Results from TxDOT Project 0-7059 were used for the validation of the single-slope concrete barrier segments with J-J Hooks connections (33). In that project, a bogie vehicle weighing 5000 lb impacted the center joint of a four-segment barrier assembly at a nominal speed of 18 mi/h and an impact angle of 90 degrees. The height of the bottom edge of the bogie nose was 26.5 inches above the ground. A model of the bogie vehicle nose assembly was developed for use in calibrating the barrier model. The model captured the strength and stiffness of the actual bogie vehicle nose, and mass was assigned to represent the missing mass of the bogie vehicle. Figure 5.1 shows the initial setup of the bogie model and barrier assembly.

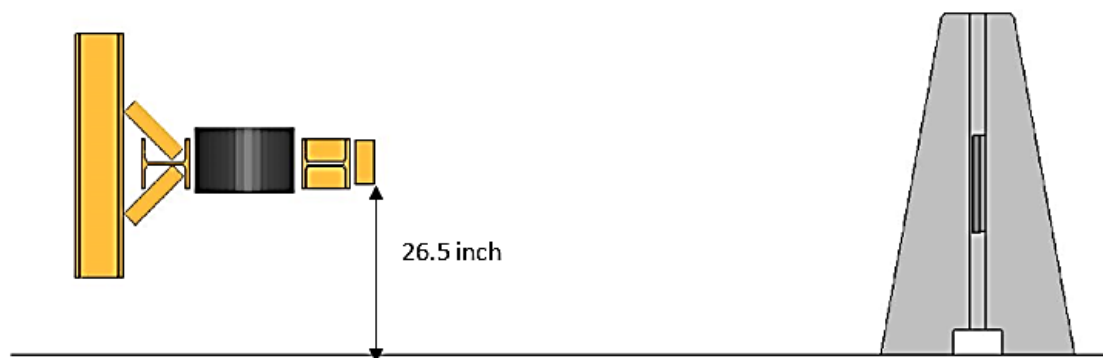


Figure 5.1. Bogie Model Positioned to Impact Center of Four-Segment Barrier Model.

Figure 5.2 shows the comparison of the dynamic impact test (left) and the simulation (right). Good correlation of barrier behavior and deflection was observed when comparing the finite element simulation to the test. Thus, the model was considered acceptable for investigation of the hydraulically efficient barrier with large scupper through predictive finite element computer simulations.

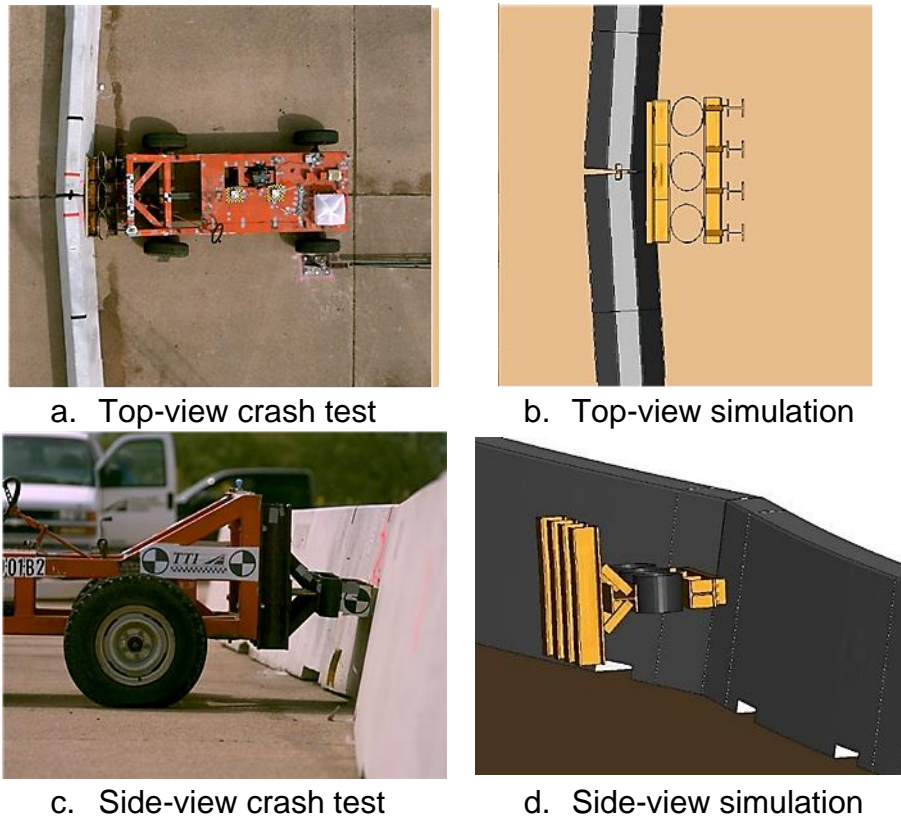


Figure 5.2. Comparison of Bogie Vehicle Test (left) and Bogie Vehicle Impact Simulation (right).

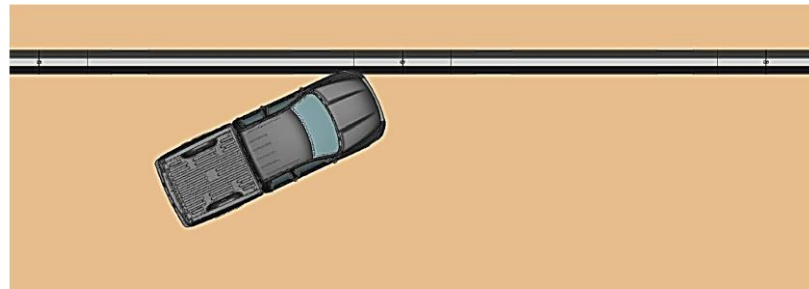
5.3. PREDICTIVE SIMULATIONS OF SINGLE-SLOPE BARRIER

The overall system model was comprised of seven single-slope barrier segments connected to achieve a total barrier length of approximately 210 ft. Baseline simulations were performed on this model following *MASH* Test 3-11 (pickup truck) and Test 3-10 (passenger car) impact conditions, which involve a speed of 62 mi/h and an angle of 25 degrees. The purpose of these runs was to establish baseline impact performance for comparison with the barrier with large scupper. Results from the simulations included OIV, RA, vehicle angular displacements (i.e., roll, pitch, and yaw angles), and lateral barrier displacement.

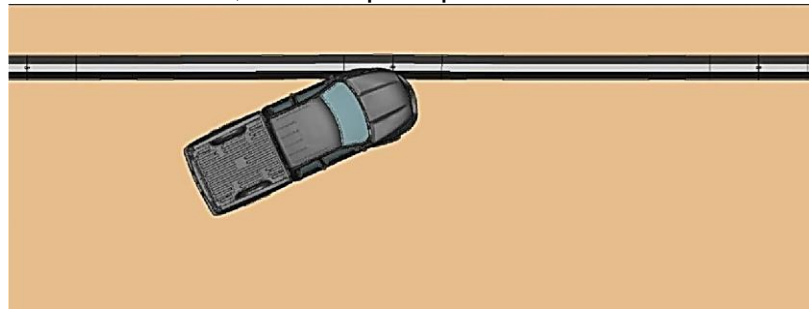
5.3.1. Baseline Impact Simulations of *MASH* Tests on Single-Slope Barrier

A baseline simulation of the single-slope barrier was performed with the 5000-lb RAM pickup truck model following *MASH* Test 3-11 impact conditions. The pickup truck impacted the barrier model 4.3 ft upstream of a joint between barrier segments at a speed of 62 mi/h and an angle of 25 degrees. The impact location was determined using Table 2-7 in *MASH*.

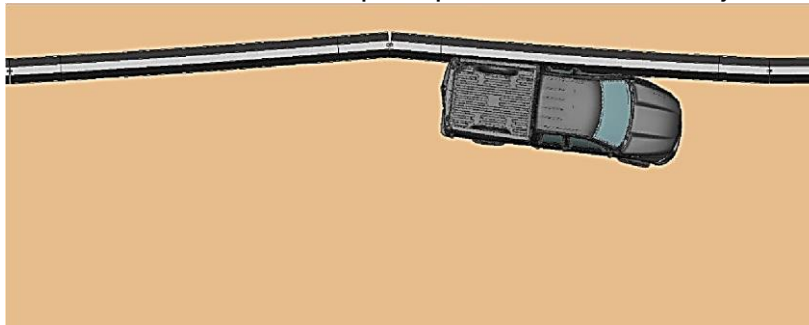
Figure 5.3 and Figure 5.4 provide sequential images of the impact simulation at selected times from an overhead and end view, respectively. Lateral displacement of the impacted barrier was 28 inches. TRAP was used to calculate OIV, RA, and maximum roll, pitch, and yaw angles. Table 5.1 summarizes the results from the simulation.



a. $t = 0.090$ s, event = pickup truck strikes the barrier



b. $t = 0.13$ s, event = pickup truck contacts the joint

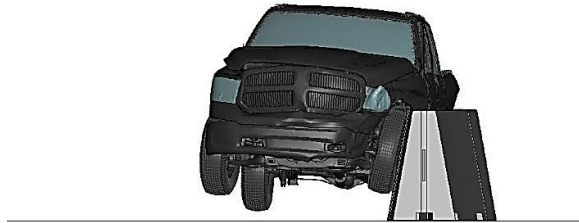


c. $t = 0.40$ s, event = pickup truck is redirected by the barrier

Figure 5.3. Overhead Images of *MASH* Test 3-11 Simulation with Single-Slope Barrier.



a. $t = 0.10$ s, event = front right tire contacts the barrier



b. $t = 0.31$ s, event = rear right tire contacts the barrier



c. $t = 0.54$ s, event = vehicle stabilizes post impact

Figure 5.4. End-View Images of *MASH* Test 3-11 with Single-Slope Barrier.

Table 5.1. Occupant Risk Values for Pickup Truck Impacting Single-Slope Barrier.

Parameter	<i>MASH</i> Threshold	Simulation Result
OIV (ft/s)	40	23.6
RA (g)	20.49	14.4
Yaw (deg)	N/A	31.6
Pitch (deg)	75	7.5
Roll (deg)	75	16.5

Note: N/A = not applicable.

A baseline simulation of the single-slope barrier was performed with the 2420-lb Toyota Yaris passenger car model following *MASH* Test 3-10 impact conditions. The passenger car impacted the barrier model 3.6 ft upstream of a joint between barrier segments at a speed of 62 mi/h and an angle of 25 degrees. The impact location was determined using Table 2-7 in *MASH*.

Figure 5.5 and Figure 5.6 provide sequential images of the impact simulation at selected times from an overhead and end view, respectively. Lateral displacement of the impacted barrier was 28 inches. TRAP was used to calculate OIV, RA, and maximum roll, pitch, and yaw angles. Table 5.2 summarizes the results from the simulation.

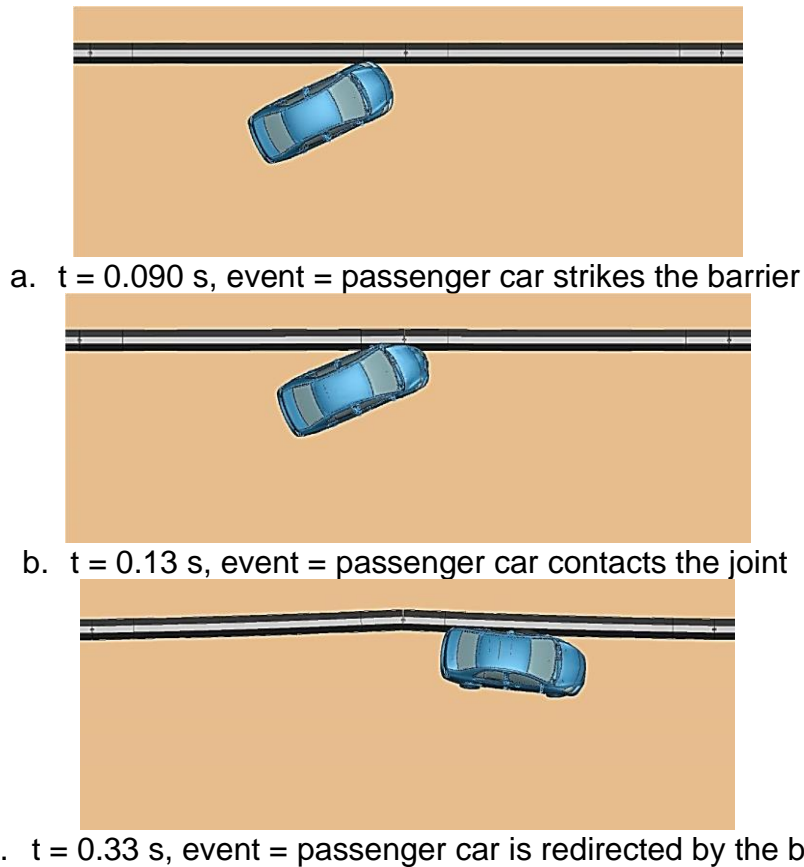


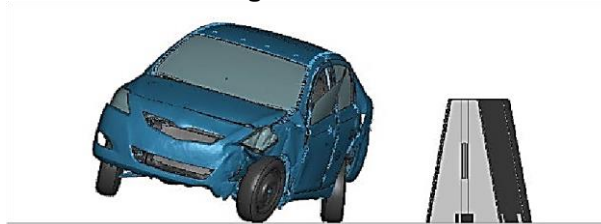
Figure 5.5. Overhead Images of *MASH* Test 3-10 Simulation with Single-Slope Barrier.



a. $t = 0.10$ s, event = front right tire contacts the barrier



b. $t = 0.23$ s, event = rear right tire contacts the barrier, windowpane snags against the barrier



c. $t = 0.91$ s, event = rear right tire stabilizes on ground

Figure 5.6. End-View Images of *MASH* Test 3-10 Simulation with Single-Slope Barrier.

Table 5.2. Occupant Risk Values for Passenger Car Impacting Single-Slope Barrier.

Parameter	<i>MASH</i> Threshold	Simulation Result
OIV (ft/s)	40	24.6
RA (g)	20.49	17.2
Yaw (deg)	N/A	37.2
Pitch (deg)	75	8.2
Roll (deg)	75	27.7

Note: N/A = not applicable.

5.3.2. Impact Simulations of Single-Slope Barrier with Scupper and J-J Hooks Connections

Predictive simulations of the single-slope PCB with large scupper and J-J Hooks connections were performed to assess the impact performance of the conceptualized geometry. The simulations followed impact conditions of *MASH* Test 3-21 and Test 3-20 with the 2270P pickup truck and 1100C passenger car, respectively.

Various reference points along the length of the single-slope PCB segment were investigated. These included the center of the long beam spanning the drainage opening, the connection between segments, and the end of the drainage opening or

scupper. The impact location was 4.3 ft upstream of each reference location for the pickup truck and 3.6 ft upstream of each reference location for the passenger car. These distances were determined using Table 2-7 in *MASH*. Details of these simulations are presented next.

5.3.2.1. Impact Location A—Center of Barrier Segment with Pickup Truck

Impact location A was 4.3 ft upstream from the center of the barrier. This location evaluated the structural adequacy of the barrier where material was removed for the introduction of the scupper.

Figure 5.7 and Figure 5.8 provide sequential images of the impact simulation at selected times from an overhead and end view, respectively. Lateral displacement of the impacted barrier was 12 inches. TRAP was used to calculate OIV, RA, and maximum roll, pitch, and yaw angles. Table 5.3 summarizes the results from the simulation. The simulated impact of the pickup truck at the center of the barrier segment satisfied *MASH* criteria.

5.3.2.2. Impact Location B—End of Scupper with Pickup Truck

Impact location B was 4.3 ft upstream of the end of the scupper. This location evaluated vehicle snagging on the tapered end of the scupper.

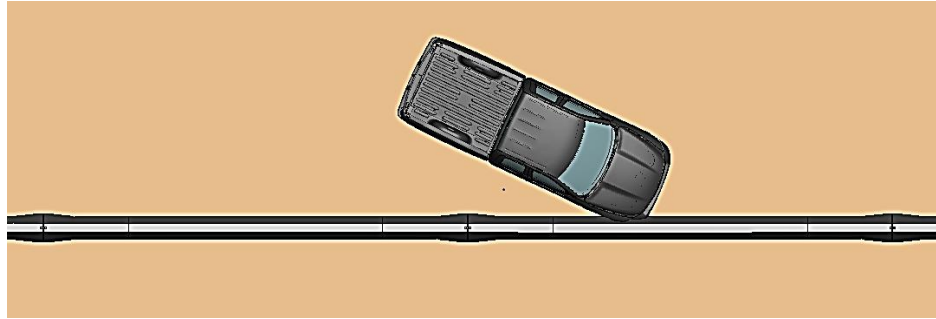
Figure 5.9 and Figure 5.10 provide sequential images of the impact simulation at selected times from an overhead and end view, respectively. Lateral displacement of the impacted barrier was 20.2 inches. TRAP was used to calculate OIV, RA, and maximum roll, pitch, and yaw angles.

Table 5.4 summarizes the results from the simulation. The simulated impact of the pickup truck at the end of the scupper satisfied *MASH* criteria.

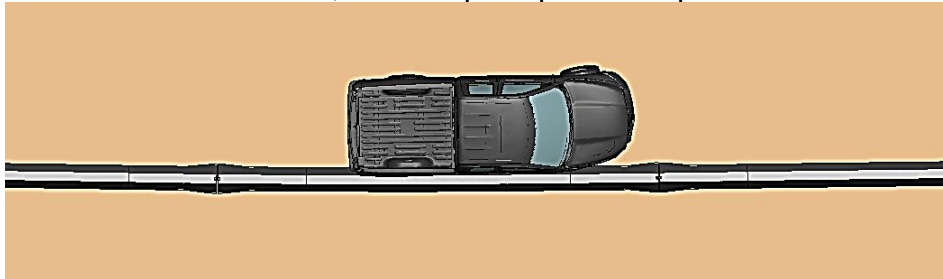
5.3.2.3. Impact Location C—Barrier Segment Connection with Pickup Truck

Impact location C was 4.3 ft upstream of a joint between barrier segments. This location evaluated the structural adequacy of the barrier connection and other factors such as vehicle stability. It was also likely to result in the largest lateral deflection due to the proximity of the impact point to the joint.

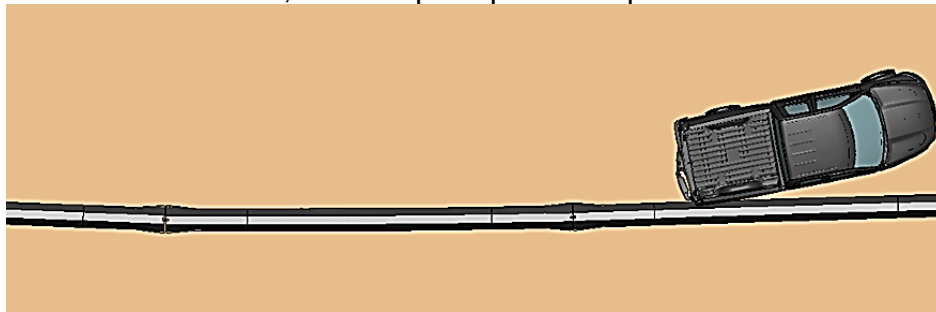
Figure 5.11 and Figure 5.12 provide sequential images of the impact simulation at selected times from an overhead and end view, respectively. Lateral displacement of the impacted barrier was 27.8 inches. TRAP was used to calculate OIV, RA, and maximum roll, pitch, and yaw angles. Table 5.5 summarizes the results from the simulation. The simulated impact of the pickup truck at the barrier segment connection satisfied *MASH* criteria.



a. $t = 0.17$ s, event = pickup truck impacts barrier



b. $t = 0.34$ s, event = pickup truck is parallel with barrier

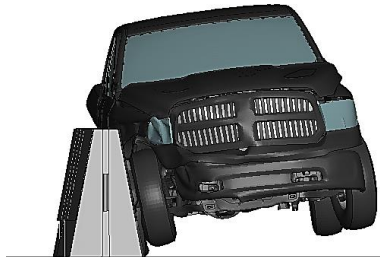


c. $t = 0.70$ s, event = pickup truck exits barrier

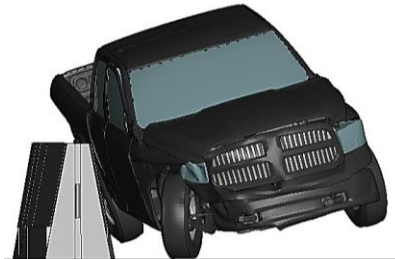
Figure 5.7. Overhead Images of *MASH* Test 3-11 Simulation of Single-Slope Barrier with Scupper—Impact Location A.



a. $t = 0.18$ s, event = pickup truck impacts barrier



b. $t = 0.35$ s, event = pickup truck is parallel with barrier



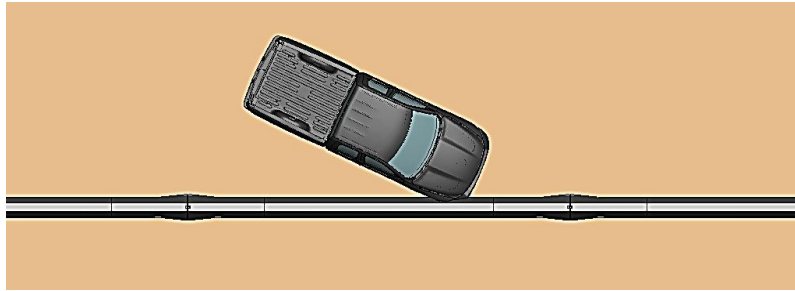
c. $t = 0.54$ s, event = pickup truck front right tire contacts ground

Figure 5.8. End-View Images of *MASH* Test 3-11 Simulation of Single-Slope Barrier with Scupper—Impact Location A.

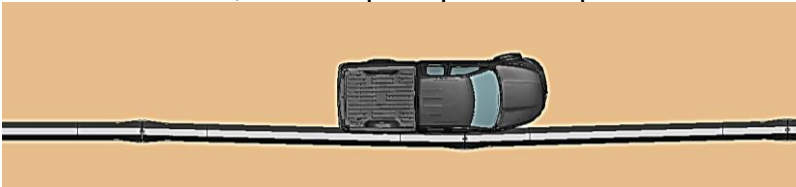
Table 5.3. Occupant Risk Values for Pickup Truck Impacting Single-Slope Barrier with Scupper—Impact Location A.

Parameter	<i>MASH</i> Threshold	Simulation Result
OIV (ft/s)	40	25.6
RA (g)	20.49	13.9
Yaw (deg)	N/A	36.8
Pitch (deg)	75	5.5
Roll (deg)	75	17.6

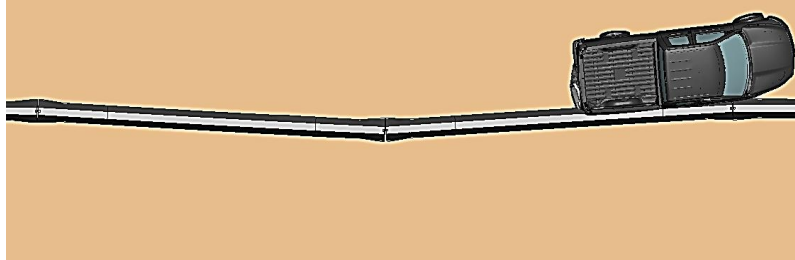
Note: N/A = not applicable.



a. $t = 0.17$ s, event = pickup truck impacts barrier



b. $t = 0.34$ s, event = pickup truck is parallel with barrier

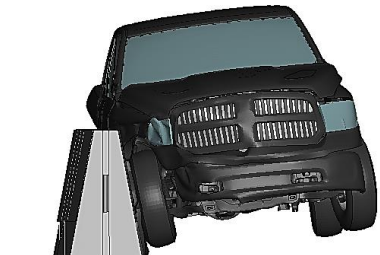


c. $t = 0.70$ s, event = pickup truck exits barrier

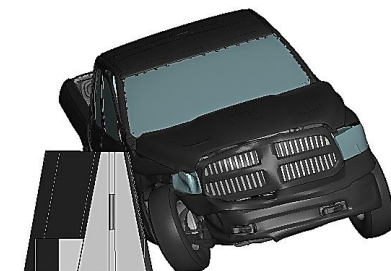
Figure 5.9. Overhead Images of *MASH* Test 3-11 Simulation of Single-Slope Barrier with Scupper—Impact Location B.



a. $t = 0.18$ s, event = pickup truck impacts barrier



b. $t = 0.35$ s, event = pickup truck is parallel with barrier



c. $t = 0.57$ s, event = pickup truck front right tire contacts ground

Figure 5.10. End-View Images of *MASH* Test 3-11 Simulation of Single-Slope Barrier with Scupper—Impact Location B.

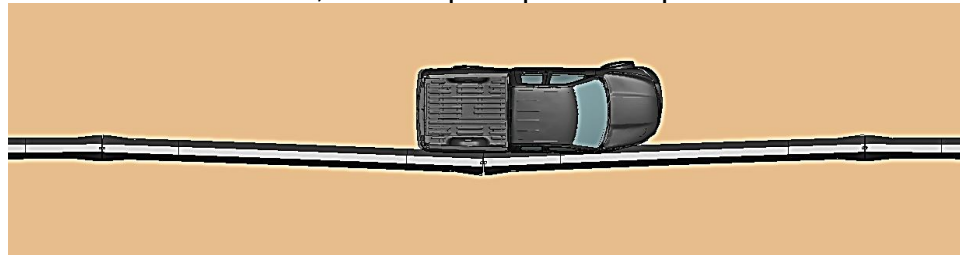
Table 5.4. Occupant Risk Values for Pickup Truck Impacting Single-Slope Barrier with Scupper—Impact Location B.

Parameter	<i>MASH</i> Threshold	Simulation Result
OIV (ft/s)	40	26
RA (g)	20.49	15.6
Yaw (deg)	N/A	34.3
Pitch (deg)	75	8.9
Roll (deg)	75	18.4

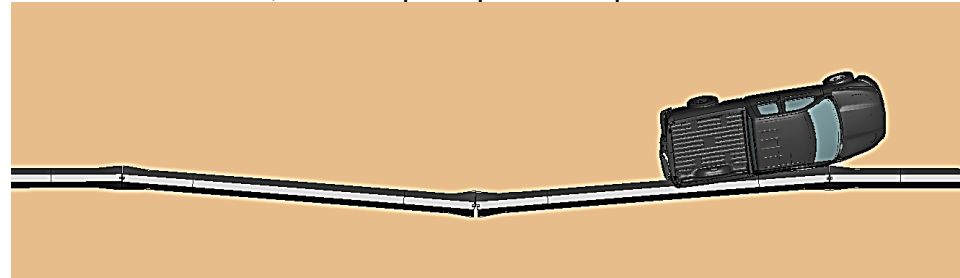
Note: N/A = not applicable.



a. $t = 0.17$ s, event = pickup truck impacts barrier



b. $t = 0.34$ s, event = pickup truck is parallel with barrier

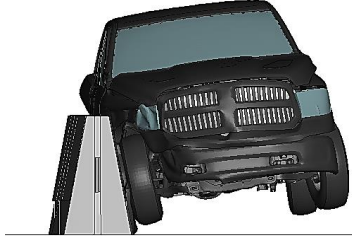


c. $t = 0.70$ s, event = pickup truck exits barrier

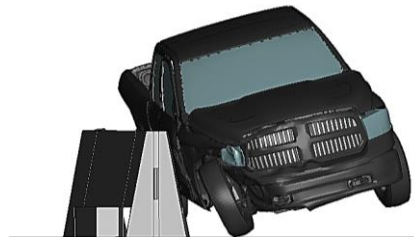
Figure 5.11. Overhead Images of *MASH* Test 3-11 Simulation of Single-Slope Barrier with Scupper—Impact Location C.



a. $t = 0.18$ s, event = pickup truck impacts barrier



b. $t = 0.35$ s, event = pickup truck is parallel with barrier



c. $t = 0.57$ s, event = pickup truck front right tire contacts ground

Figure 5.12. End-View Images of *MASH* Test 3-11 Simulation of Single-Slope Barrier with Scupper—Impact Location C.

Table 5.5. Occupant Risk Values for Pickup Truck Impacting Single-Slope Barrier with Scupper—Impact Location C.

Parameter	<i>MASH</i> Threshold	Simulation Result
OIV (ft/s)	40	23.3
RA (g)	20.49	16.2
Yaw (deg)	N/A	34
Pitch (deg)	75	7.7
Roll (deg)	75	16.9

Note: N/A = not applicable.

5.3.2.4. *Impact Location A—Center of Barrier Segment with Passenger Car*

Impact location A was 3.6 ft upstream from the center of the barrier. Figure 5.13 and Figure 5.14 provide sequential images of the impact simulation at selected times from an overhead and end view, respectively. Lateral displacement of the impacted barrier was 4.8 inches. TRAP was used to calculate OIV, RA, and maximum roll, pitch, and yaw angles. Table 5.6 summarizes the results from the simulation. The simulated impact of the passenger car at the center of the barrier segment satisfied *MASH* criteria.

5.3.2.5. *Impact Location B—End of Scupper with Passenger Car*

Impact location B was 3.6 ft upstream of the end of the scupper. This location was likely to result in the highest snagging severity. Figure 5.15 and Figure 5.16 provide sequential images of the impact simulation at selected times from an overhead and end view, respectively. Lateral displacement of the impacted barrier was 8.4 inches. TRAP was used to calculate OIV, RA, and maximum roll, pitch, and yaw angles. Table 5.7 summarizes the results from the simulation. The simulated impact of the passenger car at the end of the scupper satisfied *MASH* criteria.

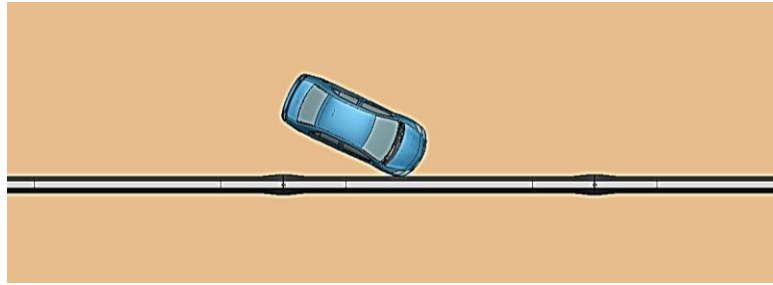
5.3.2.6. *Impact Location C—Barrier Segment Connection with Passenger Car*

Impact location C was 3.6 ft upstream of a joint between barrier segments. Figure 5.17 and Figure 5.18 provide sequential images of the impact simulation at selected times from an overhead and end view, respectively. Lateral displacement of the impacted barrier was 11.2 inches. TRAP was used to calculate OIV, RA, and maximum roll, pitch, and yaw angles. Table 5.8 summarizes the results from the simulation. The simulated impact of the passenger car at the barrier segment connection satisfied *MASH* criteria.

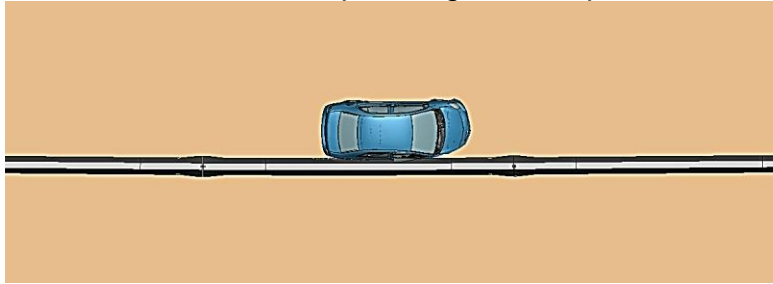
5.3.3. **Conclusions for Impact Simulations of Single-Slope Barrier with Scupper and J-J Hooks Connections**

The researchers evaluated the impact performance of the single-slope PCB with scupper and J-J Hooks segment connections through finite element simulations following *MASH* TL-3 impact conditions. Simulations were conducted with both the 2270P pickup truck model and the 1100C passenger car model. Three different reference impact locations were investigated for each vehicle to examine barrier strength, vehicle stability, snagging severity, and dynamic deflection.

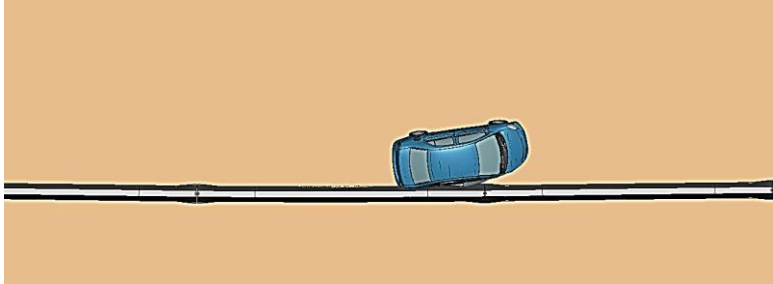
In all simulations, the vehicles were contained and redirected in a stable manner. The occupant risk indices and vehicular angular displacements (e.g., roll and pitch angle) were well below *MASH* thresholds for both vehicles for all three impact locations. The OIV for all simulations was below the preferred value in *MASH*. The highest RA was 16.6 g for the small car impact at the scupper end. The maximum roll angle was 20.9 degrees for the small car at the barrier joint. The maximum lateral barrier deflection was 27.8 inches. Barrier deflection is not a *MASH* criterion, but it is an important parameter to consider for barrier implementation.



a. $t = 0.17$ s, event = passenger car impacts barrier



b. $t = 0.33$ s, event = passenger car is parallel with barrier

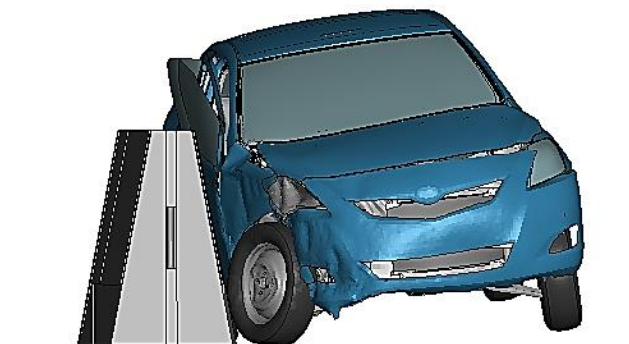


c. $t = 0.46$ s, event = passenger car exits barrier

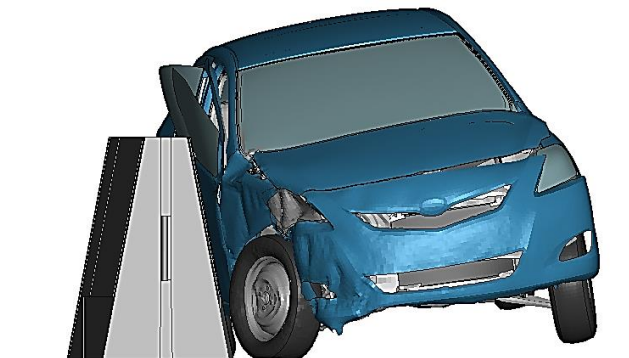
Figure 5.13. Overhead Images of *MASH* Test 3-10 Simulation of Single-Slope Barrier with Scupper—Impact Location A.



a. $t = 0.19$ s, event = passenger car impacts barrier



b. $t = 0.37$ s, event = passenger car is parallel with barrier



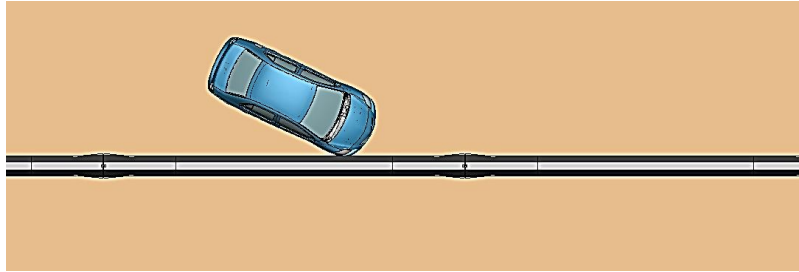
c. $t = 0.50$ s, event = passenger car exits barrier

Figure 5.14. End-View Images of *MASH* Test 3-10 Simulation of Single-Slope Barrier with Scupper—Impact Location A.

Table 5.6. Occupant Risk Values for Passenger Car Impacting Single-Slope Barrier with Scupper—Impact Location A.

Parameter	<i>MASH</i> Threshold	Simulation Result
OIV (ft/s)	40	26.0
RA (g)	20.49	13.0
Yaw (deg)	N/A	34.6
Pitch (deg)	75	4.4
Roll (deg)	75	12.2

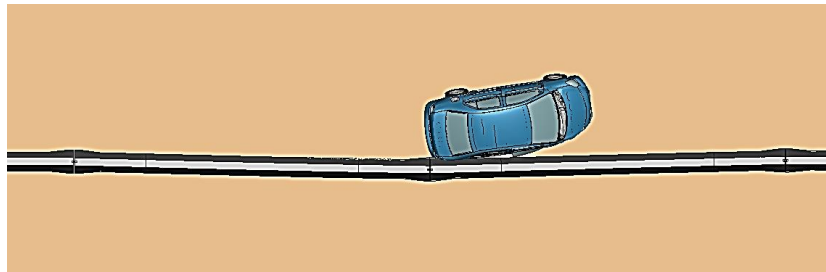
Note: N/A = not applicable.



a. $t = 0.17$ s, event = passenger car impacts barrier



b. $t = 0.33$ s, event = passenger car parallel is with barrier

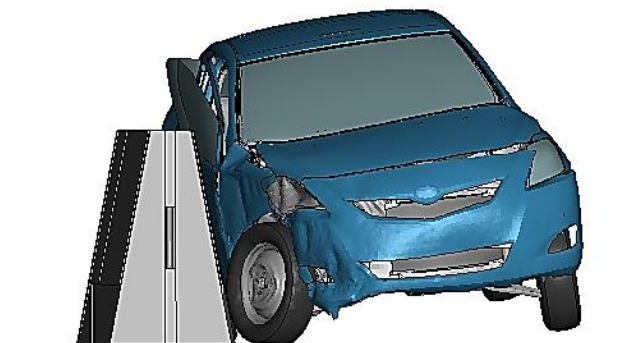


c. $t = 0.46$ s, event = passenger car exits barrier

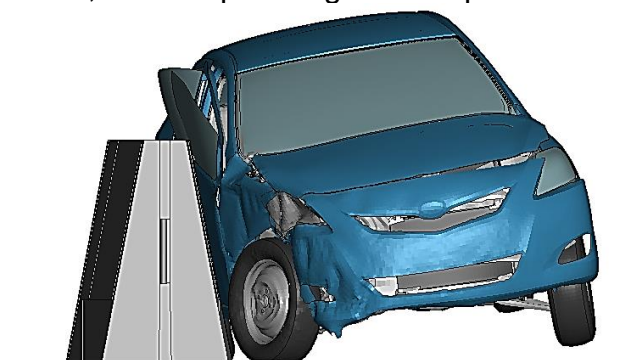
Figure 5.15. Overhead Images of *MASH* Test 3-10 Simulation of Single-Slope Barrier with Scupper—Impact Location B.



a. $t = 0.19$ s, event = passenger car impacts barrier



b. $t = 0.37$ s, event = passenger car is parallel with barrier



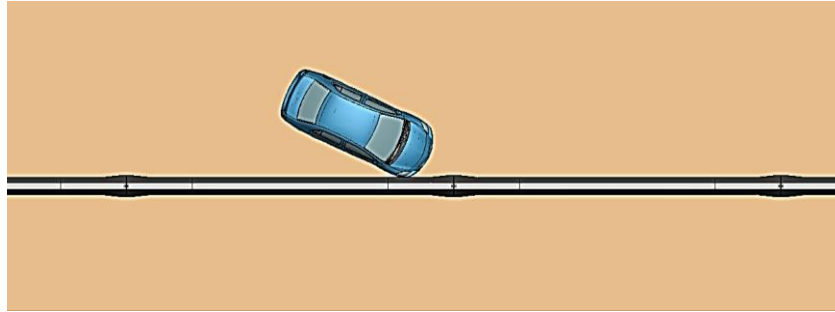
c. $t = 0.50$ s, event = passenger car exits barrier

Figure 5.16. End-View Images of *MASH* Test 3-10 Simulation of Single-Slope Barrier with Scupper—Impact Location B.

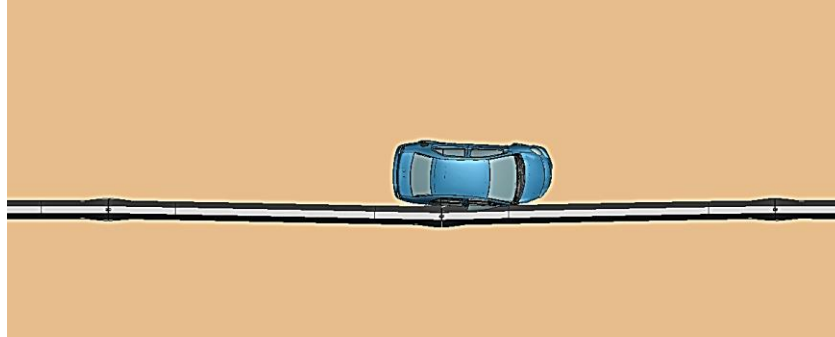
Table 5.7. Occupant Risk Values for Passenger Car Impacting Single-Slope Barrier with Scupper—Impact Location B.

Parameter	<i>MASH</i> Threshold	Simulation Result
OIV (ft/s)	40	26.2
RA (g)	20.49	16.6
Yaw (deg)	N/A	35.8
Pitch (deg)	75	4.3
Roll (deg)	75	13.9

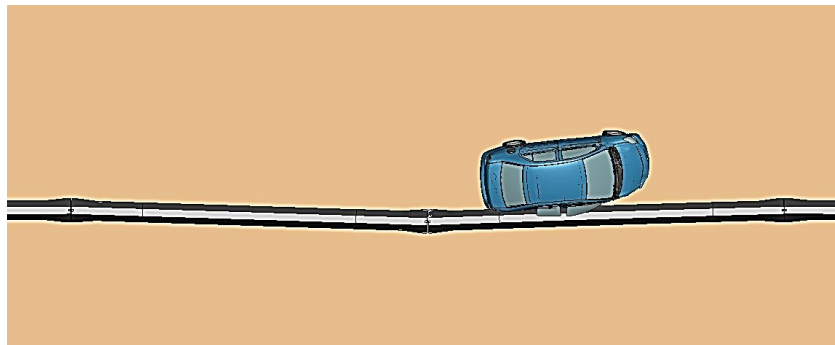
Note: N/A = not applicable.



a. $t = 0.17$ s, event = passenger car impacts barrier



b. $t = 0.33$ s, event = passenger car is parallel with barrier

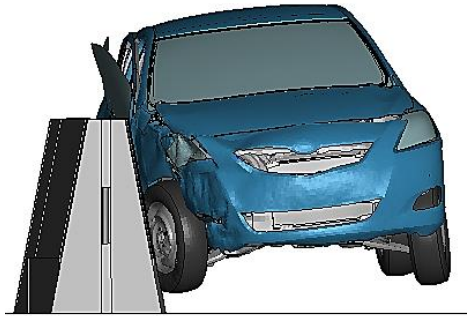


c. $t = 0.46$ s, event = passenger car exits barrier

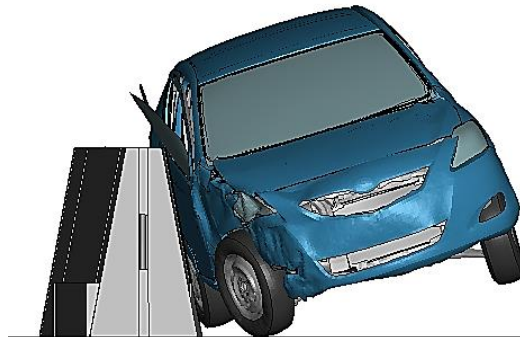
Figure 5.17. Overhead Images of *MASH* Test 3-10 Simulation of Single-Slope Barrier with Scupper—Impact Location C.



a. $t = 0.19$ s, event = passenger car contacts barrier



b. $t = 0.37$ s, event = passenger car is parallel with barrier



c. $t = 0.50$ s, event = passenger car exits barrier

Figure 5.18. End-View Images of *MASH* Test 3-10 Simulation of Single-Slope Barrier with Scupper—Impact Location C.

Table 5.8. Occupant Risk Values for Passenger Car Impacting Single-Slope Barrier with Scupper—Impact Location C.

Parameter	<i>MASH</i> Threshold	Simulation Result
OIV (ft/s)	40	24.2
RA (g)	20.49	13.5
Yaw (deg)	N/A	30.0
Pitch (deg)	75	4.9
Roll (deg)	75	20.9

Note: N/A = not applicable.

5.3.4. Impact Simulations of Single-Slope Barrier with Scupper and X-bolt Connections

Predictive simulations of the single-slope PCB with large scupper and X-bolt connections were performed to assess the impact performance of the conceptualized geometry. The model of the single-slope barrier with scupper was modified to include the X-bolt connection details as depicted in Figure 5.19. The simulations followed impact conditions of *MASH* Test 3-21 and Test 3-20 with the 2270P pickup truck and 1100C passenger car, respectively.

As with the system with J-J Hooks connections, various reference points along the length of the single-slope PCB segment were investigated for the barrier with X-bolt connections. These included the center of the long beam spanning the drainage opening, the connection between segments, and the end of the drainage opening or scupper. The impact location was 4.3 ft upstream of each reference location for the pickup truck and 3.6 ft upstream of each reference location for the passenger car. These distances were determined using Table 2-7 in *MASH*. Details of these simulations are presented next.

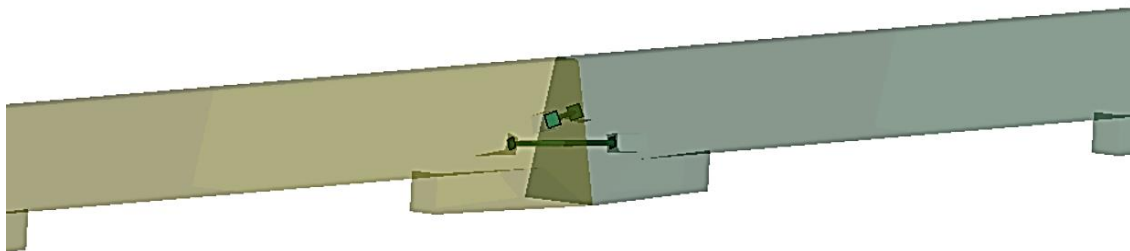


Figure 5.19. Single-Slope PCB Model with X-bolt Connection.

5.3.4.1. Impact Location A—Center of Barrier Segment with Pickup Truck

Impact location A was 4.3 ft upstream from the center of the barrier. This location evaluated the structural adequacy of the barrier where material was removed for the introduction of the scupper. The X-bolt connection reduces dynamic deflection compared to the J-J Hooks connection. Therefore, the impact load may increase given that the barrier movement will be less.

Figure 5.20 and Figure 5.21 provide sequential images of the impact simulation at selected times from an overhead and end view, respectively. Lateral displacement of the impacted barrier was 8.7 inches. TRAP was used to calculate OIV, RA, and maximum roll, pitch, and yaw angles. Table 5.9 summarizes the results from the simulation. The simulated impact of the pickup truck at the center of the barrier segment satisfied *MASH* criteria.

5.3.4.2. Impact Location B—End of Scupper with Pickup Truck

Impact location B was 4.3 ft upstream of the end of the scupper. This location evaluated vehicle snagging on the tapered end of the scupper.

Figure 5.22 and Figure 5.23 provide sequential images of the impact simulation at selected times from an overhead and end view, respectively. Lateral displacement of

the impacted barrier was 8.9 inches. TRAP was used to calculate OIV, RA, and maximum roll, pitch, and yaw angles. Table 5.10 summarizes the results from the simulation. The simulated impact of the pickup truck at the end of the scupper satisfied *MASH* criteria.

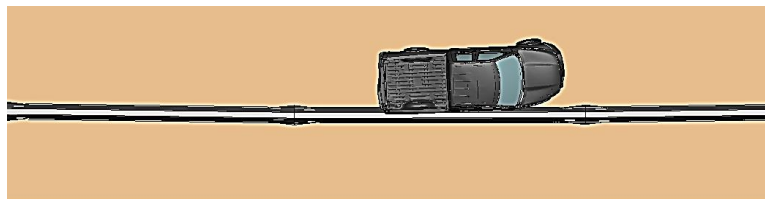
5.3.4.3. Impact Location C—Barrier Segment Connection with Pickup Truck

Impact location C was 4.3 ft upstream of a joint between barrier segments. This location evaluated the structural adequacy of the barrier connection and other factors such as vehicle stability. It is also likely to result in the largest lateral deflection due to the proximity of the impact point to the joint.

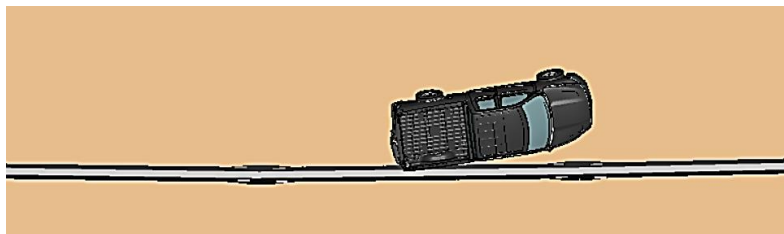
Figure 5.24 and Figure 5.25 provide sequential images of the impact simulation at selected times from an overhead and end view, respectively. Lateral displacement of the impacted barrier was 12.1 inches. TRAP was used to calculate OIV, RA, and maximum roll, pitch, and yaw angles. Table 5.11 summarizes the results from the simulation. The simulated impact of the pickup truck at the barrier segment connection satisfied *MASH* criteria.



a. $t = 0.17$ s, event = pickup truck strikes the barrier



b. $t = 0.34$ s, event = pickup truck rear contacts the barrier



c. $t = 0.70$ s, event = pickup truck is redirected by the barrier

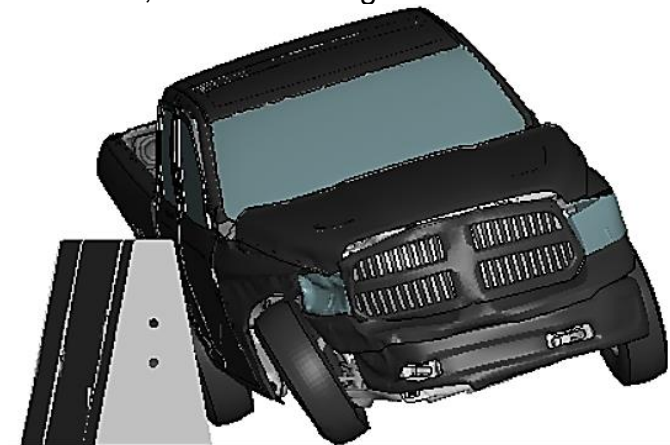
Figure 5.20. Overhead Images of *MASH* Test 3-11 Simulation of Single-Slope Barrier with Scupper and X-bolt Connections—Impact Location A.



a. $t = 0.17$ s, event = front right tire contacts the barrier



b. $t = 0.35$ s, event = rear right tire contacts the barrier



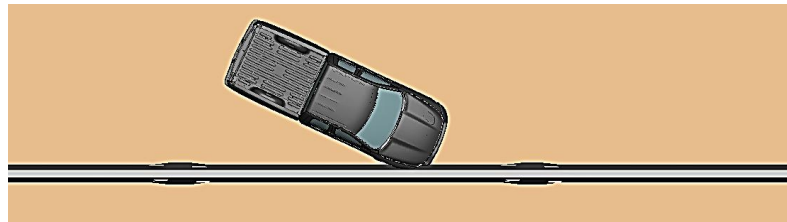
c. $t = 0.57$ s, event = front right tire touches the ground

Figure 5.21. End-View Images of *MASH* Test 3-11 Simulation of Single-Slope Barrier with Scupper and X-bolt Connections—Impact Location A.

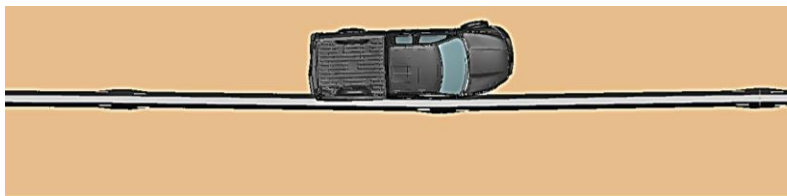
Table 5.9. Occupant Risk Values for Pickup Truck Impacting Single-Slope Barrier with Scupper and X-bolt Connections—Impact Location A.

Parameter	<i>MASH</i> Threshold	Simulation Result
OIV (ft/s)	40	27.5
RA (g)	20.49	15.0
Yaw (deg)	N/A	38
Pitch (deg)	75	4.9
Roll (deg)	75	23.0

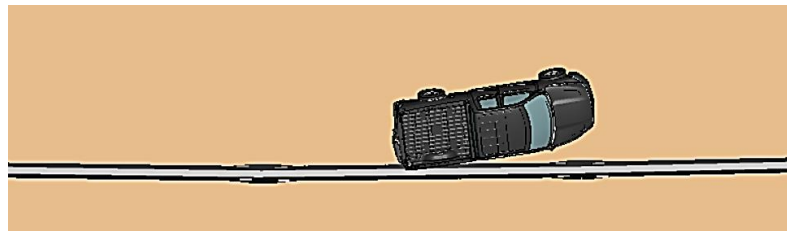
Note: N/A = not applicable.



a. $t = 0.17$ s, event = pickup truck strikes the barrier



b. $t = 0.34$ s, event = pickup truck rear contacts the barrier



c. $t = 0.70$ s, event = pickup truck is redirected by the barrier

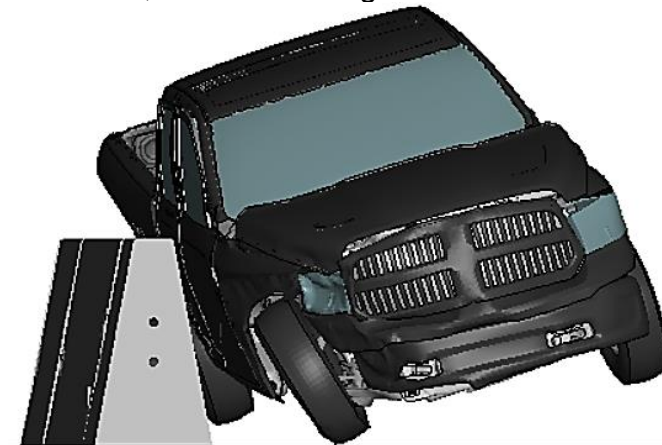
Figure 5.22. Overhead Images of *MASH* Test 3-11 Simulation of Single-Slope Barrier with Scupper and X-bolt Connections—Impact Location B.



a. $t = 0.17$ s, event = front right tire contacts the barrier



b. $t = 0.35$ s, event = rear right tire contacts the barrier



c. $t = 0.57$ s, event = front right tire touches the ground

Figure 5.23. End-View Images of *MASH* Test 3-11 Simulation of Single-Slope Barrier with Scupper and X-bolt Connections—Impact Location B.

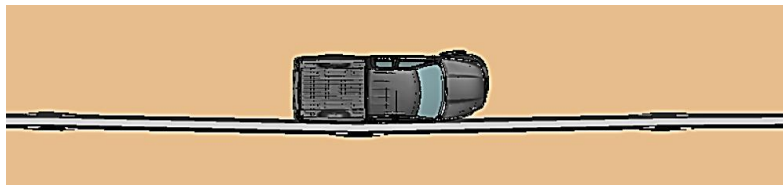
Table 5.10. Occupant Risk Values for Pickup Truck Impacting Single-Slope Barrier with Scupper and X-bolt Connections—Impact Location B.

Parameter	<i>MASH</i> Threshold	Simulation Result
OIV (ft/s)	40	26.5
RA (g)	20.49	14.0
Yaw (deg)	N/A	35
Pitch (deg)	75	4.7
Roll (deg)	75	19.4

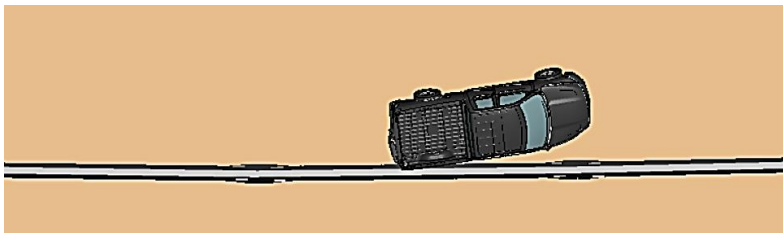
Note: N/A = not applicable.



a. $t = 0.17$ s, event = pickup truck strikes the barrier



b. $t = 0.34$ s, event = pickup truck rear contacts the barrier

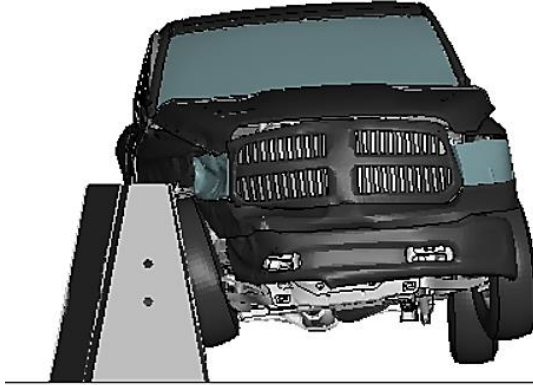


c. $t = 0.70$ s, event = pickup truck is redirected by the barrier

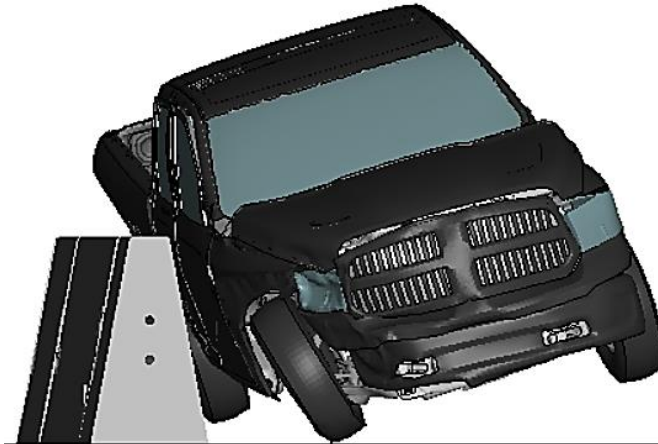
Figure 5.24. Overhead Images of *MASH* Test 3-11 Simulation of Single-Slope Barrier with Scupper and X-bolt Connections—Impact Location C.



a. $t = 0.17$ s, event = front right tire contacts the barrier



b. $t = 0.35$ s, event = rear right tire contacts the barrier



c. $t = 0.57$ s, event = front right tire touches the ground

Figure 5.25. End-View Images of *MASH* Test 3-11 Simulation of Single-Slope Barrier with Scupper and X-bolt Connections—Impact Location C.

Table 5.11. Occupant Risk Values for Pickup Truck Impacting Single-Slope Barrier with Scupper and X-bolt Connections—Impact Location C.

Parameter	MASH Threshold	Simulation Result
OIV (ft/s)	40	24.0
RA (g)	20.49	17.1
Yaw (deg)	N/A	33
Pitch (deg)	75	4.3
Roll (deg)	75	17.7

Note: N/A = not applicable.

5.3.4.4. *Impact Location A—Center of Barrier Segment with Passenger Car*

Impact location A was 3.6 ft upstream from the center of the barrier. Figure 5.26 and Figure 5.27 provide sequential images of the impact simulation at selected times from an overhead and end view, respectively. Lateral displacement of the impacted barrier was 3.6 inches. TRAP was used to calculate OIV, RA, and maximum roll, pitch, and yaw angles. Table 5.12 summarizes the results from the simulation. The simulated impact of the passenger car at the center of the barrier segment satisfied *MASH* criteria.

5.3.4.5. *Impact Location B—End of Scupper with Passenger Car*

Impact location B was 3.6 ft upstream of the end of the scupper. This location was likely to result in the highest snagging severity. Figure 5.28 and Figure 5.29 provide sequential images of the impact simulation at selected times from an overhead and end view, respectively. Lateral displacement of the impacted barrier was 5.5 inches. TRAP was used to calculate OIV, RA, and maximum roll, pitch, and yaw angles. Table 5.13 summarizes the results from the simulation. The simulated impact of the passenger car at the end of the scupper satisfied *MASH* criteria.

5.3.4.6. *Impact Location C—Barrier Segment Connection with Passenger Car*

Impact location C was 3.6 ft upstream of a joint between barrier segments. Figure 5.30 and Figure 5.31 provide sequential images of the impact simulation at selected times from an overhead and end view, respectively. Lateral displacement of the impacted barrier was 6.2 inches. TRAP was used to calculate OIV, RA, and maximum roll, pitch, and yaw angles. Table 5.14 summarizes the results from the simulation. The simulated impact of the passenger car at the barrier segment connection satisfied *MASH* criteria.

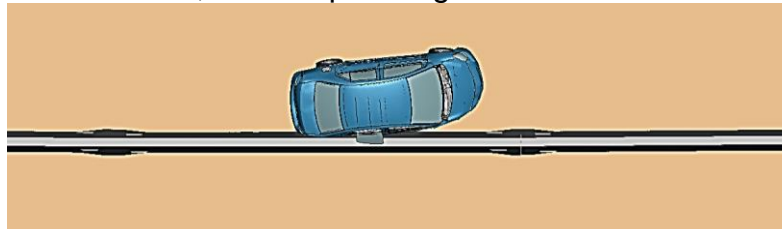
5.3.5. **Conclusions for Impact Simulations of Single-Slope Barrier with Scupper and X-bolt Connections**

The researchers evaluated the impact performance of the single-slope PCB with scupper and X-bolt segment connections through finite element simulations following *MASH* TL-3 impact conditions. Simulations were conducted with both the 2270P pickup truck and 1100C passenger car models. Three different reference impact locations were investigated for each vehicle to examine barrier strength, vehicle stability, snagging severity, and dynamic deflection.

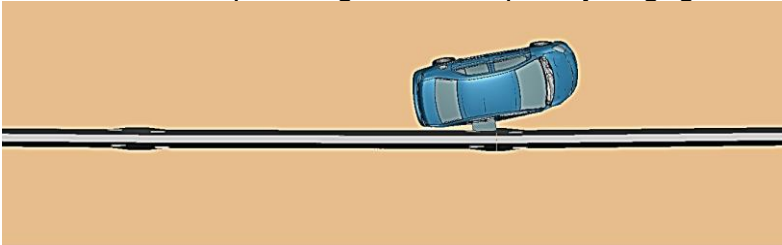
In all simulations, the vehicles were contained and redirected in a stable manner. The occupant risk indices and vehicular angular displacements (e.g., roll and pitch angle) were below *MASH* thresholds for both vehicles for all three impact locations. The OIV was below the preferred *MASH* value for all simulations. The simulation of the small car impacting at the end of the scupper had the highest RA (20.0 g), which was just below the threshold value of 20.49 g. The maximum roll angle of 23.0 degrees was obtained in the simulation of the pickup truck impacting at the center of the segment. The maximum lateral barrier deflection was only 12.1 inches, compared to 27.8 inches with the J-J Hooks connections. Barrier deflection is not a *MASH* criterion, but it is an important parameter to consider for barrier implementation.



a. $t = 0.17$ s, event = passenger car strikes the barrier

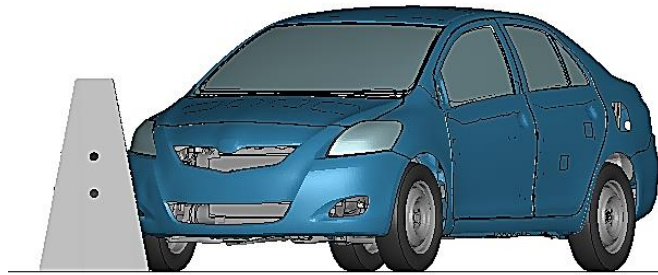


b. $t = 0.33$ s, event = passenger car completely engages the barrier

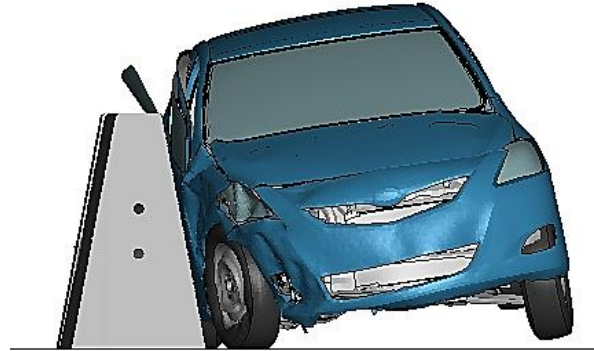


c. $t = 0.46$ s, event = passenger car is redirected by the barrier

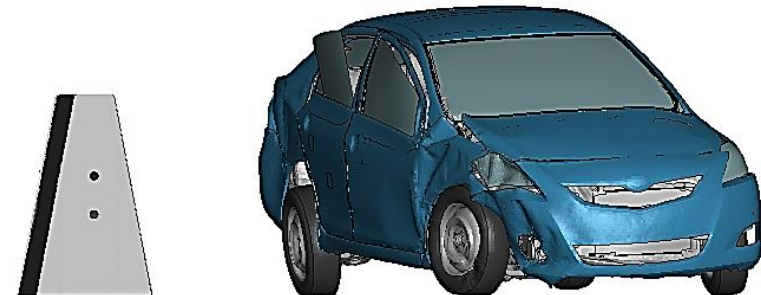
Figure 5.26. Overhead Images of *MASH* Test 3-10 Simulation of Single-Slope Barrier with Scupper and X-bolt Connections—Impact Location A.



a. $t = 0.19$ s, event = front right tire contacts the barrier



b. $t = 0.37$ s, event = rear right tire contacts the barrier, windowpane snags against the barrier



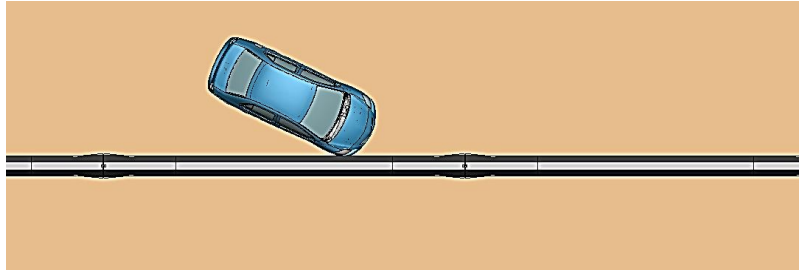
c. $t = 0.71$ s, event = vehicle stabilizes on the ground

Figure 5.27. End-View Images of *MASH* Test 3-10 Simulation of Single-Slope Barrier with Scupper and X-bolt Connections—Impact Location A.

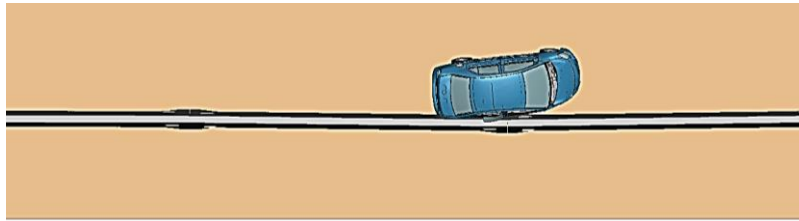
Table 5.12. Occupant Risk Values for Passenger Car Impacting Single-Slope Barrier with Scupper and X-bolt Connections—Impact Location A.

Parameter	<i>MASH</i> Threshold	Simulation Result
OIV (ft/s)	40	29.0
RA (g)	20.49	16.0
Yaw (deg)	N/A	34.6
Pitch (deg)	75	11.3
Roll (deg)	75	12.0

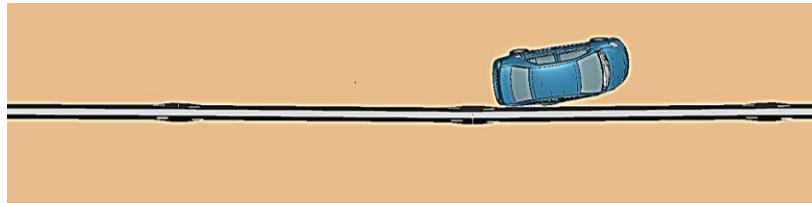
Note: N/A = not applicable.



a. $t = 0.17$ s, event = passenger car strikes the barrier

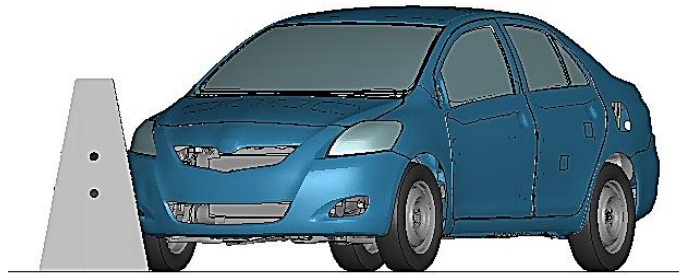


b. $t = 0.33$ s, event = passenger car completely engages the barrier

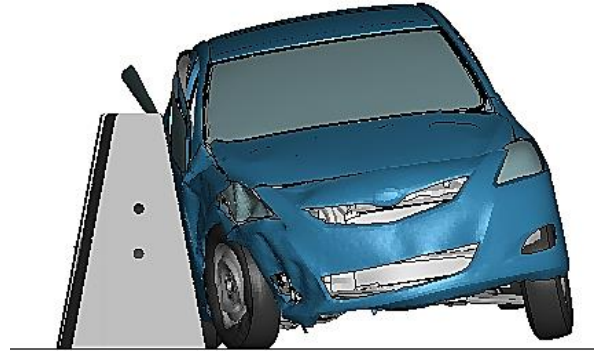


c. $t = 0.46$ s, event = passenger car is redirected by the barrier

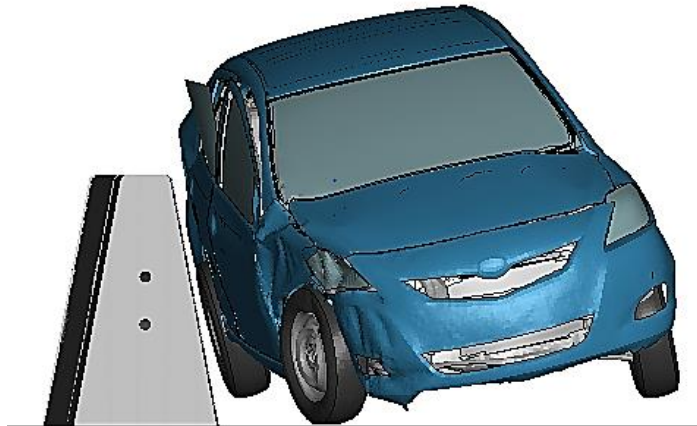
Figure 5.28. Overhead Images of *MASH* Test 3-10 Simulation of Single-Slope Barrier with Scupper and X-bolt Connections—Impact Location B.



a. $t = 0.19$ s, event = front right tire contacts the barrier



b. $t = 0.37$ s, event = rear right tire contacts the barrier, windowpane snags against the barrier



c. $t = 0.50$ s, event = front right tire touches the ground

Figure 5.29. End-View Images of *MASH* Test 3-10 Simulation of Single-Slope Barrier with Scupper and X-bolt Connections—Impact Location B.

Table 5.13. Occupant Risk Values for Passenger Car Impacting Single-Slope Barrier with Scupper and X-bolt Connections—Impact Location B.

Parameter	<i>MASH</i> Threshold	Simulation Result
OIV (ft/s)	40	28.0
RA (g)	20.49	17.0
Yaw (deg)	N/A	34
Pitch (deg)	75	10.0
Roll (deg)	75	17.4

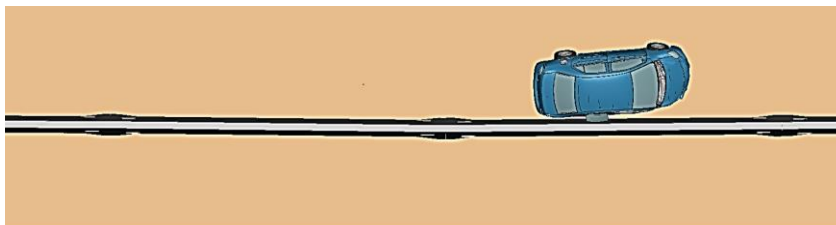
Note: N/A = not applicable.



a. $t = 0.17$ s, event = passenger car strikes the barrier

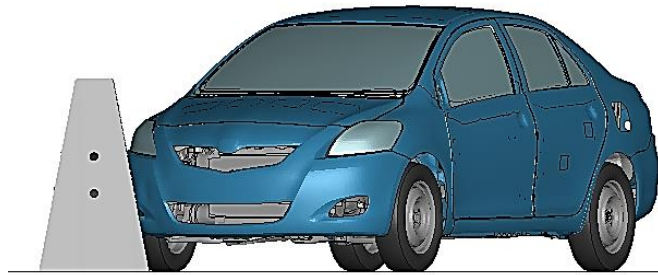


b. $t = 0.23$ s, event = passenger car contacts the joint

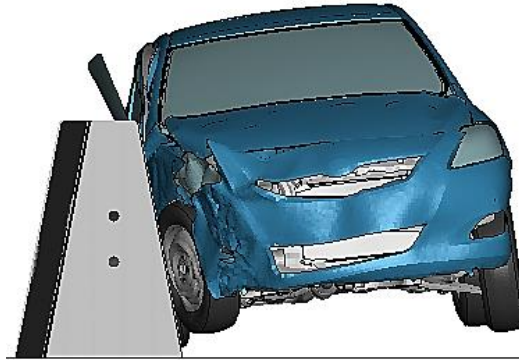


c. $t = 0.46$ s, event = passenger car is redirected by the barrier

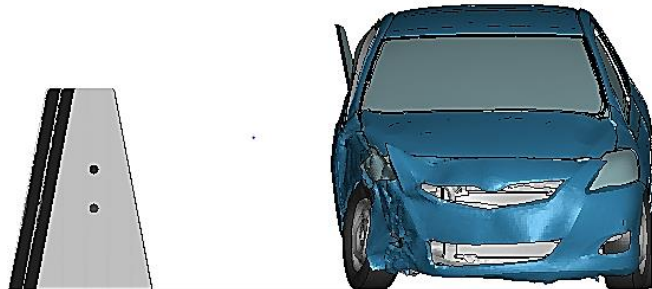
Figure 5.30. Overhead Images of *MASH* Test 3-10 Simulation of Single-Slope Barrier with Scupper and X-bolt Connections—Impact Location C.



a. $t = 0.19$ s, event = front right tire contacts the barrier



b. $t = 0.37$ s, event = rear right tire contacts the barrier, windowpane snags against the barrier



c. $t = 0.71$ s, event = vehicle stabilizes on the ground

Figure 5.31. End-View Images of *MASH* Test 3-10 Simulation of Single-Slope Barrier with Scupper and X-bolt Connections—Impact Location C.

Table 5.14. Occupant Risk Values for Passenger Car Impacting Single-Slope Barrier with Scupper and X-bolt Connections—Impact Location C.

Parameter	<i>MASH</i> Threshold	Simulation Result
OIV (ft/s)	40	26.0
RA (g)	20.49	20.0
Yaw (deg)	N/A	32.0
Pitch (deg)	75	9.6
Roll (deg)	75	17.4

Note: N/A = not applicable.

5.4. MODEL CALIBRATION

Initially, the project scope was to develop a hydraulically efficient portable concrete barrier that complied with *MASH* TL-3. After the *MASH* TL-3 tests were performed, it was noted that the barrier performed well and seemingly had the height and additional structural capacity to satisfy *MASH* TL-4 requirements. The *MASH* TL-4 test matrix for longitudinal barriers includes similar passenger vehicle tests to TL-3 with the addition of Test 4-12. Test 4-12 involves a 22,000-lb single-unit truck (denoted 10000S) impacting the barrier at a speed of 56 mi/h and an angle of 15 degrees. The project scope was amended to include additional evaluation of the precast single-slope concrete barrier with scupper to *MASH* TL-4.

The project panel decided to perform the full-scale crash testing on the single-slope portable concrete barrier with scupper with X-bolt connections. The previously reported predictive *MASH* TL-3 simulations were compared to the *MASH* TL-3 crash test results. It was noted that the simulation underpredicted the maximum lateral deflection of the barrier in both the passenger car test (Test 3-10) and the pickup truck test (Test 3-11). A comparison of the predicted and measured deflections is provided in Table 5.15.

Table 5.15. Lateral Deflection for Predictive Simulations and Crash Tests.

Test Designation	Predictive Simulation (inch)	Test (inch)
3-10	6.2	9.5
3-11	12.14	15.5

TTI researchers calibrated the model of the single-slope portable concrete barrier with scupper by varying the coefficient of friction between the barrier and ground. Table 5.16 lists the initial predictive and final calibrated friction coefficient values. As shown in Table 5.17, the calibrated friction values resulted in lateral deflections that were within 10 percent of the measured values in the crash tests.

Table 5.16. Friction Coefficient Values for the Calibrated Simulation.

Description	Static Coefficient	Dynamic Coefficient
Initial Friction	0.46	0.4
Final Friction	0.2	0.2

Table 5.17. Lateral Deflection for Crash Test and Calibrated Simulation.

Test Level	Test (inch)	Calibrated Simulation (inch)
3-10	9.5	10.1
3-11	15.5	17.3

Occupant risk factors and angular vehicle displacements were also computed from the impact simulations with the calibrated barrier model and compared to the values obtained in the crash results. Table 5.18 and Table 5.19 provide a comparison of these

parameters for Test 3-10 and Test 3-11, respectively. As shown in these tables, the parameters are very comparable for the passenger car test (Test 3-10) and reasonably comparable for the pickup truck test (Test 3-11).

Table 5.18. Occupant Risk Factors for Single-Slope Barrier with Passenger Car.

Test Parameter	Limits	Test	Calibrated Simulation
OIV, Longitudinal (ft/s)	≤40.0	29.8	30.0
OIV Lateral (ft/s)	≤40.0	28.9	27.3
Ridedown, Longitudinal (g)	≤20.49	6.1	4.2
Ridedown, Lateral (g)	≤20.49	8.8	5
Roll (deg)	≤75	7	8.2
Pitch (deg)	≤75	6	6.4
Yaw (deg)	N/A	36	34

Note: N/A = not applicable.

Table 5.19. Occupant Risk Factors for Single-Slope Barrier with Pickup Truck.

Test Parameter	Limits	Test	Calibrated Simulation
OIV, Longitudinal (ft/s)	≤40.0	16.7	23
OIV Lateral (ft/s)	≤40.0	18.8	24
Ridedown, Longitudinal (g)	≤20.49	3.4	3
Ridedown, Lateral (g)	≤20.49	9.3	12
Roll (deg)	≤75	12	14
Pitch (deg)	≤75	6	7
Yaw (deg)	N/A	36	45

Note: N/A = not applicable.

5.5. MASH TEST 4-12 PREDICTIVE SIMULATION

Using the model calibrated against the *MASH* TL-3 crash tests, TTI researchers performed a predictive simulation of *MASH* Test 4-12 with the 10000S single-unit truck (SUT). The simulation model setup with the SUT model and eight barrier segments is shown in Figure 5.32. The impact conditions followed *MASH* Test 4-12, which involves the SUT impacting the barrier at a speed of 56 mi/h and an angle of 15 degrees. The critical reference location for the test was selected to be the center of the barrier. This location evaluated the structural adequacy of the barrier where material was removed for the introduction of the scupper. The impact point was 5 ft upstream of the center of the barrier based on *MASH* Table 2-7.

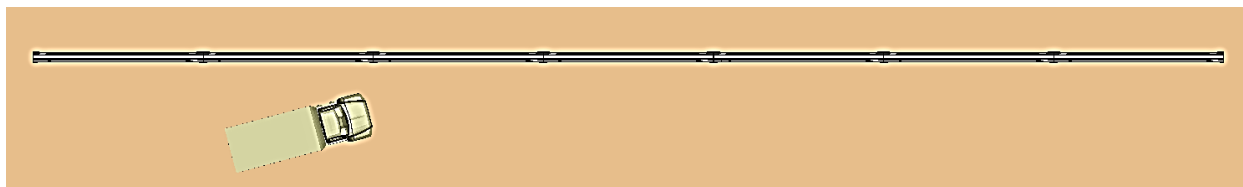
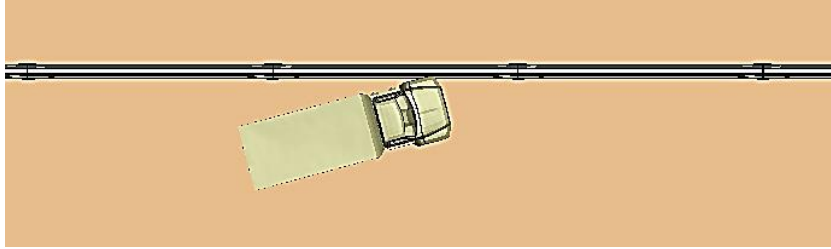


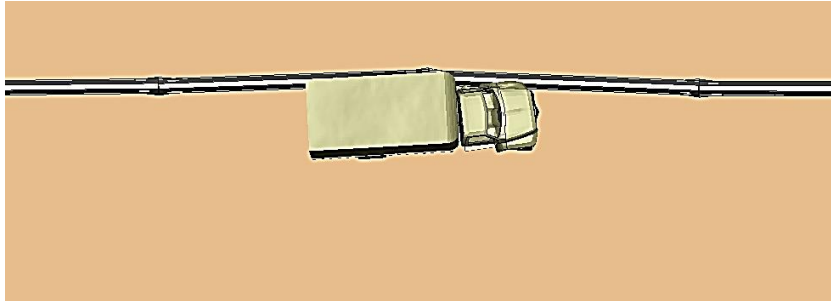
Figure 5.32. Pre-impact Finite Element Model Setup for SUT.

Figure 5.33 and Figure 5.34 provide sequential images of the impact simulation at selected times from an overhead and end view, respectively. Lateral displacement of the impacted barrier was 43 inches. Note that occupant risk indices are not included in the evaluation criteria for Test 4-12. However, TRAP was used to calculate OIV, RA, and maximum roll, pitch, and yaw angles for information purposes. Table 5.20 summarizes the results from the simulation. The simulated impact of the SUT at the center of the barrier segment satisfied *MASH* criteria. Based on these results, a decision was made to proceed with *MASH* Test 4-12.

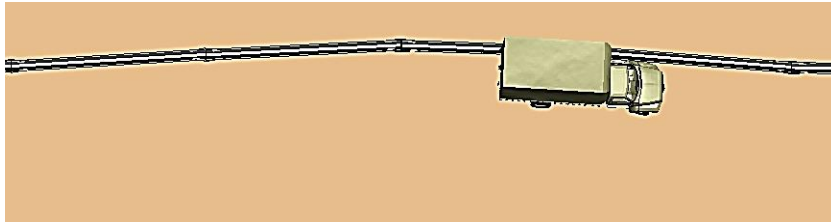
The following chapters present the crash testing procedures and results. Since *MASH* Test 4-12 was run on the barrier system after completion of the passenger car and pickup truck tests, the report documents testing in accordance with *MASH* TL-4 for longitudinal barriers.



a. $t = 0.27$ s, event = SUT strikes the barrier



b. $t = 0.53$ s, event = SUT completely engages with the system



c. $t = 0.94$ s, event = SUT completely disengages with the system

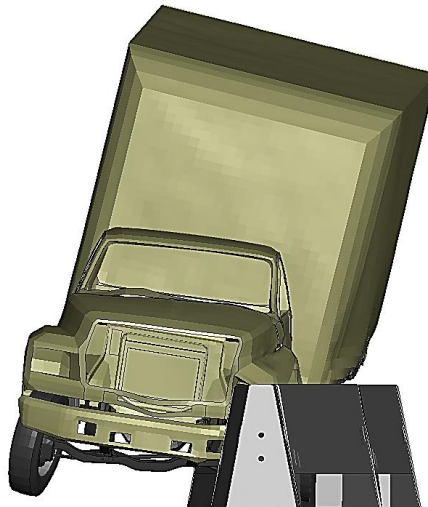
Figure 5.33. Overhead Images of *MASH* Test 4-12 Simulation of Single-Slope Barrier with Scupper and X-bolt Connections.



a. $t = 0.27$ s, event = SUT strikes the barrier



b. $t = 0.53$ s, event = SUT completely engages with the system



c. $t = 0.94$ s, event = front SUT tire stabilizes on the ground

Figure 5.34. End-View Images of *MASH* Test 4-12 Simulation of Single-Slope Barrier with Scupper and X-bolt Connections.

Table 5.20. Occupant Risk Values.

Parameter	Absolute Value
OIV (ft/s)	13
RA (g)	6
Yaw (deg)	15
Pitch (deg)	6
Roll (deg)	20

Chapter 6. SYSTEM DETAILS

6.1. TEST ARTICLE AND INSTALLATION DETAILS

The test installation for *MASH* Test 4-10 and Test 4-11 consisted of seven single-slope portable concrete barriers with large scupper connected using X-bolt connections. Each 30-ft barrier segment was 42 inches tall, 24 inches wide at the bottom, and 8 inches wide at the top. The large scupper was 18 ft long and 12 inches high, and it was centered on the barrier segment. The ends of the scupper were tapered to a width of 9 inches to reduce snagging interaction with the impacting vehicle. The X-bolt connection was comprised of two $\frac{7}{8}$ -inch-diameter B7 threaded steel rods. The overall length of the installation was 210 ft for *MASH* Test 4-10 and Test 4-11. For Test 4-12, the installation had eight segments, with a total length of 240 ft, to provide additional length for evaluating stability of the single-unit truck.

Figure 6.1 presents the overall information on the large-scupper portable concrete barrier, and Figure 6.2 through Figure 6.7 provide photographs of the installation. Appendix A provides further details on the large-scupper portable concrete barrier. Drawings were provided by the TTI Proving Ground, and the assembly of the test article was performed by TTI Proving Ground personnel.

6.2. DESIGN MODIFICATIONS DURING TESTS

No modifications were made to the installation during the testing phase.

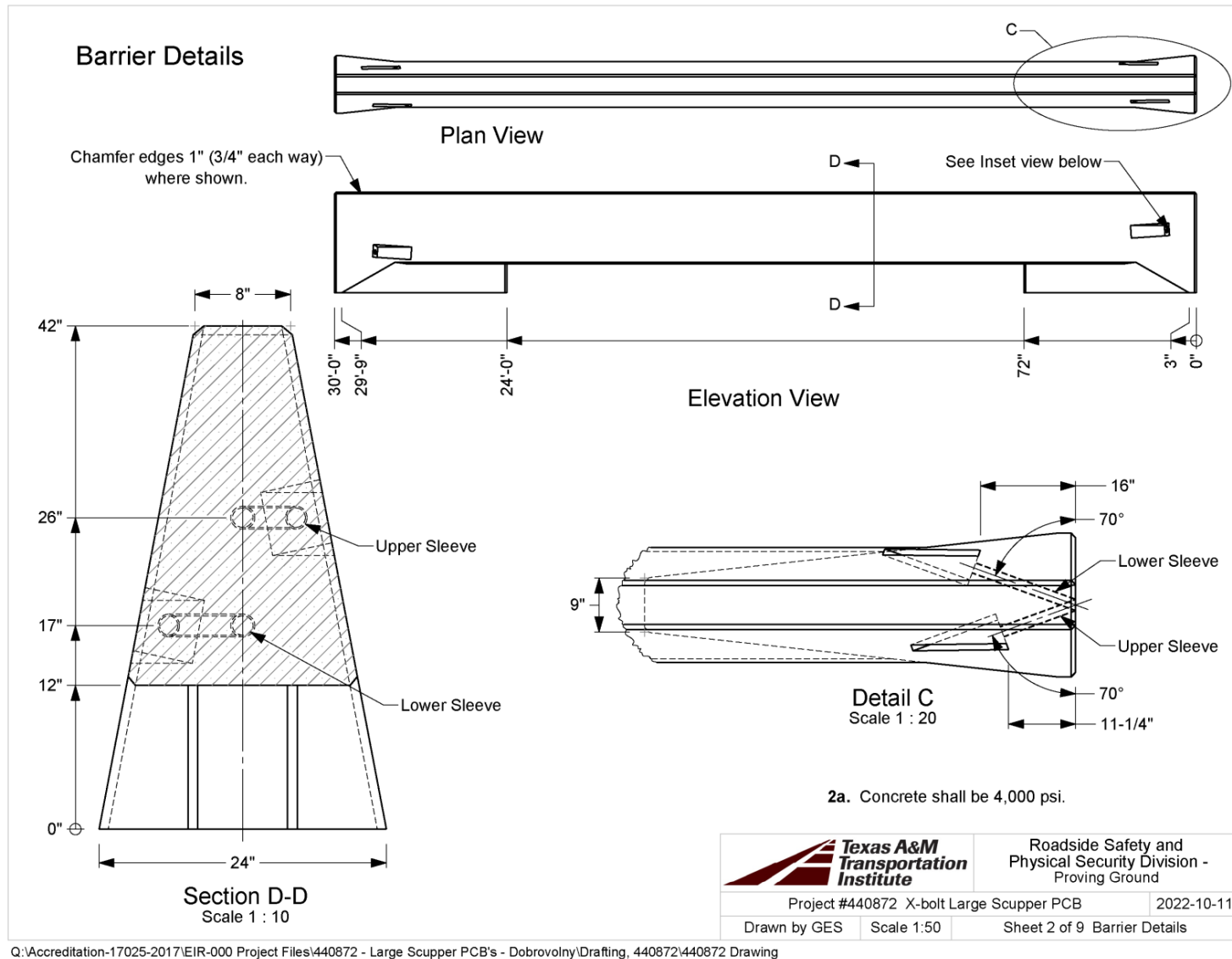


Figure 6.1. Details of Large-Scupper Portable Concrete Barrier.



Figure 6.2. Large-Scupper Portable Concrete Barrier prior to Testing.



Figure 6.3. Large-Scupper Portable Concrete Barrier at the Joint of Barriers 3 and 4 prior to Testing.



Figure 6.4. X-bolt Connection on the Large-Scupper Portable Concrete Barrier prior to Testing.



Figure 6.5. Close-Up of the End of the Scupper on the Large-Scupper Portable Concrete Barrier prior to Testing.



Figure 6.6. Upstream View of the Large-Scupper Portable Concrete Barrier prior to Testing.



Figure 6.7. Field Side of the Large-Scupper Portable Concrete Barrier prior to Testing.

6.3. MATERIAL SPECIFICATIONS

Appendix B provides material certification documents for the materials used to install/construct the large-scupper portable concrete barrier. Table 6.1 shows the average compressive strengths of the barrier concrete on the day of the first test on December 1, 2022.

Table 6.1. Concrete Strength.

Location	Design Strength (psi)	Avg. Strength (psi)	Age (days)	Detailed Location
Barrier	4000	4587	20	Barriers 1, 2, and 50% of 3
Barrier	4000	5110	28	50% of barrier 3 and all of 4
Barrier	4000	5590	12	Barriers 5 and 6
Barrier	4000	5463	12	Barrier 7
Barrier	4000	7640	N/A	Core of new barrier after Test 440873-01-3

Note: N/A = not applicable.

Chapter 7. TEST REQUIREMENTS AND EVALUATION CRITERIA

7.1. TEST PERFORMED/MATRIX

Table 7.1 shows the test conditions and evaluation criteria for *MASH* TL-4 for longitudinal barriers. The target critical impact points (CIPs) for each test were determined using information in *MASH* Table 2-7 and finite element computer simulation. Figure 7.1 shows the target CIP for *MASH* Tests 4-10 and 4-11 on the large-scupper portable concrete barrier. Figure 7.2 shows the target CIP for *MASH* Test 4-12 on the large-scupper portable concrete barrier.

Table 7.1. Test Conditions and Evaluation Criteria Specified for *MASH* TL-4 Longitudinal Barriers.

Test Designation	Test Vehicle	Impact Speed	Impact Angle	Evaluation Criteria
4-10	1100C	62 mi/h	25°	A, D, F, H, I
4-11	2270P	62 mi/h	25°	A, D, F, H, I
4-12	10000S	56 mi/h	15°	A, D, G

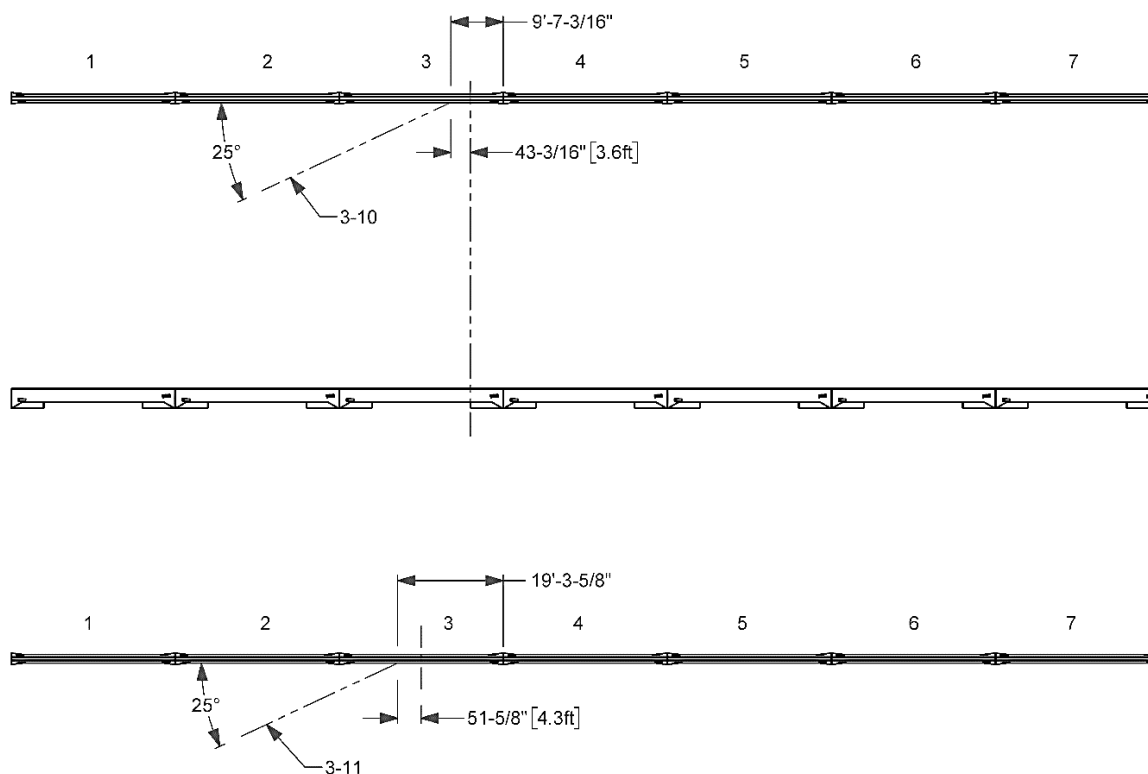


Figure 7.1. Target CIP for *MASH* 4-10 and 4-11 Tests on Large-Scupper Portable Concrete Barrier.

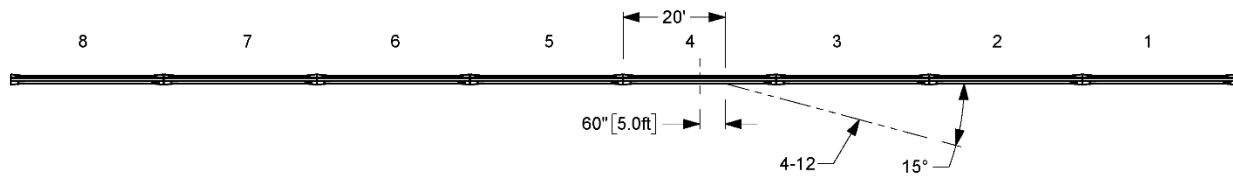


Figure 7.2. Target CIP for *MASH* 4-12 Test on Large-Scupper Portable Concrete Barrier.

The crash tests and data analysis procedures were in accordance with guidelines presented in *MASH*. Chapter 4 presents brief descriptions of these procedures.

7.2. EVALUATION CRITERIA

The appropriate safety evaluation criteria from Tables 2.2 and 5.1 of *MASH* were used to evaluate the crash tests reported herein. Table 7.1 lists the test conditions and evaluation criteria required for *MASH* TL-4, and Table 7.2 provides detailed information on the evaluation criteria.

Table 7.2. Evaluation Criteria Required for *MASH* Testing.

Evaluation Factors	Evaluation Criteria	<i>MASH</i> Test
A.	Test article should contain and redirect the vehicle or bring the vehicle to a controlled stop; the vehicle should not penetrate, underride, or override the installation, although controlled lateral deflection of the test article is acceptable.	10, 11, 12
D.	Detached elements, fragments, or other debris from the test article should not penetrate or show potential for penetrating the occupant compartment, or present undue hazard to other traffic, pedestrians, or personnel in a work zone. Deformations of, or intrusions into, the occupant compartment should not exceed limits set forth in Section 5.2.2 and Appendix E of <i>MASH</i> .	10, 11, 12
F.	The vehicle should remain upright during and after collision. The maximum roll and pitch angles are not to exceed 75 degrees.	10, 11
G.	It is preferable, although not essential, that the vehicle remain upright during and after the collision.	12
H.	Occupant impact velocities (OIV) should satisfy the following limits: Preferred value of 30 ft/s, or maximum allowable value of 40 ft/s. Occupant impact velocities (OIV) should satisfy the following limits: Preferred value of 10 ft/s, or maximum allowable value of 16 ft/s.	10, 11
I.	The occupant ridedown accelerations should satisfy the following: Preferred value of 15.0 g, or maximum allowable value of 20.49 g.	10, 11

Chapter 8. TEST CONDITIONS

8.1. TEST FACILITY

The full-scale crash tests reported herein were performed at the TTI Proving Ground, an International Standards Organization (ISO)/International Electrotechnical Commission (IEC) 17025-accredited laboratory with American Association for Laboratory Accreditation (A2LA) Mechanical Testing Certificate 2821.01. The full-scale crash tests were performed according to TTI Proving Ground quality procedures, as well as *MASH* guidelines and standards.

The test facilities of the TTI Proving Ground are located on The Texas A&M University System RELIS Campus, which consists of a 2000-acre complex of research and training facilities situated 10 mi northwest of the flagship campus of Texas A&M University. The site, formerly a United States Army Air Corps base, has large expanses of concrete runways and parking aprons well suited for experimental research and testing in the areas of vehicle performance and handling, vehicle-roadway interaction, highway pavement durability and efficacy, and roadside safety hardware and perimeter protective device evaluation. The site selected for testing was the surface of an out-of-service apron. The apron consists of an unreinforced jointed-concrete pavement in 12.5-ft × 15-ft blocks nominally 6 inches deep. The aprons were built in 1942, and the joints have some displacement but are otherwise flat and level.

8.2. VEHICLE TOW AND GUIDANCE SYSTEM

For the testing utilizing the 1100C, 2270P, and 10000S vehicles, each was towed into the test installation using a steel cable guidance and reverse tow system. A steel cable for guiding the test vehicle was tensioned along the path, anchored at each end, and threaded through an attachment to the front wheel of the test vehicle. An additional steel cable was connected to the test vehicle, passed around a pulley near the impact point and through a pulley on the tow vehicle, and then anchored to the ground such that the tow vehicle moved away from the test site. A 2:1 speed ratio between the test and tow vehicle existed with this system. Just prior to impact with the installation, the test vehicle was released and ran unrestrained. The vehicle remained freewheeling (i.e., no steering or braking inputs) until it cleared the immediate area of the test site.

8.3. DATA ACQUISITION SYSTEMS

8.3.1. Vehicle Instrumentation and Data Processing

Each test vehicle was instrumented with a self-contained onboard data acquisition system. The signal conditioning and acquisition system is a multi-channel data acquisition system (DAS) produced by Diversified Technical Systems Inc. The accelerometers, which measure the x, y, and z axis of vehicle acceleration, are strain gauge type with linear millivolt output proportional to acceleration. Angular rate sensors, measuring vehicle roll, pitch, and yaw rates, are ultra-small, solid-state units designed

for crash test service. The data acquisition hardware and software conform to the latest SAE J211, Instrumentation for Impact Test. Each of the channels is capable of providing precision amplification, scaling, and filtering based on transducer specifications and calibrations. During the test, data are recorded from each channel at a rate of 10,000 samples per second with a resolution of one part in 65,536. Once data are recorded, internal batteries back these up inside the unit in case the primary battery cable is severed. Initial contact of the pressure switch on the vehicle bumper provides a time zero mark and initiates the recording process. After each test, the data are downloaded from the DAS unit into a laptop computer at the test site. The TRAP software then processes the raw data to produce detailed reports of the test results.

Each DAS is returned to the factory annually for complete recalibration and to ensure that all instrumentation used in the vehicle conforms to the specifications outlined by SAE J211. All accelerometers are calibrated annually by means of an ENDEVCO® 2901 precision primary vibration standard. This standard and its support instruments are checked annually and receive a National Institute of Standards Technology (NIST) traceable calibration. The rate transducers used in the data acquisition system receive calibration via a Genisco Rate-of-Turn table. The subsystems of each data channel are also evaluated annually, using instruments with current NIST traceability, and the results are factored into the accuracy of the total data channel per SAE J211. Calibrations and evaluations are also made anytime data are suspect. Acceleration data are measured with an expanded uncertainty of ± 1.7 percent at a confidence factor of 95 percent ($k = 2$).

TRAP uses the DAS-captured data to compute the occupant/compartment impact velocities, time of occupant/compartment impact after vehicle impact, and highest 10-millisecond (ms) average ridedown acceleration. TRAP calculates change in vehicle velocity at the end of a given impulse period. In addition, maximum average accelerations over 50-ms intervals in each of the three directions are computed. For reporting purposes, the data from the vehicle-mounted accelerometers are filtered with an SAE Class 180-Hz low-pass digital filter, and acceleration versus time curves for the longitudinal, lateral, and vertical directions are plotted using TRAP.

TRAP uses the data from the yaw, pitch, and roll rate transducers to compute angular displacement in degrees at 0.0001-s intervals, and then plots yaw, pitch, and roll versus time. These displacements are in reference to the vehicle-fixed coordinate system with the initial position and orientation being initial impact. Rate of rotation data is measured with an expanded uncertainty of ± 0.7 percent at a confidence factor of 95 percent ($k = 2$).

8.3.2. Anthropomorphic Dummy Instrumentation

An Alderson Research Laboratories Hybrid II, 50th percentile male anthropomorphic dummy, restrained with lap and shoulder belts, was placed in the front seat on the impact side of the 1100C vehicle. The dummy was not instrumented.

According to *MASH*, use of a dummy in the 2270P vehicle is optional. However, *MASH* recommends that a dummy be used when testing “any longitudinal barrier with a height greater than or equal to 33 inches.” More specifically, use of the dummy in the

2270P vehicle is recommended for tall rails to evaluate the “potential for an occupant to extend out of the vehicle and come into direct contact with the test article.” Although this information is reported, it is not part of the impact performance evaluation. Since the rail height of the large-scurper portable concrete barrier was 42 inches, a dummy was placed in the front seat of the 2270P vehicle on the impact side and restrained with lap and shoulder belts.

MASH does not suggest using a dummy in a 10000S vehicle, and no dummy was used.

8.3.3. Photographic Instrumentation Data Processing

Photographic coverage of each test included three digital high-speed cameras:

- One located overhead with a field of view perpendicular to the ground and directly over the impact point.
- One placed upstream from the installation at an angle to have a field of view of the interaction of the rear of the vehicle with the installation.
- A third placed with a field of view parallel to and aligned with the installation at the downstream end.

A flashbulb on the impacting vehicle was activated by a pressure-sensitive tape switch to indicate the instant of contact with the large-scurper portable concrete barrier. The flashbulb was visible from each camera. The video files from these digital high-speed cameras were analyzed to observe phenomena occurring during the collision and to obtain time-event, displacement, and angular data. A digital camera recorded and documented conditions of each test vehicle and the installation before and after the test.

Chapter 9. *MASH* TEST 4-10 (TEST 440873-01-1)

9.1. TEST DESIGNATION AND ACTUAL IMPACT CONDITIONS

See Table 9.1 for details on the impact conditions and Table 9.2 for the exit parameters for Test 440873-01-1. Figure 9.1 and Figure 9.2 depict the target impact setup.

Table 9.1. Impact Conditions for *MASH* Test 4-10 (440873-01-1).

Test Parameter	Specification	Tolerance	Measured
Impact Speed (mi/h)	62	±2.5 mi/h	62.0
Impact Angle (deg)	25	±1.5°	25.1
Impact Severity (kip-ft)	51	≥51 kip-ft	56.6
Impact Location	9.6 ft upstream from the joint of barriers 3 and 4	±1 ft	9.2 ft upstream from the joint of barriers 3 and 4

Table 9.2. Exit Parameters for *MASH* Test 4-10 (440873-01-1).

Exit Parameter	Measured
Speed (mi/h)	42.3
Trajectory angle (deg)	5
Heading angle (deg)	10
Brakes applied post impact (s)	Brakes were not applied
Vehicle at rest position	217 ft downstream of impact point 105 ft to the field side 90° left
Comments:	Vehicle remained upright and stable. Vehicle did not cross the exit box. ^a

^a Not less than 32.8 ft downstream from loss of contact for cars and pickups is optimal.



Figure 9.1. Large-Scupper Portable Concrete Barrier/Test Vehicle Geometrics for Test 440873-01-1.



Figure 9.2. Large-Scupper Portable Concrete Barrier/Test Vehicle Impact Location for Test 440873-01-1.

9.2. WEATHER CONDITIONS

Table 9.3 provides the weather conditions for Test 440873-01-1.

Table 9.3. Weather Conditions for Test 440873-01-1.

Date of Test	2022-12-01
Wind Speed (mi/h)	3
Wind Direction (deg)	145
Temperature (°F)	51
Relative Humidity (%)	60
Vehicle Traveling (deg)	350

9.3. TEST VEHICLE

Figure 9.3 and Figure 9.4 show the 2017 Nissan Versa used for the crash test. Table 9.4 shows the vehicle measurements. Figure C.1 in Appendix C.1 gives additional dimensions and information on the vehicle.



Figure 9.3. Impact Side of Test Vehicle before Test 440873-01-1.



Figure 9.4. Opposite Impact Side of Test Vehicle before Test 440873-01-1.

Table 9.4. Vehicle Measurements for Test 440873-01-1.

Test Parameter	<i>MASH</i>	Allowed Tolerance	Measured
Dummy (if applicable) ^a (lb)	165	N/A	165
Test Inertial Weight (lb)	2420	±55	2448
Gross Static Weight ^a (lb)	2585	±55	2613
Wheelbase (inches)	98	±5	102.4
Front Overhang (inches)	35	±4	32.5
Overall Length (inches)	169	±8	175.4
Overall Width (inches)	65	±3	66.7
Hood Height (inches)	28	±4	30.5
Track Width ^b (inches)	59	±2	58.4
CG aft of Front Axle ^c (inches)	39	±4	41.4
CG above Ground ^{c,d} (inches)	N/A	N/A	N/A

Note: N/A = not applicable; CG = center of gravity.

^a If a dummy is used, the gross static vehicle mass should be increased by the mass of the dummy.

^b Average of front and rear axles.

^c For test inertial mass.

^d 2270P vehicle must meet minimum CG height requirement.

9.4. TEST DESCRIPTION

Table 9.5 lists events that occurred during Test 440873-01-1. Figures C.4 through C.6 in Appendix C.2 present sequential photographs during the test.

Table 9.5. Events during Test 440873-01-1.

Time (s)	Events
0.0000	Vehicle impacted installation
0.0430	Vehicle began to redirect
0.0660	Back right tire lifted off ground
0.0680	Segments 3 and 4 began to move toward field side
0.2340	Vehicle was parallel with installation
0.2870	Rear bumper of vehicle impacted installation
0.4430	Vehicle exited installation at 42.4 mi/h with a heading angle of 10 degrees and a trajectory angle of 5.4 degrees
1.0060	Vehicle made secondary contact with installation

9.5. DAMAGE TO TEST INSTALLATION

There was some scuffing and gouging at impact and spalling on the traffic side of barrier 4 at the joint between barriers 3 and 4. Additional scuffing resulted from the second and third impacts on the barrier. Table 9.6 describes the barrier movement at the joints of the large-scupper portable concrete barrier. Table 9.7 describes the damage to the large-scupper portable concrete barrier. Figure 9.5 and Figure 9.6 show the damage to the large-scupper portable concrete barrier.

Table 9.6. Movement of the Large-Scupper Portable Concrete Barrier at the Joints for Test 440873-01-1.

Barrier Joint	Barrier Joint Movement
2/3	0.25 inches f/s
3/4	9.5 inches f/s
4/5	1 inch f/s
5/6	1 inch f/s

Note: f/s = field side.

Table 9.7. Damage to Large-Scupper Portable Concrete Barrier for Test 440873-01-1.

Test Parameter	Measured
Permanent Deflection/Location	9.5 inches toward field side at joint between segments 3 and 4
Dynamic Deflection	10.2 inches toward field side at top of barrier at joint between segments 3 and 4
Working Width ^a and Height	33.5 inches, at a height of 0 inches, at the field side toe at joint between segments 3 and 4

^a Per *MASH*, "The working width is the maximum dynamic lateral position of any major part of the system or vehicle. These measurements are all relative to the pre-impact traffic face of the test article." In other words, working width is the total barrier width plus the maximum dynamic intrusion of any portion of the barrier or test vehicle past the field side edge of the barrier.



Figure 9.5. Large-Scupper Portable Concrete Barrier after Test at Impact Location for Test 440873-01-1.

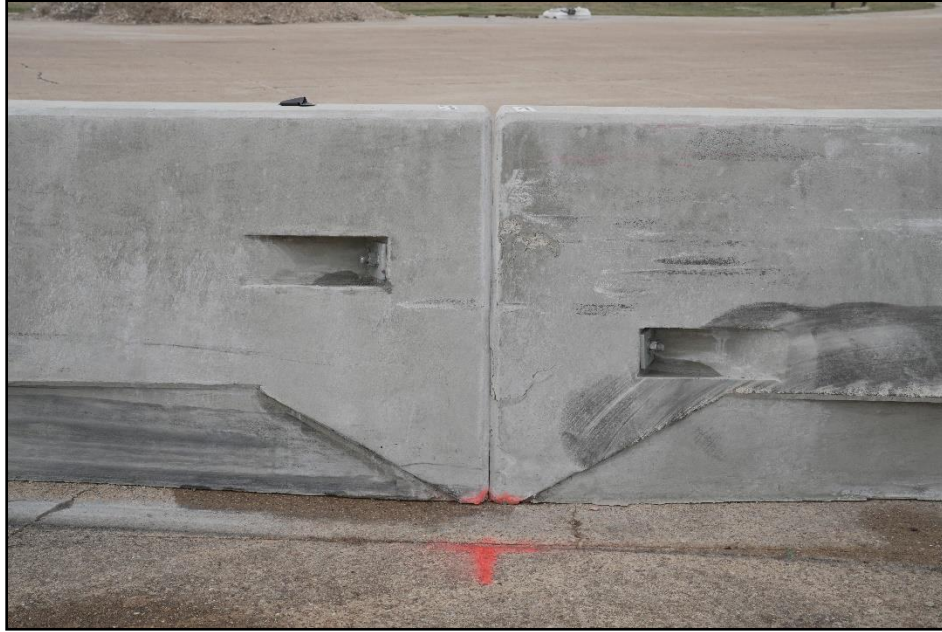


Figure 9.6. Large-Scupper Portable Concrete Barrier after Test at the Joint between Segments 3 and 4 for Test 440873-01-1.

9.6. DAMAGE TO TEST VEHICLE

Figure 9.7 and Figure 9.8 show the damage sustained by the vehicle. Figure 9.9 and Figure 9.10 show the interior of the test vehicle. Table 9.8 and Table 9.9 provide details on the occupant compartment deformation and exterior vehicle damage. Figures C.2 and C.3 in Appendix C.1 provide exterior crush and occupant compartment measurements.



Figure 9.7. Impact Side of Test Vehicle after Test 440873-01-1.



Figure 9.8. Rear Impact Side of Test Vehicle after Test 440873-01-1.



Figure 9.9. Overall Interior of Test Vehicle after Test 440873-01-1.



Figure 9.10. Interior of Test Vehicle on Impact Side after Test 440873-01-1.

Table 9.8. Occupant Compartment Deformation for Test 440873-01-1.

Test Parameter	Specification	Measured
Roof	≤4.0 inches	0 inches
Windshield	≤3.0 inches	0 inches
A and B Pillars	≤5.0 overall/≤3.0 inches lateral	0 inches
Foot Well/Toe Pan	≤9.0 inches	2.5 inches
Floor Pan/Transmission Tunnel	≤12.0 inches	0 inches
Side Front Panel	≤12.0 inches	2 inches
Front Door (above Seat)	≤9.0 inches	2 inches
Front Door (below Seat)	≤12.0 inches	0 inches

Table 9.9. Exterior Vehicle Damage for Test 440873-01-1.

Side Windows	Side windows remained intact
Maximum Exterior Deformation	10 inches in the front plane at the left front corner at bumper height
VDS	11LFQ4
CDC	11FLEW3
Fuel Tank Damage	None
Description of Damage to Vehicle:	The front bumper, hood, grill, right and left headlights, radiator and support, left front quarter fender, left front tire and rim, left front strut and tire, windshield, left front door, left front floor pan, left rear door, left rear quarter fender, left taillight, and rear bumper were damaged. The windshield had a 24-inch by 12-inch crack caused by the hood, but there was no hole or tearing in the lining. The left front door had a 5-inch gap at the top.

9.7. OCCUPANT RISK FACTORS

Data from the accelerometers were digitized for evaluation of occupant risk, and the results are shown in Table 9.10. Figure C.7 in Appendix C.3 shows the vehicle angular displacements, and Figures C.8 through C.10 in Appendix C.4 show acceleration versus time traces.

Table 9.10. Occupant Risk Factors for Test 440873-01-1.

Test Parameter	<i>MASH</i>	Measured	Time
OIV, Longitudinal (ft/s)	≤ 40.0 <i>30.0^a</i>	29.8	0.0809 seconds on left side of interior
OIV, Lateral (ft/s)	≤ 40.0 <i>30.0</i>	28.9	0.0809 seconds on left side of interior
Ridedown, Longitudinal (g)	≤ 20.49 <i>15.0</i>	6.1	1.0838–1.0938 seconds
Ridedown, Lateral (g)	≤ 20.49 <i>15.0</i>	8.8	1.0871–1.0971 seconds
Theoretical Head Impact Velocity (THIV) (m/s)	N/A	12.8	0.0790 seconds on left side of interior
Acceleration Severity Index (ASI)	N/A	2.7	0.0503–0.1003 seconds
50-ms Moving Avg. Accelerations (MA) Longitudinal (g)	N/A	–17.5	0.0250–0.0750 seconds
50-ms MA Lateral (g)	N/A	17.9	0.0237–0.0737 seconds
50-ms MA Vertical (g)	N/A	5.4	0.0025–0.0525 seconds
Roll (deg)	≤ 75	7	2.7693 seconds
Pitch (deg)	≤ 75	6	0.3699 seconds
Yaw (deg)	N/A	36	0.3314 seconds

^a Values in italics are the preferred *MASH* values.

9.8. TEST SUMMARY

Figure 9.11 summarizes the results of *MASH* Test 4-10 (Test 440873-01-1).





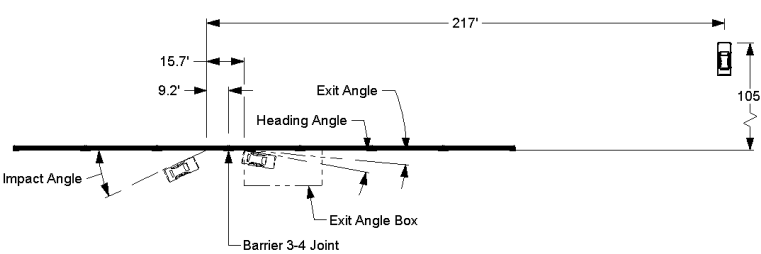
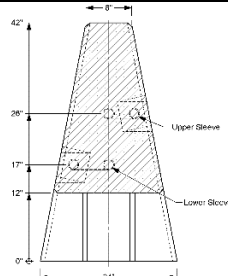
	Test Agency		Texas A&M Transportation Institute (TTI)					
	Test Standard/Test		MASH 2016 Test 4-10					
	TTI Project No.		440873-01-1					
	Test Date		2022-12-01					
	TEST ARTICLE							
	Type		Longitudinal Barrier					
	Name		Large-Scupper Portable Concrete Barrier					
	Length		210 ft					
Key Materials		30 ft large-scupper barriers with X-bolt connections x 7						
Soil Type and Condition		Concrete, damp						
TEST VEHICLE								
Type/Designation		1100C						
Year, Make and Model		2017 Nissan Versa						
Inertial Weight (lb)		2448						
Dummy (lb)		165						
Gross Static (lb)		2613						
IMPACT CONDITIONS								
Impact Speed (mi/h)		62.0						
Impact Angle (deg)		25.1						
Impact Location		9.2 ft upstream from the joint of barriers 3 and 4						
Impact Severity (kip-ft)		56.6						
EXIT CONDITIONS								
Exit Speed (mi/h)		42.3						
Trajectory/Heading Angle (deg)		5/10						
Exit Box Criteria		Vehicle did not cross						
Stopping Distance		217 ft downstream 105 ft to the field side						
TEST ARTICLE DEFLECTIONS								
Dynamic (inches)		10.2						
Permanent (inches)		9.5						
Working Width/Height (inches)		33.5/0						
VEHICLE DAMAGE								
VDS		11LFQ4						
CDC		11FLEW3						
Max. Ext. Deformation		10						
Max Occupant Compartment Deformation		2.5 inches in the toe pan						
OCCUPANT RISK VALUES								
Long. OIV (ft/s)	29.8	Long. Ridedown (g)	6.1	Max 50-ms Long. (g)	-17.5	Max Roll (deg)	7	
Lat. OIV (ft/s)	28.9	Lat. Ridedown (g)	8.8	Max 50-ms Lat. (g)	17.9	Max Pitch (deg)	6	
THIV (m/s)	12.8	ASI	2.7	Max 50-ms Vert. (g)	5.4	Max Yaw (deg)	36	
								

Figure 9.11. Summary of Results for *MASH* Test 4-10 on Large-Scupper Portable Concrete Barrier.

Chapter 10. *MASH* TEST 4-11 (TEST 440873-01-2)

10.1. TEST DESIGNATION AND ACTUAL IMPACT CONDITIONS

See Table 10.1 for details on the impact conditions and Table 10.2 for the exit parameters for Test 440873-01-2. Figure 10.1 and Figure 10.2 depict the target impact setup.

Table 10.1. Impact Conditions for *MASH* Test 4-11 (440873-01-2).

Test Parameter	Specification	Tolerance	Measured
Impact Speed (mi/h)	62 mi/h	±2.5 mi/h	61.7
Impact Angle (deg)	25°	±1.5°	26.5
Impact Severity (kip-ft)	106 kip-ft	≥106 kip-ft	127.5
Impact Location	19.3 ft upstream from the joint of barriers 3 and 4	±1 ft	19.5 ft upstream from the joint of barriers 3 and 4

Table 10.2. Exit Parameters for *MASH* Test 4-11 (440873-01-2).

Exit Parameter	Measured
Speed (mi/h)	42.1
Trajectory angle (deg)	5.2
Heading angle (deg)	11.2
Brakes applied post impact (s)	2.5
Vehicle at rest position	271 ft downstream of impact point 32 ft to the traffic side 0° downstream
Comments:	Vehicle remained upright and stable. Vehicle crossed exit box ^a 102 ft downstream from loss of contact.

^a Not less than 32.8 ft downstream from loss of contact for cars and pickups is optimal.



Figure 10.1. Large-Scupper Portable Concrete Barrier/Test Vehicle Geometrics for Test 440873-01-2.



Figure 10.2. Large-Scupper Portable Concrete Barrier/Test Vehicle Impact Location for Test 440873-01-2.

10.2. WEATHER CONDITIONS

Table 10.3 provides the weather conditions for Test 440873-01-2.

Table 10.3. Weather Conditions for Test 440873-01-2.

Date of Test	2022-12-13
Wind Speed (mi/h)	10
Wind Direction (deg)	173
Temperature (°F)	73
Relative Humidity (%)	95
Vehicle Traveling (deg)	350

10.3. TEST VEHICLE

Figure 10.3 and Figure 10.4 show the 2017 RAM 1500 used for the crash test. Table 10.4 shows the vehicle measurements. Figure D.1 in Appendix D.1 gives additional dimensions and information on the vehicle.



Figure 10.3. Impact Side of Test Vehicle before Test 440873-01-2.



Figure 10.4. Opposite Impact Side of Test Vehicle before Test 440873-01-2.

Table 10.4. Vehicle Measurements for Test 440873-01-2.

Test Parameter	<i>MASH</i>	Allowed Tolerance	Measured
Dummy (if applicable) ^a (lb)	165	N/A	165
Test Inertial Weight (lb)	5000	±110	5031
Gross Static Weight ^a (lb)	5165	±110	5196
Wheelbase (inches)	148	±12	140.5
Front Overhang (inches)	39	±3	40
Overall Length (inches)	237	±13	227.5
Overall Width (inches)	78	±2	78.5
Hood Height (inches)	43	±4	46
Track Width ^b (inches)	67	±1.5	68.25
CG aft of Front Axle ^c (inches)	63	±4	61.9
CG above Ground ^{c,d} (inches)	28	≥28	28.75

Note: N/A = not applicable; CG = center of gravity.

^a If a dummy is used, the gross static vehicle mass should be increased by the mass of the dummy.

^b Average of front and rear axles.

^c For test inertial mass.

^d 2270P vehicle must meet minimum CG height requirement.

10.4. TEST DESCRIPTION

Table 10.5 lists events that occurred during Test 440873-01-2. Figures D.4 through D.6 in Appendix D.2 present sequential photographs during the test.

Table 10.5. Events during Test 440873-01-2.

Time (s)	Events
0.0000	Vehicle impacted installation
0.0290	Segment 3 began to flex toward field side
0.0390	Vehicle began to redirect
0.0790	Segments 2, 3, and 4 began to slide toward field side
0.0800	Front passenger-side tire began to lift off pavement
0.2190	Vehicle was parallel with installation
0.2350	Rear bumper of vehicle impacted installation
0.5190	Vehicle exited installation at 42.1 mi/h with a heading angle of 11.2 degrees and a trajectory angle of 5.2 degrees
0.6160	Front passenger-side tire contacted pavement

10.5. DAMAGE TO TEST INSTALLATION

There were multiple cracks on the field side of segment 3, and the barrier was also bent. Minor gouging occurred on the traffic side of the barriers at impact, and there was significant spalling on the field side downstream end of segment 3.

Table 10.6 describes the barrier movement at the joints of the large-scupper portable concrete barrier. Table 10.7 describes the damage to the large-scupper portable concrete barrier. Figure 10.5 and Figure 10.6 show the damage to the large-scupper portable concrete barrier.

Table 10.6. Movement of the Large-Scupper Portable Concrete Barrier at the Joints for Test 440873-01-2.

Barrier Joint	Barrier Joint Movement
Upstream end of 1	2 inches t/s
1/2	1.5 inches t/s
2/3	13.5 inches f/s
3/4	15.5 inches f/s
4/5	0.5 inches f/s

Note: f/s = field side; t/s = traffic side.

Table 10.7. Deflection of the Large-Scupper Portable Concrete Barrier for Test 440873-01-2.

Test Parameter	Measured
Permanent Deflection/Location	15.5 inches toward field side at the joint between segments 3 and 4
Dynamic Deflection	22.2 inches toward field side at the top of segment 3 near midspan
Working Width ^a and Height	36.7 inches, at a height of 42 inches, on the field side at the top of segment 3 near midspan

^a Per *MASH*, "The working width is the maximum dynamic lateral position of any major part of the system or vehicle. These measurements are all relative to the pre-impact traffic face of the test article." In other words, working width is the total barrier width plus the maximum dynamic intrusion of any portion of the barrier or test vehicle past the field side edge of the barrier.



Figure 10.5. Large-Scupper Portable Concrete Barrier after Test at Impact Location for Test 440873-01-2.



Figure 10.6. Large-Scupper Portable Concrete Barrier at the Joint of Barriers 3 and 4 after Test 440873-01-2.

10.6. DAMAGE TO TEST VEHICLE

Figure 10.7 and Figure 10.8 show the damage sustained by the vehicle. Figure 10.9 and Figure 10.10 show the interior of the test vehicle. Table 10.8 and Table 10.9 provide details on the occupant compartment deformation and exterior vehicle damage. Figures D.2 and D.3 in Appendix D.1 provide exterior crush and occupant compartment measurements.



Figure 10.7. Impact Side of Test Vehicle after Test 440873-01-2.



Figure 10.8. Rear Impact Side of Test Vehicle after Test 440873-01-2.



Figure 10.9. Overall Interior of Test Vehicle after Test 440873-01-2.



Figure 10.10. Interior of Test Vehicle on Impact Side after Test 440873-01-2.

Table 10.8. Occupant Compartment Deformation for Test 440873-01-2.

Test Parameter	Specification	Measured
Roof	≤ 4.0 inches	0 inches
Windshield	≤ 3.0 inches	0 inches
A and B Pillars	≤ 5.0 overall/ ≤ 3.0 inches lateral	0 inches
Foot Well/Toe Pan	≤ 9.0 inches	0 inches
Floor Pan/Transmission Tunnel	≤ 12.0 inches	0 inches
Side Front Panel	≤ 12.0 inches	0 inches
Front Door (above Seat)	≤ 9.0 inches	0 inches
Front Door (below Seat)	≤ 12.0 inches	0 inches

Table 10.9. Exterior Vehicle Damage for Test 440873-01-2.

Side Windows	The side windows remained intact
Maximum Exterior Deformation	12 inches in the front plane at the left front corner at bumper height
VDS	11LFQ4
CDC	11FLEW3
Fuel Tank Damage	None
Description of Damage to Vehicle:	The front bumper, hood, grill, left headlight, radiator and support, left front quarter fender, left front lower control arm, left front door, left rear door, left cab corner, left rear quarter fender, left rear rim, left taillight, and rear bumper were damaged from the initial impact. The right side of the front bumper, right headlight, right edge of the hood, and windshield were damaged after the second impact with the installation. The windshield was cracked due to flexing of the body, but there was no deformation and no holes or tears in the laminate.

10.7. OCCUPANT RISK FACTORS

Data from the accelerometers were digitized for evaluation of occupant risk, and the results are shown in Table 10.10. Figure D.7 in Appendix D.3 shows the vehicle angular displacements, and Figures D.8 through D.10 in Appendix D.4 show acceleration versus time traces.

Table 10.10. Occupant Risk Factors for Test 440873-01-2.

Test Parameter	<i>MASH</i>	Measured	Time
OIV, Longitudinal (ft/s)	≤ 40.0 <i>30.0^a</i>	16.7	0.1044 seconds on left side of interior
OIV, Lateral (ft/s)	≤ 40.0 <i>30.0</i>	18.8	0.1044 seconds on left side of interior
Ridedown, Longitudinal (g)	≤ 20.49 <i>15.0</i>	3.4	0.2419–0.2519 seconds
Ridedown, Lateral (g)	≤ 20.49 <i>15.0</i>	9.3	0.2411–0.2511 seconds
THIV (m/s)	N/A	7.6	0.1004 seconds on left side of interior
ASI	N/A	1.4	0.0501–0.1001 seconds
50-ms MA Longitudinal (g)	N/A	–8.1	0.0280–0.0780 seconds
50-ms MA Lateral (g)	N/A	10.7	0.0288–0.0788 seconds
50-ms MA Vertical (g)	N/A	3.5	0.2387–0.2887 seconds
Roll (deg)	≤ 75	12	0.5364 seconds
Pitch (deg)	≤ 75	6	0.5513 seconds
Yaw (deg)	N/A	36	0.5056 seconds

^a Values in italics are the preferred *MASH* values.

10.8. TEST SUMMARY

Figure 10.11 summarizes the results of *MASH* Test 4-11 (440873-01-2).





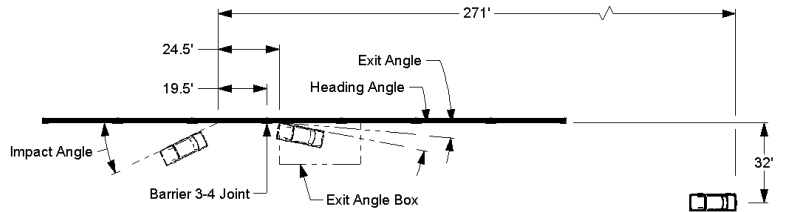
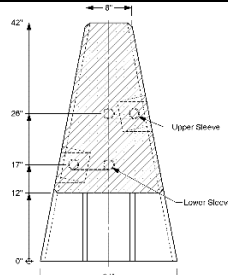
	Test Agency		Texas A&M Transportation Institute (TTI)					
	Test Standard/Test		MASH 2016, Test 4-11					
	TTI Project No.		440873-01-2					
	Test Date		2022-12-13					
	TEST ARTICLE							
	Type	Longitudinal Barrier						
	Name	Large-Scupper Portable Concrete Barrier						
	Length	210 ft						
	Key Materials	30 ft large-scupper barriers with X-bolt connections x 7						
	Soil Type and Condition	Concrete, damp						
	TEST VEHICLE							
	Type/Designation	2270P						
	Year, Make and Model	2017 RAM 1500						
	Inertial Weight (lb)	5031						
	Dummy (lb)	165						
	Gross Static (lb)	5196						
	IMPACT CONDITIONS							
	Impact Speed (mi/h)	61.7						
	Impact Angle (deg)	26.5						
	Impact Location	19.5 ft upstream from the joint of barriers 3 and 4						
	Impact Severity (kip-ft)	127.5						
	EXIT CONDITIONS							
	Exit Speed (mi/h)	42.1						
	Trajectory/Heading Angle (deg)	5.2/11.2						
	Exit Box Criteria	The vehicle crossed the exit box						
	Stopping Distance	271 ft downstream 32 ft to the traffic side						
	TEST ARTICLE DEFLECTIONS							
	Dynamic (inches)	22.2						
	Permanent (inches)	15.5						
	Working Width/Height (inches)	36.7/42						
	VEHICLE DAMAGE							
	VDS	11LFQ4						
	CDC	11FLEW3						
	Max. Ext. Deformation	12						
	Max Occupant Compartment Deformation	No occupant compartment deformation						
	OCCUPANT RISK VALUES							
Long. OIV (ft/s)	16.7	Long. Ridedown (g)	3.4	Max 50-ms Long. (g)	-8.1	Max Roll (deg)	12	
Lat. OIV (ft/s)	18.8	Lat. Ridedown (g)	9.3	Max 50-ms Lat. (g)	10.7	Max Pitch (deg)	6	
THIV (m/s)	7.6	ASI	1.4	Max 50-ms Vert. (g)	3.5	Max Yaw (deg)	36	
								

Figure 10.11. Summary of Results for *MASH* Test 4-11 on Large-Scupper Portable Concrete Barrier.

Chapter 11. *MASH* TEST 4-12 (TEST 440873-01-3)

11.1. TEST DESIGNATION AND ACTUAL IMPACT CONDITIONS

See Table 11.1 for details on the impact conditions and Table 11.2 for the exit parameters for Test 440873-01-3. Figure 11.1 and Figure 11.2 depict the target impact setup.

Table 11.1. Impact Conditions for *MASH* Test 4-12 (440873-01-3).

Test Parameter	Specification	Tolerance	Measured
Impact Speed (mi/h)	56	±2.5 mi/h	56.1
Impact Angle (deg)	15	±1.5°	14.9
Impact Severity (kip-ft)	106	≥106 kip-ft	154.1
Impact Location	240 inches upstream from the centerline of the joint between barriers 4 and 5	±12 inches	239 inches upstream from the centerline of the joint between barriers 4 and 5

Table 11.2. Exit Parameters for *MASH* Test 4-12 (440873-01-3).

Exit Parameter	Measured
Speed (mi/h)	Not measurable, out of frame
Trajectory (deg)	Not measurable, out of frame
Heading (deg)	Not measurable, out of frame
Brakes applied post impact (s)	2.8
Vehicle at rest position	308 ft downstream of impact point 50 ft to the traffic side 110° left
Comments:	Vehicle remained upright and stable



Figure 11.1. Large-Scupper Portable Concrete Barrier/Test Vehicle Geometrics for Test 440873-01-3.



Figure 11.2. Large-Scupper Portable Concrete Barrier/Test Vehicle Impact Location for Test 440873-01-3.

11.2. WEATHER CONDITIONS

Table 11.3 provides the weather conditions for Test 440873-01-3.

Table 11.3. Weather Conditions for Test 440873-01-3.

Date of Test	2023-08-17
Wind Speed (mi/h)	6
Wind Direction (deg)	174
Temperature (°F)	92
Relative Humidity (%)	54
Vehicle Traveling (deg)	350

11.3. TEST VEHICLE

Figure 11.3 and Figure 11.4 show the 2013 Hino L Series used for the crash test. Table 11.4 shows the vehicle measurements. Figure E.1 in Appendix E.1 gives additional dimensions and information on the vehicle.



Figure 11.3. Impact Side of Test Vehicle before Test 440873-01-3.



Figure 11.4. Opposite Impact Side of Test Vehicle before Test 440873-01-3.

Table 11.4. Vehicle Measurements for Test 440873-01-3.

Test Parameter	Specification	Tolerance	Measured
Dummy (if applicable) ^a (lb)	165	N/A	N/A
Curb Weight (lb)	13,200	±2200 lb	13,490
Test Inertial Weight (lb)	22,046	±660 lb	22,150
Wheelbase (inches)	240	≤240 inches	205.0
Overall Length (inches)	394	≤394 inches	333.0
Cargo Bed Height (inches) ^b	49	±2 inches	51.0
CG of Ballast above Ground ^c (inches)	63	±2 inches	64.5

Note: N/A = not applicable; CG = center of gravity.

^a If a dummy is used, the gross static vehicle mass should be increased by the mass of the dummy.

^b Without ballast.

^c See Section 4.2.1.2 in *MASH* 2016 for recommended ballasting procedures.

11.4. TEST DESCRIPTION

Table 11.5 lists events that occurred during Test 440873-01-3. Figures E.2, E.3, and E.4 in Appendix E.2 present sequential photographs during the test.

Table 11.5. Events during Test 440873-01-3.

Time (s)	Events
0.0000	Vehicle impacted installation
0.0030	Segment 4 began to flex toward field side
0.0400	Vehicle began to redirect
0.0800	Segments 3, 4, and 5 began to slide toward the field side
0.1070	Concrete on field side of barriers at joint between segments 4 and 5 began to spall
0.2840	Vehicle was parallel with installation
0.3180	Rear passenger-side bumper of vehicle impacted installation
1.4080	Vehicle lost contact with barrier

11.5. DAMAGE TO TEST INSTALLATION

Barrier 2 had spalling on the traffic-side downstream end. Barrier 3 had minor concrete damage on the field-side upstream end and on the traffic-side downstream end. Barrier 4 had scuffing and gouging with spalling and exposed rebar in multiple places. It was bowed 3.5 inches toward the field side, and there were multiple vertical cracks on the field side. Barrier 5 had some major spalling on the upstream end, with exposed rebar on the field side and minor damage on the traffic side. Barrier 6 had spalling on the field side at both ends, and Barrier 7 had spalling with exposed rebar on the upstream field side. Table 11.6 describes the barrier movement at the joints of the large-scupper portable concrete barrier. Table 11.7 describes the deflection and working width of the large-scupper portable concrete barrier. Figure 11.5 and Figure 11.6 show the damage to the large-scupper portable concrete barrier.

Table 11.6. Movement of the Large-Scupper Portable Concrete Barrier at the Joints for Test 440873-01-3.

Barrier Joint	Barrier Joint Movement
Upstream end of 1	1 inch d/s
1/2	1 inch d/s; 0.5 inch f/s
2/3	1.5 inch t/s; 1.5 inch d/s
3/4	27 inches f/s; 2 inches d/s
4/5	40 inches f/s
5/6	3 inches f/s
6/7	3 inches t/s

Note: d/s = downstream; f/s = field side; t/s = traffic side.

Table 11.7. Deflection and Working Width of the Large-Scupper Portable Concrete Barrier for Test 440873-01-3.

Test Parameter	Measured
Permanent Deflection/Location	40 inches toward field side at joint between segments 4 and 5
Dynamic Deflection	44.3 inches toward field side at the top of barrier 4 at the joint between segments 4 and 5
Working Width ^a and Height	94.2 inches, at a height of 128.9 inches, at the top rear passenger-side corner of the truck box

^a Per *MASH*, "The working width is the maximum dynamic lateral position of any major part of the system or vehicle. These measurements are all relative to the pre-impact traffic face of the test article." In other words, working width is the total barrier width plus the maximum dynamic intrusion of any portion of the barrier or test vehicle past the field side edge of the barrier.



Figure 11.5. Large-Scupper Portable Concrete Barrier at Impact Location after Test 440873-01-3.



Figure 11.6. Large-Scupper Portable Concrete Barrier at the Field Side after Test 440873-01-3.

11.6. DAMAGE TO TEST VEHICLE

Figure 11.7 and Figure 11.8 show the damage sustained by the vehicle. Figure 11.9 and Figure 11.10 show the interior of the test vehicle. Table 11.8 and Table 11.9 provide details on the occupant compartment deformation and exterior vehicle damage.



Figure 11.7. Impact Side of Test Vehicle after Test 440873-01-3.



Figure 11.8. Rear Impact Side of Test Vehicle after Test 440873-01-3.



Figure 11.9. Overall Interior of Test Vehicle after Test 440873-01-3.



Figure 11.10. Interior of Test Vehicle on Impact Side after Test 440873-01-3.

Table 11.8. Occupant Compartment Deformation for Test 440873-01-3.

Test Parameter	Specification	Measured
Roof	≤4.0 inches	0.0 inches
Windshield	≤3.0 inches	N/A
A and B Pillars	≤5.0 overall/≤3.0 inches lateral	0.0 inches
Foot Well/Toe Pan	≤9.0 inches	0.0 inches
Floor Pan/Transmission Tunnel	≤12.0 inches	0.0 inches
Side Front Panel	≤12.0 inches	0.0 inches
Front Door (above Seat)	≤9.0 inches	0.0 inches
Front Door (below Seat)	≤12.0 inches	0.0 inches

Note: N/A = not applicable.

Table 11.9. Exterior Vehicle Damage for Test 440873-01-3.

Side Windows	The side windows remained intact
Maximum Exterior Deformation	13 inches in the front plane at right side at bumper height
VDS	01RFQ2
CDC	01FREW1
Fuel Tank Damage	None
Description of Damage to Vehicle:	The windshield, right fender, front bumper, right front shock, right front wheel, def tank, and right side of the box were damaged. The windshield popped out of place and fell off the vehicle. This was due to flexing of the cab and not penetration of the test article.

11.7. OCCUPANT RISK FACTORS

Data from the accelerometers were digitized for information purposes, and the results are shown in Table 11.10. Figure E.5 in Appendix E.3 shows the vehicle angular displacements, and Figures E.6 through E.8 in Appendix E.4 show acceleration versus time traces.

Table 11.10. Occupant Risk Factors for Test 440873-01-3.

Test Parameter	Measured	Time
OIV, Longitudinal (ft/s)	6.8	0.2252 seconds on right side of interior
OIV, Lateral (ft/s)	9.4	0.2252 seconds on right side of interior
Ridedown, Longitudinal (g)	1.8	0.6398–0.6498 seconds
Ridedown, Lateral (g)	6.5	0.3963–0.4063 seconds
THIV (m/s)	3.6	0.2153 seconds on right side of interior
ASI	0.4	0.3712–0.4212 seconds
50-ms MA Longitudinal (g)	–2.0	0.0400–0.0900 seconds
50-ms MA Lateral (g)	–4.1	0.3555–0.4055 seconds
50-ms MA Vertical (g)	–2.5	1.5754–1.6254 seconds
Roll (deg)	29.2	0.7296 seconds
Pitch (deg)	5.6	0.6903 seconds
Yaw (deg)	24.1	2.4986 seconds

11.8. TEST SUMMARY

Figure 11.11 summarizes the results of *MASH* Test 4-12 (440873-01-3).

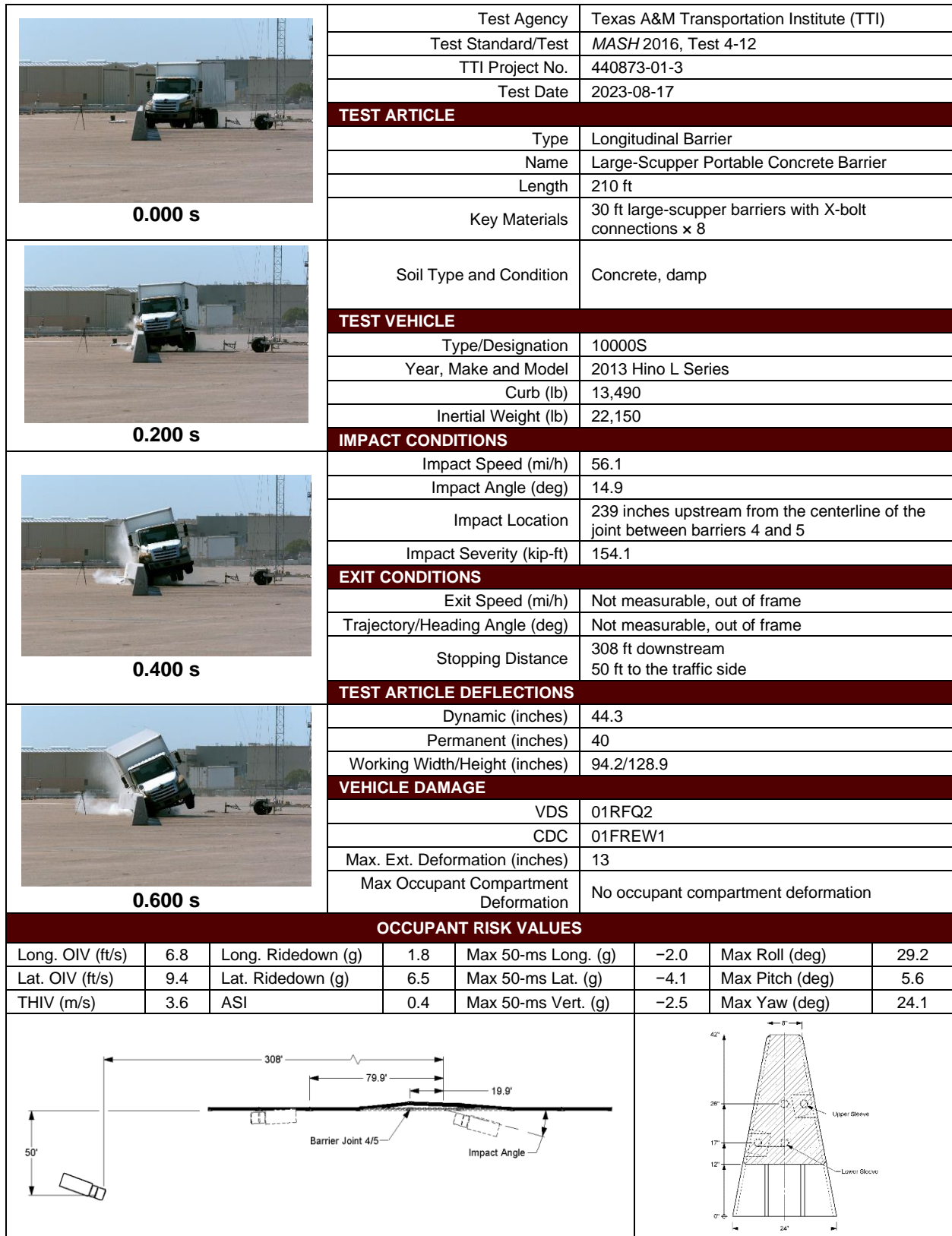


Figure 11.11. Summary of Results for *MASH* Test 4-12 on Large-Scupper Portable Concrete Barrier.

Chapter 12. CRASH TEST SUMMARY AND CONCLUSIONS

12.1. ASSESSMENT OF TEST RESULTS

The crash tests reported herein on the large-scupper portable concrete barrier were performed in accordance with *MASH* TL-4. The *MASH* matrix for longitudinal barriers consists of three tests, and all tests were performed.

12.2. CONCLUSIONS

Table 12.1 shows that the large-scupper portable concrete barrier met the performance criteria for *MASH* TL-4 longitudinal barriers.

Table 12.1. Assessment Summary for *MASH* TL-4 Tests on Large-Scupper Portable Concrete Barrier.

Evaluation Criteria	Description ^a	Test 440873-01-1 (Test 4-10)	Test 440873-01-2 (Test 4-11)	Test 440873-01-3 (Test 4-12)
A	Contain, Redirect, or Controlled Stop	S	S	S
D	No Penetration into Occupant Compartment	S	S	S
F	Roll and Pitch Limit	S	S	N/A
G	Rolling Is Acceptable	N/A	N/A	S
H	OIV Threshold	S	S	N/A
I	Ridedown Threshold	S	S	N/A
Overall	Evaluation	Pass	Pass	Pass

Note: S = satisfactory; N/A = not applicable.

^a See Table 7.2 for details.

Chapter 13. IMPLEMENTATION

The single-slope precast concrete barrier with large scupper is designed to mitigate roadway flooding and damming effects that can occur with solid-profile concrete barrier systems. The barrier is a modified version of the TxDOT Type 1, precast, 42-inch-tall SSCB. The hydraulically efficient barrier can be implemented in both temporary and permanent applications as needed to help alleviate the consequences of severe flooding.

The single-slope portable concrete barrier with large scupper was determined to be *MASH* TL-4 compliant. The full matrix of crash tests, including test designations 4-10 (passenger car), 4-11 (pickup truck), and 4-12 (single-unit truck), was successfully performed. Implementation of the hydraulically efficient precast barrier can be achieved by the TxDOT Design Division through development of standard sheets based on the detailed drawings for the barrier system provided in Appendix A.

An estimate of the value of research (VoR) associated with the implementation of this hydraulically efficient precast concrete barrier is provided in Appendix F. The benefit areas used in this assessment include both economic and safety-based factors.

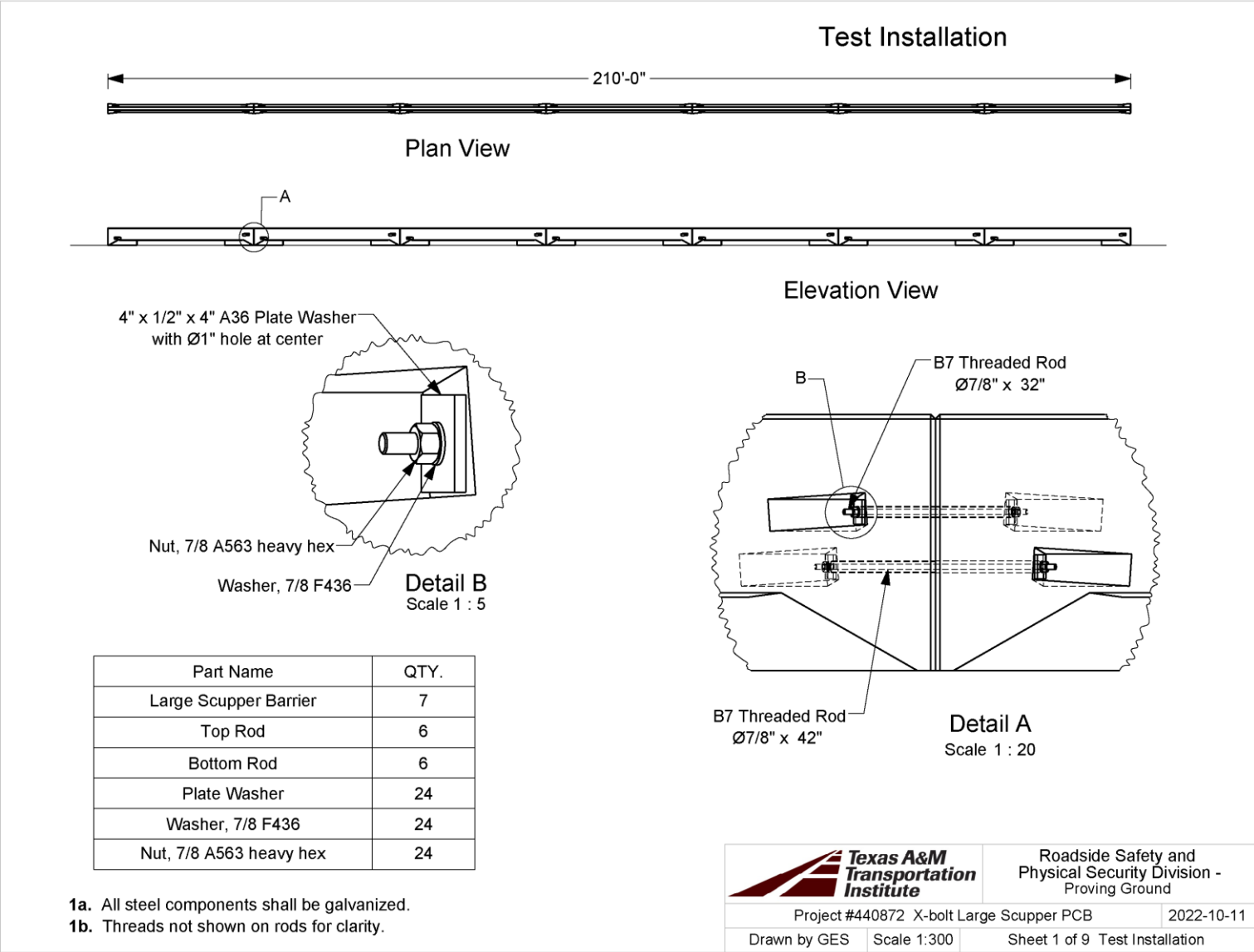
REFERENCES

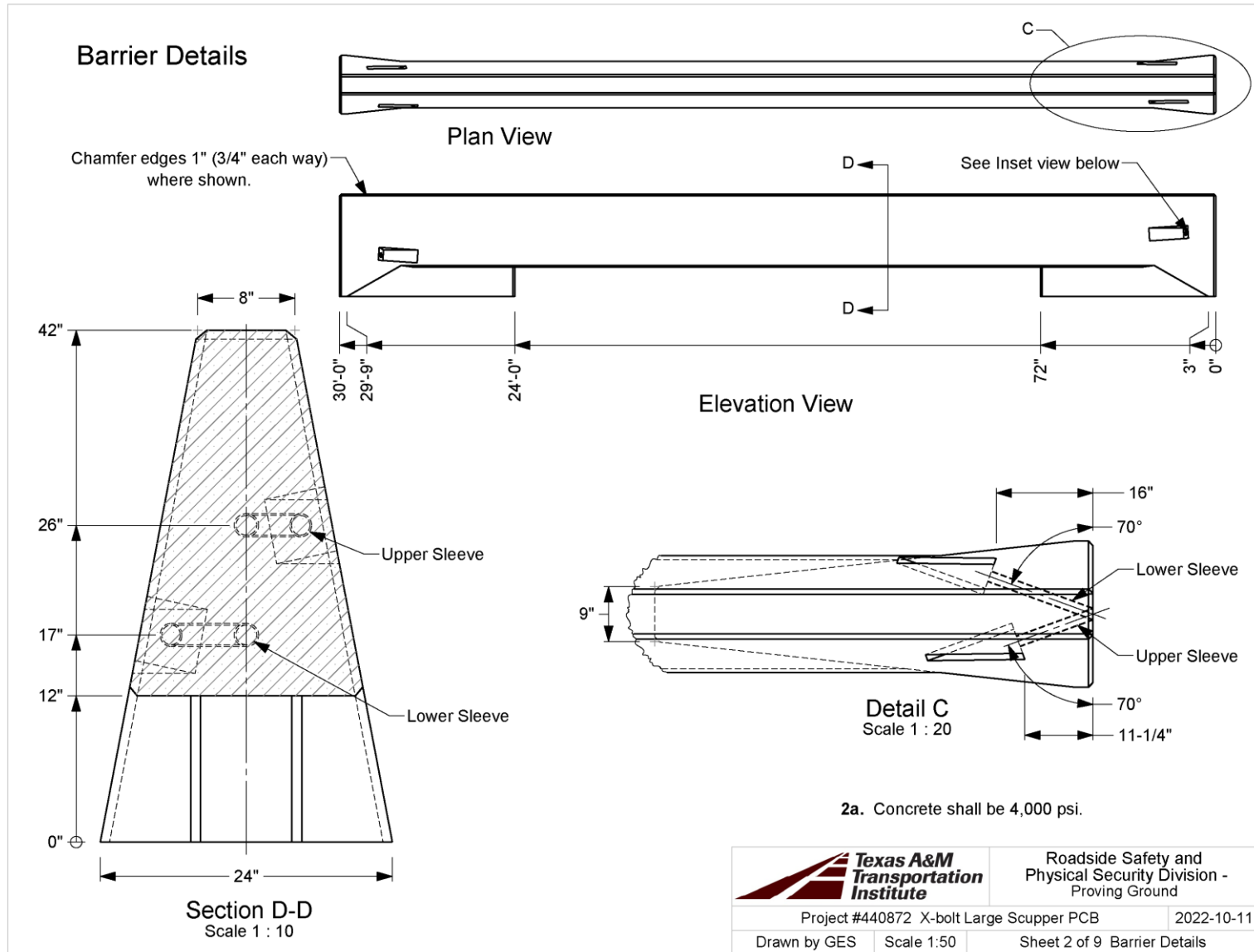
1. American Association of State Highway and Transportation Officials. (2016). *Manual for Assessing Roadside Safety Hardware*, Second Edition. AASHTO.
2. Beaumont Enterprise. (2017, September 1). "An Island."
3. Kinchen, H. (2017). "Median wall caused flooding in Livingston and EBR parishes, cities claim in class-action suit against DOTD."
https://www.theadvocate.com/baton_rouge/news/courts/article_895ea4b6-d38d-11e6-a75e-e70090be9b62.html. Retrieved November 12, 2018.
4. ABC13 Eyewitness News. "Floodwaters wreck concrete median on Texas interstate." <https://abc13.com/weather/floodwaters-wreck-concrete-median-on-texas-interstate/2359907/>. Retrieved November 12, 2018.
5. KJ Productions. (2017). "Freeway concrete barrier broke away." YouTube.
<https://www.youtube.com/watch?v=SZ58UxBB88w>. Retrieved November 12, 2018.
6. FHWA. (1992). Federal-Aid Policy Guide 23 CFR § 650.105.
<https://www.fhwa.dot.gov/legregs/directives/fapg/cfr0650a.htm>. Retrieved November 27, 2018.
7. Texas Department of Transportation. (2016). *Hydraulic Design Manual*. TxDOT.
8. Chow, V.T. (1959). *Open-Channel Hydraulics*. McGraw-Hill.
9. Charbeneau, R., Klenzendorf, J., & Barrett, M. (2008). *Hydraulic Performance of Bridge Rails* (Report No. FHWA/TX-08/0-5492-1). TxDOT.
10. Bin-Shafique, S., Barrett, M., Sharif, H., Charbeneau, R., Ali, K., & Hudson, C. (2011). *Mitigation Methods for Temporary Concrete Traffic Barrier Effects on Flood Water Flows* (Report No. FHWA/TX-11/0-6094-1). TxDOT.
11. Mays, L. (2011). *Water Resources Engineering*. John Wiley & Sons.
12. Crowe, C., Elger, D., & Roberson, J. (2005). *Engineering Fluid Mechanics* (8th ed.). John Wiley & Sons.
13. Warnock, J. (1950). Hydraulic similitude. In H. Rouse (Ed.), *Engineering Hydraulics*. John Wiley & Sons.
14. Charbeneau, R., Henderson, A., & Sherman, L. (2006). Hydraulic performance curves for highway culverts. *Journal of Hydraulic Engineering*, 132(5), 474–481.
15. Hendrickson, G. (2020). *Hydraulic analysis of highway median barriers for flood-prone areas* (master's thesis). The University of Texas at Austin.
16. King, H., & Brater, E. (1963). *Handbook of Hydraulics* (5th ed.). McGraw-Hill.
17. Bos, M. (1989). *Discharge Measurement Structures* (3rd ed., Vol. 20). International Institute for Land Reclamation and Improvement.
18. Klenzendorf, J. B., & Charbeneau, R. J. (2009). Bridge rail rating curves and submergence characteristics. *Journal of Hydraulic Engineering*, 135(2), 88–95.
19. Akiba, M., Morooka, S., Shirakawa, K., & Chuman, K. (2001). Experimental study on improvement of inlet orifice in BWR Core. *Journal of Nuclear Science and Technology*, 38(9), 793–798.
20. Coduto, D. (2001). *Foundation Design: Principles and Practices* (2nd ed.). Prentice Hall.
21. Hibbeler, R. (2008). *Mechanics of Materials* (7th ed.). Prentice Hall.
22. Ferziger, J., Perić, M., Street, R. (2020). *Computational Methods for Fluid Mechanics* (4th ed.) Springer Nature Switzerland.

23. Williams, W.F., Sheikh, N., & Menges, W.L. (2010). *MASH Test 3-11 of the WsDOT Pin and Loop Concrete Barrier with Drainage Slots* (TM 405160-18-1). Texas A&M Transportation Institute.
24. Williams, W.F., & Menges, W.L. (2012). *Washington State Department of Transportation Pin and Loop Barrier with Drainage Slots* (TM 405160-30-1). Texas A&M Transportation Institute.
25. Williams, W.F., & Menges, W.L. (2010). *F-shape Concrete Barrier with Slotted Drain Holes* (Report No. 405160-19). Texas A&M Transportation Institute.
26. Abu-Odeh, A., et al. (2018). *Development and MASH TL-4 Evaluation of Rubber Mounted Single-Slope Barrier* (Report No. 468958). Texas A&M Transportation Institute.
27. Dobrovolny, C.S., Bligh, R.P., & Menges, W.L. (2017). *MASH Testing and Evaluation of the MassDOT Portable Concrete Barrier* (Report No. 605611-03-F). Texas A&M Transportation Institute.
28. Sheikh, N.M., Moran, S.M., Menges, W.L., Griffith, B.L., & Kuhn, D.L. (2020). *MASH Evaluation of F-shape and Single-Slope Concrete Barrier with Drainage Scuppers* (Report No. 0-612831-01). Texas A&M Transportation Institute.
29. Dobrovolny, C.S., Kovar, J.C., Bligh, R.P., Johnson, B.A., Barrett, M.E., Klenzendorf, B., Hendrickson, G., Menges, W.L., Schroeder, W., & Kuhn, D.L. (2020). *Development and MASH TL-4 Evaluation of TxDOT Large-Scupper Median Barrier for Flood-Prone Areas* (Report No. 0-6976-R1). Texas A&M Transportation Institute.
30. Benson, K.S. (2004). *Hydraulic Effects of Safety End Treatments on Culvert Performance*, M.S. Thesis in Engineering, The University of Texas at Austin.
31. Nortek USA. (Undated). *Vectrino 3D Water Velocity Sensor Lab Probe*. <https://www.environmental-expert.com/downloads/vectrino-3d-water-velocity-sensor-lab-probe-datasheet-834473>. Retrieved November 12, 2018.
32. Ansys. (Undated). LS-DYNA Software. <https://www.ansys.com/products/structures/ansys-ls-dyna>. Retrieved November 12, 2018.
33. Dobrovolny, C., Bhutani, S., Zalani, A., Bligh, R., Hurlebaus, S., Aldahlki, H., Schroeder, W., & Kuhn, D. (2022). *Development of Guidelines for Inspection, Repair, and Use of Portable Concrete Barriers—Volume 1: Technical Report* (Report No. FHWA/TX-22/0-7059-R1-Vol1). Texas A&M Transportation Institute.
34. George Mason University, Center for Collision Safety and Analysis. (Undated). Vehicle modeling. <https://www.ccsa.gmu.edu/models/>. Retrieved November 12, 2018.

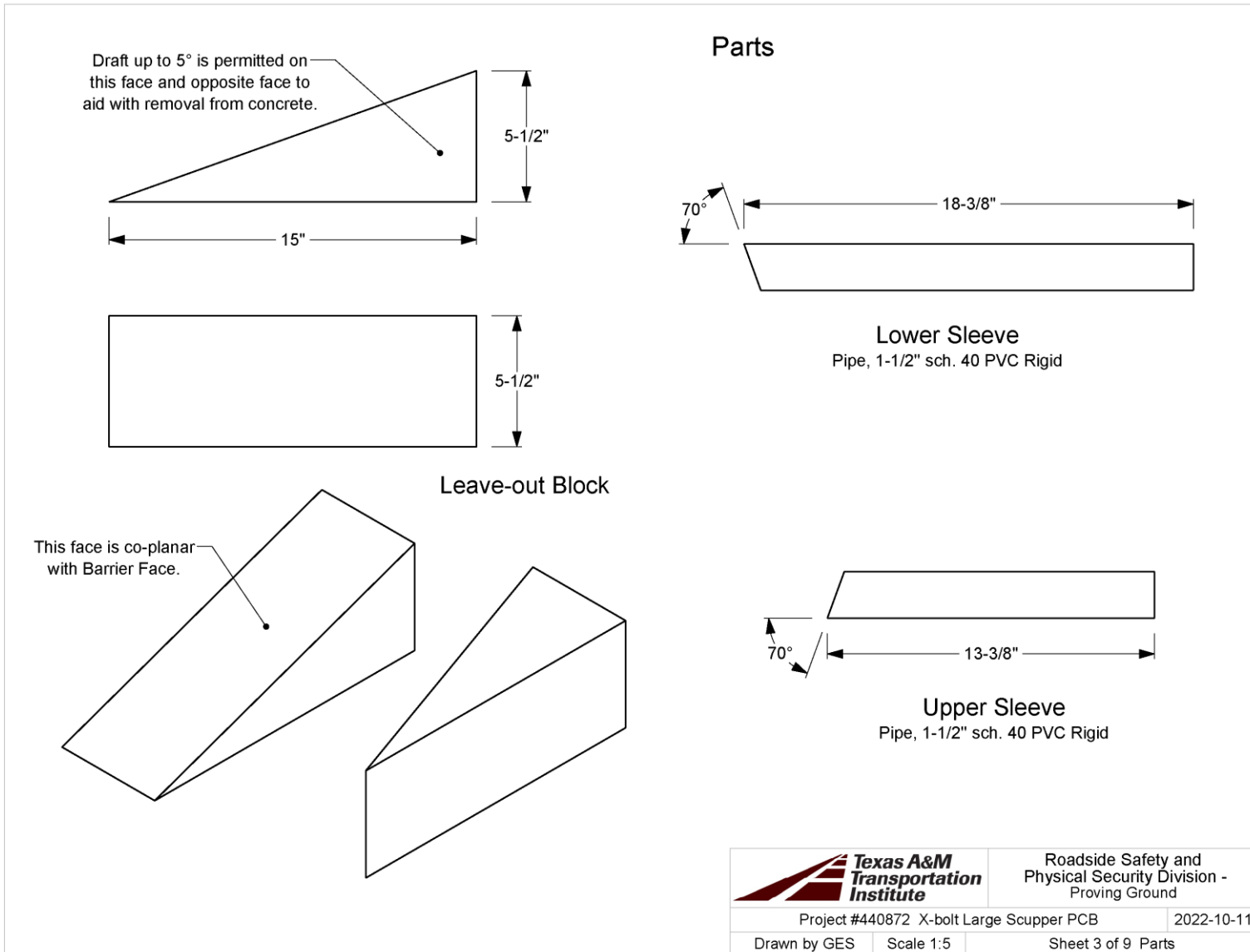
APPENDIX A. DETAILS OF LARGE-SCUPPER PORTABLE CONCRETE BARRIER

A.1. DETAILS OF LARGE-SCUPPER PORTABLE CONCRETE BARRIER FOR TESTS 440873-01-1 AND 440873-01-2





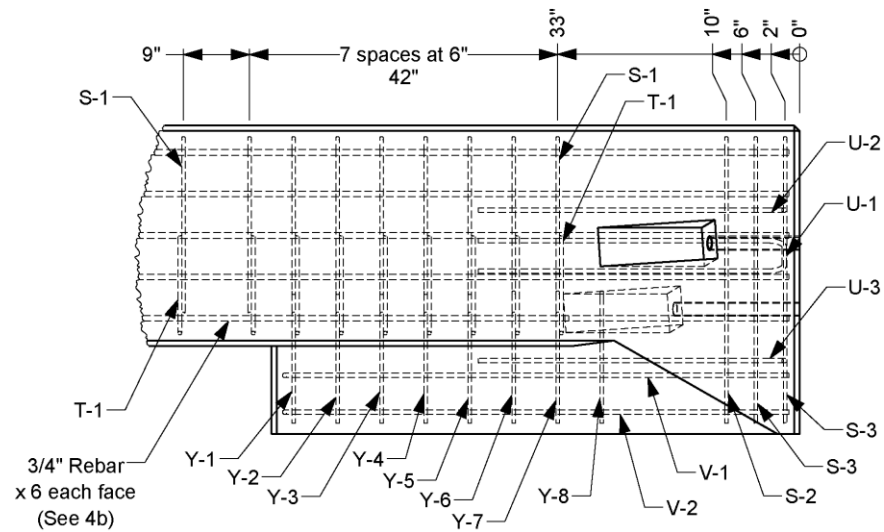
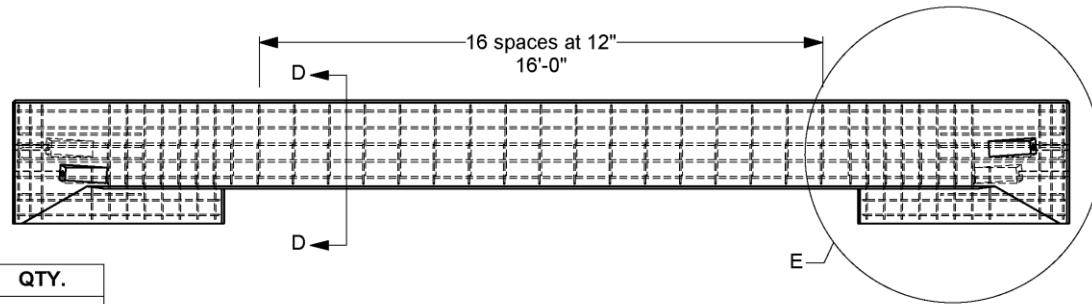
Q:\Accreditation-17025-2017\EIR-000 Project Files\440872 - Large Scupper PCB's - Dobrovoly\Drafting, 440872\440872 Drawing



Rebar Details

Section View on next sheet

Bar Name	Length	QTY.
Y-1	40"	2
Y-2	41 1/2"	2
Y-3	42 3/4"	2
Y-4	44"	2
Y-5	45 1/4"	2
Y-6	41 3/4"	2
Y-8	41 3/4"	2
V-2	141 1/2"	2
V-1	141 1/2"	2
Y-7	42 3/4"	2
S-3	83"	4
S-2	83"	2
T-1	40 1/2"	33
S-1	52 1/2"	33
U-1	89"	2
U-2	92 1/4"	2
U-3	97 1/4"	2



Detail E
Scale 1 : 20
Typ each end

4a. All rebar is grade 60. Rebar dimensions are to center unless otherwise indicated by "cvt" (cover).

4b. 22-1/2" laps on longitudinal bars. Longitudinal bars have 1-1/2" cover at ends, except 31-1/2" cover at connection pockets (see Isometric Views sheet).

4c. Lengths in table above are for reference only, and do not supersede dimensions on following sheets. Longitudinal bars not shown in table.



Roadside Safety and
Physical Security Division -
Proving Ground

Project #440872 X-bolt Large Scupper PCB

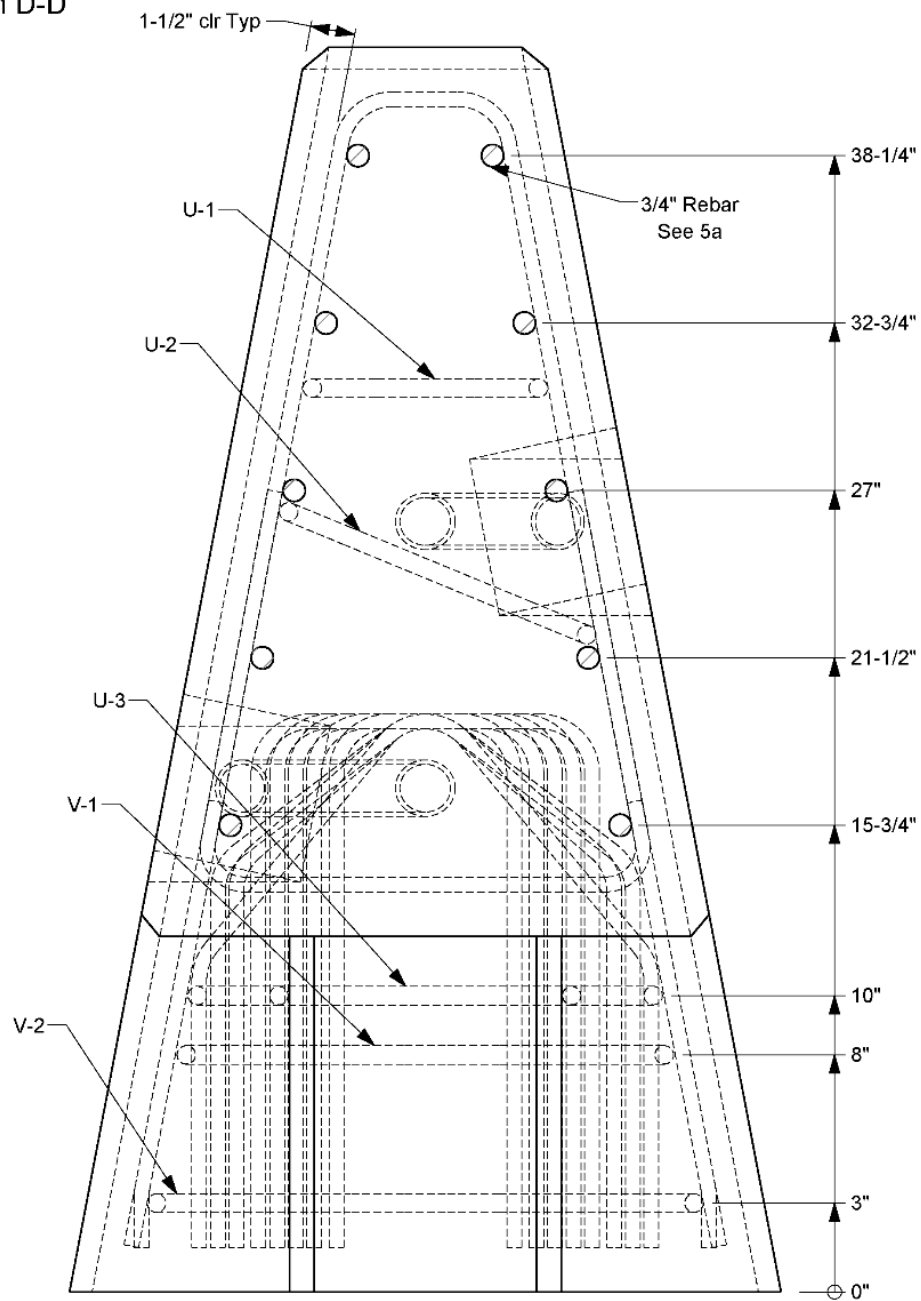
2022-10-11

Drawn by GES

Scale 1:50

Sheet 4 of 9 Rebar Details

Section D-D



5a. Ten longitudinal bars; six full length and four shorter bars at connection pockets (see previous sheet and next sheet).



**Texas A&M
Transportation
Institute**

Roadside Safety and
Physical Security Division -
Proving Ground

Project #440872 X-bolt Large Scupper PCB

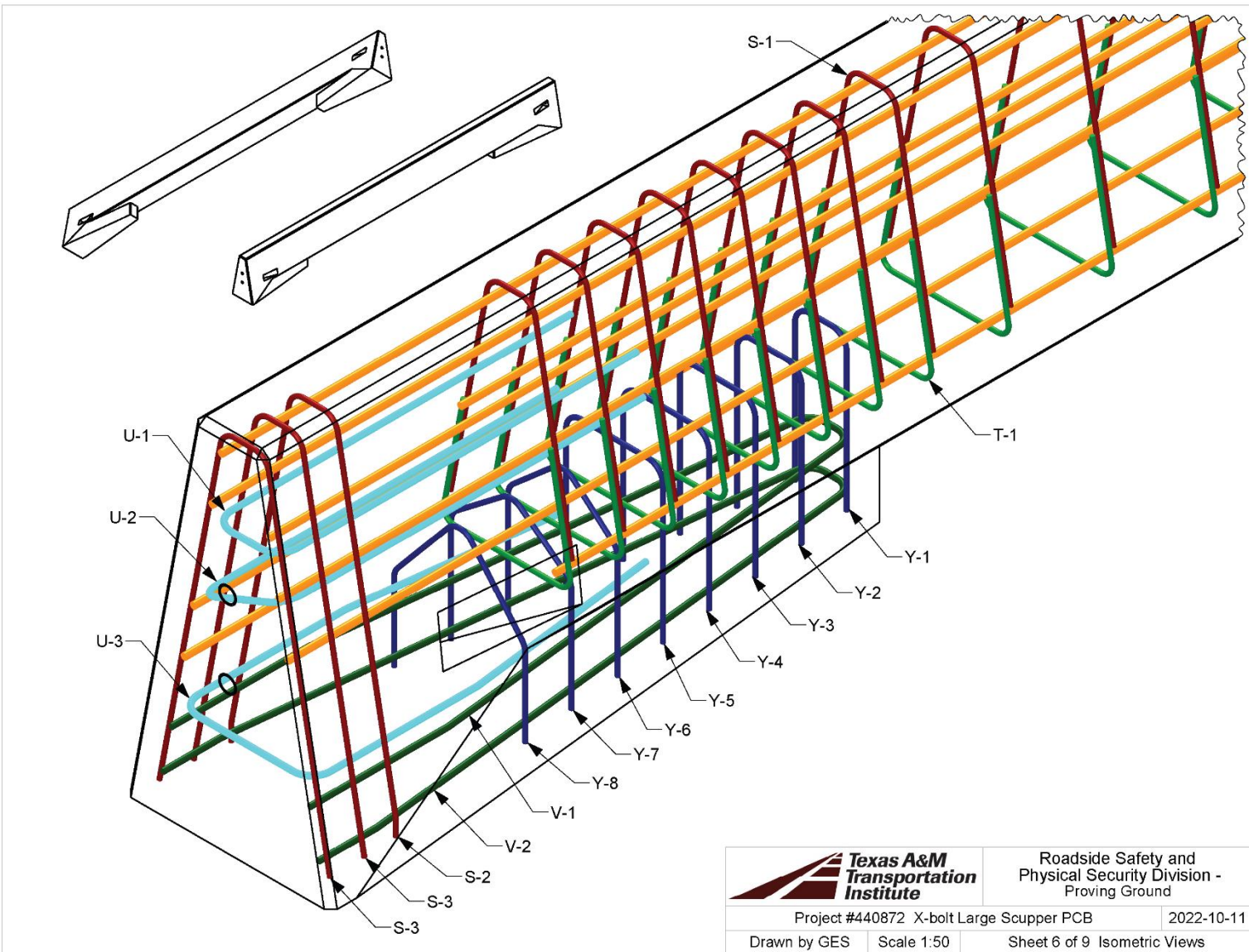
2022-10-11

Drawn by GES

Scale 1:5

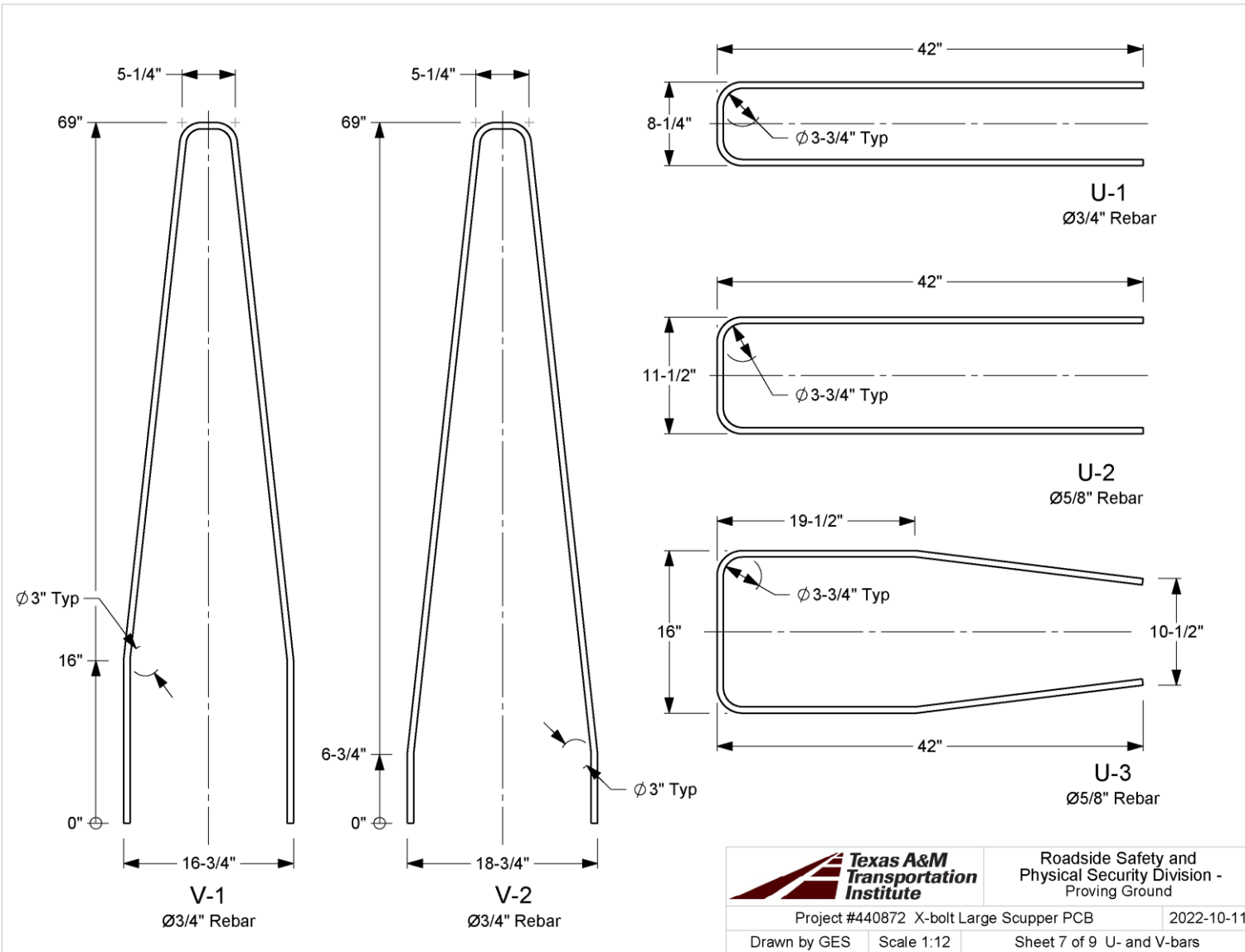
Sheet 5 of 9 / Cross Section

Q:\Accreditation-17025-2017\EIR-000 Project Files\440872 - Large Scupper PCB's - Dobrovolsky\Drafting, 440872\440872 Drawing




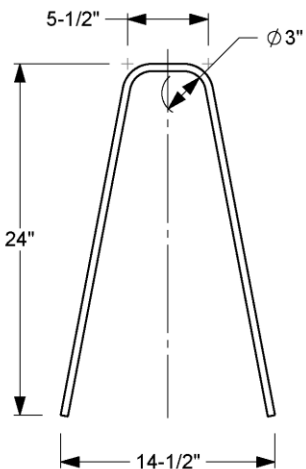
		Roadside Safety and Physical Security Division - Proving Ground	
Project #440872 X-bolt Large Scupper PCB		2022-10-11	
Drawn by GES	Scale 1:50	Sheet 6 of 9 Isometric Views	

Q:\Accreditation-17025-2017\EIR-000 Project Files\440872 - Large Scupper PCB's - Dobrovoly\Drafting, 440872\440872 Drawing

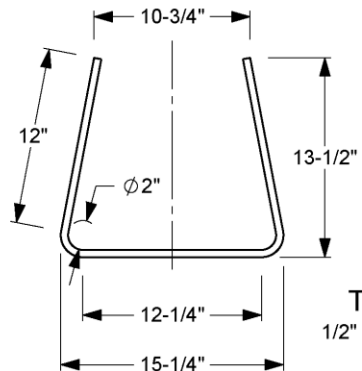


Q:\Accreditation-17025-2017\ElR-000 Project Files\440872 - Large Scupper PCB's - Dobrovlny\Drafting, 440872\440872 Drawing

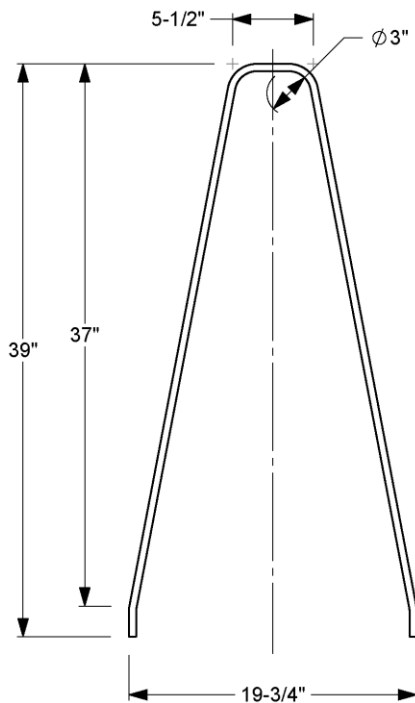
		Roadside Safety and Physical Security Division - Proving Ground	
Project #440872 X-bolt Large Scupper PCB		2022-10-11	
Drawn by GES	Scale 1:12	Sheet 7 of 9 U- and V-bars	



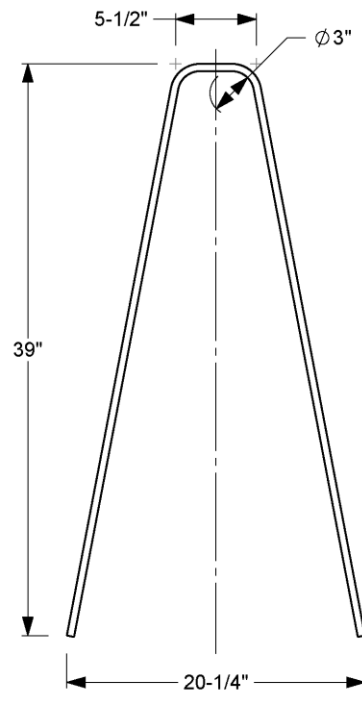
S-1
1/2" Rebar




T-1
1/2" Rebar

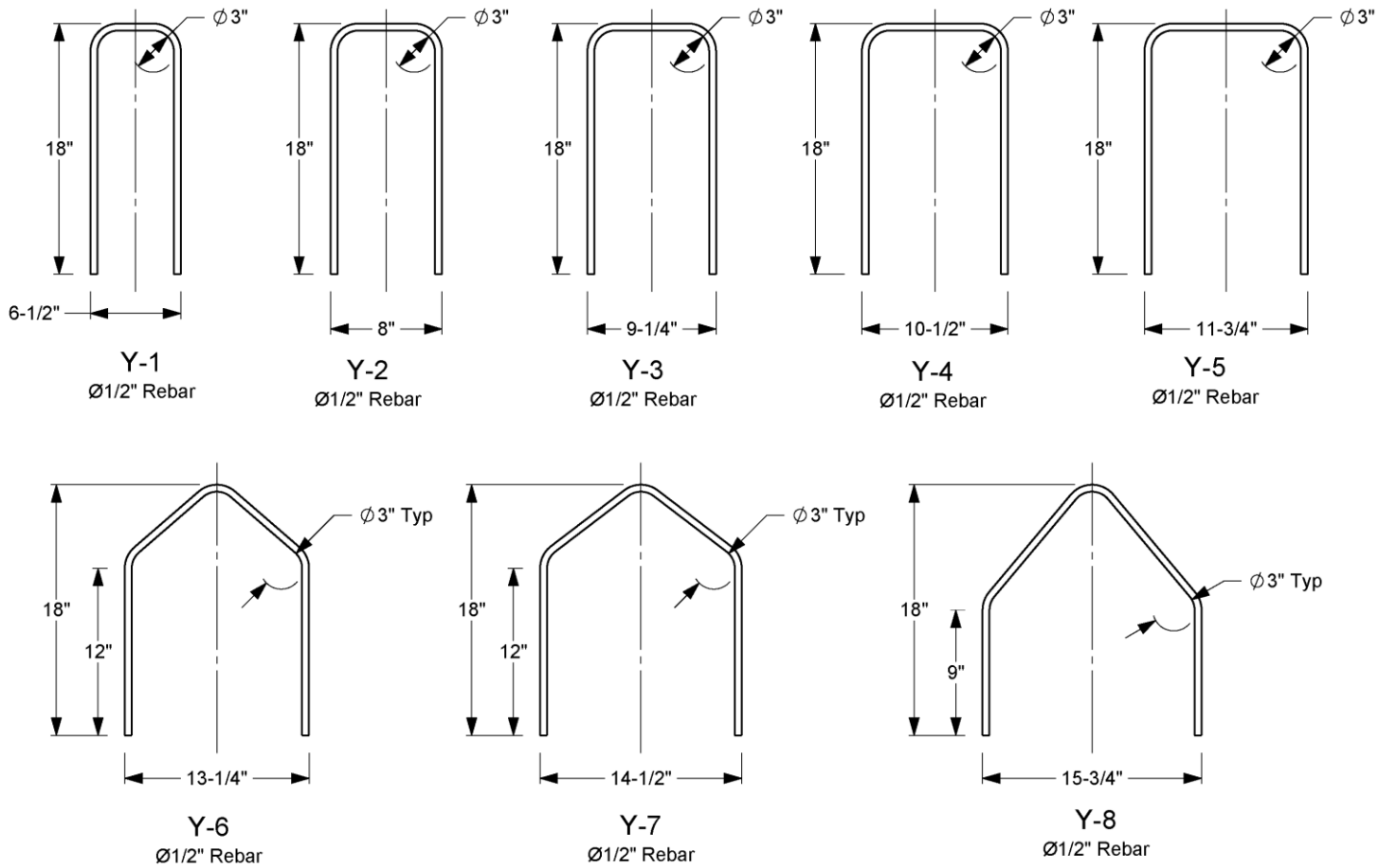



S-2
1/2" Rebar



S-3
1/2" Rebar

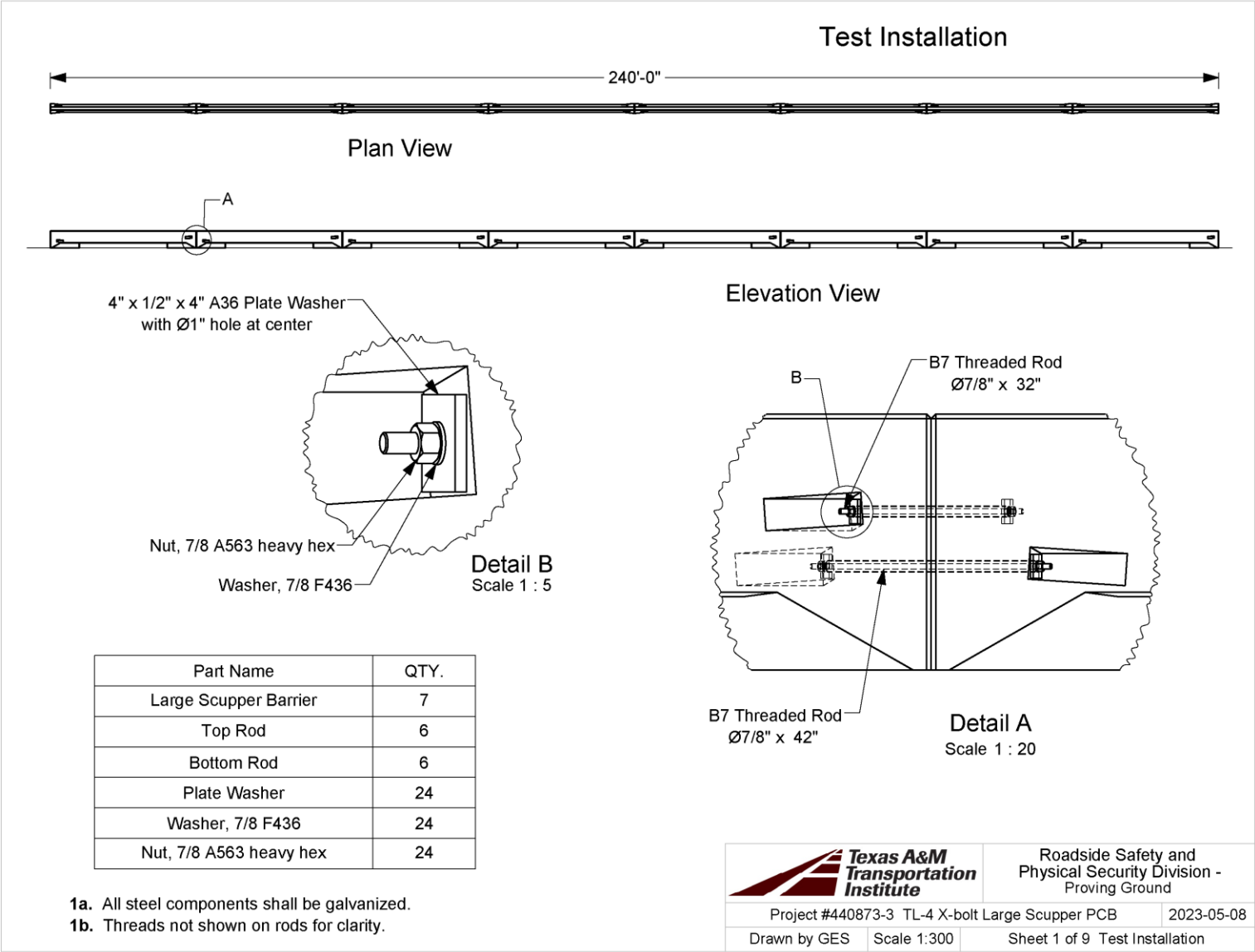
		Roadside Safety and Physical Security Division - Proving Ground	
Project #440872 X-bolt Large Scupper PCB		2022-10-11	
Drawn by GES	Scale 1:10	Sheet 8 of 9 S- and T-bars	

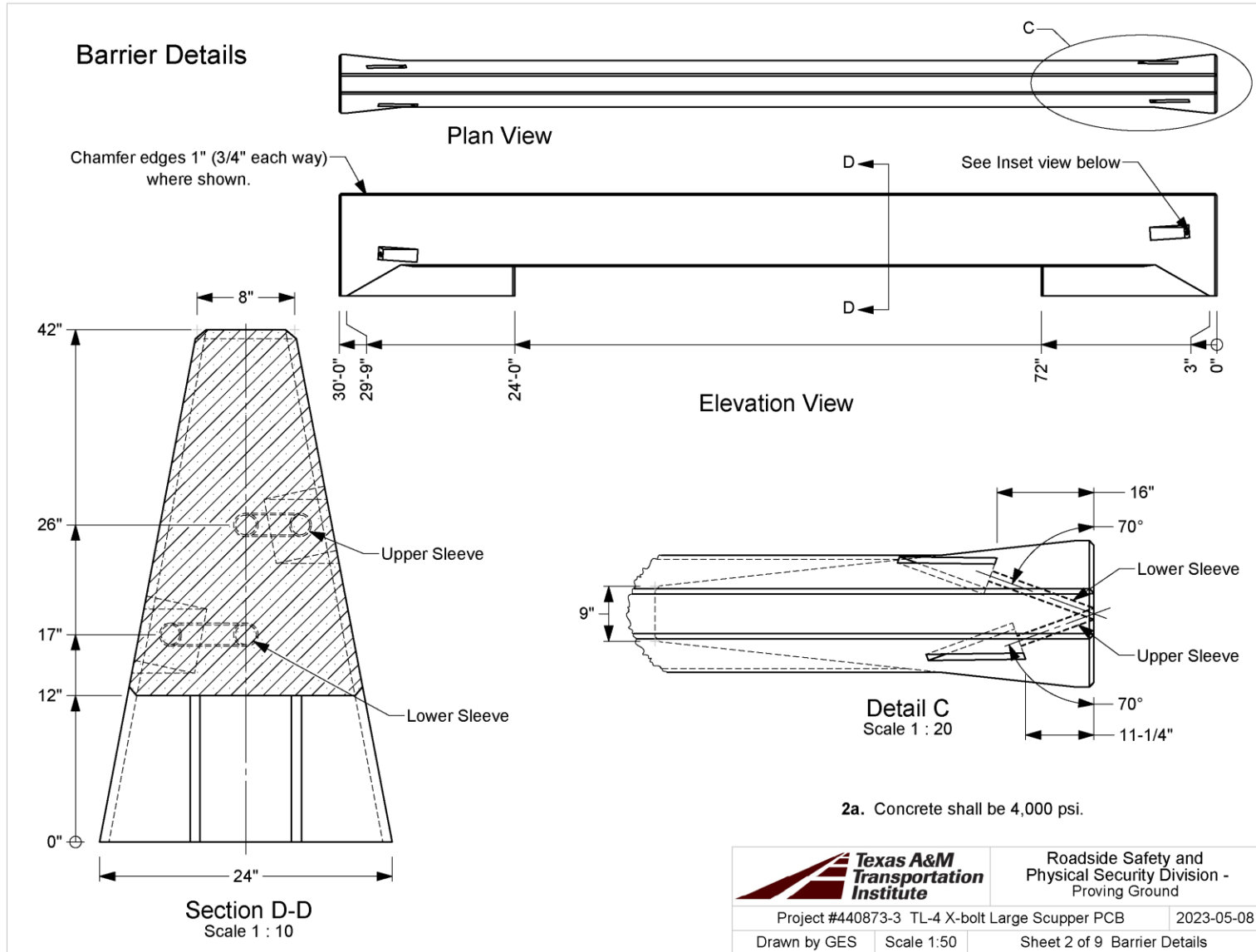


		Roadside Safety and Physical Security Division - Proving Ground	
Project #440872 X-bolt Large Scupper PCB		2022-10-11	
Drawn by GES	Scale 1:10	Sheet 9 of 9 Y-bars	

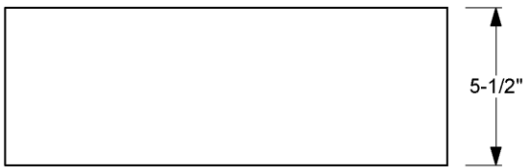
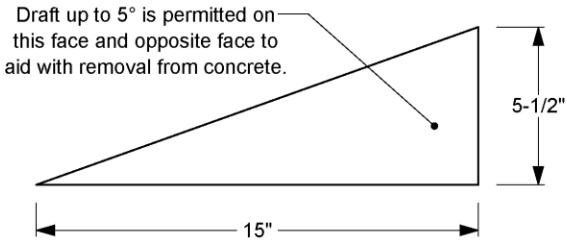
Q:\Accreditation-17025-2017\ElR-000 Project Files\440872 - Large Scupper PCB's - Dobrovoly\Drafting, 440872\440872 Drawing

A.2. DETAILS OF LARGE-SCUPPER PORTABLE CONCRETE BARRIERS FOR TEST 440873-01-3

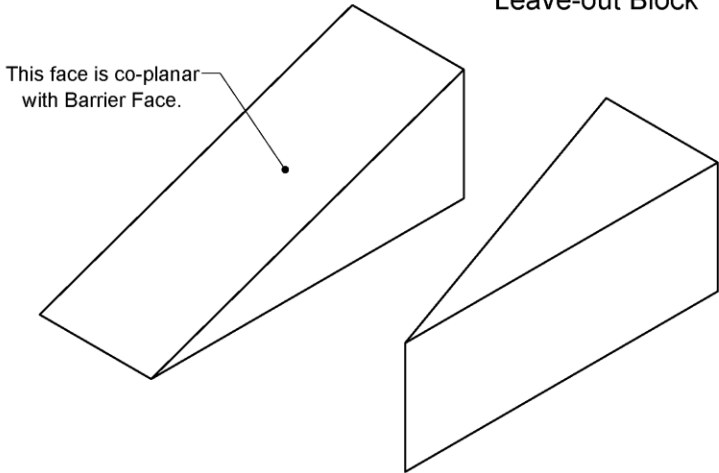




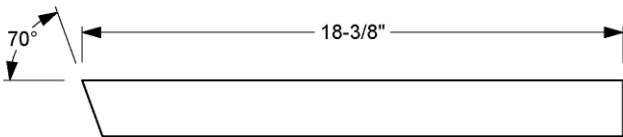
S:\Accreditation-17025-2017\EIR-000 Project Files\440873 - Large Scupper PCB's - Dobrovolny (440872)\Drafting, 440872\440872-3 Drawing



Leave-out Block

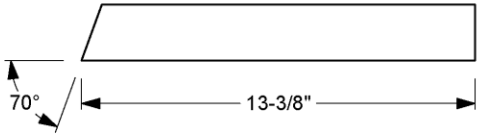


Parts




Lower Sleeve

Pipe, 1-1/2" sch. 40 PVC Rigid



Upper Sleeve

Pipe, 1-1/2" sch. 40 PVC Rigid

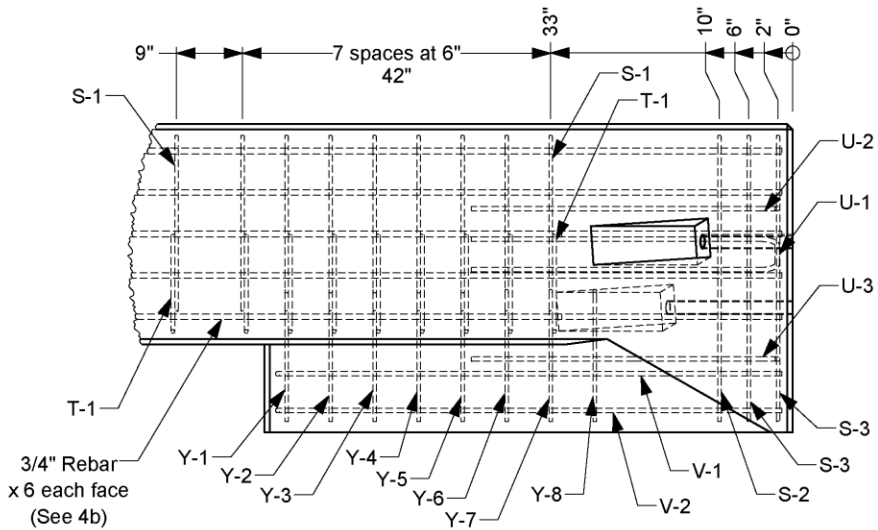
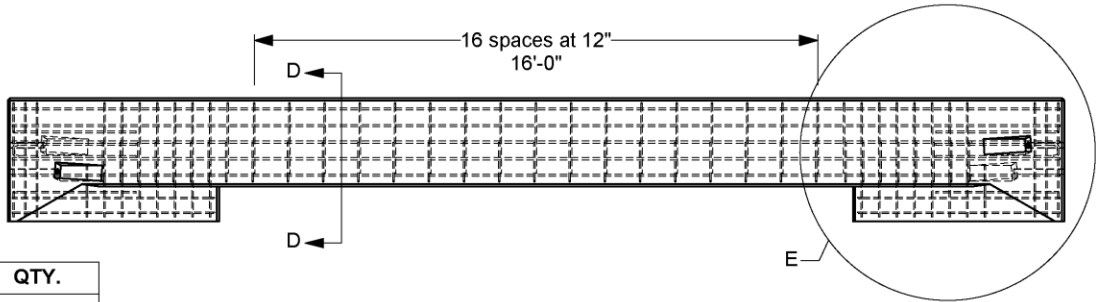
		Roadside Safety and Physical Security Division - Proving Ground	
Project #440873-3 TL-4 X-bolt Large Scupper PCB		2023-05-08	
Drawn by GES	Scale 1:5	Sheet 3 of 9 Parts	

Rebar Details


Section View on next sheet

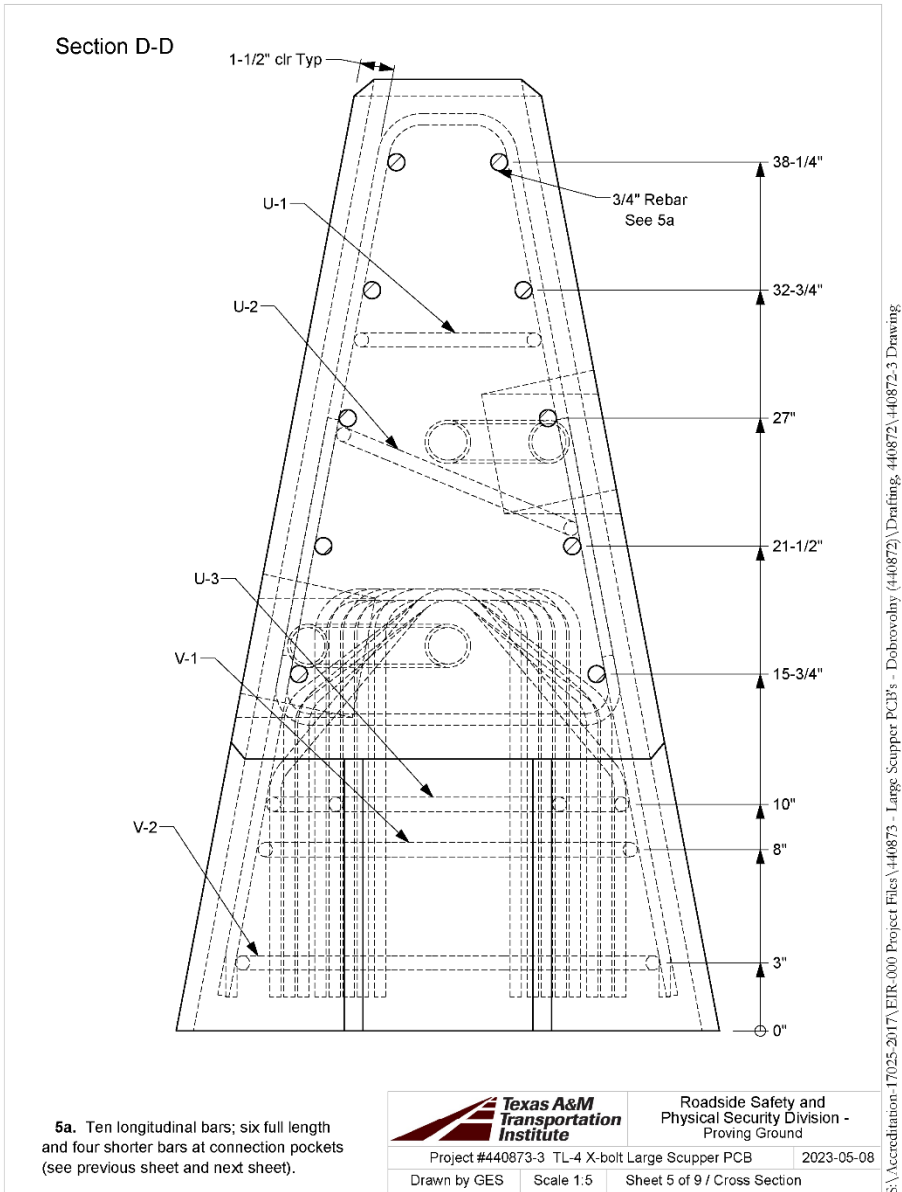
Bar Name	Length	QTY.
Y-1	40"	2
Y-2	41 1/2"	2
Y-3	42 3/4"	2
Y-4	44"	2
Y-5	45 1/4"	2
Y-6	41 3/4"	2
Y-8	41 3/4"	2
V-2	141 1/2"	2
V-1	141 1/2"	2
Y-7	42 3/4"	2
S-3	83"	4
S-2	83"	2
T-1	40 1/2"	33
S-1	52 1/2"	33
U-1	89"	2
U-2	92 1/4"	2
U-3	97 1/4"	2

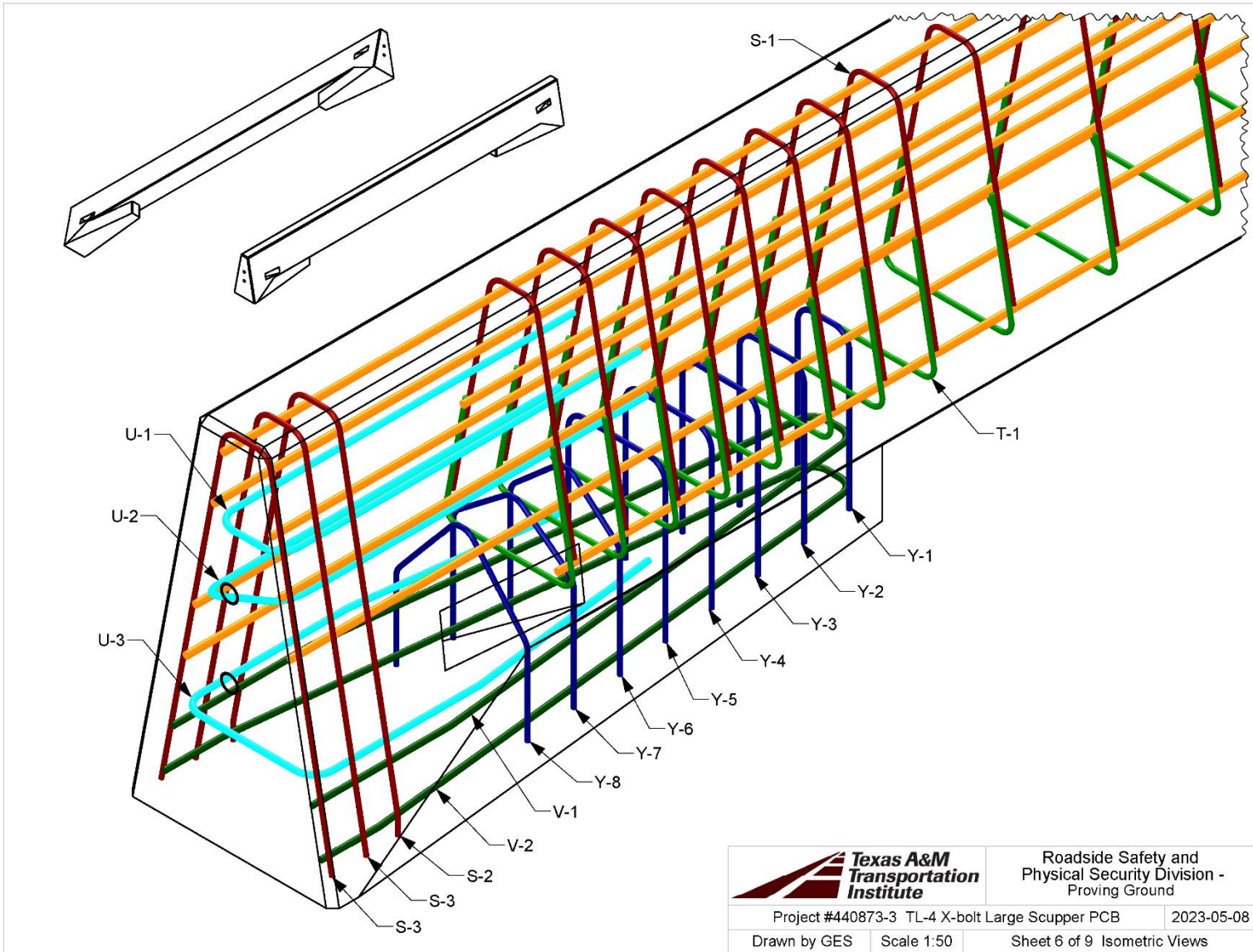
- 4a. All rebar is grade 60. Rebar dimensions are to center unless otherwise indicated by "cvt" (cover).
- 4b. 22-1/2" laps on longitudinal bars. Longitudinal bars have 1-1/2" cover at ends, except 31-1/2" cover at connection pockets (see Isometric Views sheet).
- 4c. Lengths in table above are for reference only, and do not supersede dimensions on following sheets. Longitudinal bars not shown in table.



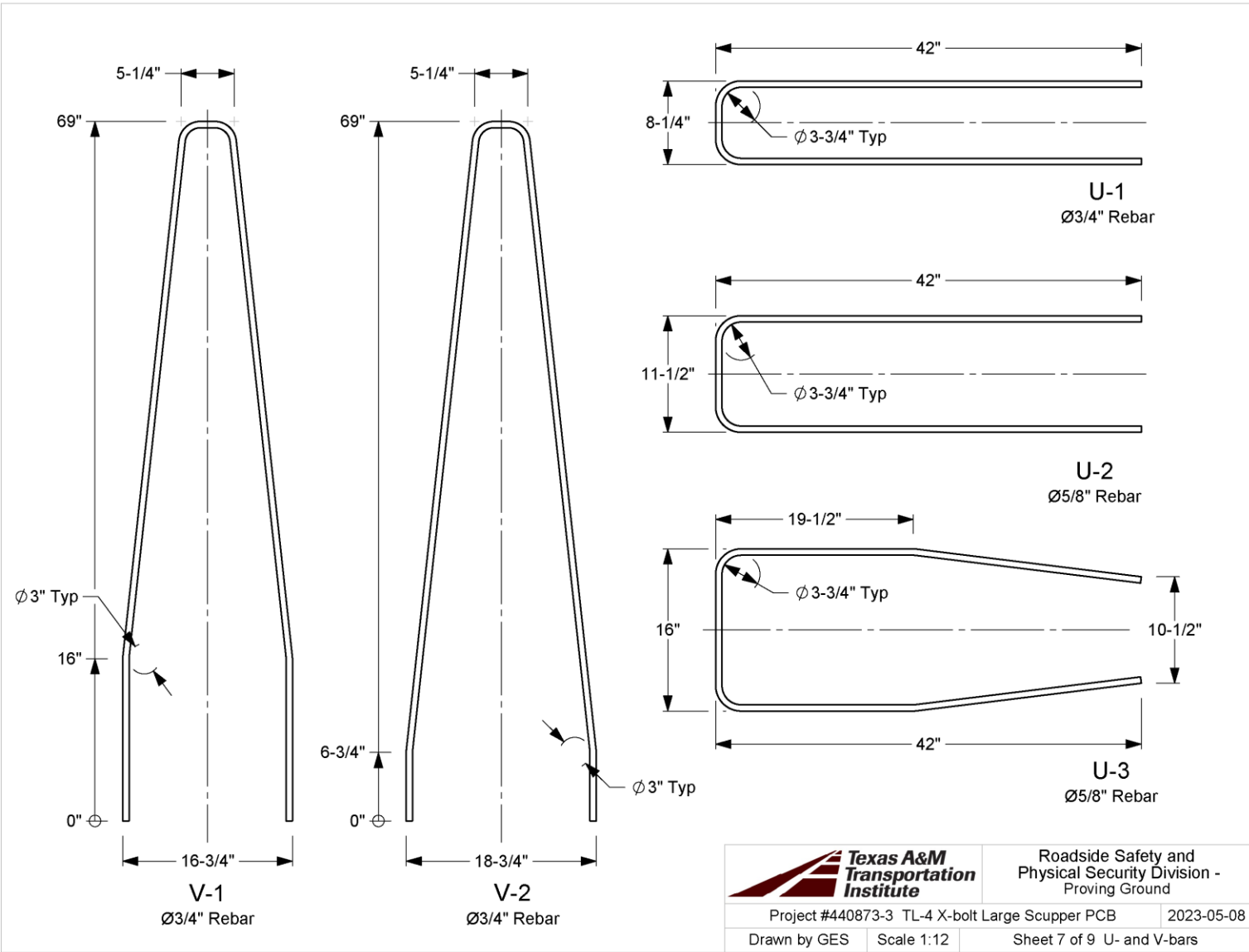
Detail E
Scale 1 : 20
Typ each end

		Roadside Safety and Physical Security Division - Proving Ground
Project #440873-3 TL-4 X-bolt Large Scupper PCB		2023-05-08
Drawn by GES	Scale 1:50	Sheet 4 of 9 Rebar Details

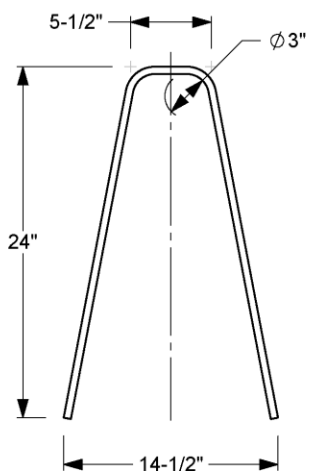




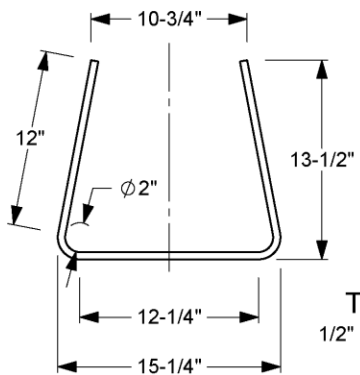
S:\Accreditation-17025-2017\EIR-000 Project Files\440873 - Large Scupper PCB's - Dobrovlny (440872)\Drafting, 440872\440872-3 Drawing



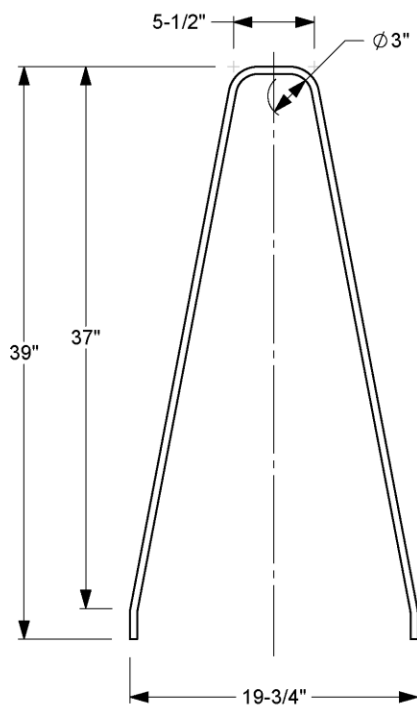
S:\Accreditation-17025-2017\EIR-000 Project Files\440873 - Large Scupper PCB's - Dobrovolny (440872)\Drafting, 440872\440872-3 Drawing



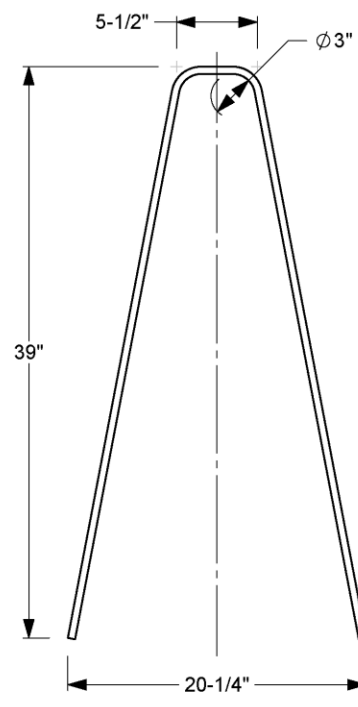
S-1
1/2" Rebar



T-1
1/2" Rebar



S-2
1/2" Rebar



S-3
1/2" Rebar



Roadside Safety and
Physical Security Division -
Proving Ground

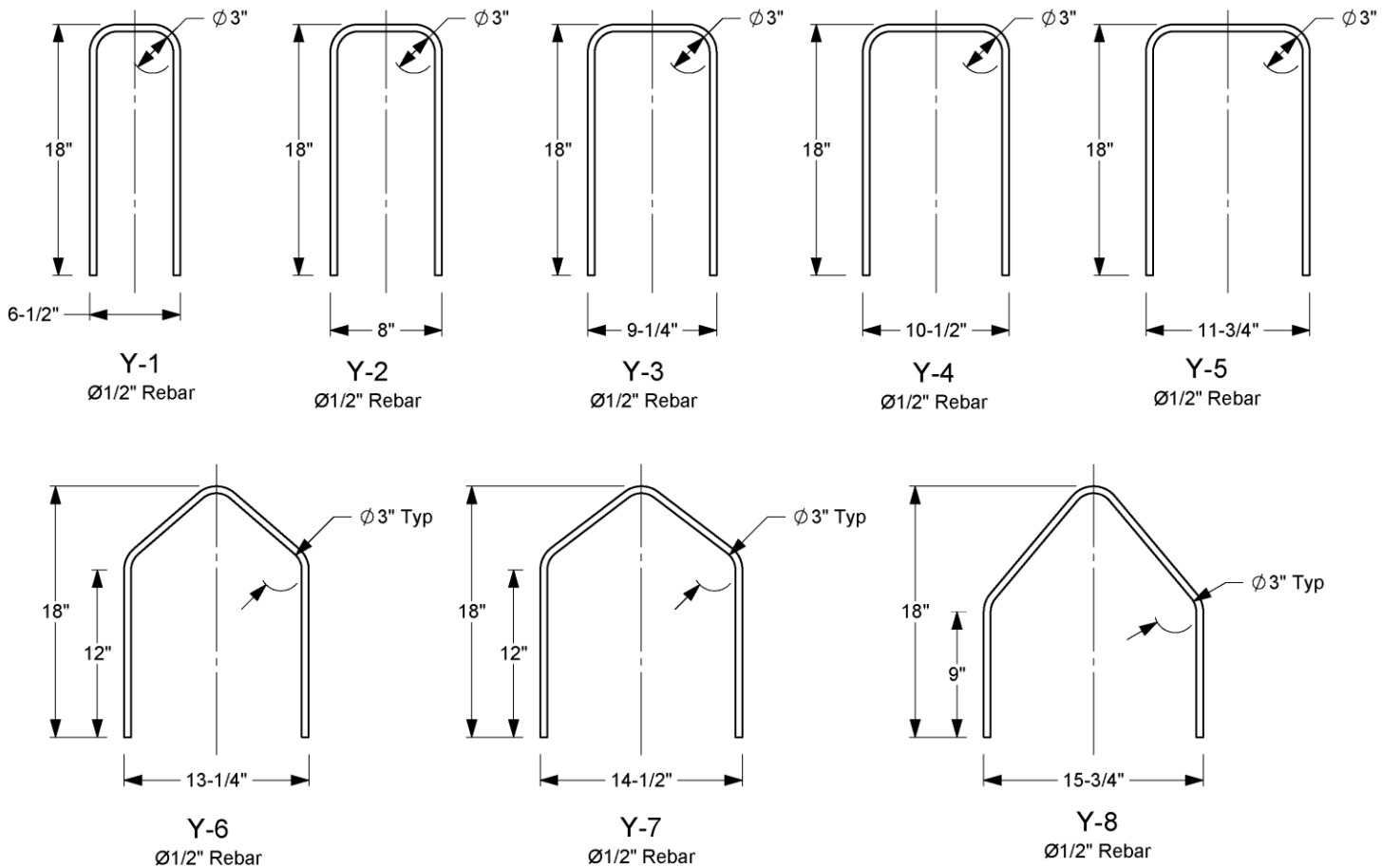
Project #440873-3 TL-4 X-bolt Large Scupper PCB


2023-05-08

Drawn by GES


Scale 1:10

Sheet 8 of 9 S- and T-bars



		Roadside Safety and Physical Security Division - Proving Ground	
Project #440873-3 TL-4 X-bolt Large Scupper PCB		2023-05-08	
Drawn by GES	Scale 1:10	Sheet 9 of 9 Y-bars	

APPENDIX B. SUPPORTING CERTIFICATION DOCUMENTS

	QF 7.3-01 Concrete Sampling	Doc. No. QF 7.3-01	Revision Date: 2020-07-29
Quality Form	Revised by: B.L. Griffith Approved by: D. L. Kuhn	Revision: 7	Page: 1 of 1

Project No: 440873 **Casting Date:** 11/10/2022 **Mix Design (psi):** 4000 psi

Name of Technician Taking Sample _____ Signature of Technician Taking Sample _____ <div style="text-align: center;">Terracon</div>	Name of Technician Breaking Sample _____ Signature of Technician Breaking Sample _____ <div style="text-align: center;">Terracon</div>
--	--

Load No.	Truck No.	Ticket No.	Location (from concrete map)
T1	Raymond G. 145	121864	Barriers 1, 2, 50% of 3
T2	Derickbrewer3	121872	Barriers 4, and 50% of 3

Load No.	Break Date	Cylinder Age	Total Load (lbs)	Break (psi)	Average

TEXCRETE
Ready-mix Concrete Company

TEXCRETE

121864

REMIT PAYMENT TO:
P.O. BOX 138
KURTEN, TX 77862

5222 Sandy Point RD.
Bryan, Tx 77807

17534 SH 6 South
College Station, TX 77845

18935 Circle Lake Dr.
Pinehurst, TX 77362

BCS DISPATCH - 979-316-2906
PINEHURST DISPATCH - 936-232-5815
OFFICE - 979-985-3636

MBC MANAGEMENT
3100 SH47 Bryan, TX

TTI Warehouse (RT 2818, RT HWY 21, LT
SILVER HILL RD, RT AT "T", RT HWY 47, LT INTO
RELLIS CAMPUS STAYSTRAIGHT)

TIME	FORMULA	LOAD SIZE	YARD ORDERED		DRIVER/TRUCK		PLANT TRANSACTION#
13:58	CN350CC070	10.00	17.00	PO#	RAYMOND G. 145		71006
DATE	PROJECT	LOAD#	YARDS DEL.	BATCH#	WATER TRIM	SLUMP	TICKET NUMBER
11/10/22	X-BOLT	10.00	10.00			7.00 in	69192

QUANTITY	CODE	DESCRIPTION	UNIT PRICE	EXTENDED PRICE
10.00 CY	CN350CC0700	CON, 5000, REG, 7",		
1.00 ea	FUEL	Fuel Charge		

Thank you for your business

LEFT PLANT	ARRIVED JOB	START UNLOADING	SLUMP	CONCRETE TEMP.	AIR TEMP.
2:14	2:33				
FINISH UNLOADING	LEFT JOB	ARRIVED AT PLANT	ON SITE TESTING		
			TESTING LAB:	TERRACON GESSNER CME	OTHER
			TESTED	AIR	CYLINDERS
			<input type="checkbox"/> YES <input type="checkbox"/> NO		

Tax
Prev. AMT
Ticket Total

ADDITIONAL CHARGE 1

ADDITIONAL CHARGE 2

GRAND TOTAL

WARNING
IRRITATING TO THE SKIN AND EYES
Contains Portland Cement; Wear Rubber Boots and Gloves; PROLONGED CONTACT MAY CAUSE BURNS. Avoid Contact With Eyes and Prolonged Contact with Skin. In Case of Contact with Skin or Eyes, Rinse Thoroughly With Water. If Irritation Persists, Get Medical Attention. **KEEP CHILDREN AWAY.**

CONCRETE is a PERISHABLE COMMODITY and BECOMES THE PROPERTY of the PURCHASER UPON LEAVING the PLANT. ANY CHANGES or CANCELLATION of ORIGINAL INSTRUCTIONS MUST be TELEPHONED to the OFFICE BEFORE LOADING starts. The undersigned promises to pay all costs, including reasonable attorney's fees, incurred in collecting any sums owed.
All accounts not paid within 30 days of delivery will bear interest at the rate of 18% per annum. Not Responsible For Reactive Aggregate or Color Quality. No Claim Allowed Unless Made at Time Material is Delivered.
A \$25.00 Service Charge and Loss of the Cash Discounted will be Collected on all Returned Checks. Demerge charge after 90 min. will be \$100.00/hr.

PROPERTY DAMAGE RELEASE
(TO BE SIGNED IF DELIVERY TO BE MADE INSIDE CURB LINE)
Dear Customer - The driver of this truck in presenting this RELEASE to you for your signature is of the opinion that the size and weight of this truck may possibly cause damage to the premises and/or adjacent property. If he places the material in this load where you desire it, it is our wish to help you in every way that we can, but in order to do this the driver is requesting that you sign this RELEASE relieving him and this supplier from any responsibility from damage that may occur to the premises and/or adjacent property, buildings, sidewalks, driveways, curbs, etc. by the delivery of this material and that you also agree to help him remove the mud from the wheels of his vehicle so that he will not filth the public streets. Further as additional consideration, the undersigned agrees to indemnify and hold harmless the driver of this truck and this supplier for any and all damage to the premises and/or adjacent property, which may be claimed by anyone to have arisen out of delivery of this order SIGNED:

Excessive Water is Detrimental to Concrete Performance.
H₂O Added by Request/Authorized By:

GAL X
WEIGHMASTER

Surcharge for credit cards

NOTICE: MY SIGNATURE BELOW INDICATES THAT I HAVE READ THE HEALTH WARNING NOTICE AND SUPPLIER WILL NOT BE RESPONSIBLE FOR ANY DAMAGE CAUSED WHEN DELIVERING INSIDE CURB LINE.

LOAD RECEIVED BY

X

X

121864

TEXCRETE
Real-time Concrete Dispatching

REMIT PAYMENT TO:
P.O. BOX 138
KURTEN, TX 77862

5222 Sandy Point RD.
Bryan, TX 77807

MBC MANAGEMENT
3100 SH47 Bryan, TX

TEXCRETE

17534 SH 6 South
College Station, TX 77845

18935 Circle Lake Dr.
Pinehurst, TX 77362

121872

BCS DISPATCH - 979-316-2906
PINEHURST DISPATCH - 936-232-5815
OFFICE - 979-985-3636

TTI Warehouse (RT 2618, RT HWY 21, LT
SILVER HILL RD, RT AT "T", RT HWY 47, LT INTO
RELLIS CAMPUS STAY STRAIGHT)

TIME	FORMULA	LOAD SIZE	YARD ORDERED	DRIVER/TRUCK	PLANT TRANSACTION#
14:49	CN350CC070	7.00	17.00	DERICK	71014
DATE	PROJECT	LOAD#	YARDS DEL	BATCH#	TICKET NUMBER
11/10/22	X-BOLT	7.00	17.00		69200
QUANTITY	CODE	DESCRIPTION	UNIT PRICE	EXTENDED PRICE	
7.00 CY	CN350CC0700	COM, 5000, REG, 7",			
1.00 ea	FUEL	Fuel Charge			

Thank you for your business

Tax
Prey. RRT
Ticket Total

ADDITIONAL CHARGE 1
ADDITIONAL CHARGE 2
GRAND TOTAL

LEFT PLANT	ARRIVED JOB	START UNLOADING	SLUMP	CONCRETE TEMP.	AIR TEMP.
300	320				
FINISH UNLOADING	LEFT JOB	ARRIVED AT PLANT	ON SITE TESTING	TESTING LAB.	TESTED
				TESTING LAB. DESIGNER CME OTHER	<input type="checkbox"/> YES <input type="checkbox"/> NO
				AIR CYLINDERS	

WARNING
IRRITATING TO THE SKIN AND EYES
contains Portland Cement, Wear Rubber Boots and Gloves. PROLONGED CONTACT MAY CAUSE BURNS. Avoid Contact With Eyes and Prolonged Contact with Skin. In Case of Contact with Skin or Eyes, Rinse Thoroughly With Water. If Irritation Persists, Get Medical Attention. **KEEP CHILDREN AWAY.**
CONCRETE is a PERISHABLE COMMODITY and BECOMES THE PROPERTY of the PURCHASER UPON LEAVING the PLANT. ANY CHARGES or CANCELLATION of ORDERS MUST be TELEPHONED to the OFFICE BEFORE LOADING begins. The undersigned promises to pay all costs, including reasonable attorney's fees, incurred in collecting any sums owed.
Accounts not paid within 30 days of delivery will bear interest at the rate of 18% per annum. Not Responsible For Reactive Aggregate or Color Quality. No Claim Allowed Unless made at Time Material is Delivered.
\$25.00 Service Charge and Loss of the Cash Discounted will be Collected on all Returned orders. Damage charge after 90 min. will be \$100.00/hr.

PROPERTY DAMAGE RELEASE
(TO BE SIGNED IF DELIVERY TO BE MADE INSIDE CURB LINE)
Dear Customer - The driver of this truck in presenting this RELEASE to you for your signature is of the opinion that the size and weight of this truck may possibly cause damage to the premises and/or adjacent property if he places the material in this load where you desire it. It is our wish to help you in every way that we can, but in order to do this the driver is requesting that you sign this RELEASE relieving him and this supplier from any responsibility from damage that may occur to the premises and/or adjacent property, buildings, sidewalks, driveways, curbs, etc. by the delivery of this material and that you also agree to help him remove mud from the wheels of his vehicle so that he will not litter the public streets. Further as additional consideration, the undersigned agrees to indemnify and hold harmless the driver of this truck and this supplier for any and all damage to the premises and/or adjacent property which may be caused by anyone to have arisen out of delivery of this order SIGNED.

Excessive Water is Detrimental to Concrete Performance.
H₂O Added by Request/Authorized By:
GAL X
WEIGHMASTER
Surcharge for credit cards
NOTICE: MY SIGNATURE BELOW INDICATES THAT I HAVE READ THE WARNING NOTICE AND SUPPLIER WILL NOT BE RESPONSIBLE FOR ANY DAMAGE CAUSED WHEN DELIVERING INSIDE CURB LINE.

LOAD RECEIVED BY
X

121872

CONCRETE COMPRESSIVE STRENGTH TEST REPORT

Report Number: A1171057.0255
Service Date: 11/10/22
Report Date: 12/14/22 Revision 1 - Incomplete
Task: PO# 440873-01



6198 Imperial Loop
College Station, TX 77845-5765
979-846-3767 Reg No: F-3272

Client

Texas Transportation Institute
Attn: Bill Griffith
TTI Business Office
3135 TAMU
College Station, TX 77843-3135

Project

Riverside Campus
Riverside Campus
Bryan, TX

Project Number: A1171057

Material Information

Specified Strength: 5,000 psi @ 28 days
Mix ID: CN350CC070
Supplier: Texcrete
Batch Time: 1358 **Plant:** Sandy Point Plant
Truck No.: 145 **Ticket No.:** 71006

Sample Information

Sample Date: 11/10/22 **Sample Time:** 1444
Sampled By: David Carpio
Weather Conditions: Clear
Accumulative Yards: 10 **Batch Size (cy):** 10
Placement Method: Direct Discharge
Water Added Before (gal): 0
Water Added After (gal): 0
Sample Location: Set #1
Placement Location: TTI Box Larger Scooper #1

Field Test Data

Test	Result	Specification
------	--------	---------------

Air Content (%):

Concrete Temp. (F): 84
Ambient Temp. (F): 81

Plastic Unit Wt. (pcf):

Yield (Cu. Yds.):

Laboratory Test Data

Set No.	Spec ID	Cyl. Cond.	Avg Diam. (in)	Area (sq in)	Date Received	Date Tested	Age at Test (days)	Max Load (lbs)	Comp Strength (psi)	Frac Type	Tested By
1	A	Good	6.00	28.27		11/30/22	20 F	130,110	4,600	2	ARH
1	B	Good	6.00	28.27		11/30/22	20 F	135,680	4,800	2	ARH
1	C	Good	6.00	28.27		11/30/22	20 F	123,410	4,360	5	ARH
1	D						Hold				

Initial Cure: Outside

Final Cure: Field Cured

Sample Description: 6-inch diameter cylinders

Comments: Not tested for plastic unit weight. F = Field Cured

Note: Reported air content does not include Aggregate Correction Factor (ACF).

Samples Made By: Terracon

Services: Obtain samples of fresh concrete at the placement locations (ASTM C 172), perform required field tests and cast, cure, and test compressive strength samples (ASTM C 31, C 39, C 1231).

Terracon Rep.: David Carpio

Start/Stop: 1330-1530

Reported To:

Contractor:

Report Distribution:

(1) Texas Transportation Institute, Bill Griffith

Test Methods: ASTM C 31, ASTM C143, ASTM C231, ASTM C1064

The tests were performed in general accordance with applicable ASTM, AASHTO, or DOT test methods. This report is exclusively for the use of the client indicated above and shall not be reproduced except in full without the written consent of our company. Test results transmitted herein are only applicable to the actual samples tested at the location(s) referenced and are not necessarily indicative of the properties of other apparently similar or identical materials.

CONCRETE COMPRESSIVE STRENGTH TEST REPORT

Report Number: A1171057.0255
Service Date: 11/10/22
Report Date: 12/14/22 Revision 1 - Incomplete
Task: PO# 440873-01



6198 Imperial Loop
College Station, TX 77845-5765
979-846-3767 Reg No: F-3272

Client

Texas Transportation Institute
Attn: Bill Griffith
TTI Business Office
3135 TAMU
College Station, TX 77843-3135

Project

Riverside Campus
Riverside Campus
Bryan, TX

Project Number: A1171057

Material Information

Specified Strength: 5,000 psi @ 28 days
Mix ID: CN350CC070
Supplier: Texcrete
Batch Time: 1449 **Plant:** Sandy Point Plant
Truck No.: 103 **Ticket No.:** 69200

Sample Information

Sample Date: 11/10/22 **Sample Time:** 1530
Sampled By: David Carpio
Weather Conditions: Clear
Accumulative Yards: 17 **Batch Size (cy):** 7
Placement Method:
Water Added Before (gal): 0
Water Added After (gal): 0
Sample Location: Set 2
Placement Location: TTI Box Larger Scooper #1

Field Test Data

Test	Result	Specification
------	--------	---------------

Air Content (%):
Concrete Temp. (F): 85
Ambient Temp. (F): 81
Plastic Unit Wt. (pcf):
Yield (Cu. Yds.):

Laboratory Test Data

Set No.	Spec ID	Cyl. Cond.	Avg Diam. (in)	Area (sq in)	Date Received	Date Tested	Age at Test (days)	Max Load (lbs)	Comp Strength (psi)	Frac Type	Tested By
2	A	Good	6.00	28.27		11/17/22	7 F	138,410	4,900	2	AWD
2	B	Good	6.00	28.27		12/08/22	28 F	147,300	5,210	5	AWD
2	C	Good	6.00	28.27		12/08/22	28 F	141,520	5,010	5	AWD
2	D						Hold				

Initial Cure: Outside **Final Cure:** Field Cured **Sample Description:** 6-inch diameter cylinders

Comments: Not tested for plastic unit weight. F = Field Cured

Note: Reported air content does not include Aggregate Correction Factor (ACF).

Samples Made By: Terracon

Services: Obtain samples of fresh concrete at the placement locations (ASTM C 172), perform required field tests and cast, cure, and test compressive strength samples (ASTM C 31, C 39, C 1231).

Terracon Rep.: David Carpio

Reported To:

Contractor:

Report Distribution:

(1) Texas Transportation Institute, Bill Griffith


Start/Stop: 1330-1530

Reviewed By:

Alexander Dunigan
Project Manager

Test Methods: ASTM C 31, ASTM C143, ASTM C231, ASTM C1064

The tests were performed in general accordance with applicable ASTM, AASHTO, or DOT test methods. This report is exclusively for the use of the client indicated above and shall not be reproduced except in full without the written consent of our company. Test results transmitted herein are only applicable to the actual samples tested at the location(s) referenced and are not necessarily indicative of the properties of other apparently similar or identical materials.

	QF 7.3-01 Concrete Sampling	Doc. No. QF 7.3-01	Revision Date: 2020-07-29
		Quality Form	Revised by: B.L. Griffith Approved by: D. L. Kuhn

Project No: 440873 **Casting Date:** 11/18/2022 **Mix Design (psi):** 4000 psi

Name of Technician Taking Sample	<u>Terracon</u>	Name of Technician Breaking Sample	<u>Terracon</u>
Signature of Technician Taking Sample	<u>Terracon</u>	Signature of Technician Breaking Sample	<u>Terracon</u>

Load No.	Truck No.	Ticket No.	Location (from concrete map)
T1	Jjames Whit.131	122196	Barriers 5, and 6
T2	Chris Burns 130	122192	Barrier 7

Load No.	Break Date	Cylinder Age	Total Load (lbs)	Break (psi)	Average

TEXCRETE
Ready-mix Concrete Company

REMIT PAYMENT TO:
P.O. BOX 138
KURTEN, TX 77862

5222 Sandy Point RD.
Bryan, TX 77807

TEXCRETE

17534 SH 6 South
College Station, TX 77845

18935 Circle Lake Dr.
Pinehurst, TX 77362

122196

BCS DISPATCH - 979-316-2906
PINEHURST DISPATCH - 936-232-5815
OFFICE - 979-985-3636

MBC MANAGEMENT
3100 SH47 Bryan

TTI Warehouse (RT 2818, RT 21, LTSILVER
HILL RD, RT @ THE T, RT HWY47, LT INTO
RELLIS CAMPUS, STAY STRAIGHT

TIME	FORMULA	LOAD SIZE	YARD ORDERED		DRIVER/TRUCK		PLANT TRANSACTION#
10:34	CN350CC070	6.00	13.00	PD#	JJAMES	WHIT. 131	71340
DATE	PROJECT	LOAD#	YARDS DEL.	BATCH#	WATER TRIM	SLUMP	TICKET NUMBER
11/18/22	X-BOLT	6.00	13.00			7.00 in	69526
QUANTITY	CODE	DESCRIPTION	UNIT PRICE	EXTENDED PRICE			

6.00 CY CN350CC0700

COM, 5000, REG, 7",

1.00 ea FUEL

Fuel Charge

Thank you for your business

LEFT PLANT	ARRIVED JOB	START UNLOADING	SLUMP	CONCRETE TEMP	AIR TEMP
644	1102				
FINISH UNLOADING	LEFT JOB	ARRIVED AT PLANT	ON SITE TESTING		
			TESTING LAB:	TERRACON GESSNER CME	OTHER
		TESTED	AIR	CYLINDERS	
		<input type="checkbox"/> YES <input type="checkbox"/> NO			

Tax
Prev. AMT
Ticket Total

ADDITIONAL CHARGE 1

ADDITIONAL CHARGE 2

GRAND TOTAL

WARNING
IRRITATING TO THE SKIN AND EYES
Contains Portland Cement, Wear Rubber Boots and Gloves. PROLONGED
CONTACT MAY CAUSE BURNS. Avoid Contact With Eyes and Prolonged
Contact with Skin. In Case of Contact with Skin or Eyes, Rinse Thoroughly With
Water. If Irritation Persists, Get Medical Attention. **KEEP CHILDREN AWAY.**
CONCRETE is a PERISHABLE COMMODITY and BECOMES THE PROPERTY of the
PURCHASER UPON LEAVING THE PLANT. ANY CHANGES or CANCELLATION of
ORIGINAL INSTRUCTIONS MUST be TELEPHONED to the OFFICE BEFORE LOADING
starts. The undersigned promises to pay all costs, including reasonable attorney's fees,
incurred in collecting any sums owed.

All accounts not paid within 30 days of delivery will bear interest at the rate of 18% per
annum. Not Responsible For Reactive Aggregate or Color Quality. No Claim Allowed Unless
Made at Time Material is Delivered.
A \$25.00 Service Charge and Loss of the Cash Discounted will be Collected on all Returned
Checks. Densurge charge after 90 min. will be \$100.00/hr.

PROPERTY DAMAGE RELEASE
(TO BE SIGNED IF DELIVERY TO BE MADE INSIDE CURB LINE)
Dear Customer - The driver of this truck in presenting this
RELEASE to you for your signature is of the opinion that the
size and weight of this truck may possibly cause damage to
the premises and/or adjacent property if he places the
material in the load where you desire it. It is our wish to
help you in every way that we can, but in order to do this the
driver is requesting that you sign this RELEASE relieving him
and this supplier from any responsibility from damage that
may occur to the premises and/or adjacent property
buildings, sidewalks, driveways, curbs, etc. by the delivery of
this material and that you also agree to help him remove
mud from the wheels of his vehicle so that he will not litter the
public streets. Further as additional consideration, the
undersigned agrees to indemnify and hold harmless the
driver of this truck and this supplier for any and all damage to
the premises and/or adjacent property which may be
claimed by anyone to have arisen out of delivery of this order
SIGNED:

X

Excessive Water is Detrimental to Concrete Performance.
H₂O Added by Request/Authorized By:

GAL X

WEIGHMASTER

Surcharge for credit cards

NOTICE: MY SIGNATURE BELOW INDICATES THAT I HAVE READ THE HEALTH
WARNING NOTICE AND SUPPLIER WILL NOT BE RESPONSIBLE FOR ANY DAMAGE
CAUSED WHEN DELIVERING INSIDE CURB LINE.

LOAD RECEIVED BY

x

122196

TEXCRETE
Ready-mix Concrete Company

REMIT PAYMENT TO:
P.O. BOX138
KURTEN, TX 77862

5222 Sandy Point RD.
Bryan, Tx 77807

TEXCRETE

17534 SH 6 South
College Station, TX 77845

18935 Circle Lake Dr.
Pinehurst, TX 77362

122192

* BCS DISPATCH - 979-316-2906
PINEHURST DISPATCH - 936-232-5815
OFFICE - 979-985-3636

MBC MANAGEMENT
3100 SH47 Bryan

TTI Warehouse (RT 2818, RT 21, LTB SILVER
HILL RD, RT @ THE T, RT HWY47, LT INTO
RELLIS CAMPUS, STAY STRAIGHT

TIME	FORMULA	LOAD SIZE	YARD ORDERED	DRIVER/TRUCK	PLANT TRANSACTION#
10:15	CN350CC070	7.00	13.00 P#	CHRIS BURNS130	71336
DATE	LOAD#	YARDS DEL.	BATCH#	WATER TRIM	TICKET NUMBER
11/18/22	X-BOLT	7.00	7.00		69522

QUANTITY	CODE	DESCRIPTION	UNIT PRICE	EXTENDED PRICE
7.00 CY	CN350CC0700	COM, 5000, REQ, 7"		
1.00 ea	FUEL	Fuel Charge		

Thank you for your business

LEFT PLANT	ARRIVED JOB	START UNLOADING	SLUMP	CONCRETE TEMP.	AIR TEMP
1024	1043	1044			
FINISH UNLOADING	LEFT JOB	ARRIVED AT PLANT	ON SITE TESTING		
			TESTING LAB:	TERRACON GESSNER CME	OTHER
		TESTED	AIR	CYLINDERS	
		<input type="checkbox"/> YES <input type="checkbox"/> NO			

Tax
Prev. AMT
Ticket Total

ADDITIONAL CHARGE 1

ADDITIONAL CHARGE 2

GRAND TOTAL

WARNING
IRRITATING TO THE SKIN AND EYES
Contains Portland Cement. Wear Rubber Boots and Gloves. PROLONGED CONTACT MAY CAUSE BURNS. Avoid Contact With Eyes and Prolonged Contact with Skin. In Case of Contact with Skin or Eyes, Rinse Thoroughly With Water. If Irritation Persists, Get Medical Attention. **KEEP CHILDREN AWAY.**
CONCRETE is a PERISHABLE COMMODITY and BECOMES THE PROPERTY of the PURCHASER UPON LEAVING the PLANT. ANY CHANGES or CANCELLATION of ORIGINAL INSTRUCTIONS MUST be TELEPHONED to the OFFICE BEFORE LOADING starts. The undersigned promises to pay all costs, including reasonable attorney's fees, incurred in collecting any sums owed.
All accounts not paid within 30 days of delivery will bear interest at the rate of 18% per annum. Not Responsible For Reactive Aggregate or Color Quality. No Claim Allowed Unless Made at Time Material is Delivered.
A \$25.00 Service Charge and Loss of the Cash Discounted will be Collected on all Returned Checks. Demerage charge after 90 min. will be \$100.00/hr.

PROPERTY DAMAGE RELEASE
(TO BE SIGNED IF DELIVERY TO BE MADE INSIDE CURB LINE)
Dear Customer - The driver of this truck in presenting this RELEASE to you for your signature is of the opinion that the size and weight of this truck may possibly cause damage to the premises and/or adjacent property if he places the material in this load where you desire it. It is our wish to help you in anyway that we can, but in order to do this the driver is requesting that you sign this RELEASE relieving him and this supplier from any responsibility from damage that may occur to the premises and/or adjacent property, this material and that you also agree to help him remove mud from the wheels of this vehicle so that he will not stir the public streets. Further as additional consideration: the undersigned agrees to indemnify and hold harmless the driver of this truck and this supplier for any and all damage to the premises and/or adjacent property which may be claimed by anyone to have arisen out of delivery of this order SIGNED:

Excessive Water is Detrimental to Concrete Performance.
H₂O Added by Request/Authorized By:

GAL X

WEIGHMASTER

Surcharge for credit cards

NOTICE: MY SIGNATURE BELOW INDICATES THAT I HAVE READ THE HEALTH WARNING NOTICE AND SUPPLIER WILL NOT BE RESPONSIBLE FOR ANY DAMAGE CAUSED WHEN DELIVERING INSIDE CURB LINE.

LOAD RECEIVED BY

X

X

122192

CONCRETE COMPRESSIVE STRENGTH TEST REPORT

Report Number: A1171057.0256
Service Date: 11/18/22
Report Date: 12/14/22 Revision 1 - Data Correction
Task: PO# 440873-01



6198 Imperial Loop
College Station, TX 77845-5765
979-846-3767 Reg No: F-3272

Client

Texas Transportation Institute
Attn: Bill Griffith
TTI Business Office
3135 TAMU
College Station, TX 77843-3135

Project

Riverside Campus
Riverside Campus
Bryan, TX

Project Number: A1171057

Material Information

Specified Strength:

Mix ID:

Supplier:

Batch Time: 1015

Truck No.: 130

Plant:

Ticket No.: 69522

Sample Information

Sample Date:

11/18/22 Sample Time: 1050

Sampled By:

Patrick Moore

Weather Conditions:

Cloudy, light breeze

Accumulative Yards:

7/13 Batch Size (cy): 7

Placement Method:

Direct Discharge

Water Added Before (gal):

0

Water Added After (gal):

0

Sample Location:

Crash Barriers 1 & 2

Placement Location:

Concrete Crash Barriers 1, 2, & 3

Field Test Data

Test	Result	Specification
Slump (in):	4	
Air Content (%):	1.4	
Concrete Temp. (F):	71	
Ambient Temp. (F):	49	
Plastic Unit Wt. (pcf):	151.6	
Yield (Cu. Yds.):		

Laboratory Test Data

Set No.	Spec ID	Cyl. Cond.	Avg Diam. (in)	Area (sq in)	Date Received	Date Tested	Age at Test (days)	Max Load (lbs)	Comp Strength (psi)	Frac Type	Tested By
1	A	Good	6.00	28.27		11/30/22	12 F	150,400	5,320	5	ARH
1	B	Good	6.00	28.27		11/30/22	12 F	156,480	5,540	2	ARH
1	C	Good	6.00	28.27		11/30/22	12 F	156,380	5,530	2	ARH
1	D						Hold				
1	E						Hold				

Initial Cure: Outside

Final Cure: Field Cured

Sample Description: 6-inch diameter cylinders

Comments: F = Field Cured

Note: Reported air content does not include Aggregate Correction Factor (ACF).

Samples Made By: Terracon

Services: Obtain samples of fresh concrete at the placement locations (ASTM C 172), perform required field tests and cast, cure, and test compressive strength samples (ASTM C 31, C 39, C 1231).

Terracon Rep.: Patrick Moore

Start/Stop: 0930-1230

Reported To: Bill at TTI

Contractor: MDC

Report Distribution:

(1) Texas Transportation Institute, Bill Griffith

Test Methods: ASTM C 31, ASTM C143, ASTM C231, ASTM C1064

The tests were performed in general accordance with applicable ASTM, AASHTO, or DOT test methods. This report is exclusively for the use of the client indicated above and shall not be reproduced except in full without the written consent of our company. Test results transmitted herein are only applicable to the actual samples tested at the location(s) referenced and are not necessarily indicative of the properties of other apparently similar or identical materials.

CR0001, 3-31-22, Rev.7

Page 1 of 2

CONCRETE COMPRESSIVE STRENGTH TEST REPORT

Report Number: A1171057.0256
Service Date: 11/18/22
Report Date: 12/14/22 Revision 1 - Data Correction
Task: PO# 440873-01



6198 Imperial Loop
College Station, TX 77845-5765
979-846-3767 Reg No: F-3272

Client

Texas Transportation Institute
Attn: Bill Griffith
TTI Business Office
3135 TAMU
College Station, TX 77843-3135

Project

Riverside Campus
Riverside Campus
Bryan, TX

Project Number: A1171057

Material Information

Specified Strength:

Mix ID:

Supplier:

Batch Time: 1034

Truck No.: 131

Plant:

Ticket No.: 69526

Sample Information

Sample Date:

11/18/22 Sample Time: 1130

Sampled By:

Patrick Moore

Weather Conditions:

Cloudy, light breeze

Accumulative Yards:

13/13 Batch Size (cy): 6

Placement Method:

Direct Discharge

Water Added Before (gal):

0

Water Added After (gal):

0

Sample Location:

Crash Barriers 2 & 3

Placement Location:

Concrete Crash Barriers 1, 2, & 3

Field Test Data

Test	Result	Specification
Slump (in):	7 1/4	
Air Content (%):	1.1	
Concrete Temp. (F):	70	
Ambient Temp. (F):	49	
Plastic Unit Wt. (pcf):	151.0	
Yield (Cu. Yds.):		

Laboratory Test Data

Set No.	Spec ID	Cyl. Cond.	Avg Diam. (in)	Area (sq in)	Date Received	Date Tested	Age at Test (days)	Max Load (lbs)	Comp Strength (psi)	Frac Type	Tested By
2	A	Good	6.00	28.27		11/30/22	12 F	152,340	5,390	5	AWD
2	B	Good	6.00	28.27		11/30/22	12 F	150,920	5,340	3	AWD
2	C	Good	6.00	28.27		11/30/22	12 F	170,740	6,040	5	AWD
2	D						Hold				

Initial Cure: Outside

Final Cure: Field Cured

Sample Description: 6-inch diameter cylinders

Comments: F = Field Cured

Note: Reported air content does not include Aggregate Correction Factor (ACF).

Samples Made By: Terracon

Services: Obtain samples of fresh concrete at the placement locations (ASTM C 172), perform required field tests and cast, cure, and test compressive strength samples (ASTM C 31, C 39, C 1231).

Terracon Rep.: Patrick Moore

Reported To: Bill at TTI

Contractor: MDC

Report Distribution:

(1) Texas Transportation Institute, Bill Griffith

Start/Stop: 0930-1230

Reviewed By:


Alexander Dunigan
Project Manager

Test Methods: ASTM C 31, ASTM C143, ASTM C231, ASTM C1064

The tests were performed in general accordance with applicable ASTM, AASHTO, or DOT test methods. This report is exclusively for the use of the client indicated above and shall not be reproduced except in full without the written consent of our company. Test results transmitted herein are only applicable to the actual samples tested at the location(s) referenced and are not necessarily indicative of the properties of other apparently similar or identical materials.

Concrete Core Test Report

Report Number: A1171057.0279
Service Date: 08/18/23
Report Date: 08/28/23 Revision 1 -
Task: PO# 440873-01


6198 Imperial Loop
College Station, TX 77845-5765
979-846-3767 Reg No: F-3272

Client

Texas Transportation Institute
Attn: Bill Griffith
TTI Business Office
3135 TAMU
College Station, TX 77843-3135

Project

Riverside Campus
Riverside Campus
Bryan, TX

Project Number: A1171057

Material Information

Specified Strength:

Specified Length:

Mix ID:

Nominal Maximum Size Aggregate:

Sample Information

Placement Date:

Date Tested: 08/23/23

Time: 0000

Sampled By:

Drill Directions: Vertical

Date Core Obtained: 08/18/23

Time: 0000

Date Ends Trimmed: 08/18/23

Time: 0000

Moisture Conditioning History: According to ASTM C-42

Laboratory Test Data		Cored Length	Trim Length	Capped Length	Avg. Dia.	Area	Length / Diam. Ratio	Max Load	Corr. Factor	Comp. Strength	Fracture Type	Density
Core ID	Location	(in)	(in)	(in)	(in)	(sq in)		(lbs)		(psi)		(pcf)
1	Barrier 1	14.25	8.14	8.14	3.95	12.25	2.06	93680	1.000	7640	3	

Comments:

Services:

Terracon Rep.: Mateek, James

Reported To:

Contractor:

Report Distribution:

(1) Texas Transportation Institute, Bill Griffith (1) Texas Transportation Institute, Adam Mayer

Start/Stop: 0845-1145

Reviewed By:


Alexander Dungan, P.E.
Project Manager

Test Methods:

The tests were performed in general accordance with applicable ASTM, AASHTO, or DOT test methods. This report is exclusively for the use of the client indicated above and shall not be reproduced except in full without the written consent of our company. Test results transmitted herein are only applicable to the actual samples tested at the location(s) referenced and are not necessarily indicative of the properties of other apparently similar or identical materials.

APPENDIX C. MASH TEST 4-10 (TEST 440873-01-1)

C.1. VEHICLE PROPERTIES AND INFORMATION

Date: 2022-12-01 Test No.: 440873-01-1 VIN No.: 3N1CN7AP3HL877232

Year: 2017 Make: Nissan Model: Versa

Tire Inflation Pressure: 36 PSI Odometer: 78756 Tire Size: P185/65R15

Describe any damage to the vehicle prior to test: None

- Denotes accelerometer location.

NOTES: None

Engine Type: 4 CYL

Engine CID: 1.6 L

Transmission Type:

☒ Auto or ☐ Manual
☒ FWD ☐ RWD ☐ 4WD

Optional Equipment:

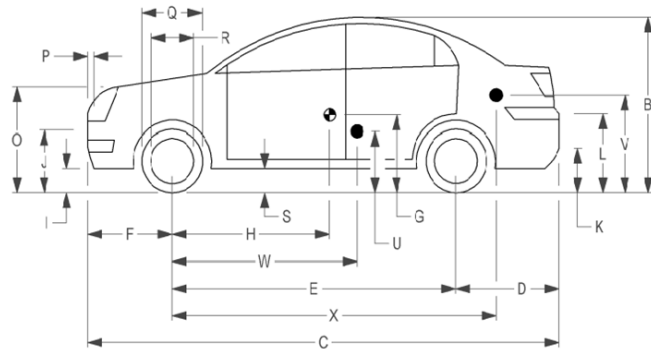
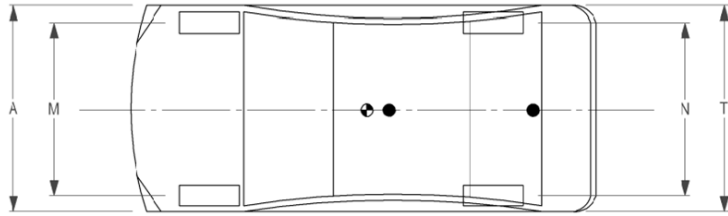
None

Dummy Data:

Type: 50th Percentile Male

Mass: 165 lb

Seat Position: IMPACT SIDE



Geometry: inches

A <u>66.70</u>	F <u>32.50</u>	K <u>12.50</u>	P <u>4.50</u>	U <u>15.50</u>
B <u>59.60</u>	G <u> </u>	L <u>26.00</u>	Q <u>24.00</u>	V <u>21.25</u>
C <u>175.40</u>	H <u>41.36</u>	M <u>58.30</u>	R <u>16.25</u>	W <u>41.30</u>
D <u>40.50</u>	I <u>7.00</u>	N <u>58.50</u>	S <u>7.50</u>	X <u>79.75</u>
E <u>102.40</u>	J <u>22.50</u>	O <u>30.50</u>	T <u>64.50</u>	
Wheel Center Ht Front <u>11.50</u>		Wheel Center Ht Rear <u>11.50</u>		W-H <u>-0.06</u>

RANGE LIMIT: A = 65 ±3 inches; C = 169 ±8 inches; E = 98 ±5 inches; F = 35 ±4 inches; H = 39 ±4 inches; O (Top of Radiator Support) = 28 ±4 inches
(M+N)/2 = 59 ±2 inches; W-H < 2 inches or use MASH Paragraph A4.3.2

GVWR Ratings:

	Mass: lb	Curb	Test Inertial	Gross Static
Front	<u>1750</u>	<u>M_{front} 1443</u>	<u>1459</u>	<u>1544</u>
Back	<u>1687</u>	<u>M_{rear} 956</u>	<u>989</u>	<u>1069</u>
Total	<u>3389</u>	<u>M_{Total} 2399</u>	<u>2448</u>	<u>2613</u>

Allowable TIM = 2420 lb ±55 lb | Allowable GSM = 2585 lb ± 55 lb

Mass Distribution:

lb LF: 710 RF: 749 LR: 526 RR: 463

Figure C.1. Vehicle Properties for Test 440873-01-1.

Date: 2022-12-01 Test No.: 440873-01-1 VIN No.: 3N1CN7AP3HL877232
 Year: 2017 Make: Nissan Model: Versa

VEHICLE CRUSH MEASUREMENT SHEET¹

Complete When Applicable	
End Damage Undeformed end width _____ Corner shift: A1 _____ A2 _____ End shift at frame (CDC) (check one) < 4 inches _____ ≥ 4 inches _____	Side Damage Bowing: B1 _____ X1 _____ B2 _____ X2 _____ Bowing constant $\frac{X1 + X2}{2} = \underline{\hspace{2cm}}$

Note: Measure C₁ to C₆ from Driver to Passenger Side in Front or Rear Impacts – Rear to Front in Side Impacts.

Specific Impact Number	Plane* of C-Measurements	Direct Damage		Field L**	C ₁	C ₂	C ₃	C ₄	C ₅	C ₆	±D
		Width*** (CDC)	Max**** Crush								
1	AT FT BUMPER	14	10	28							-14
2	ABOVE FT BUMPER	14	10	44							60
	Measurements recorded										
	<input checked="" type="checkbox"/> inches or <input type="checkbox"/> mm										

¹Table taken from National Accident Sampling System (NASS).

*Identify the plane at which the C-measurements are taken (e.g., at bumper, above bumper, at sill, above sill, at beltline, etc.) or label adjustments (e.g., free space).

Free space value is defined as the distance between the baseline and the original body contour taken at the individual C locations. This may include the following: bumper lead, bumper taper, side protrusion, side taper, etc. Record the value for each C-measurement and maximum crush.

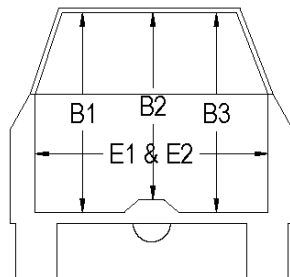
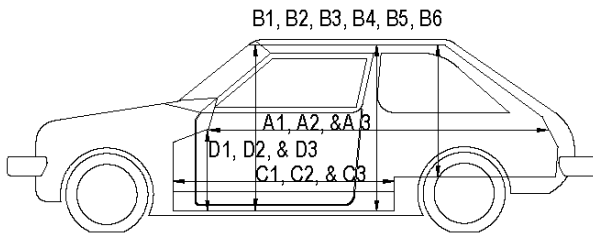
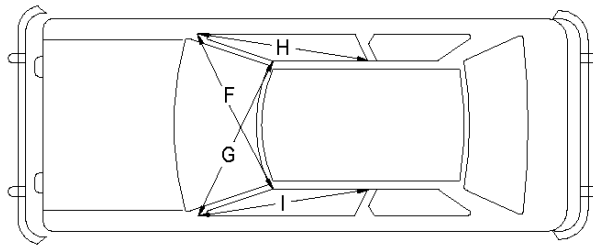
**Measure and document on the vehicle diagram the beginning or end of the direct damage width and field L (e.g., side damage with respect to undamaged axle).

***Measure and document on the vehicle diagram the location of the maximum crush.

Note: Use as many lines/columns as necessary to describe each damage profile.

Figure C.2. Exterior Crush Measurements for Test 440873-01-1.

Date: 2022-12-01 Test No.: 440873-01-1 VIN No.: 3N1CN7AP3HL877232
 Year: 2017 Make: Nissan Model: Versa



OCCUPANT COMPARTMENT DEFORMATION MEASUREMENT

	Before	After (inches)	Differ.
A1	67.50	67.50	0.00
A2	67.25	67.25	0.00
A3	67.75	67.75	0.00
B1	40.50	40.50	0.00
B2	39.00	39.00	0.00
B3	40.50	40.50	0.00
B4	36.25	36.25	0.00
B5	36.00	36.00	0.00
B6	36.25	36.25	0.00
C1	26.00	23.50	-2.50
C2	0.00	0.00	0.00
C3	26.00	26.00	0.00
D1	9.50	9.50	0.00
D2	0.00	0.00	0.00
D3	9.50	9.50	0.00
E1	51.50	49.50	-2.00
E2	51.00	51.00	0.00
F	51.00	51.00	0.00
G	51.00	51.00	0.00
H	37.50	37.50	0.00
I	37.50	37.50	0.00
J*	48.00	46.00	-2.00

*Lateral area across the cab from driver's side kick panel to passenger's side kick panel.

Figure C.3. Occupant Compartment Measurements for Test 440873-01-1.

C.2. SEQUENTIAL PHOTOGRAPHS

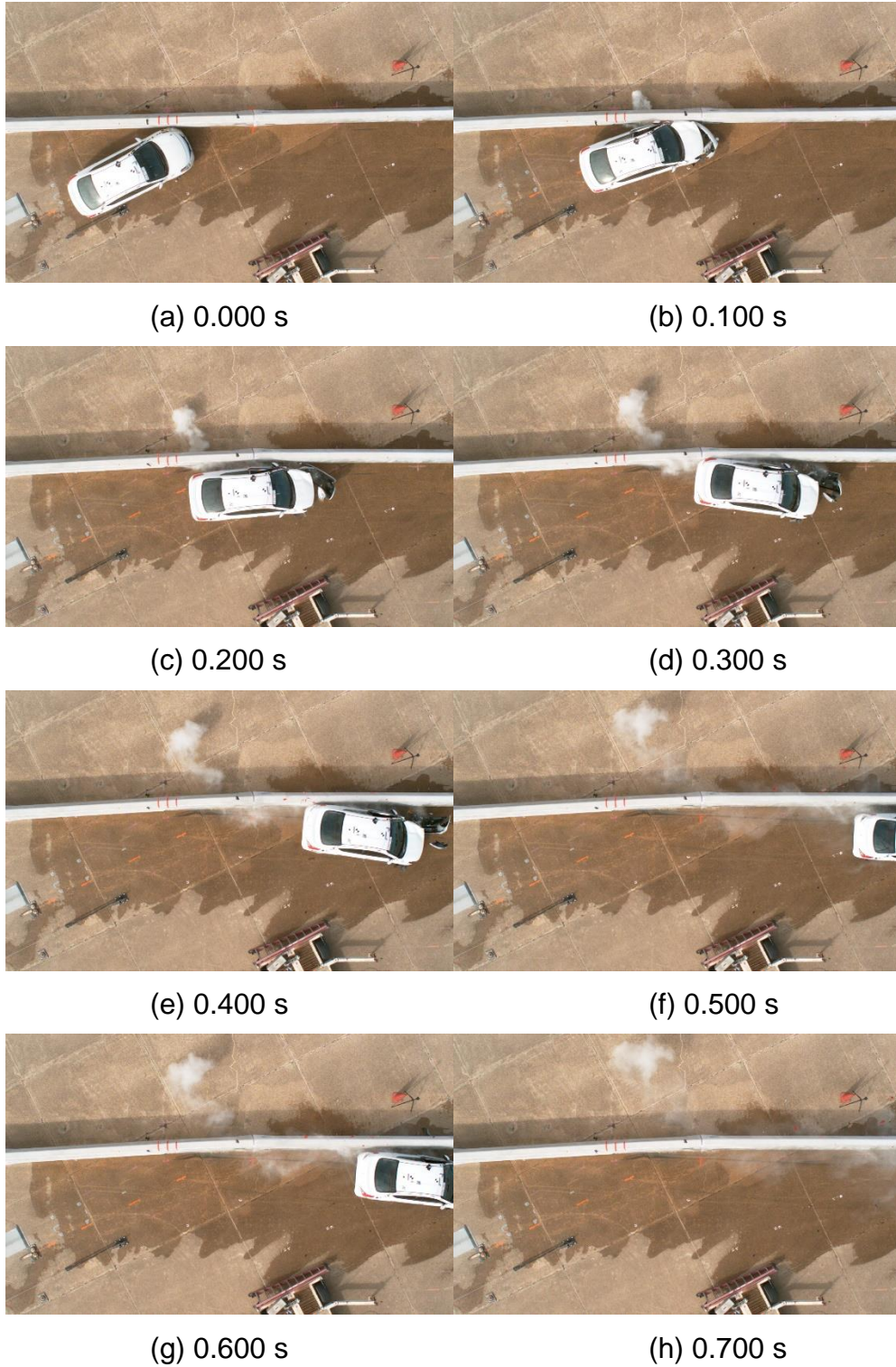


Figure C.4. Sequential Photographs for Test 440873-01-1 (Overhead Views).



(a) 0.000 s

(b) 0.100 s



(c) 0.200 s

(d) 0.300 s



(e) 0.400 s

(f) 0.500 s



(g) 0.600 s

(h) 0.700 s

Figure C.5. Sequential Photographs for Test 440873-01-1 (Frontal Views).



(a) 0.000 s

(b) 0.100 s



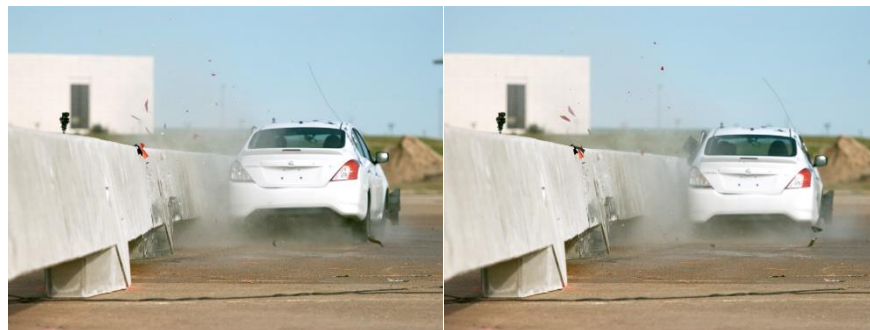
(c) 0.200 s

(d) 0.300 s



(e) 0.400 s

(f) 0.500 s



(g) 0.600 s

(h) 0.700 s

Figure C.6. Sequential Photographs for Test 440873-01-1 (Rear Views).

C.3. VEHICLE ANGULAR DISPLACEMENTS

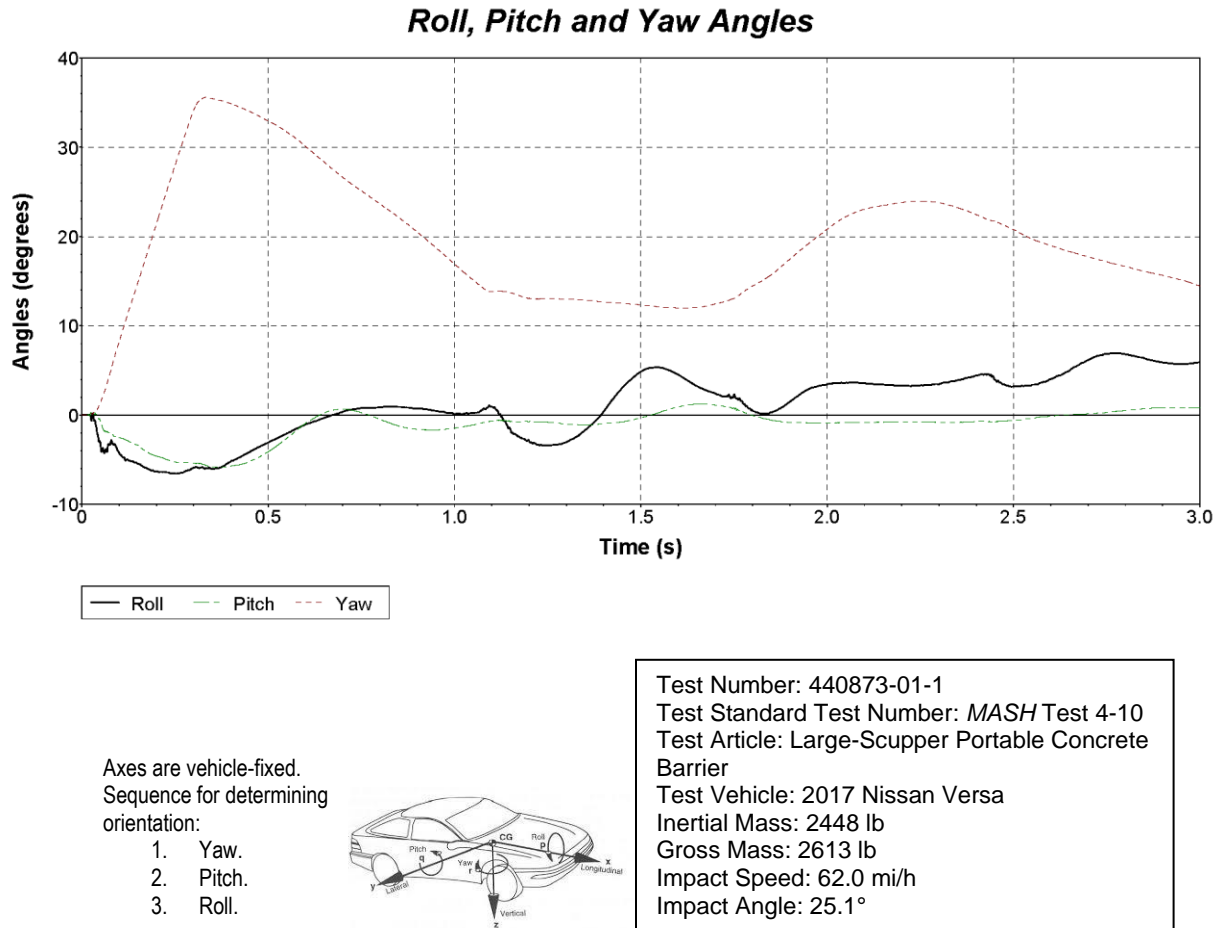
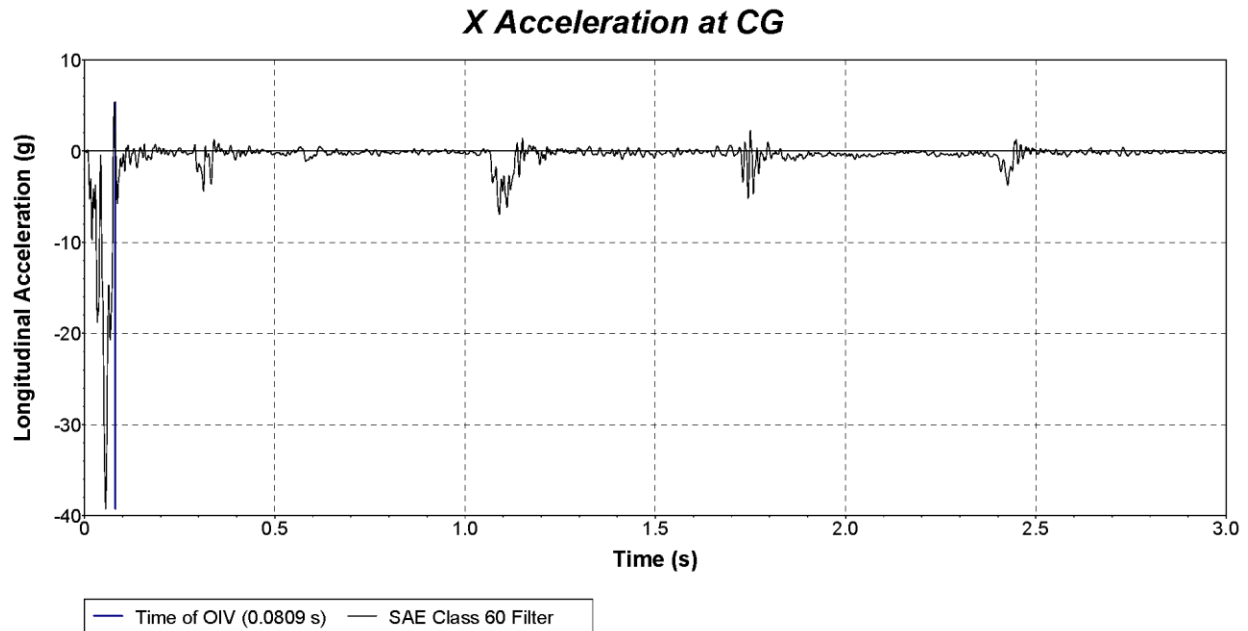
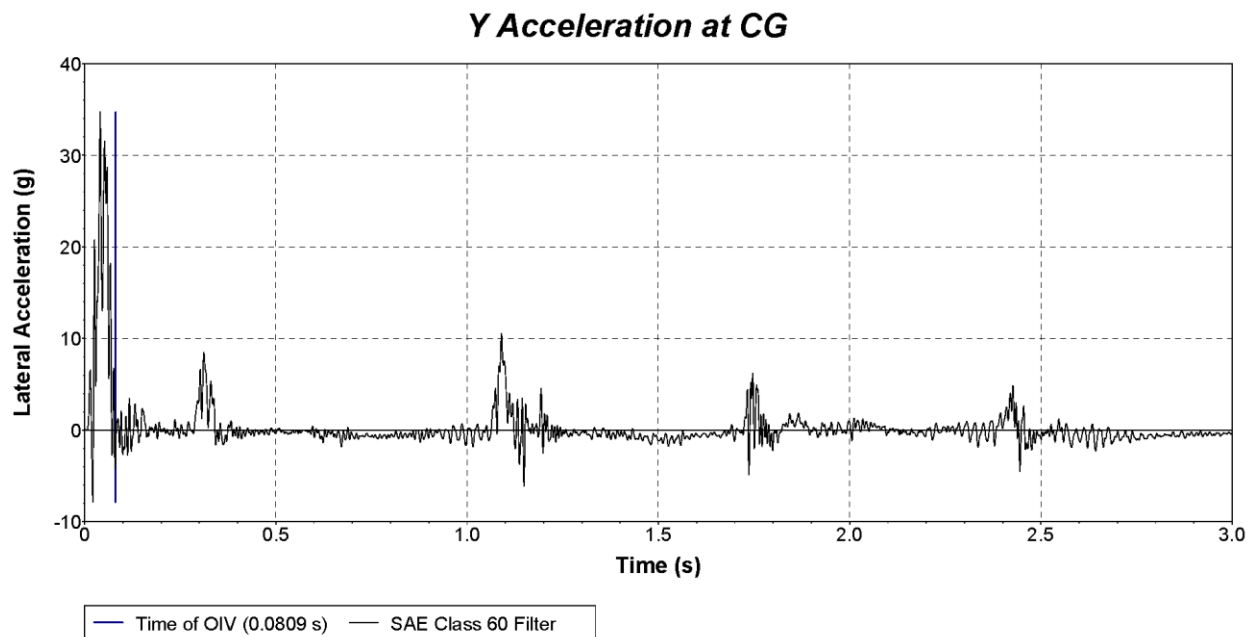


Figure C.7. Vehicle Angular Displacements for Test 440873-01-1.

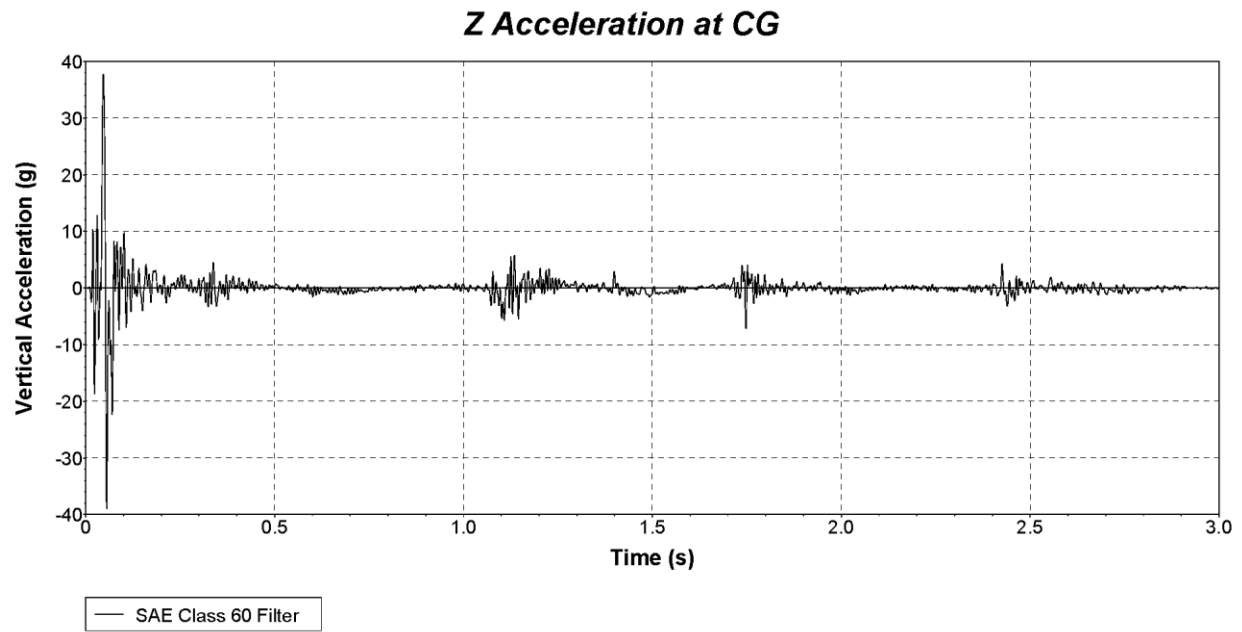
C.4. VEHICLE ACCELERATIONS



**Figure C.8. Vehicle Longitudinal Accelerometer Trace for Test 440873-01-1
(Accelerometer Located at Center of Gravity).**



**Figure C.9. Vehicle Lateral Accelerometer Trace for Test 440873-01-1
(Accelerometer Located at Center of Gravity).**



**Figure C.10. Vehicle Vertical Accelerometer Trace for Test 440873-01-1
(Accelerometer Located at Center of Gravity).**

APPENDIX D. MASH TEST 4-11 (TEST 440873-01-2)

D.1. VEHICLE PROPERTIES AND INFORMATION

Date: 2022-12-13 Test No.: 440873-01-2 VIN No.: 1C6RR6FT3HS769343
 Year: 2017 Make: RAM Model: 1500
 Tire Size: 265/70 R 17 Tire Inflation Pressure: 35 psi
 Tread Type: Highway Odometer: 147360
 Note any damage to the vehicle prior to test: None

- Denotes accelerometer location.

NOTES: None

Engine Type: V-8
 Engine CID: 5.7 liter

Transmission Type:

☒ Auto or ☐ Manual
☐ FWD ☒ RWD ☐ 4WD

Optional Equipment:
None

Dummy Data:

Type: 50th Percentile Male
 Mass: 165 lb
 Seat Position: IMPACT SIDE

Geometry: inches

A	78.50	F	40.00	K	20.00	P	3.00	U	26.75
B	74.00	G	28.75	L	30.00	Q	30.50	V	30.25
C	227.50	H	61.94	M	68.50	R	18.00	W	62.00
D	44.00	I	11.75	N	68.00	S	13.00	X	79.00
E	140.50	J	27.00	O	46.00	T	77.00		
Wheel Center Height Front		14.75	Wheel Well Clearance (Front)		6.00	Bottom Frame Height - Front		12.50	
Wheel Center Height Rear		14.75	Wheel Well Clearance (Rear)		9.25	Bottom Frame Height - Rear		22.50	

RANGE LIMIT: A=78 ±2 inches; C=237 ±13 inches; E=148 ±12 inches; F=39 ±3 inches; G = > 28 inches; H = 63 ±4 inches; I=43 ±4 inches; (M+N)/2=67 ±1.5 inches

GVWR Ratings:

	Mass: lb	Curb	Test Inertial	Gross Static
Front	3700	2893	2813	2898
Back	3900	1974	2218	2298
Total	6700	4867	5031	5196

(Allowable Range for TIM and GSM = 5000 lb ±110 lb)

Mass Distribution:

lb LF: 1414 RF: 1399 LR: 1125 RR: 1093

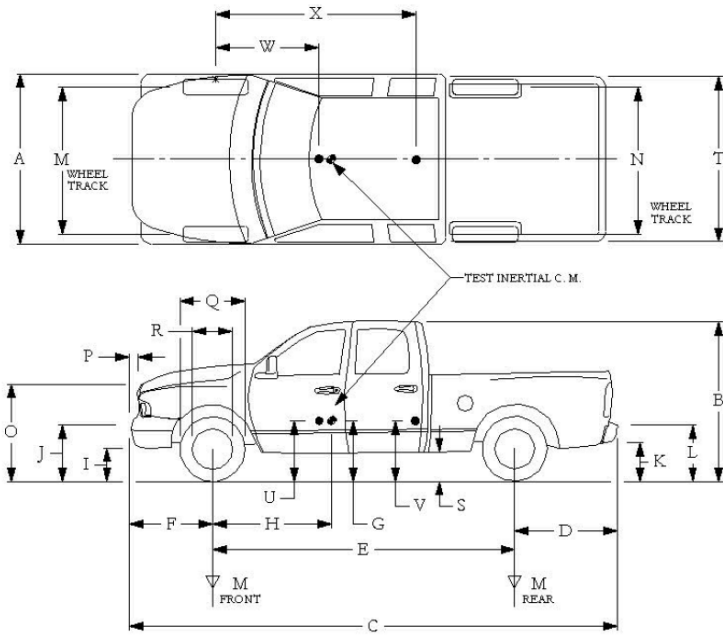


Figure D.1. Vehicle Properties for Test 440873-01-2.

Date: 2022-12-13 Test No.: 440873-01-2 VIN No.: 1C6RR6FT3HS769343
 Year: 2017 Make: RAM Model: 1500

VEHICLE CRUSH MEASUREMENT SHEET¹

Complete When Applicable	
End Damage	Side Damage
Undeformed end width _____ Corner shift: A1 _____ A2 _____ End shift at frame (CDC) (check one) < 4 inches _____ ≥ 4 inches _____	Bowing: B1 _____ X1 _____ B2 _____ X2 _____ Bowing constant $\frac{X1 + X2}{2} = \underline{\hspace{2cm}}$

Note: Measure C₁ to C₆ from Driver to Passenger Side in Front or Rear Impacts – Rear to Front in Side Impacts.

Specific Impact Number	Plane* of C-Measurements	Direct Damage		Field L**	C ₁	C ₂	C ₃	C ₄	C ₅	C ₆	±D
		Width*** (CDC)	Max**** Crush								
1	AT FT BUMPER	12	12	36							-18
2	ABOVE FT BUMPER	12	12	60							62
	Measurements recorded										
	<input checked="" type="checkbox"/> inches or <input type="checkbox"/> mm										

¹Table taken from National Accident Sampling System (NASS).

*Identify the plane at which the C-measurements are taken (e.g., at bumper, above bumper, at sill, above sill, at beltline, etc.) or label adjustments (e.g., free space).

Free space value is defined as the distance between the baseline and the original body contour taken at the individual C locations. This may include the following: bumper lead, bumper taper, side protrusion, side taper, etc. Record the value for each C-measurement and maximum crush.

**Measure and document on the vehicle diagram the beginning or end of the direct damage width and field L (e.g., side damage with respect to undamaged axle).

***Measure and document on the vehicle diagram the location of the maximum crush.

Note: Use as many lines/columns as necessary to describe each damage profile.

Figure D.2. Exterior Crush Measurements for Test 440873-01-2.

Date: 2022-12-13 Test No.: 440873-01-2 VIN No.: 1C6RR6FT3HS769343
 Year: 2017 Make: RAM Model: 1500

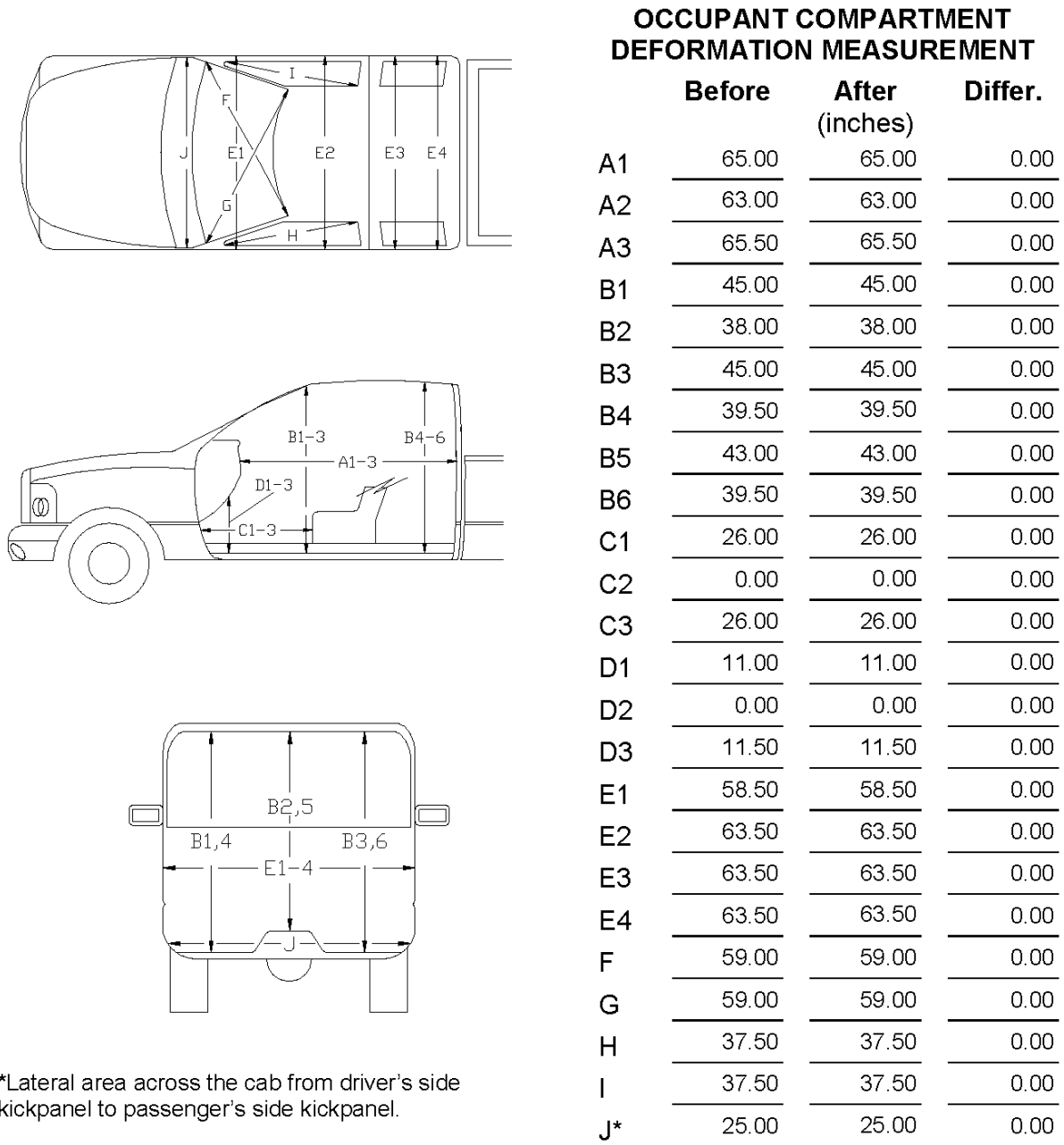


Figure D.3. Occupant Compartment Measurements for Test 440873-01-2.

D.2. SEQUENTIAL PHOTOGRAPHS



(a) 0.000 s

(b) 0.100 s



(c) 0.200 s

(d) 0.300 s



(e) 0.400 s

(f) 0.500 s



(g) 0.600 s

(h) 0.700 s

Figure D.4. Sequential Photographs for Test 440873-01-2 (Overhead Views).



(a) 0.000 s

(b) 0.100 s



(c) 0.200 s

(d) 0.300 s



(e) 0.400 s

(f) 0.500 s



(g) 0.600 s

(h) 0.700 s

Figure D.5. Sequential Photographs for Test 440873-01-2 (Frontal Views).



(a) 0.000 s

(b) 0.100 s



(c) 0.200 s

(d) 0.300 s



(e) 0.400 s

(f) 0.500 s

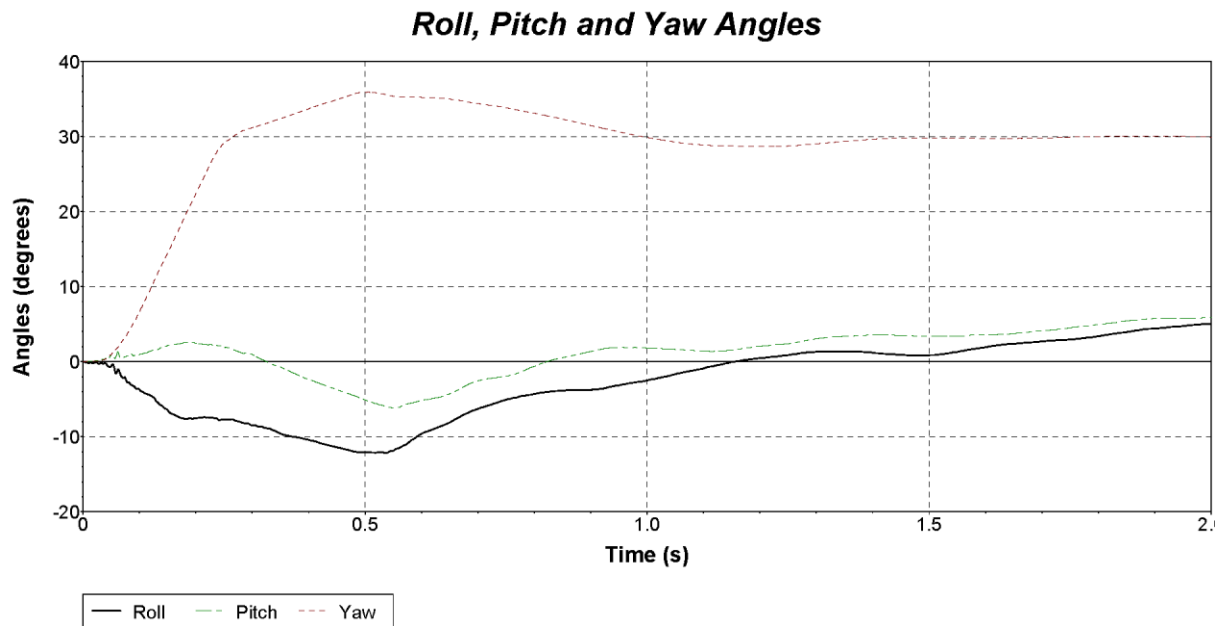


(g) 0.600 s

(h) 0.700 s

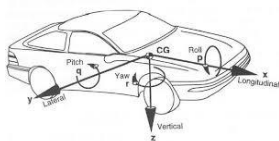
Figure D.6. Sequential Photographs for Test 440873-01-2 (Rear Views).

D.3. VEHICLE ANGULAR DISPLACEMENTS



Axes are vehicle-fixed.
Sequence for determining
orientation:

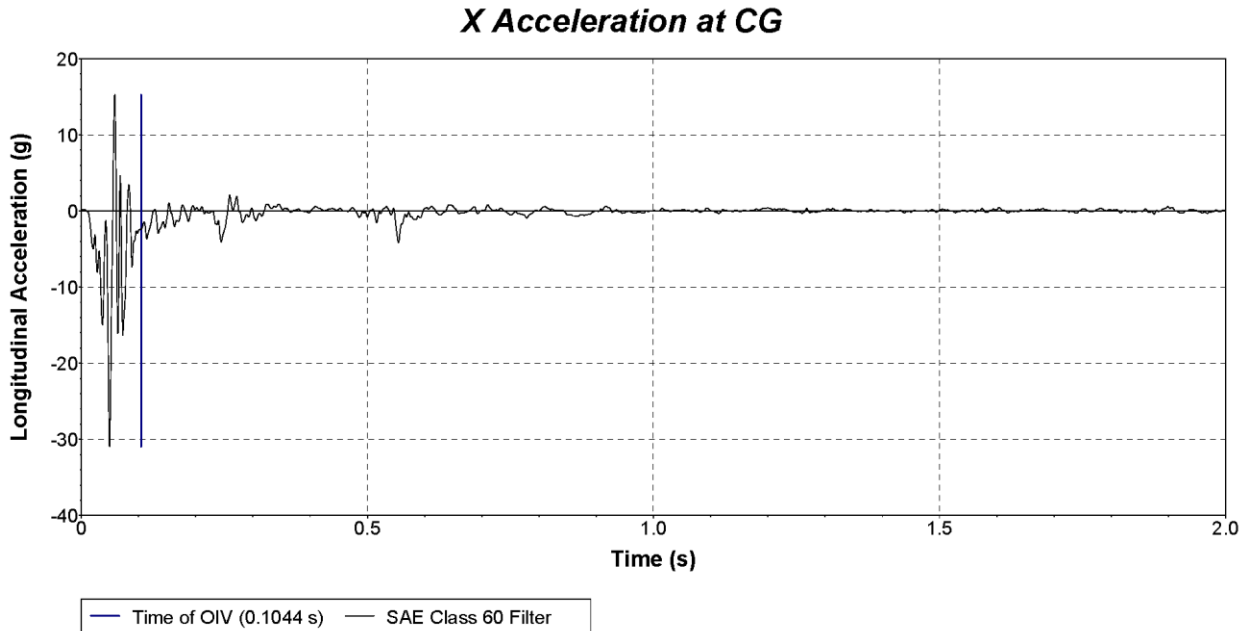
4. Yaw.
5. Pitch.
6. Roll.



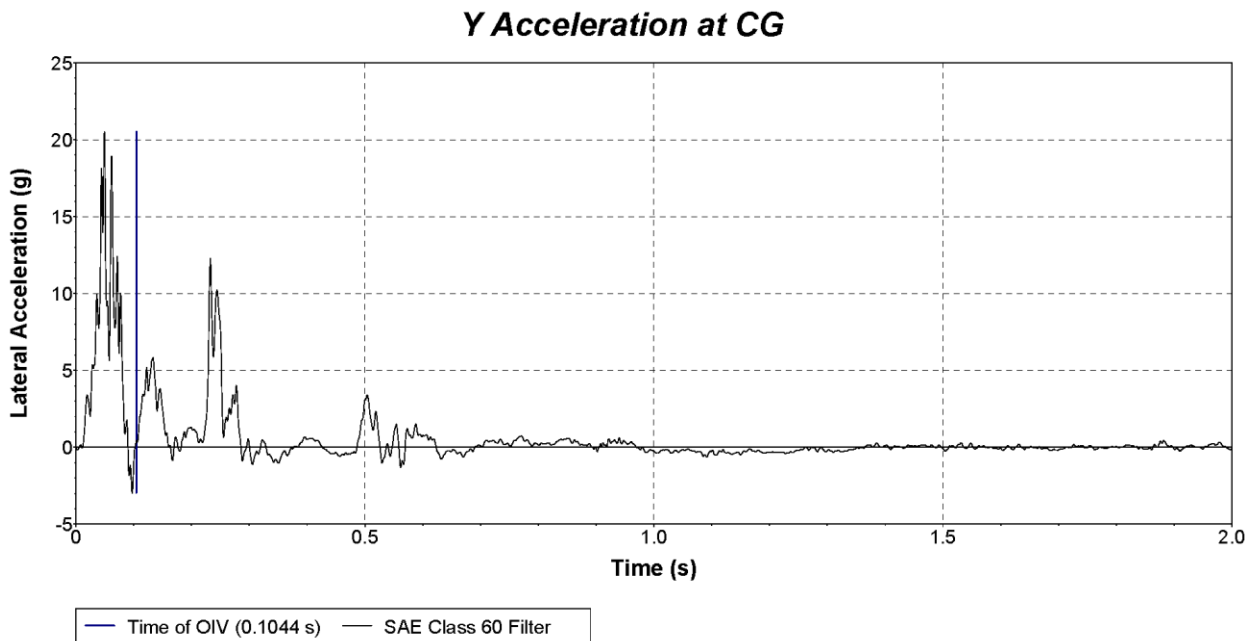
Test Number: 440873-01-2
Test Standard Test Number: *MASH* Test 4-11
Test Article: Large-Scupper Portable Concrete Barrier
Test Vehicle: 2017 RAM 1500
Inertial Mass: 5031 lb
Gross Mass: 5196 lb
Impact Speed: 61.7 mi/h
Impact Angle: 26.5°

Figure D.7. Vehicle Angular Displacements for Test 440873-01-2.

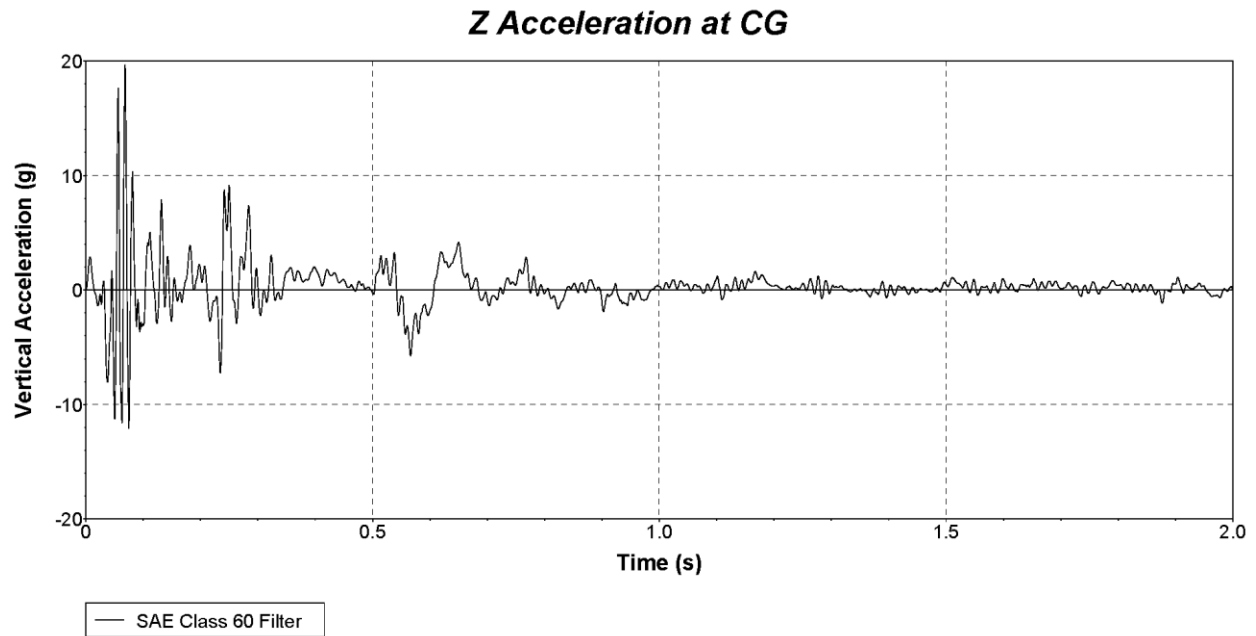
D.4. VEHICLE ACCELERATIONS



**Figure D.8. Vehicle Longitudinal Accelerometer Trace for Test 440873-01-2
(Accelerometer Located at Center of Gravity).**



**Figure D.9. Vehicle Lateral Accelerometer Trace for Test 440873-01-2
(Accelerometer Located at Center of Gravity).**

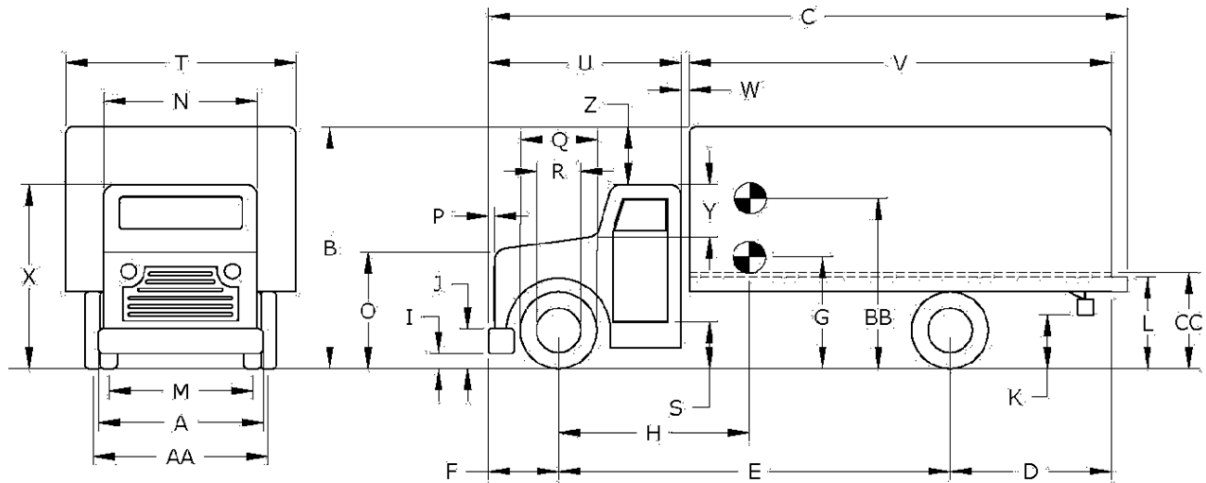


**Figure D.10. Vehicle Vertical Accelerometer Trace for Test 440873-01-2
(Accelerometer Located at Center of Gravity).**

APPENDIX E. MASH TEST 4-12 (TEST 440873-01-3)

E.1. VEHICLE PROPERTIES AND INFORMATION

Date: 2023-08-17 Test No.: 440873-1-3 VIN No.: 5PVNV8JM3D4S50368
 Year: 2013 Make: HINO Model: L SERIES
 Odometer: 244672 Tire Size Front: 275/80R22.5 Tire Size Rear: 275/80R22.5



Vehicle Geometry:		<input checked="" type="checkbox"/> inches	or	<input type="checkbox"/> mm				
A	Front Bumper Width:	92.00	K	Rear Bumper Bottom:	0.00	U	Cab Length:	108.00
B	Overall Height:	134.75	L	Rear Frame Top:	38.50	V	Trailer/Box Length:	224.50
C	Overall Length:	333.00	M	Front Track Width:	79.50	W	Gap Width:	2.50
D	Rear Overhang:	88.50	N	Roof Width:	72.00	X	Overall Front Height:	104.00
E	Wheel Base:	205.00	O	Hood Height:	59.25	Y	Roof-Hood Distance:	34.25
F	Front Overhang:	39.50	P	Bumper Extension:	1.00	Z	Roof-Box Height Difference:	29.50
G	C.G. Height:	51.75	Q	Front Tire Width:	40.00	AA	Rear Track Width:	72.50
H	C.G. Horizontal Dist. w/Ballast:	131.14	R	Front Wheel Width:	225.00	BB	Ballast Center of Mass:	64.50
I	Front Bumper Bottom:	16.50	S	Bottom Door Height:	37.75	CC	Cargo Bed Height:	51.00
J	Front Bumper Top:	31.50	T	Overall Width:	96.00			
Allowable Range: C = 394 inches max.; E = 240 inches max.; CC = 49 ±2 inches; BB = 63 ±2 inches above ground;								
	Wheel Center Height Front	19.00		Wheel Well Clearance (Front)	12.00		Bottom Frame Height (Front)	24.50
	Wheel Center Height Rear	19.50		Wheel Well Clearance (Rear)	4.00		Bottom Frame Height (Rear)	28.75

More information needed on next page →

Figure E.1. Vehicle Properties for Test 440873-01-3.

Date: 2023-08-17 Test No.: 440873-1-3 VIN No.: 5PVNV8JM3D4S50368
Year: 2013 Make: HINO Model: L SERIES

WEIGHTS
(☒ lb or ☐ kg)

CURB

TEST INERTIAL

W _{front axle}	6740	7980
W _{rear axle}	6750	14170
W _{TOTAL}	13490	22150

Allowable Range for CURB = 13,200 ±2200 lb | Allowable Range for TIM = 22,046 ±660 lb

Ballast: 8660 (☒ lb or ☐ kg) (as-needed)
(See MASH Section 4.2.1.2 for recommended ballasting)

Mass Distribution

(☐ lb or ☐ kg): LF: 4070 RF: 3910 LR: 7160 RR: 7010

Engine Type: CUMMINS

Accelerometer Locations (☐ inches or ☐ mm)

Engine Size: 7.0 LITER

x¹ y z²

Transmission Type:

☒ Auto or ☐ Manual

☐ FWD ☒ RWD ☐ 4WD

Front: 0.00 0.00 0.00

Center: 131.14 0.00 50.00

Rear: 143.14 0.00 50.00

Describe any damage to the vehicle prior to test:

Other notes to include ballast type, dimensions, mass, location, center of mass, and method of attachment:

TWO BLOCKS 30W X 30H X 60L

CENTERED IN MIDDLE OF BED

TIED DOWN WITH FOUR 3/8 INCH CABLES PER BLOCK

64.5 INCHES FROM GROUND TO CENTER OF BLOCK

Figure E.1. Vehicle Properties for Test 440873-01-3 (Continued).

E.2. SEQUENTIAL PHOTOGRAPHS



(a) 0.000 s

(b) 0.100 s



(c) 0.200 s

(d) 0.300 s



(e) 0.400 s

(f) 0.500 s



(g) 0.600 s

(h) 0.700 s

Figure E.2. Sequential Photographs for Test 440873-01-3 (Overhead Views).



(a) 0.000 s

(b) 0.100 s



(c) 0.200 s

(d) 0.300 s



(e) 0.400 s

(f) 0.500 s



(g) 0.600 s

(h) 0.700 s

Figure E.3. Sequential Photographs for Test 440873-01-3 (Frontal Views).



(a) 0.000 s

(b) 0.100 s



(c) 0.200 s

(d) 0.300 s



(e) 0.400 s

(f) 0.500 s



(g) 0.600 s

(h) 0.700 s

Figure E.4. Sequential Photographs for Test 440873-01-3 (Rear Views).

E.3. VEHICLE ANGULAR DISPLACEMENTS

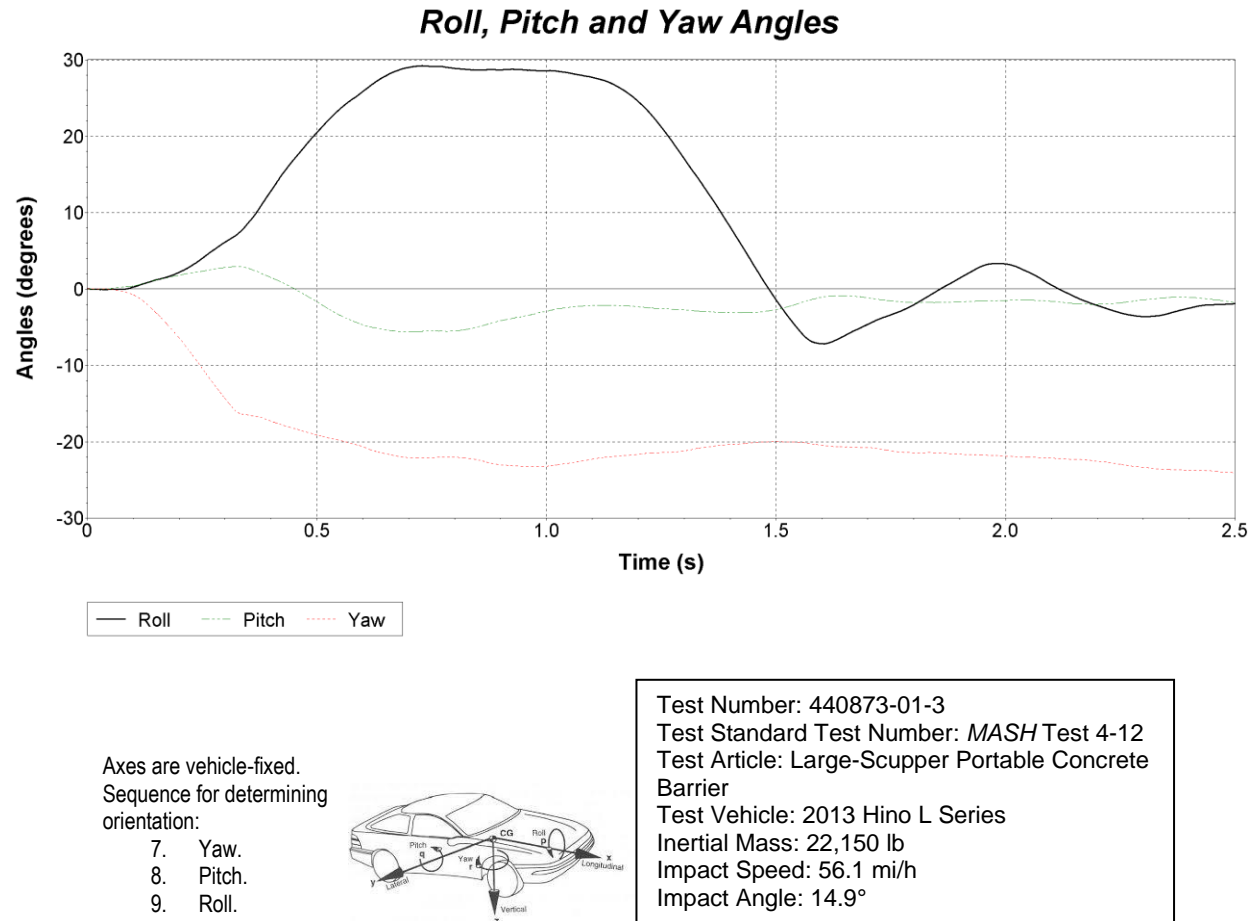
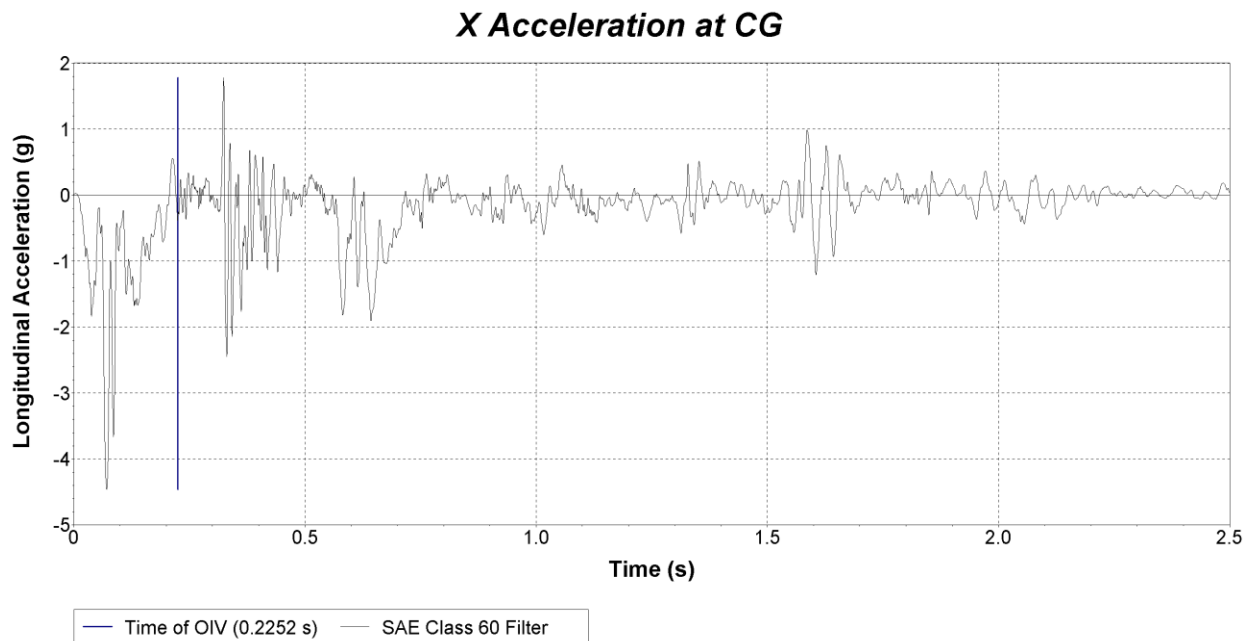
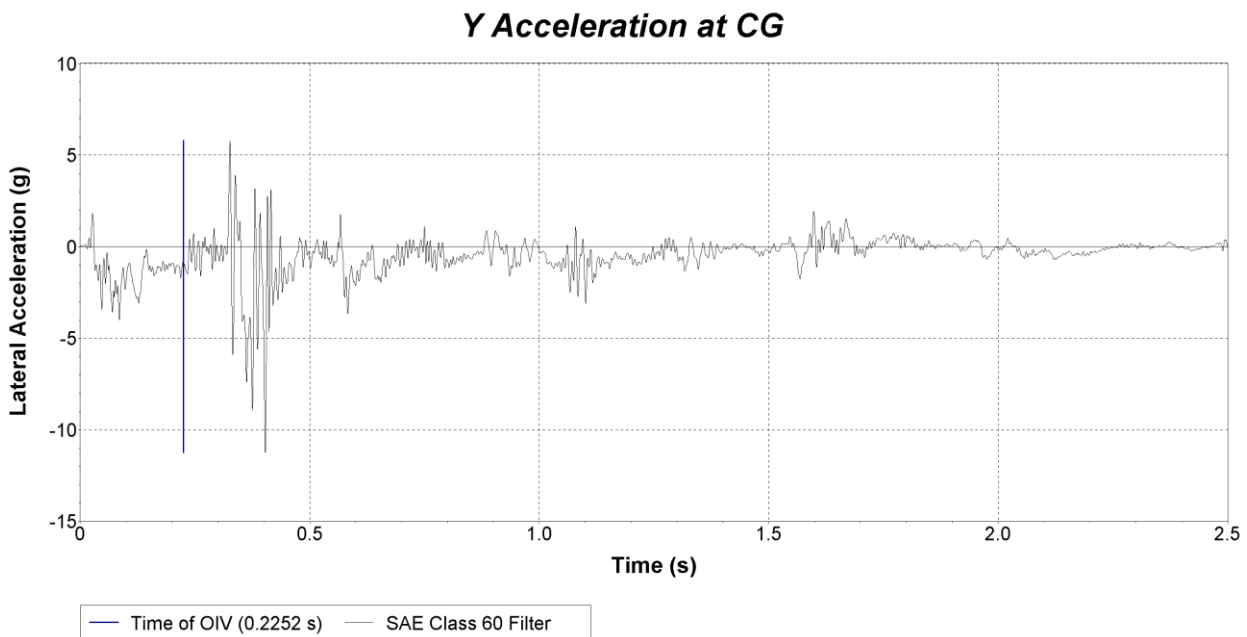


Figure E.5. Vehicle Angular Displacements for Test 440873-01-3.

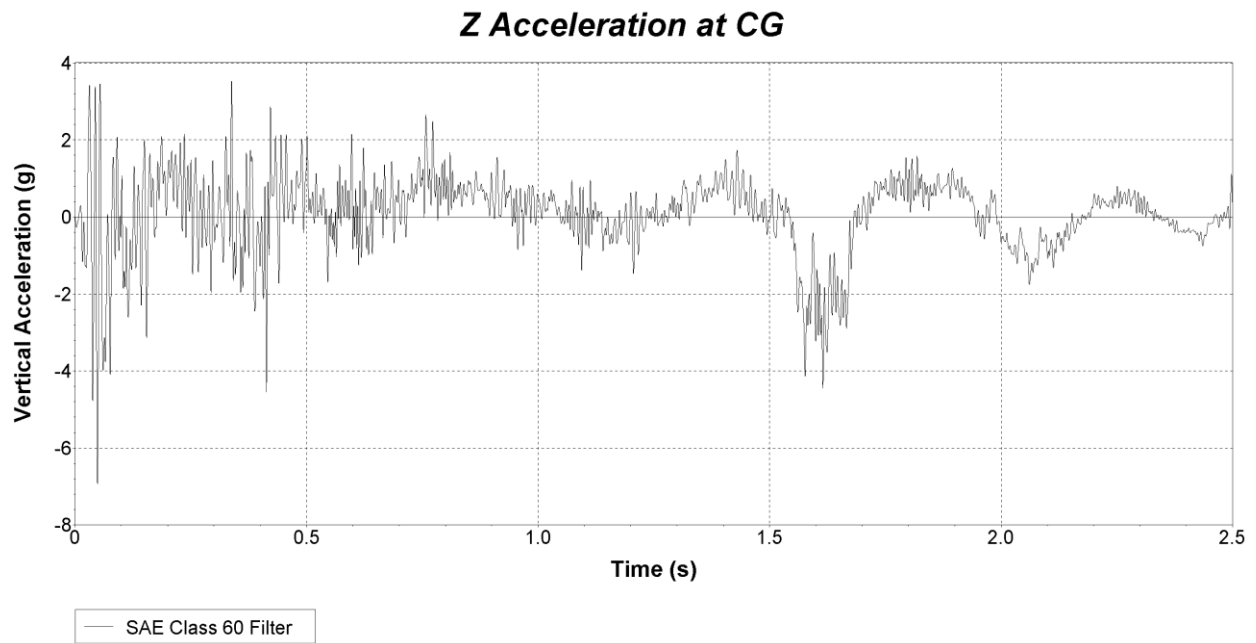
E.4. VEHICLE ACCELERATIONS



**Figure E.6. Vehicle Longitudinal Accelerometer Trace for Test 440873-01-3
(Accelerometer Located at Center of Gravity).**



**Figure E.7. Vehicle Lateral Accelerometer Trace for Test 440873-01-3
(Accelerometer Located at Center of Gravity).**



**Figure E.8. Vehicle Vertical Accelerometer Trace for Test 440873-01-3
(Accelerometer Located at Center of Gravity).**

APPENDIX F. VALUE OF RESEARCH

F.1. INTRODUCTION

In accordance with the scope of TxDOT Project 0-7087, Develop Standards for Temporary Concrete Median Barrier in Flood-Prone Areas, the research teams at TTI and the Center for Transportation Research (CTR) prepared an estimate for the VoR associated with the research products delivered for this project.

The benefit areas deemed relevant and identified in the project agreement for the purpose of establishing the VoR encompass both qualitative and economic areas. The benefit areas identified for this project are summarized in Table F.1.

Table F.1. Selected Benefit Areas for Project 0-7087.

Selected	Benefit Area	Qual	Econ	Both	TxDOT	State	Both
	Level of Knowledge	X			X		
	Management and Policy	X			X		
	Quality of Life	X			X		
	Customer Satisfaction	X			X		
	Environmental Sustainability	X				X	
X	System Reliability		X		X		
	Increased Service Life		X		X		
	Improved Productivity and Work Efficiency		X		X		
	Expedited Project Delivery		X		X		
	Reduced Administrative Costs		X		X		
	Traffic and Congestion Reduction		X			X	
	Reduced User Cost		X			X	
	Reduced Construction, Operations, and Maintenance Cost		X			X	
	Materials and Pavements		X			X	
X	Infrastructure Condition		X				X
	Freight Movement and Economic Vitality		X				X
	Intelligent Transportation Systems		X				X
X	Engineering Design Improvement			X			X
X	Safety			X			X

F.2. QUALITATIVE BENEFIT AREAS

F.2.1. Engineering Design Development/Improvement

One of the primary outcomes of Project 0-7087 was to provide rating curves showing the hydraulic efficiency of a concrete median barrier with a scupper, designed uniquely for this project, to reduce highway flooding, specifically in comparison to existing barrier designs with openings already used by TxDOT in various applications. These rating curves need to be determined experimentally on a case-by-case basis, and they can be used as a reference for implementation of any of these types of barriers without further need for experimental testing. Further, the researchers performed a detailed flow analysis of water traveling upstream of the barrier and through the scupper to inform hydraulic loading on the barrier and identify regions of potential concern in the design for a portable barrier.

F.2.2. Safety

Flooded highways negatively affect safety for road users in Texas. At best, traffic may be diverted to alternate and unfamiliar routes during flooding. Drivers attempting to navigate flooded highways are at an increased likelihood of being involved in an accident—relative to driving on dry, unobstructed highways—causing potential harm to themselves and to others, including property and infrastructure damage that may have longstanding consequences. At construction sites or regions of highways with portable barriers, risks are elevated because the barriers can become mobilized, either sliding or overturning into vehicles and/or displacing into lanes of traffic, subsequently impeding the flow of vehicles even after subsidence of floodwater. Therefore, it is necessary to understand the forces acting on portable barriers to ensure safe design of connections and features that will ensure stability of barriers in flood conditions.

F.3. ECONOMIC BENEFITS

Economic analysis pertaining to four functional areas relevant to the performance of this project and identified in the project agreement was requested.

1. System Reliability.
2. Infrastructure Condition.
3. Engineering Design Improvement.
4. Safety.

After analyzing these functional areas, the research team generated Figure F.1. The considerations that went into the computation of the VoR (explained in greater detail below) are summarized next.

If a road is flooded (water coverage exceeding a safe threshold for passage), it cannot be used. This road closure reduces commercial transport of goods and services, exacerbated when (a) significant distances of highway are closed, (b) segments are closed for substantial amounts of time, or (c) some combination thereof. Personal travel is also impacted, which can range from mere inconveniences and delays to more substantial health outcomes.

Several detrimental effects can occur as a result of highway flooding. For example, there is an increased risk of potholes or damage to the highway surface that require repair or replacement, in particular in coastal regions where saline or brackish water may intrude inland during an extreme storm event. There is also risk of debris accumulating on roadways, which needs to be manually removed. Further, as in the case of Hurricane Harvey when explosives were used to remove a portion of median barriers that were contributing to upstream flooding, follow-up maintenance may be required to return a highway to its normal safely functioning condition. With portable barriers, additional damage can result from mobilized barriers that were not adequately supported. These barriers can slide across the roadway, or overturn—requiring subsequent removal, repair, or replacement to their intended positions to ensure continued safe passage of vehicles and use of the highway.

In addition to concerns associated with the roadway itself, flooding exacerbated by highway median barriers can persist through commercial and residential zones adjacent to the highway. The cost is highly variable by region, depending on topography (i.e., likelihood to flood) and level of development (commercial, residential, medical, industrial, etc.). Given that portable barriers are often located at construction sites, displaced barriers may further delay construction progress or damage surrounding structures.

F.4. COMPUTED VALUE OF RESEARCH

Figure F.1 presents a summary of the VoR calculations for this project:

- Project Budget: \$639,000.
- Project Duration: 2.0 years.
- Expected Value (per year): \$51,000,000.
- Expected Value Duration (years): 15.
- Total Savings: \$458,361,000.
- Net Present Value (NPV): \$376,760,050.
- Payback Period (years): 0.012529.
- Cost Benefit Ratio (CBR, \$1: \$): \$590.

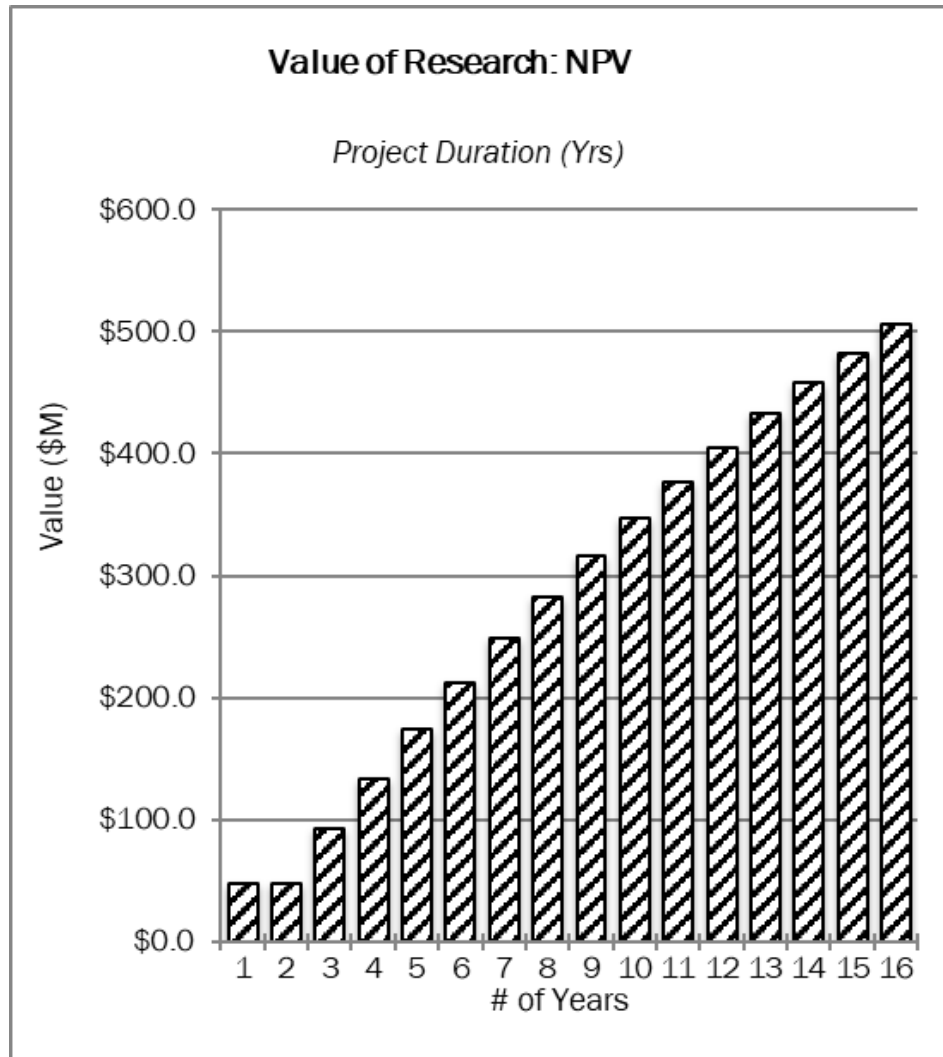


Figure F.1. Summary of VoR Calculations for Project 0-7087.

The explanation for values assigned in Figure F.1 are attributed to two primary sources:

- Costs attributed to reduction in accidents in suboptimal (i.e., wet or submerged) roadway conditions in work zones (i.e., with likely use of portable median barriers) leading to personal injury or fatality.
- The economic cost due to loss of commerce, transit, and so forth from highway closures during sustained flooding as a result of damming effects of a traditional solid concrete median barrier.

These two factors were identified as the leading drivers of quantifiable cost savings, and details are provided below.

According to the annual Texas motor vehicle crash statistics published by TxDOT for 2022 (1), approximately 12 percent of reported vehicular crashes occurred on rural roads that were wet or contained standing water, whereas 10 percent of reported vehicular crashes occurred in urban areas where roads were wet or contained standing

water. Of the reported crashes in either wet or standing water conditions, approximately 2 percent of accidents sustained either fatal (type K) or severe personal injury (type A) in urban areas, compared to 4 percent in rural areas, while 11 percent were of type B (non-incapacitating injury) in both rural and urban areas.

The 2022 *Highway Safety Improvement Program Guidelines* assign the cost associated with either a fatal (K) or severe injury (A) event to be \$4.0 million, while the cost associated with a non-incapacitating injury (B) is equal to \$540,000. Given the total number of reported type A, B, and K injuries in either wet or standing water conditions, the total cost associated with these incidents is equal to \$9.7 billion for 2022, statewide (2).

While wet roadway conditions are inevitable during and immediately following rainfall, sustained wet roads or roads with standing water can be mitigated by improving drainage. The installation of median barriers with openings will be limited to highways; however, these barriers will improve conditions of standing water on not only highways but also smaller roads upstream that remain submerged when traditional concrete median barriers cause damming and backwater effects. The research team estimated the installation of the new portable median barriers with scuppers would provide a 10 percent reduction in overall accidents attributed to either wet or standing water road surface conditions, compared to the presently installed portable barriers, by reducing the likelihood of having sustained wet or standing water conditions on highways or surface roads. Coupled with an assumption that roughly 5 percent of roads are under construction (or otherwise require the use of temporary barriers in work/emergency zones) at any given time, there would be a savings incurred of approximately **\$48 million/year**, to be included in the overall VoR calculations.

Data provided by CTR to the TxDOT Austin District estimating incremental user delay cost for highway closure of one direction of IH 35 through Austin were used to estimate a similar effect for a highway in Houston, approximating similar overall usage and cost to users given the proximity of these two metropolitan regions. Given the greater population and quantity of economic activity in Houston, it seems likely that a road closure for a highway in Houston would impede a larger volume of traffic than the same incident on IH 35 in Austin, and so costs may likely be higher. Whereas flooding can occur anywhere in the state, and whereas rural roads are shown to experience similar numbers of fatal or serious injury-sustaining crashes, the research team used Austin statistics to estimate further anticipated savings attributed to road closures. This calculation was as follows.

Assuming a value of lost time of \$27 per hour per user time for the year 2020, the following was calculated for the heaviest usage periods in a typical single day. During the morning peak, 7,641 person-hours were determined by CTR to be the volume of users affected in Austin in 2016. In the evening, this number was 5,064, and early morning (midnight to 6:00 a.m.) was 1,910. Assuming 3 closure hours during each of these periods, multiplied by the number of person-hours and the value of time per user, a total cost of lost time of **\$1.2 million per day** for a single highway closure was calculated. During Hurricane Harvey, flooding was not limited to a single highway, with several highways and dozens if not hundreds of local surface roads closed due to standing water, some for one month or more following the hurricane itself. In particular,

IH 10 and US 90 had significant multiday closures, with IH 10 closed in many locations, and additional closures on IH 45, IH 69, and other important arterial highways through Houston. Highways were closed in Beaumont and other neighboring cities as well, due to both flooding during and immediately after the storm and waiting for debris and obstructions to be cleared even after the water had subsided. Given the wide geographical region of the storm, number of highways affected, multiday closures, and significant location for major international industry, the cost incurred from a single event of the magnitude of Hurricane Harvey is likely to be on the order of \$30 million (assuming on average five roads closed for 5 days). This estimate only encompasses delays to users specifically on these highways and not the complete economic loss to industries that rely on transport, which would extend orders of magnitude above this estimate.

A hurricane of this magnitude does not occur annually, yet smaller hurricanes (e.g., Hurricane Imelda in 2019) also caused closure of IH 10 in Texas due to standing water and transport of debris in floodwaters, and rainstorms commonly close highway underpasses and access roads, thus still impacting highway traffic. Highway closures are not limited to weather, with a water main break causing closure of I-610 in Houston in early 2020 due to flooding, at an estimated cost of \$1 million by the metrics above. Given the wide range of flood-related events that can generate highway closures, a conservative estimate of **\$3 million/year** was used in the VoR calculations.

Finally, given the expected lifespan of a portable concrete median barrier to be 15–25 years, with a likely reduced lifespan of a barrier with an opening installed in locations with an increased susceptibility to flooding, the research team estimated the expected value duration to last up to 15 years. A discount rate of 5 percent was selected as a conservative estimate for future values.

F.5. DISCUSSION

This VoR estimate was developed by the researchers based on their understanding of the functional areas and their assessment of the relative importance of various factors. This estimate likely includes incomplete information and several assumptions. The research team believes this VoR estimate is extremely conservative but chose to provide such a conservative estimate because the Crash Records Information System database only shows reported crashes and does not provide data on all incidents. Further, the value of time estimates was generated by extrapolating data from Austin, which is not an area likely to be impacted by severe highway flooding, so the true cost of a highway closure is likely higher than this estimate.

F.6. REFERENCES

1. <https://www.txdot.gov/data-maps/crash-reports-records/motor-vehicle-crash-statistics.html>
2. <https://ftp.txdot.gov/pub/txdot-info/trf/hsip-guidance-program.pdf>